

THREE DIMENSIONAL PRINTING OF BONE TISSUE
ENGINEERING SCAFFOLD: DESIGN, STRUCTURE,
AND MECHANICAL PROPERTIES

MITRA ASADI-EYDIVAND

THESIS SUBMITTED IN FULFILLMENT OF THE
REQUIREMENTS FOR THE DEGREE OF
DOCTOR OF PHILOSOPHY

FACULTY OF ENGINEERING
UNIVERSITY OF MALAYA
KUALA LUMPUR

2016

UNIVERSITY MALAYA

ORIGINAL LITERARY WORK DECLARATION

Name of Candidate: **Mitra Asadi Eydivand** (I.C/Passport No :) **T27377399**

Registration/Matric No: **KHA130005**

Name of Degree: **PhD of Engineering**

Title of Project Paper/Research Report/Dissertation/Thesis (“this Work”):

**THREE DIMENSIONAL PRINTING OF BONE TISSUE ENGINEERING SCAFFOLD:
DESIGN, STRUCTURE, AND MECHANICAL PROPERTIES**

Field of Study: **Biomedical Engineering (Biomaterials and Tissue Engineering)**

I do solemnly and sincerely declare that:

- (1) I am the sole author/writer of this Work;
- (2) This Work is original;
- (3) Any use of any work in which copyright exists was done by way of fair dealing and for permitted purposes and any excerpt or extract from, or reference to or reproduction of any copyright work has been disclosed expressly and sufficiently and the title of the Work and its authorship have been acknowledged in this Work;
- (4) I do not have any actual knowledge nor ought I reasonably to know that the making of this work constitutes an infringement of any copyright work;
- (5) I hereby assign all and every rights in the copyright to this Work to the University of Malaya (“UM”), who henceforth shall be owner of the copyright in this Work and that any reproduction or use in any form or by any means whatsoever is prohibited without the written consent of UM having been first had and obtained;
- (6) I am fully aware that if in the course of making this Work I have infringed any copyright whether intentionally or otherwise, I may be subject to legal action or any other action as may be determined by UM.

Candidate’s Signature

Date: 03/11/2016

Subscribed and solemnly declared before,

Witness’s Signature

Date:

Name:

Designation:

ABSTRACT

Techniques to restore and replace bones in large fractures are still a major clinical need in the field of orthopedic surgery. Thus, tissue engineering is one of the most hopeful approaches for developing engineered alternatives for damaged bones. Scaffolds are important part of bone tissue engineering (BTE). They are three-dimensional (3D) porous structures that are expected to, at least, partially imitate the extracellular matrix (ECM) of natural bone. Due to the natural properties of bone that are similar to calcium-based ceramics, the fabrication of scaffolds with the same properties as patient's bone and adaptability to fracture defect are still a matter of concern and have remained a challenging area in the BTE field. Since the microarchitecture of a scaffold, like its pore size, and interconnectivity cannot be fully controlled by conventional techniques, recently, the additive manufacturing (AM) techniques have drawn the attention among tissue engineering experts. Other than that, solid freeform fabrication (SFF) is a well-established AM technique that can be employed to produce prototypes from complex 3D data sets. Moreover, the ability of inkjet-based 3D printing (3DP) to fabricate biocompatible ceramics has made it one of the most favorable techniques to build BTE scaffolds. Furthermore, calcium sulfates, which exhibit various beneficial characteristics, can be used as a promising biomaterial in BTE and it is a low-cost material for 3DP. Hence, this project had designed and developed the optimal processing parameters based on the design of the experimental approach and evolutionary algorithms to evaluate the ability of commercial 3D printers for making calcium sulfate-based or in other words, commercial-materials-based scaffold prototypes. Besides the simple design to fulfill the BTE requirements and to study the printing parameters, a library of triply periodic minimal surfaces (TPMS) based unit cells was subjected to finite element analysis and computational fluid dynamic (CFD) simulations. Elastic modulus, compressive strength,

as well as permeability, were characterized for different volume fractions of TPMS structures to develop structure-property correlations with emphasis on describing the architectural features of optimum models. The major printing parameters examined in this study for the simple design were layer thickness, delayed time of spreading the next layer, and build orientation of the specimens. However, low mechanical performance caused by the brittle character of ceramic materials had been the main weakness of the 3DP calcium sulfate scaffolds. Moreover, the presence of certain organic matters in the starting commercial powder and binder solution caused the products to have high toxicity levels. So, after fabrication, post-processing treatments were employed upon optimal specimens to further improve the physical, the chemical, and the biological behaviors of the printed samples. The first post-processing technique was heat treatment, while the second one was phosphate treatment of 3D-printed specimens to convert the calcium sulfate-based prototypes to calcium phosphate ones solely to improve their properties.

ABSTRAK

Teknik untuk pemulihan dan penggantian tulang pada patah yang besar masih merupakan keperluan klinikal yang utama dalam bidang pembedahan ortopedik. Justeru, kejuruteraan tisu merupakan salah satu kaedah yang berguna dalam membangunkan kaedah kejuruteraan untuk tulang yang rosak. “Scaffolds” merupakan bahagian utama dalam kejuruteraan tisu tulang (BTE). Ia adalah struktur rongga tiga dimensi (3D) yang mana dijangka sekurang-kurangnya sebahagian daripadanya menyerupai matrik “extracellular” (ECM) untuk tulang asal. Disebabkan oleh sifat-sifat tulang asal yang menyamai asas kalsium seramik, pembuatan “scaffold” dengan sifat-sifat seperti tulang pesakit dan penyesuaian kepada kesan patah masih lagi merupakan kebimbangan dan tetap sebagai cabaran di dalam bidang BTE. Sejak “scaffolds” untuk “microarchitecture”, seperti saiz rongga dan perhubungan tidak sepenuhnya dikawal oleh teknik konvensional, dan sekarang ini teknik pembuatan bahan tambahan (AM) telah mendapat perhatian oleh pakar kejuruteraan tisu. Selain daripada itu, “solid freeform fabrication” (SFF) adalah teknik terbaik AM yang boleh dipergunakan untuk prototaip bagi menghasilkan set data 3D. Selain daripada itu, kebolehan pencetakan 3D berasaskan “inkjet” untuk fabrikasikan seramik “biocompatible” telah menjadikan salah satu teknik yang disukai untuk membina “scaffolds” BTE. Juga, kalsium sulfat yang menunjukkan karakteristik kemudahan pelbagai dan boleh digunakan sebagai biobahan yang baik dalam BTE, dan juga merupakan bahan yang murah untuk 3DP. Dengan itu, projek ini merekabentuk dan membangunkan parameter yang optimum dalam merekabentuk kaedah eksperimen dan algoritma evolutari untuk menilai kebolehan bagi pencetak komersial 3D dalam membuat kalsium sulfat atau dalam perkataan lain, bahan komersial prototaip “scaffolds”. Selain daripada rekabentuk mudah untuk memenuhi keperluan BTE dan mempelajari parameter pencetakan, perpustakaan untuk sel unit bagi permukaan minimum berulang “triply”

(TPMS) adalah tertakluk kepada analisis kaedah berangka dan simulasi gerakan komputasi bendalir (CFD). “Elastic modulus”, kekuatan mampatan dan juga kebolehtelapan, dikarektarasikan dalam pelbagai pecahan isipadu untuk struktur TPMS bagi membentuk hubungan sifat-struktur dengan menekankan dalam sifat model “architectural” yang optimum. Parameter pencetakan utama yang diperiksa dalam pengajian ini adalah untuk rekabentuk ringkas, yang ketebalan lapisan, kelewatan masa dalam merebakkan lapisan seterusnya, dan membuat orientasi untuk spesimen. Walaubagaimana pun prestasi rendah mekanikal disebabkan oleh bahan seramik yang sifatnya rapuh merupakan kelemahan bagi “scaffolds” kalsium sulfat 3D. Tambahan lagi, dengan adanya sesetengah bahan organik dalam permulaan serbuk komersial dan penyelesaian pengikat untuk bahan toksin yang tinggi. Jadi, selepas fabrikasi, rawatan selepas proses akan dimulakan dengan spesimen yang optimum untuk memperbaiki fizikal, bahan kimia, dan perlakuan biologi untuk spesimen yang dicetak. Untuk teknik pemprosesan selepas yang pertama adalah untuk rawatan haba, manakala keduanya adalah untuk rawatan “phosphate” bagi spesimen pencetakan 3D untuk menukarkan bahan asas prototaip kalsium sulfat kepada hanya kalsium sulfat untuk memperbaiki sifat-sifatnya.

ACKNOWLEDGMENT

My journey towards the completion of this project has been, among other things, exciting, challenging, enlivening, arduous, and greatly satisfying. It would not have come to fruition in such a way without the support of several individuals. It has been a period of intense learning for me, not only in the scientific arena, but also on a personal level.

First and foremost, I would like to express profound gratitude to my supervisors, Prof. Ir. Dr. Noor Azuan Abu Osman, and Prof. Mehran Solati-Hashjin, for their valuable support, encouragement, supervision, and useful suggestions throughout this research work. Their moral support and continuous guidance enabled me to complete my thesis successfully.

Furthermore, I am grateful to the editors of journals and anonymous reviewers for their helpful comments and suggestions on my research during the consideration to publish our articles. Besides, I would like to thank all the staff from the laboratories and technicians.

I am, as ever, especially indebted to my family for their love and support throughout my life.

DEDICATION PAGE

To my mother and the memory of my father.

TABLE OF CONTENT

ABSTRACT.....	III
ABSTRAK.....	V
ACKNOWLEDGMENT.....	VII
DEDICATION PAGE.....	VIII
LIST OF FIGURES.....	XIII
LIST OF TABLES.....	XVIII
LIST OF ABRIVIATIONS.....	XX
LIST OF APPENDICES.....	XXII
1.INTRODUCTION.....	1
1.1 Motivation and problem statement.....	1
1.2 Aim and objectives.....	4
1.3 Outline of thesis.....	5
2. LITERATURE REVIEW.....	8
2.1 Bone.....	8
2.2 Bone tissue engineering scaffolds.....	10
2.2.1 Structural specification.....	12
2.2.2 Biocompatible materials.....	16
2.2.3 Mechanical properties.....	19

2.2.4	Fabrication methods.....	19
2.3	Powder based three dimensional printing.....	20
2.3.1	Optimization of process parameters.....	25
2.3.2	Post-treatments.....	29
2.4	Summary.....	33
3.	MATERIALS AND METHODS.....	34
3.1	Fabrication of 3d-printed prototypes.....	34
3.1.1	Printing materials.....	35
3.1.2	Design of scaffold.....	36
3.1.3	Technical parameters.....	45
3.2	Evaluation of fabricated scaffolds.....	47
3.2.1	Mechanical properties.....	48
3.2.2	Dimensional accuracy.....	49
3.2.3	Porosity.....	50
3.2.4	Thermal analysis.....	51
3.2.5	Statistical analysis.....	51
3.3	Process parameters optimization methods.....	52
3.3.1	Aggregated artificial neural network.....	52
3.3.2	Particle Swarm Optimization.....	56
3.4	Protocols of post- treatment.....	59

3.4.1 Heat-treatment.....	59
3.4.2 Phosphate treatment.....	59
3.5 Characterization of post-treated scaffolds	60
3.5.1 Mechanical testing.....	60
3.5.2 Shrinkage and density measurement.....	60
3.5.3 Composition and microstructure.....	62
3.5.4 <i>In vitro</i> protocol.....	62
3.5.5 Statistical analysis.....	63
3.6 Summery	64
4. RESULTS AND DISCUSSION.....	65
4.1 Fabricated scaffolds.....	65
4.1.1. Material characterization.....	65
4.1.2 Dimensional Features.....	75
4.1.3 Mechanical properties.....	83
4.1.4 Porosity.....	89
4.2 Optimum process parameters.....	93
4.2.1 Effect of process parameters on compressive strength.....	93
4.2.2 Effect of process parameters on porosity.....	96
4.2.3 Proposed topology for AANN and optimization.....	99
4.3. TPMS based model and simulation results.....	109

4.3.1	Voxel mesh convergence study for TPMS based unit cells.....	110
4.3.2.	Development of Structure-Elastic Properties Correlations.....	112
4.3.3.	Mechanical properties versus deformation mechanisms.....	118
4.3.4.	Bio-fluid permeability characterization of TPMS architectures..	123
4.3.5	Experimental evaluation of TPMS based ceramic scaffolds.....	126
4.4	Heat treatment.....	131
4.4.1	Composition and microstructure.....	131
4.4.2	Mechanical features, shrinkage, and density.....	142
4.4.3	<i>In vitro</i> evaluation	151
4.5	Phosphate treatment.....	152
4.5.1	Composition and microstructure.....	152
4.5.2	Mechanical features.....	163
4.6	Summary.....	166
5.	CONCLUSION AND FUTURE DIRECTION.....	168
5.1	Conclusion.....	169
5.2	Future direction.....	176
	REFERENCES.....	177
	APPENDIX A.....	191

LIST OF FIGURES

CHAPTER 2: LITERATURE REVIEW

Figure 2.1: Bone section showing cortical and trabecular bone	9
Figure 2.2: Schematic illustration of the 3DP process.....	23

CHAPTER 3: MATERIALS AND METHODS

Figure 3.1: CAD design of unit cells and porous scaffolds.....	37
Figure 3.2: Structural details of the porous scaffold CAD and the unit cell design	38
Figure 3.3: Layer by layer meshing representation of RVE of scaffolds.....	40
Figure 3.4: Theoretical parameters and boundary condition for cantilever beam.....	42
Figure 3.5: Top view of Zp450 Build bed size.....	47
Figure 3.6: Proposed structure of the AANN for 3DP process.....	53
Figure 3.7: Heat treatment of the 3D-printed specimens results in shrinkage	61

CHAPTER 4: RESULTS AND DISCUSSION

Figure 4.1: XRD patterns of the starting powder and printed scaffold	67
Figure 4.2: FTIR spectra of the zb63 binder, pure water and 2-pyrrolidinone	69
Figure 4.3: FTIR spectra of the scaffold and ZP150 starting calcium sulfate powder.....	70
Figure 4.4: Differential and cumulative particle size distributions of the zp150	72
Figure 4.5: SEM Image of powder particles after fabrication	73
Figure 4.6: Fabricated scaffold	74
Figure 4.7: Top and side views of the fabricated scaffold	74
Figure 4.8: SEM images of fabricated scaffold	75
Figure 4.9: Micro-CT images - fabricated scaffold	75
Figure 4.10: SEM image- fabricated scaffold pore and strut dimension	76
Figure 4.11: The dimensional accuracy ratio of scaffolds.....	89
Figure 4.12: Main effect plot for dimensional deviation ratio	80

Figure 4.13: Degree of anisotropy of fabricated specimens in X direction	81
Figure 4.14: Main effect plot for degree of anisotropy	83
Figure 4.15: The Micro-CT images of the front and top view of the specimens.....	86
Figure 4.16: Compressive strength of specimens which fabricated in X orientation	87
Figure4.17: Binder-jetting and powder-spreading directions.....	87
Figure 4.18: Main plot for Compressive strength	88
Figure 4.19: Main effect plot for porosity.....	91
Figure 4.20: Schematic of the build bed printing layout and printing parameters.....	92
Figure 4.21: Effect of 3DP setting parameters on the compressive strength.....	94
Figure 4.22: Effect of the 3DP setting parameters on open porosity.....	97
Figure 4.23: Training and testing accuracy of the obtained AANN in predicting the mechanical compression strength.....	103
Figure 4.24: Open porosity parameter modeling performance for both of (a) training and (b) testing phases.....	104
Figure 4.25: Variations of open porosity with respect to the variations of delay time and layer thickness for different depositing directions.....	105
Figure 4.26: Variations of mechanical strength with respect to the variations of delay time and layer thickness for different depositing directions.....	106
Figure 4.27: Pareto front of the 3D printing process.....	108
Figure 4.28: Representation of 70% porosity scaffolds designed for evaluating mechanical properties according to the critical models obtained in finite element simulations.....	110
Fig. 4.29: Convergence representation of finite element simulations for voxel based models with 11 different seed sizes of pre-selected unit cell models.....	112
Figure 4.30: The domain of numerical (a) elastic modulus and (b) compressive strength versus volume fraction.....	113

Figure 4.31: Relationships between compressive yield strength and Young's modulus for different TPMS unit cell geometries.....	116
Figure 4.32: The effect of relative density and pore architecture on the normalized yield strain.....	117
Figure 4.33: The results of calculated percentage contribution of bending in compressive deformation versus volume fraction for different TPMS topologies.....	123
Figure 4.34: Variation of computational normalized permeability with relative density for different TPMS architectures.....	125
Figure 4.35: Normalized Young's modulus versus normalized permeability.....	126
Figure 4.36: Experimental compressive stress-strain curves for Ixxx-J* and Fxyz-Fxxx2 structures.....	128
Figure 4.37: Comparing the average elastic modulus and compressive strength for three different cell sizes of Ixxx-J* and Fxyz-Fxxx2 structures.....	130
Fig 4.38: SEM Images of 3D-printed scaffolds, Ixxx-J* with cell size of (a) 6.67mm (b) 5mm (c) 4mm and Fxyz-Fxxx2 with cell size.....	130
Figure 4.39: TG curve of the as-printed scaffold and its derivative (DTG)	131
Figure 4.40: Samples heat treated at various temperatures.....	132
Figure 4.41: TG-DTA curve of as-printed scaffold.....	133
Figure4.42: XRD patterns of the printed scaffolds after heat treatment at various temperatures from 300 °C to 1300 °C.....	134
Figure 4.43: XRD pattern of the printed scaffold after heating at 1200 °C, 1250 °C, and 1300 °C.....	135
Figure 4.44: SEM backscattered mode image of the microstructures of the as-printed scaffold and samples heat treated at 300 °C, 500 °C, 900 °C, and 1000 °C.....	136

Figure 4.45: SEM backscattered mode image of the microstructures of the samples heat-treated at 1150 °C, 1200 °C, 1250 °C, and 1300 °C.....	138
Figure 4.46: SEM-EDS elemental map analysis of the as-printed scaffold.....	139
Figure 4.47: SEM-EDS (line scan) analysis of the specimen heated at 300 °C.....	139
Figure 4.48: SEM-EDS elemental map analysis of the specimen heated at 500 °C.....	140
Figure 4.49: SEM-EDS elemental map.....	141
Figure 4.50: SEM micrograph of the sample heated at 1200 °C. Formation of calcium oxide.....	141
Figure 4.51: Specimens under compression test.....	143
Figure 4.52: Strain–stress curves for porous scaffolds heat treated at 300 °C, 1000 °C, 1150 °C, 1200 °C, 1250 °C, and 1300 °C.....	144
Figure 4.53: Change in compressive strength and Young’s modulus of the porous and solid specimens with heat treatment temperature.....	146
Figure 4.54: Bulk density, volume, and weight of the porous and solid specimens versus heat treatment temperature.....	147
Figure 4.55: Thickness and diameter shrinkage percentage of the samples as a function of heat treatment temperature.....	150
Figure 4.56: Results of MTT assay on the ZP150 powder, as-printed scaffold, and samples heated at 300 °C, 1150 °C, 1200 °C, and 1300 °C.....	151
Figure 4.57: XRD patterns of the 3D-printed scaffolds after heat treatment at 1150°C and phosphate treatment for (a)4, (b)8, (c)16, and (d)24h.....	154
Figure 4.58: SEM-EDX micrograph of the sample heat-treated at 1150°C and phosphate-treated at 85°C for 24 h.....	156
Figure 4.59: XRD patterns of the 3D-printed scaffolds after hear treatment at 1200°C and phosphate treatment for 4, 8, 16, and 24h.....	156

Figure 4.60: Figure 4: SEM-EDS (line scan) analysis of the specimen heat-treated at 1200°C and phosphate-treated at 85°C for 24h.....	159
Figure 4.61: XRD patterns of the 3D-printed scaffolds after heat treatment at 1250°C and phosphate treatment for 4, 8, 16, and 24h.....	160
Figure 4.62: SEM-EDS (spot and line scan) analysis of the specimen heat-treated at 1250°C and phosphate-treated at 85°C for 24h.....	162
Figure 4.63: Trend of compressive strength and young's modulus of phosphate treated samples at different temprature and time.....	165
Figure 4.64 : strain- stress curve of phosphate treated samples at each temprature for 24 hours.....	165

LIST OF TABLES

CHAPTER 2: LITERATURE REVIEW

Table 2.1. Summary of recent studies about phosphorization of 3D printed calcium sulfate objects.....	31
---	----

CHAPTER 3: MATERIALS AND METHODS

Table 3.1. The Specification of CAD design scaffolds	36
Table 3.2. The design of experiment's factors and their levels.....	46

CHAPTER 4: RESULTS

Table 4.1: Calcium sulfate phases present in the porous and solid 3DP scaffolds	69
Table 4.2: The measurement of diameter and height	77
Table 4.3: Analysis of variance of DDR	79
Table 4.4: Degree of anisotropy of all 48 runs	80
Table 4.5: Analysis of variation of DA for full factorial design model.....	82
Table 4.6: Mechanical property assessment of porous 3D printed specimens.....	85
Table 4.7: Analyze of variance of compressive strength for full factorial design model	88
Table 4.8: Porosity of 3D printed specimens.....	89
Table 4.9: Analyze of variance of porosity for full factorial design model.....	90
Table 4.10: the optimum fabricated scaffolds in terms of compressive strength.....	92
Table 4.11: Variables of solution vector.....	100
Table 4.12: Parameters of the optimum AANN structure.....	101
Table 4.13: Parameters of optimum weighting coefficients with fixed optimum AANN structure.....	101
Table 4.14: Results of the 3DP process Pareto front.....	109
Table 4.15: Results of curve fitting to express variations of biomechanical properties..	119

Table 4.16 Chemical analysis of spots 1 and 2 (in Figure 4.32)	142
Table 4.17 Results of the compressive strength test, Young's modulus, and bulk density of the porous and solid samples after heat treatment at various temperatures.....	144
Table 4.18 Shrinkage of the cylinder-shaped porous and solid samples after heat treatment at various temperatures.....	145
Table 4.19: Results of ANOVA for diameter, height, and weight.....	149
Table 4.20: Results of the compressive strength test, Young's modulus, and bulk density of the phosphorized porous samples.....	164

LIST OF ABRIVIATIONS

3DP	Three Dimensional Printing
AANN	Aggregated Artificial Neural Network
AM	Additive Manufacturing
ANN	Artificial Neural Network
ANOVA	Analysis of Variance
BTE	Bone Tissue Engineering
ECM	Exteracellular Matrix
CAD	Computer-Aided Design
CFD	Computational Fluid Dynamic
CP	Calcium Phosphate
CS	Calcium Sulfate
DA	Degree of Anisotropy
DDR	Dimensional Distortion Ratio
DOE	Design Of Experiment
EDS	Energy Dispersive Spectroscopy
FEM	Finite Element Analysis
HA	Hydroxyapatite
Micro-CT	Micro-Computed Tomography

MRI	Magnetic Resonance Imaging
NCBI	National Cell bank of Iran
PSO	Particle Swarm Optimization
SEM	Scanning Electron Microscopy
SFF	Solid Free Form Fabrication
SNN	Stacked Neural Network
RVE	Representative Volume Element
STA	Simultaneous Thermal Analysis
TPMS	Triply Periodic Minimal Surfaces
XRD	X-Ray Diffraction

LIST OF APPENDICES

APPENDIX A: PUBLICATIONS191

CHAPTER 1

INTRODUCTION

This chapter contains the introduction to the issues in which the research is concerned. Besides, the aims and objectives of the study are in the next part of this chapter. Finally, this chapter ends with the outline of the research approach.

1.1 Motivation and problem statement

The increasing proportion of older people in this ageing population indicates that urgent action is required to tackle the projected burden of osteoporosis. Worldwide, osteoporosis had caused more than 8.9 million fractures annually, resulting in an osteoporotic fracture at every 3 seconds (Johnell, & Kanis, 2006).

Moreover, techniques to restore and replace bones in large fractures are still a major clinical need in the field of orthopedic surgery. Tissue engineering is one of the most hopeful approaches for developing engineered alternatives for damaged bones (Pina, Oliveira, & Reis, 2015). Hence, scaffolds for BTE applications are anticipated to have certain properties to encourage bone regeneration. Scaffolds are highly porous structures with interconnected pores. They should ideally be biocompatible, mechanically reliable, biodegradable, and osteoconductive (Blom, 2007; Bose, Vahabzadeh, & Bandyopadhyay, 2013a; Karande, Ong, & Agrawal, 2004; Lichte, et.al, 2011; Polo-Corrales, Esteves, & Vick, 2014). In fact, many experts believe that the progress of BTE is seemingly associated with the improvements in scaffold technology (Burg, Porter, & Kellam, 2000;

Guo, et.al, 2015). With that, numerous multidisciplinary studies have been carried out in this field; from design and modeling to material processing and post-treatments, as well as *in vitro* and *in vivo* biological evaluations (Furth, Atala, & Van , 2007; Lichte et al., 2011; Munch et al., 2008; Wu et.al, 2014). Furthermore, various processing techniques, such as salt leaching (Sadiasa, Nguyen, & Lee, 2013), foam replica (Fereshteh et.al, 2015), gas foaming (Gentile et.al, 2014), freeze casting (Sadeghpour et.al, 2014), and electrospinning (Rajzer et.al, 2014), have been used to fabricate scaffolds. However, most of these methods have failed to completely control the structural properties and the reproducibility of the scaffolds.

Therefore, a great deal of attention has been given to the additive manufacturing (AM) methods in recent years. These methods are a group of advanced fabrication methods, generally branded as solid freeform fabrication (SFF), in which three-dimensional (3D) articles can be constructed layer by layer in an additive manner straight from the data obtained by computer-aided design (CAD), computed tomography, and magnetic resonance imaging. Moreover, rapid prototyping techniques have displayed the ability for the fabrication of pre-defined, customized, and reproducible scaffolds with tailored architecture and porosity (Chen et.al, 2007; Chia, & Wu, 2015; Mazzoli et.al, 2015; Wu et al., 2014; Zhou et.al, 2014). Among the SFF methods, powder-based 3D printing (3DP) has been widely used to construct BTE scaffolds. In the 3DP method, the geometry, the shape, and the internal porous structure of the implant are first designed in a CAD environment. Afterward, the CAD model is transformed into image slices. The scaffold is then printed in a layer-by-layer manner via repetitive stacking of powder layers. Binder droplets, after that, are selectively jetted to the pre-deposited thin layer of the powder to fabricate a model based on a sequence of mathematically sliced cross sections of the CAD file. This method is a promising approach in the field of tissue

engineering, specifically for bone substitute fabrication (Butscher et.al, 2011; Leong, Cheah, & Chua, 2003; Yang, 2001). Thus, a large number of biocompatible ceramic and composite materials can be processed by using the 3DP technique (Bose et al., 2013a, Vorndran, Moseke, & Gbureck, 2015; Zhou et al., 2014).

Calcium sulfate was introduced as a bone substitute material in 1892 (Brand, 2012). In 1961, Peltier introduced calcium sulfate as a suitable material for filling bone defects (Brand, 2012). Since then, further studies have been conducted on calcium sulfate (Insights et.al, 2014; Zhou et.al , 2012). Moreover, the composites of calcium sulfate have been manufactured under commercial brands (Kassim et al., 2014; Rauschmann et al., 2010) for BTE applications. Calcium sulfate is biocompatible, osteoconductive, and highly resorbable (Doty,et.al , 2014; Rauschmann et al., 2005; Sottosanti, 1992; Thomas & Puleo, 2009; Thomas, Puleo, & Al-Sabbagh, 2005).

Moreover, previous reports by Kameda et al., (1998), and Peltier, Bickel, Lillo, and Thein (1957) suggested that the release of calcium ions from calcium sulfate implants as a result of the dissolution process increases the number of osteoblasts and osteoclasts at the wound site by enhancing cellular genesis, thereby enhancing bone regeneration. Calcium sulfate can also be considered as a promising vehicle for the delivery of therapeutic compounds, such as drugs, antibiotics, proteins, and platelet-derived growth factors (Bateman et al., 2005; Nyan et al., 2007). Therefore, calcium sulfates have exhibited several useful characteristics as an ideal bone tissue regenerative biomaterial. With recent advances in ceramic science and engineering, calcium sulfates can be considered as suitable materials for BTE applications (Hollinger, 2011; Park et al., 2011).

Nevertheless, the major weakness of 3DP porous structures with commercially available binder and powder is their relatively low mechanical performance due to the brittle nature of ceramic materials and also their biocompatibility. Therefore, post-processing treatments are usually employed to improve the strength of the printed objects. Recent studies on post-processing of 3DP scaffolds for tissue engineering applications have disclosed that post-treatments may significantly influence both the physical and the chemical properties of the fabricated 3D objects, as well as the *in vitro* behavior of them. The most common post-processing procedure to improve the strength of the ceramic-based printed objects is heat treatment (Lam, et.al, 2002; Zhou et al., 2012). Additionally, as the binders of the commercial powder-based printers contain non-biocompatible organic solutions, treatment of high temperature heat results in less toxicity in scaffolds by burning out the toxic substances. Furthermore, in this project, the transformation process of calcium sulfate (CS) 3D-printed scaffolds into calcium phosphate (CP) objects had been investigated by employing a thermo-chemical process, which can be considered as the second post-treatment to improve the properties of scaffold. Moreover, this reflects one step closer to fulfil the bone tissue engineering (BTE) requirements through the use of available commercial printers and materials (Frascati, 2007; Impens, 2015; Lam et al., 2002; Trdnost & Modelov, 2013, Utela, et.al, 2008).

1.2 Aims and Objectives

The current project has designed, fabricated, and evaluated the overall efficiency of BTE scaffold with the aid of commercial powder-based 3D printer and post-processing techniques. Hence, in order to achieve these aims, five objectives were identified, as given in the following:

- i. To design a porous structure to meet BTE scaffold requirements
- ii. To evaluate the effect of process parameters (layer thickness, delay between spreading each layer, and orientation) on dimensional accuracy, mechanical properties, and porosity of printed scaffolds
- iii. To determine the optimum printing conditions by artificial neural network for the designed scaffolds
- iv. To investigate the effect of heat treatment on structural and mechanical properties, as well as *in vitro* behavior of the 3D-printed scaffolds
- v. To explore the influence of the phosphate treatment (conversion of calcium sulfate scaffolds into calcium phosphates) on mechanical properties and morphology of 3D-printed scaffolds

1.3 Outline of thesis

Inclusive of the current introductory chapter, this thesis consists of five chapters, whose content is briefly described in the following:

The thesis begins with Chapter 1, which presents the motivation, the problem statement, and the purpose of this thesis. Next, Chapter 2 provides a review of the topics relevant to the research presented. The review examines properties of vertebrates bones, BTE scaffolds and their requirements, fabrication methods of scaffolds especially 3DP method, process parameter optimization, as well as post-treatment techniques for commercially 3D-printed objects.

A general methodology section is presented in Chapter 3. It describes the methods used to design the scaffolds (both the simple one to fulfil the BTE requirements, and also the triply periodic minimal surfaces (TPMS) model), the materials and the machines employed for fabrication and characterization of the scaffolds, the process parameters that were considered for studying their effects upon printing the scaffolds. This chapter further details the techniques used for evaluating the printed specimens for obtaining the optimal process parameters, as well as the computational methods. Furthermore, the protocols of post-treatments and *in vitro* tests are described.

As for Chapter 4 contains five subsections where each one focuses on the results and the discussions of the five objectives outlined in the thesis. The first subsection examines the characterization of the materials and the fabricated specimens, as well as the mechanical, the dimensional, and the morphological features of the scaffolds. Next, the second subsection reports and discusses the results of the design of experiment and predictive models used for obtaining the optimum printer parameters. Meanwhile, the third subsection focuses on the TPMS-based model simulation results, the mechanical properties, the deformation mechanisms, and the experimental evaluation of TPMS-based model. Moving on, the fourth subsection depicts the results and discusses the composition, the microstructure and mechanical, the shrinkage, and the density of heat-treated scaffolds, as well as *in vitro* evaluation of them. Lastly, the fifth subsection looks into the effect of phosphate treatment on composition, microstructure, and mechanical properties of 3D-printed scaffolds.

Chapter 5 provides a summary based on the findings obtained from this thesis, while the limitations are explored. This chapter is closed with recommendations for future

studies on improving the properties of commercially 3D-printed scaffolds to fulfill the requirements of BTE application.

CHAPTER 2

LITERATURE REVIEW

This chapter provides a comprehensive review on area related to 3DP of BTE. The review of previous and current literature provides an outline of the body of knowledge that explores the aspects of BTE requirements, 3DP of BTE, and post-processing techniques to fulfill the BTE requirements. The first part of this chapter discusses the overview of chemical, structural, and mechanical properties of bone. Topics relevant to requirements of BTE application are reviewed in the second part of this chapter. It continues with the third part, which explains the process of 3DP of BTE scaffolds. This part reviews the main process parameters that affect the properties of printed objects. Besides, the process parameter optimization and post-treatment methods are reviewed in this part. Finally, this chapter ends with a summary of the contribution of the current thesis to the body of knowledge related to the 3DP of BTE scaffolds.

2.1 Bone

The skeleton of vertebrates is formed by rigid organs called bones. Bone is hard, rigid, and has the ability to regenerate, as well as repair itself. The structure of bone is composed of 69% of inorganic components that are constituted by 99% of hydroxyapatite and 22% of organic components that mainly consist of collagen (90%) (Datta, et.al, 2008; Peel, 2012; Yuan, Ryd, & Huiskes, 2000). Stiffness and compression strength are attributed to the inorganic components, while organic components are mainly responsible

for the tension properties. However, diseases (i.e. osteoporosis, and cancer), sex, age, and species affect the composition of bone.

Bone has a hierarchical, porous, interconnected, non-homogeneous, and anisotropic structure. Concerning porosity, bone is divided in two types, as shown in Figure 2.1. The first kind is called cortical or compact bone, which is the dense part of the outer layer of bone with 5-10% porosity (Kim, 2005). The other is cancellous or trabecular found in the ends of long bones, flat bones, and cuboidal bones, with 50-95% porosity. The pores, which are highly interconnected, are occupied with marrow that contains several types of cells and blood vessels (Spears et al., 2000).

Except for the ability to support the body framework and to protect vital organs, bone has the power of regeneration and self-repair (fracture healing). Bone is a dynamic tissue that involves a cycle of continuous process of formation of a new tissue and resorption of the older ones. In fact, there are four types of bone cells classified based on their functions in relation to growth, modeling, remodeling, and fracture healing processes (Bulstrode et al., 2002).

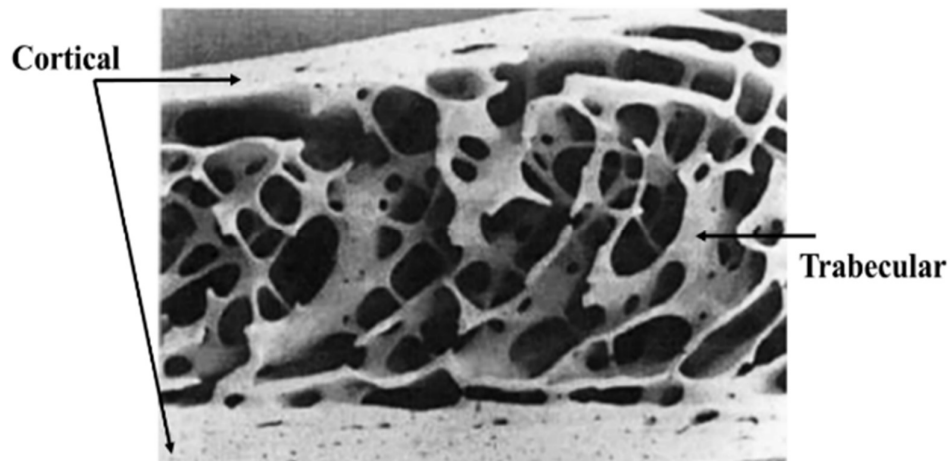


Figure 2-1: Bone section showing cortical and trabecular bone (Yuan et al., 2000)

Osteoblasts are responsible to produce bone, in contrast to osteoclasts that demineralize bone and dissolve collagen; in short, they remove bone. Osteoclasts and osteoblasts are differentiated from mesenchymal cells that exist in the bone marrow. The other kinds of bone cells are osteocytes and lining cells buried in bone matrix and new bone respectively. They are inactive osteoblasts that many authors suggest they are incorporated in bone remodeling process and control it (Andreykiv, et.al, 2005; Mann & Damron, 2002; Pérez, García, & Doblaré, 2005; Stolk, Verdonshot, & Huiskes, 2001).

A further challenge is that healing rates vary with age; for example, in young individuals, fractures normally heal to the point of weight-bearing in about six weeks, with complete mechanical integrity not returning until approximately one year after fracture, but in the elderly, the rate of repair slows down. This too must be taken into account when designing scaffolds for orthopedic applications. However, as the field has evolved, it could be argued that too much focus has been placed on trying to develop scaffolds with mechanical properties similar to bone and cartilage.

2.2 Bone tissue engineering (BTE) scaffolds

The bone is recognized for its self-healing quality. As the regular bone remodeling processes may not repair the large-scale bone defects (>10mm), amending significant bone losses is still a major challenge (Lichte et al., 2011; Salgado, Coutinho, & Reis, 2004). The focus of the traditional treatments has been on replacing the lost bone with autologous bone implants, allogeneic banked bone or from xenogeneic origins. However, all these methods result in a restricted degree of structural and functional recovery, where factors, such as the quantity of available donor tissues, and complications at the donor site, limit the efficiency of autogenous bone grafting.

Allogeneic bone grafts may provoke cell-generated immune response, and thus, possible transfer of pathogens could be challenging.

Bone tissue engineering (BTE), as a multidisciplinary approach, has the potential to find a solution to these long-established problems (Chan, & Leong, 2008; Costa-Pinto, Reis, & Neves, 2011; Moore, Graves, & Bain, 2001; Nair, et.al, 2011; Salgado et al., 2004). Scaffolds, the essential part of BTE, are highly porous 3D structures that imitate the extracellular matrix (ECM) of bone on a temporary basis. Seeding and cultivating scaffolds with bone cells is the standard method in BTE. Scaffolds for BTE applications are anticipated to have certain properties to encourage bone regeneration. In fact, many experts believe that the progress of BTE is seemingly associated with the improvements in scaffold technology (Burg et al., 2000; Guo et al., 2015).

Moreover, from the technical point of view, scaffold engineering sets high demands on design and materials. In addition to chemistry, interconnected porosity, permeability, and mechanical strength are critical parameters that define the performance of a scaffold (Blom, 2007; Bose et al., 2013a; Karande et al., 2004; Lichte et al., 2011; Polo-Corrales et al., 2014). These factors cannot be controlled precisely through conventional fabrication processes (Bose et al., 2013a; Hutmacher, 2000; Karande et al., 2004). Hence, numerous multidisciplinary studies have been carried out in this field, from design and modeling to material processing and post-treatments, as well as *in vitro* and *in vivo* biological evaluations (Furth et al., 2007; Lichte et al., 2011; Munch et al., 2008; Wu et al., 2014). Besides, a number of key considerations are important when designing or determining the suitability of a scaffold for BTE. These functions and features can be considered as given in the following sub sections.

2.2.1 Structural specification

A highly porous interconnected 3D structure is required in BTE to act as an ECM and guide for cell proliferation, differentiation, as well as eventual tissue growth. Fluid flow through a bone scaffold (permeability) is an important factor because of its ability to build living tissue. In fact, successful BTE depends on the ability of the scaffold to enable nutrient diffusion and waste removal from the regeneration site, as well as to provide an appropriate mechanical environment. That is maximum permeability is needed for the mechanical properties not to be compromised. Therefore, a trade-off exists between these two requirements (Dias, et.al, 2012).

Internal and external architectures of a scaffold, in terms of pore size, shape, and distribution, can affect both *in vivo* and mechanical performance. When it comes to morphologic design, biomechanical modulation involving simultaneous consideration of structural and bio-fluidic properties is indeed vital (Dias, et.al, 2014). The pore size must be in a critical range of size. Nonetheless, the optimal pore size for BTE is still a matter of debate. Large pore size decreases the available surface area that results in limiting cell attachment. On the other hand, small pore size reduces the permeability of scaffolds and migration of cells (Rajagopalan, & Robb, 2006). From a microscopic viewpoint, albeit the significant impact of the main topological features on biological efficiency that have been frequently addressed, there are still conflicts between the reported data (Zhang, Lu, Kawazoe, & Chen, 2014). Although the macro-pore size range of 100-1000 μ m is generally reported for cell attachment and vascularization through the pores (Voronov, et.al, 2010), some other studies have reported different ranges of pore size. The minimum pore size of 80 μ m has been found to be necessary for cell penetration (Rose et al., 2004). Many studies also have suggested the pore size values higher than 300 μ m for enhanced

cell proliferation (Karageorgiou & Kaplan, 2005; Lien, Ko, & Huang, 2009). Nevertheless, Murphy et al., in their research, revealed that scaffolds with macro-pores in the range of 300 to 800 μm caused efficacious bone growth (Han, et.al, 2013). While other researchers like Melchels et al., (2010), Vivanco, et al. ,(2012) and Lin, et al., (2004) pointed the pore size range from 200 to 400 μm , the other studies proved successful *in vitro* results with 500 μm pore size (Bose, Roy, & Bandyopadhyay, 2012; Butscher et al., 2011; Chan, & Leong, 2008; Leong et al., 2003; O'Brien, 2011). Furthermore, in the range of 300-1200 μm , no considerable difference was found in bone formation (Hollister et al., 2005). Besides, in terms of porosity, values higher than 85% had been found to improve cell penetration up to 400 μm (Ji, Khademhosseini, & Dehghani, 2011), whereas porosities larger than 75% were suggested to ensure cell proliferation (Gomes, et al., 2006; Zeltinger, et al., 2001). Moreover, Danilevicius et al., (2015) observed higher efficiency for scaffold with 86% porosity compared to those with 82% and 90%. Given these disparity and complications, many attempts have been made to quantitatively describe the permeability of porous scaffolds to conglomerate the main topological features, such as porosity, pore architecture, pore size, and interconnectivity, through which the biological efficiency of pore morphology is characterized (Dias et al., 2012; Sandino, et.al, 2014; Widmer & Ferguson, 2013). Furthermore, a study by Syahrom, et.al.,(2013) claimed that the prismatic plate and the rod model displayed similar permeability as natural bone and higher permeability was attributed to structures that comprised of tetrakaidecahedral unit cells. Moreover, the accuracy of computational fluid dynamic (CFD) calculations in predicting permeability of regular scaffolds was looked into by Truscello et al., (2012) and their results were in agreement with the experimental data by less than 27% error. In addition, it is imminent to note that only open and interconnected pores contribute to permeability and cell in-growth, whereas closed pores only reduce the strength.

At a macroscopic level, particularly in the case of metallic scaffolds and those biomaterials with higher stiffness, mismatches between elastic properties and host tissue interface bring about bone resorption as a result of stress shielding and consequently, leads to mechanical loosening in the implantation site (Hoyt, et al., 2015). For instance, titanium is reported to have elastic modulus of 110GPa, which is overwhelmingly higher than that of cancellous and cortical bones with the reported range of 0.05-0.5GPa (Henkel et al., 2013) and 12-18GPa (Jamshidinia, et al., 2014), respectively. Hence, for an improved osteointegration, highly porous structures with adequate interconnectivity is proposed (Zhu et al., 2014) by providing high permeability values in low stiffness materials. Nevertheless, increasing porosity leads to poor mechanical strength and especially in higher pore sizes, the cell differentiation process can be affected. Therefore, a trade-off should be made between structural properties and biological considerations (Bernstein et al., 2013). Besides, cells are believed to sense physiological loads in the form of local strains, thereby scaffolds are expected to be non-toxic and provide adequate rigidity for controlled differentiation (Rajagopalan, & Robb, 2006; Voronov et al., 2010). This issue can also be addressed by getting insight into the deformation behavior of micro-struts under physiological loadings through structure-property relationships between cellular architecture and deformation modes, and thereby, the mechanical properties of scaffolds. Additionally, the current trend on deformation mechanism of porous materials is to classify porous architectures to bending and stretching dominated structures based on internal pore architecture. However, no quantitative evaluation has been developed to distinct the trend of structure to bending or stretching deformation and to show how relative density affect the failure behavior of cellular materials.

In addition, since the advent of additive manufacturing (AM) techniques, triply periodic minimal surfaces (TPMS) have served as a promising tool for microstructure design due to their intrinsic superior features, such as interconnectivity, tortuosity, and high surface to volume ratio. Design space is partitioned into two or more phases by applying TPMS equations, resulting in open periodic porous structures with smooth joints and curvatures (Yan, et al., 2015; Yoo, 2011). Besides, Olivares, et al., (2009) discovered the higher capability of Gyroid surface compared to conventional hexagonal architecture in promoting the differentiation process. Moreover, cell response in Gyroid structure is shown to be substantially enhanced in comparison to salt-leached scaffolds since the 10-fold improvement in permeability, thereby cell penetration into the center of scaffolds (Melchels et al., 2010). In addition to the smooth topology that is aimed to enhance cell response, TPMS has exhibited a superior potential for designing gradient structures both in morphology and relative density by manipulating implicit constitutive equations of TPMS (Almeida, & Bártolo, 2014). Hence, designing multifunctional scaffolds is feasible by locally modulating biomechanical properties provided that the characteristics of uniform constitutive unit cells have been adequately recognized. For instance, Kapfer, et al., (2011) described the mechanical properties of sheet and network solid models for different scaffolds made of TPMS-based geometries at 50% relative density. In this study, a library of TPMS-based unit cells were subjected to finite element analysis and CFD simulations. Elastic modulus, compressive strength, as well as permeability, were characterized for different volume fractions of TPMS structures to develop structure-property correlations with emphasis on describing the architectural features of optimum models. Since conflicting biological requirements with the mechanical considerations had been observed, permeability was discussed versus structural properties. In addition, the concept of stretching and bending that dominated deformations was introduced through the analysis of strain energy to take the effect of porosity on deformation mechanism into

account. Then, relationships between deformation behavior and mechanical properties were discussed. Furthermore, in order to evaluate the versatility of the current powder-based 3DP techniques, calcium sulfate scaffolds were designed based on the critical results of computational properties and printed with different cell sizes to address how representative volume elements can be generalized to scaffolds that comprised of the same pore architecture.

2.2.2 Biocompatible materials

The aim of tissue engineering is using the scaffold as a temporary implant that with the aid of the patient's own cells to regenerate the tissue and eventually degrade in the body without any toxicity of degradation by-products and interference from the surrounding tissues and other organs. Therefore, the scaffold must be biocompatible and also biodegradable to allow cells to produce their own ECM (Bose, Roy, & Bandyopadhyay, 2012; Chan, & Leong, 2008; Leong et al., 2003).

2.2.2.1 Calcium sulfates

Calcium sulfate was introduced as a bone substitute material in 1892 by Dreesman (Brand, 2012). In 1961, Peltier introduced it as a suitable material for filling bone defects (Brand, 2012). Since then, further studies have been conducted on calcium sulfate (Kassim et al., 2014; Zhou et al., 2012). Moreover, the composites of calcium sulfates have been manufactured under commercial brands (Kassim et al., 2014; Rauschmann et al., 2010) for BTE applications. Calcium sulfate is biocompatible, osteoconductive, and highly resorbable (Doty et al., 2014; Rauschmann et al., 2005; Sottosanti, 1992; Thomas & Puleo, 2009; Thomas et al., 2005).

In fact, Kameda et al., (1998), and Peltier et al., (1957) suggested the release of calcium ions from calcium sulfate implants as a result of the dissolution process that increases the number of osteoblasts and osteoclasts at the wound site by enhancing the cellular genesis, and thus, enhancing bone regeneration. Calcium sulfate can also be considered as a promising vehicle for delivery of therapeutic compounds, such as drugs, antibiotics, proteins, and platelet-derived growth factor (Bateman et al., 2005; Nyan et al., 2007). Therefore, calcium sulfates have projected many useful characteristics as an ideal bone tissue regenerative biomaterial. With recent advances in ceramic science and engineering, calcium sulfates can be considered as a suitable material for BTE applications (Hollinger, 2011; Park et al., 2011).

The three common forms of available calcium sulfates are dihydrate or gypsum ($\text{CaSO}_4 \cdot 2\text{H}_2\text{O}$), hemihydrate or basanite ($\text{CaSO}_4 \cdot 0.5\text{H}_2\text{O}$), and anhydrous calcium sulfate or anhydrite (CaSO_4). Medical grade calcium sulfate is a highly degradable biocompatible material that when implanted inside the body, the by-products of the degradation process do not cause adverse effects in the body (Shen et al., 2014; Thomas, & Puleo, 2009). Calcium sulfate hemihydrate as hydraulic cement is one of the most widely used ceramics in printing 3D objects. The water-based binder reacts with the powder particles, which results in the formation of calcium sulfate dihydrate crystals (Butscher et al., 2011; Zhou et al., 2014).

2.2.2.2 Calcium phosphates

Calcium phosphates are broadly used in medicine due to the apatite-like structure of enamel, dentin, and bones known as “hard tissue”. Furthermore, hydroxyapatite

crystals with a chemical formula of $\text{Ca}_{10}(\text{PO}_4)_6(\text{OH})_2$ and Ca/P ratio of 1.67, can generally make up to 69% of the weight of the natural bone. Hydroxapatite has a hexagonal structure and it is the most stable phase among various calcium phosphates. Hydroxyapatite is stable in body fluid, as well as in dry or moist air up to 1200 °C (Vallet-Regi, & González-Calbet, 2004). Moreover, it does not decompose and has shown to be bioactive. The β -tricalcium phosphate (β -TCP), represented by the chemical formula of $\text{Ca}_3(\text{PO}_4)_2$ with Ca/P ratio of 1.5, has also a hexagonal crystal structure. The biocompatibility and the similarity of calcium phosphates like hydroxyapatite and tricalcium phosphate to the mineral composition of human bone and teeth have made them suitable for substitution of damaged segments of the human skeleton system (Tay, Patel, & Bradford, 1999). Besides, the bioactivity of calcium phosphate materials depends on many factors during the synthesis procedure, including precursor reagents, impurity contents, crystal size and morphology, concentration and mixture order of reagents, pH, and temperature. Such conditions are application specific and should be controlled by synthesis preparation parameters. As mentioned before, HA is stable in the body fluid, while TCP is rather soluble. The dissolution rate of HA in body fluid is too low, but that of β -TCP is too fast for bone bonding. Therefore, biphasic calcium phosphate that consists of HA and TCP can be used to control the bioresorbability and achieve optimal results. Biphasic calcium phosphate composites and BCP; consisting of HA and β -TCP, have many applications in the human body (Bergmann et al., 2010). However, the major disadvantage of bioactive ceramics is their low fracture toughness and brittleness (Klammert et al., 2010).

2.2.3 Mechanical properties

In BTE, the development of new tissue with required properties extremely depends on the mechanical properties of the scaffolds. At the macroscopic level, the scaffold needs to withstand mechanical loads to offer firmness to tissues during the tissue formation stage. Microscopically, cell growth and differentiation, as well as final tissue formation, depend on the mechanical load that is imposed to cells. Therefore, the scaffold should be capable of enduring particular loads and convey them in a proper way to the developing and nearby cells and tissues. The mechanical properties of a produced part are not solely controlled by the base material, but also influenced by the production process (Chan & Leong, 2008).

Many materials have been produced with good mechanical properties, but to the detriment of retaining high porosity and many materials, which have demonstrated potential *in vitro*, have failed when implanted *in vivo* due to insufficient capacity for vascularization. Hence, it is clear that a balance between mechanical properties and porous architecture, which are sufficient to allow cell infiltration and vascularization, is a key factor to the success of any scaffold (Bose et al., 2012; Chan, & Leong, 2008; Leong et al., 2003).

2.2.4 Fabrication methods

The formation of a porous structure constitutes a central goal of scaffold fabrication and in order to achieve this aim, various processing techniques have been developed, such as salt leaching (Sadiasa et al., 2013), foam replica (Fereshteh et al., 2015), gas foaming (Gentile et al., 2014), freeze casting (Sadeghpour et al., 2014), and

electrospinning (Rajzer et al., 2014), to fabricate scaffolds. However, most of these methods have failed in completely controlling the structural properties and the reproducibility of the scaffolds.

Furthermore, a core limitation of these technologies is the lack of precise control over scaffold specifications, such as pore size, shape, distribution, and interconnectivity, as well as the overall scaffold shape, and the porosity of the material, which is defined as the proportion of void space in a solid, is still a critical factor (Liu, Xia, & Czernuszka, 2007).

The additive manufacturing (AM) is a layer-over-layer manufacturing technique. In most cases, it enables complex components to be manufactured that are difficult to fabricate or those that cannot be generated via conventional methods. Among AM practices, the powder-based three-dimensional printing (3DP) is the most capable technique for BTE applications (Butscher et al., 2011; Butscher et al., 2012; Castilho et al., 2014; Klammert et al., 2010; Lee, & Wu, 2012; Zhou et al., 2014).

2.3 Powder-based three dimensional printing (3DP)

The immense potential for fabrication of scaffolds due to its maximum control over porosity and its ability to reproduce the customized anatomical design with great fidelity to the 3D medical pictures are the main advantages of the powder-based 3DP (Hollister, Maddox, & Taboas, 2002; Leong et al., 2003; Leong, et al., 2008).

Figure 2.2 shows a schematic illustration of the 3DP process. First, the chosen physical object is modeled on a computer-aided design (CAD) system. Then, the CAD model is converted to the stereolithography (STL) file format. A software program analyzes the STL file and mathematically slices the model into cross sections based on the selected layer thickness. The cross sections are recreated by using the reaction of the powder and the binder. This process is repeated layer by layer until a 3D object similar to the design is formed. During the fabrication process, the printer head jets a liquid into thin layers of powder according to the object profile created by the software. Subsequently, a build chamber (build-bed) containing the powder bed is lowered to enable the spreading of the next powder layer. Following the consecutive application of layers, the unbound powder is removed, and the 3D part is produced (Butscher, et al., 2013; Cox, et al., 2015; Sachs, et al., 1992; Utela et al., 2008; Withell et al., 2011). However, setting the 3DP process parameters is a complex and time-consuming task, as many variables influence the printed part quality for particular applications. In many cases, these variables contradict each other. In recent years, many reports have been published on the 3DP fabrication of BTE scaffolds, as well as its critical process factors and parameters (Asadi-Eydivand, et al., 2016; Lowmunkong, et al., 2009; Suwanprateeb, et al., 2010; Suwanprateeb, et al., 2012; Vaezi, & Chua, 2011). Other than that, many studies have focused on improving the dimensional accuracy (DA) and the mechanical properties of 3D-printed objects, which have displayed sensitive process parameters that can be tuned to improve the desired attributes. These characteristics are related to the process parameters and can be improved with proper adjustment (Castilho et al., 2013; Castilho et al., 2014; Castilho, et al., 2011; Hsu, & Lai, 2010; Suwanprateeb et al., 2010; Suwanprateeb et al., 2012).

Although a number of successful production experiments have been conducted, the quality assessment of the fabricated parts has remained to be one of the main challenges. Factors influencing quality have been studied through diverse indicators. However, those significant amounts of work did not focus on mechanical properties and porosity together for the fabrication of tiny pores on scaffolds in the application of BTE. The cost of the end products of the process is rather high. Therefore, from the technological and the economic points of view, selecting the process parameters for the optimization of manufactured parts is indeed highly essential.

In addition, various parameters have been found to affect the dimensional accuracy and the mechanical properties of 3D-printed specimens, which are the most important factors for evaluation of fabricated parts. These parameters can be categorized into three main groups: 1) the machine setting parameters, 2) the chemical and the physical properties of the powder and the binder, as well as 3) the structural design of the scaffolds. In fact, many studies that have focused on improving the dimensional accuracy and the mechanical properties of 3D-printed objects have shown sensitivity to process parameters, which can be tuned to improve the desired attributes. For instance, Patirupanusara, et al., (2008) looked at the effect of different compositions on physical and mechanical properties of fabricated 3D-printed samples.

In addition, Castilho et al., (2013) fabricated cylindrical scaffolds with biocompatible and biodegradable materials, besides evaluating them in terms of geometric accuracy and uniaxial compression behavior on the process directionality. Another study by Castilho et al., (2014) focused on the synthesis and the characterization of a novel powder system for a 3DP process. Meanwhile, Butscher et al., (2012) evaluated the 3DP process in terms of powder physical properties and reported the

relationship between the properties of the powder, including flowability and wettability with the final 3D-printed scaffold properties.

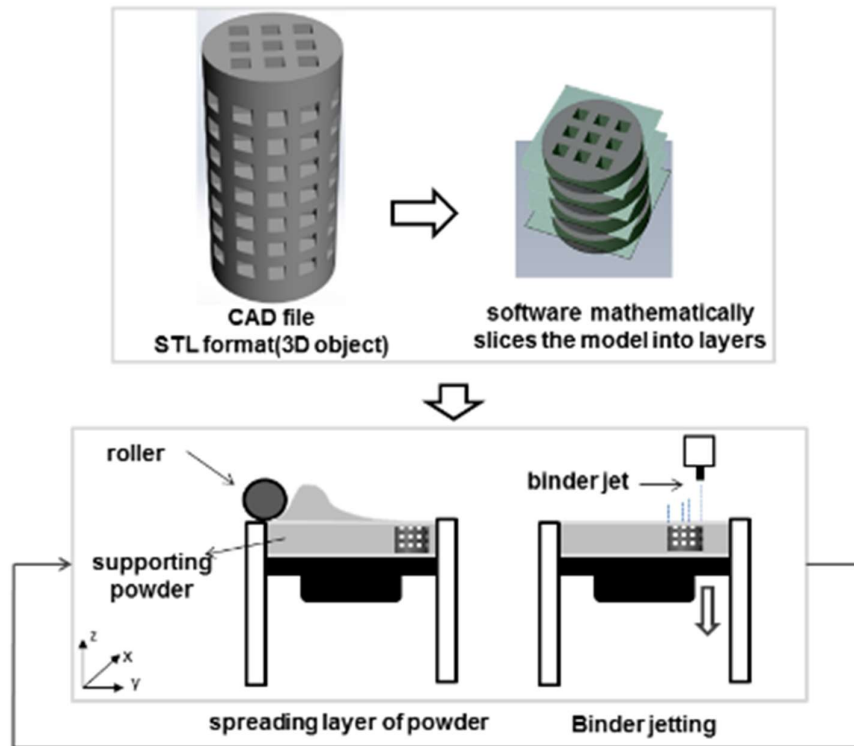


Figure 2.2: Schematic illustration of the 3DP process.

Many recent studies regarding the complexity of 3DP processes have focused on proper printer setting parameters. In another study, Butscher et al., (2012) systematically analyzed the relationship between layer thickness and layer stability with the quality of the final printed specimens. Alternatively, Suwanprateeb et al., (2010) prepared adhesive pre-coated hydroxyapatite powders using hot plate drying coupled with a grinding technique with the aim of increasing the mechanical properties of the 3D-printed samples.

Several other studies have also focused on process parameter optimization with commercially available materials. For instance, Hsu and Lai (2010) studied the Taguchi experimental design method for optimizing part dimensional accuracy,

reducing fabrication time, and reducing binder consumption by controlling four factors: the layer thickness, the binder saturation values shell and core, the location of green-parts, and the powder type of the specimens printed by ZCorp Z402 3DP. Although they managed to achieve their stated goals, the specimens were not optimized for specific application. In addition, Suwanprateeb et al., (2012) investigated printer parameters, including layer thickness and saturation ratio, as well as their effects on microstructure and mechanical properties by using ZCorp Z400. Meanwhile, Castilho et al., (2011) studied the potential of 3DP technology to fabricate scaffold prototypes for tissue engineering in terms of geometry. The smallest size for a well-defined pore they could achieve was 1 mm for a cubic unit cell with a side length of 10 mm (Castilho et al., 2011).

Nonetheless, the design, the geometry optimization, and the mechanical assessment of porous scaffolds still need further development. This is necessary for successful use of the scaffolds in BTE. Furthermore, while the behavior of scaffold geometries can be accurately simulated with finite element modeling (FEM), predicting real strength and stiffness values depends on dimensional accuracy. Although several experiments have been conducted by using the 3DP technology to make scaffolds, there is still a need for further development focused on identifying mechanical and biological properties that are suitable for bone regeneration. Additionally, the limits and difficulties described in the literature also provide motivation for developing improved fabrication methods that would allow the user some control over the internal structure of the scaffold. One way to achieve these goals, without major changes to the already developed hardware and software architecture, is to re-tune and fine-tune the control factors of the existing rapid prototyping process for a given machine.

Other than that, powder and binder selection are some examples of factors that are not process parameters, but vital in determining part structure and quality. However, without comprehensive knowledge of design and process parameters, the resultant 3D-printed parts may not have the desired properties or internal structure despite of using proper materials. Thus, one of the purposes of this study was to determine the optimal processing parameters based on the design of experimental approach, as well as to evaluate the 3DP process potential by employing the optimized parameters for porous prototype fabrication.

2.3.1 Optimization of process parameters

Achieving the optimal process parameters for fabricating 3D parts using the experimental tests is a time-consuming and costly approach. Numerical models of the process can be effective tools in finding the appropriate process parameters based on the demanded characteristics. From the physical modeling point of view, the 3DP process is complex. Many physical phenomena (e.g., powder and binder reaction, as well as removing unbound powder) could affect the quality of the product. Based on the experiments and the analyses carried out in this research, it had been observed that the relationship between porosity and compression strength of the porous structures, as well as the influential parameters, had been non-linear and uncertain. On the other hand, it is a very formidable task to provide an authentic and exact physics-based mathematical formulation, which can effectively represent the effect of layer thickness, delay time between spreading of each powder layer, as well as printing orientation on the porosity and the compression strength of the porous structures. Solving all the related governing equations using the analytical or numerical methods to obtain a mathematical model of the 3DP process is not only difficult, but may also be impossible. Hence, in order to

overcome this problem, the best way is to use a soft method to obtain a data-driven mapping system to approximately analyze the destined properties of the porous structures. Moreover, many researchers prefer using semi-experimental models instead of numerical models to model the physical process, such as the 3DP process. Additionally, artificial neural network (ANN) (Huang, & Hong-Chao, 1993; Kar, Das, & Ghosh, 2014; Zhang, 2000), fuzzy system (Mozaffari, et al., 2013; Rahmani-Monfared, et al., 2012), Hammerstein–Wiener (Fathi, & Mozaffari, 2013; Yu, Mao, Jia, & Yuan, 2014), time series (Yu et al., 2014), and Kalman filter are some of the well-known methods for establishing an experimental model of a system based on the available experimental data. Thus, to select a soft method that can be reliably used for this case study, the authors considered several techniques and conducted a primitive study, such as neural networks, polynomials, splines, etc. Published papers on ANNs suggested that this modeling methodology is a promising alternative tool for process modeling (Nelles, 2013; Lee, et al, 2005; Cao, & Qiao, 2008; Yeung, & Smith, 2005; Cao, Qiao, & Ren, 2009; Ni, Zhou, & Ko, 2006). This method can overcome conventional modeling difficulties as it has the advantages of ease of implementation and capability of constructing a complex non-linear map between inputs and outputs of a system. In fact, a few studies have been conducted on ANN modeling concerning the 3DP process. With that, this research developed an experimental-based predictive model for the 3DP process by using the aggregated artificial neural network (AANN) method. The AANN algorithm is one of the well-known variants of the neural networks models, which has been used in many engineering applications (Furtuna, Curteanu, & Leon, 2012; Granitto, et al., 2002; Mirhassani, Zourmand, & Ting, 2014; Palaniappan, & Paramesran, 2002; Ting, Yong, & Mirhassani, 2013). Aggregating multiple neural model for improving the generalization of neural networks is its main contribution. Many researchers have shown that a more accurate predictive model can be obtained in comparison with a single neural network with the

same number of neurons by aggregating several neural networks (Furtuna, Curteanu, & Cazacu, 2011; Zhou, Wu, & Tang, 2002). Finding a single neural network that can model a highly uncertain complex engineering phenomenon is often difficult. The major drawbacks of these artificial machines often result from over fitting and high computational complexity. However, combining a set of independent networks as cooperative learnable agents has appeared to be a promising strategy in enhancing the robustness and the generalization of these artificial machines. Another promising aspect in designing a modeling machine is to find a system that can handle more than one task simultaneously. To the knowledge of the author, ensemble artificial machines are best suited in this case, as a single network may concentrate on modeling a specific task while neglecting others. The predominance of AANN for modeling multi-output phenomena, nevertheless, has been reported in many studies (Zhou et al., 2002). In a recent study conducted by Furtuna et al., (2011), a stacked neural network (SNN) and an evolutionary hyper-heuristic method were developed for the optimum modeling of a complex chemical process. Their results implied the obvious advantages of AANNs for modeling complex engineering application. However, selecting the best topology is the main drawback of AANN. For training an AANN, one needs to select a number of neural networks, neurons, and hidden layers in each neural network. However, no convenient approach exists for the optimal design of these systems. Therefore, many researchers have proposed different methods for grasping an optimal topology for AANNs. For example, Zhou et al., (2002) applied a simple genetic algorithm (named GASEN) and proved that GASEN could generate an aggregated neural network with a far smaller size and stronger generalization ability compared to other common techniques. In another study, they developed a non-dominated sorting genetic algorithm as a high-level heuristic algorithm and a well-known back propagation method called quasi Newton training as a low-level heuristic algorithm for optimizing the structure of AANN (Furtuna et al., 2011). They reported the

effectiveness of their method, but it had some limitations, such as high computational time and complexity.

In this study, meta-heuristic algorithms were used as supervised algorithms in identifying the stage of the optimum topology of the AANN. Meta-heuristic algorithms are population-based artificial methods that are widely used to handle real-life and hard non-linear engineering problems (Chaturvedi, 2008; Yang, 2008). These algorithms initiate the natural evolutionary mechanisms and offer many advantages compared to the conventional methods. The particle swarm optimization (PSO) algorithm is the selected algorithm for constructing the optimal topology of the AANN. To select PSO, the authors considered some potential training methods, such as PSO, GA, ABC, and FA. It was observed that PSO displayed very high computational speed and did not result in computational stagnation. However, this is not the case when using GA and ABC, which have relatively complicated algorithmic structures, and should activate so many exploration/exploitation operators at each iteration. Given the fact that training AANN is a time-consuming task, and PSO can effectively balance the exploration and the exploitation over the searching period, it was selected as the fit algorithm for evolving the architecture of AANN. Furthermore, the experiments conducted by the authors revealed that, at-least for the current case study, PSO could afford the best results as it is just related to inertia weight and can converge to an acceptable solution in a logical period of time. However, this was not the case when GA and ABC were employed in this study. As for AG, several parameters, e.g. the number of elite chromosomes, the probabilities of mutation and crossover, etc., should be taken into account to result in a complex optimization algorithm. The same observation was valid for ABC in which there was a need for fine-tuning of several parameters, such as the number of employed and onlooker bees, as well as the number of limits for abounding a site. Moreover, the simulations

clearly demonstrated that PSO can show a faster and much robust exploration/exploitation over the procedure, and also can guarantee the convergence to a near optimum structure for AANN, which was not the case when using the other methods. Such observations have brought the authors to the conclusion that, in spite of its simplicity, PSO is the most logical choice for evolving the architecture of AANN.

Therefore, the main objective of the present study was to develop the best AANN model to analyze the non-linear effect of 3D printer machine parameters on the compressive strength and the porosity of printed porous structures, which are some of the more widely challenging aspects of printing scaffolds. To the best knowledge of the authors, using an aggregated structure has not been proposed before for the considered case study. This is when it is highly necessary to ensure that the developed soft sensor possesses an acceptable generalization, as the number of data points is often limited for such applications and there is a possibility for over fitting or under fitting, which makes the soft-sensor unreliable for unseen data (testing phase). As such, the experiments of the current study had taken a stride towards indicating that the aggregated structures are best suited for applications of the similar scaffold modeling as it is not easy to gather a rich database. Besides, it takes a long time (even years) to come up with an exhaustive database that can be fed to simple soft models, such as NN and ANFIS.

2.3.2 Post-treatments

Post-treatments are various processes that are carried out to improve the structure/properties of fabricated parts. The major weakness of 3D-printed porous bio-ceramics is the relatively low mechanical performance owing to the brittle nature of ceramic materials. Therefore, usually, a post-processing treatment is employed to

improve the strength of the printed objects. Recent studies on post-processing of 3D-printed scaffolds for tissue engineering applications have disclosed that post-treatments may have a significant influence on physical and chemical properties of fabricated 3D objects, as well as their *in vitro* behavior (Lam et al., 2002; Zhou et al., 2012). The two most common post-processing procedures are sintering and infiltration (Fascati, 2007; Impens, 2015; Lam et al., 2002; Trdnost, & Modelov, 2013; Utela et al., 2008).

Additionally, as the binders of the commercial powder-based printers contain non-biocompatible organic solutions, a high temperature heat-treatment results in less toxicity in scaffolds by burning out the toxic substances. Since the calcium phosphates are 1) more similar to the natural bone's inorganic part, 2) show better mechanical behavior in comparison to calcium sulfates, and 3) printing calcium phosphate with commercial printers without changing the hardware of the machine needs a lot of customization in powder and binder physical properties. Therefore, in this project, calcium sulfate had been attempted to transform into calcium phosphate by employing a thermo-chemical process, a second post-treatment, in order to investigate the feasibility of improving the scaffold properties to get one step closer to fulfil the BTE requirements by using available commercial printers and materials (Fascati, 2007; Impens, 2015; Lam et al., 2002; Trdnost, & Modelov, 2013; Utela et al., 2008; Bergmann et al., 2010; Khalyfa et al., 2007; Mazzoli et al., 2015; Suwanprateeb, Suvannapruk, & Wasoontararat, 2010). In addition, a few studies have looked into sintering the calcium sulfate 3D-printed prototypes. For instance, Zhou et al., (2012) studied the sintering of 3D-printed calcium sulfate specimens up to 861°C. However, there is no report on higher temperatures.

Recently, many studies have been reported to fabricate bone scaffolds via ink-jet 3D printer with calcium phosphate materials like hydroxyapatite and β -TCP due to their

great osteoconductivity and chemical similarity to the natural bone. However, choosing the suitable binder for reaction with calcium phosphate with the aim of printing robust scaffolds is limited to acidic solutions (tartaric acid, citric acid, and phosphoric acid). Nonetheless, the main drawback of acidic binders is that they reduce the working life and the performance of the print head. This disadvantage significantly limits the fabrication of calcium phosphate scaffolds in a large scale via ink- jet 3D printer. One possible solution to overcome this weakness is blending calcium phosphate with calcium sulfate powder due to the fast and reliable reaction of calcium sulfates with water binder, as determined by Zhou, et al., (2014). For all these reasons, at present, only calcium sulfate-based models have been fabricated by using commercial inkjet 3D printers.

Table 2.1. Summary of recent studies pertaining to phosphorization of 3D-printed calcium sulfate objects

Studied by	(Lowmunkong et al., 2009)	(Bingol & Durucan, 2012)	(Suwanprateeb et al., 2012)	(Suwanprateeb et al., 2010)
Design	Solid block	Powder	Solid and porous	Solid
Material Powder	Plaster of Paris	CaSO ₄ + 0.5 H ₂ O	CaSO ₄ + 0.5 H ₂ O	CaSO ₄ + 0.5 H ₂ O
Binder	Zb7 (commercial)	-	Zb7 (commercial)	Water based
Fabrication	(ZCorp-Z310)	-	(ZCorp-Z400)	(ZCorp-Z400)
Preheating	200 °C – 1h	-	-	-
Solution	Ammonium Phosphate	di-ammonium hydrogen phosphate	di-sodium hydrogen phosphate	di-sodium hydrogen phosphate
Temperature (°C)	80	25, 50, 90, 120	80	80
Conversion result	HA	HA	Monetite, HA	HA

There are a few studies on the phosphorization of 3D-printed calcium sulfate. Previous studies suggested converting calcium sulfate-based objects into calcium phosphate by immersing the objects in phosphate solution at different temperatures and time ranges is a promising technique for 3D-printed objects. The outcomes of the studies on the conversion of calcium sulfates to calcium phosphates are summarized in Table 2.1. The differences of the previous studies with this project are 1) calcium sulfate-based 3D-printed objects were fabricated by using the commercial binder, as no study had looked into the cytotoxicity of the printed scaffolds; and 2) the heat treatment process before phosphorization was limited to 200°C. Thus, the feasibility of transforming calcium sulfate heat-treated 3D-printed scaffolds with adequate strength into calcium phosphate or CS/CP composites had been investigated in this research by studying the composition, the microstructure, the morphology, and the mechanical properties of phosphorized specimens.

2.4 Summary

In the past, several other studies have focused on 3DP of BTE and process parameter optimization by employing commercially available materials. Although a number of successful production experiments have been conducted, the quality assessment of the fabricated parts has remained a main challenge. Moreover, the factors that influence quality have been studied through diverse indicators. However, these studies did not focus on mechanical properties and porosity together for the fabrication of tiny pores on scaffolds in the application of BTE. Therefore, from the technological and the economic points of view, selecting the process parameters for the optimization of manufactured parts is highly essential. Besides, The design, the geometry optimization, and the mechanical assessment of porous scaffolds still need further development. This

is necessary for the successful use of the scaffolds in BTE. Furthermore, while the behavior of scaffold geometries can be accurately simulated with finite element modeling (FEM), predicting real strength and stiffness values depends on dimensional accuracy. Additionally, the limits and the difficulties described in the literature also provide motivation for developing improved fabrication methods that would allow the user some control over the internal structure of the scaffold. Furthermore, recently, many studies have been reported to fabricate bone scaffolds via ink-jet 3D printer with calcium phosphate materials like hydroxyapatite and β -TCP due to their great osteoconductivity and chemical similarity to the natural bone. However, choosing the suitable binder for reaction with calcium phosphate with the aim of printing robust scaffolds is limited to acidic solutions (tartaric acid, citric acid, and phosphoric acid). Nonetheless, the main drawback of acidic binders is that they reduce the working life and the performance of the print head. This disadvantage significantly limits the fabrication of calcium phosphate scaffolds in a large scale via ink-jet 3D printer.

CHAPTER 3

MATERIALS AND METHODS

The current chapter discusses the overall flow of the study, the design of scaffold methods (both cylindrical and TPMS-based), and the material characterization techniques. Technical parameters that were selected for optimization are elaborated in this chapter. Consideration for the use of equipment and outcome measures are also included. Moreover, computational techniques, as well as properties that were selected for evaluation of the printed objects, are described in this chapter. Following these, heat treatment, phosphate treatment, and *in vitro* protocols are further depicted. Finally, statistical data analysis procedures are detailed in this chapter.

3.1 Fabrication of 3D-Printed prototypes

The 3D-printing machine Zprinter[®]450 (Z-Corporation, Burlington, USA) was used to produce cylindrical scaffold (6mm in diameter and 12mm in height) prototypes. After printing, all the specimens were held in the machine and dried for 90 min at ambient temperature. Then, the printed porous bodies were de-powdered by compressed air to remove any trapped and unbound powder. In the study of optimum machine parameters, any further post-hardened or infiltrate was avoided to eliminate parameters other than the design of experiment factors, which might affect the mechanical properties, the dimensional accuracy, and the porosity of the printed parts.

3.1.1 Printing materials

All the materials used, the high performance composite material (Zp150), and the water-based binder (Zb63) were supplied by 3D Systems Inc., USA, and used without further treatment.

3.1.1.1 Composition analysis

Powder X-ray diffraction (XRD) characterization was carried out by using PANalytical Empyrean (Serial No: DY1032, PANalytical, Netherlands) X-ray diffractometer with Cu-K α radiation. JCPDS files were used to identify the main components in both powder and printed samples. Besides, the presence of chemical groups that existed in the calcium sulfate powder, the binder, and the printed samples was determined by using Fourier transform infrared (FTIR) spectrometer (IFS66v/S, Bruker, Germany). The spectra were collected in transmittance mode in the range of 4,000 to 450 cm^{-1} .

3.1.1.2 Particle size and surface area analysis

The particle size and the particle size distribution of 3DP Zp150 powders were determined by using a particle size analyzer (Mastersizer MV, Malvern Instruments Ltd, UK). The powder materials were scanned thrice to determine the D₁₀, D₅₀, and D₉₀ values, as the diameters were 10%, 50%, and 90% of the particles that lied below those sizes, respectively. Other than that, a surface area analyzer (ASAP2020, Micromeritics, USA) was used to obtain the BET specific surface area value of the powder.

3.1.2 Design of scaffold

In this study, the scaffold was considered as a cylindrical structure shaped by an extruding cut by small cubicle elements named unit cell. The height and the diameter of the scaffolds circumscribed the number of unit cells in each class of the scaffold.

The geometry of the scaffold was chosen as it represented the typical features and the sizes of features found in BTE scaffolds intended to replace or repair an anatomical deficiency of *in vivo* tests (Hutmacher, 2000). However, the definition of an adequate pore size is still a matter of debate (Bohner, et al., 2011). However, it has been generally reported to be in the range of 100-800 μm (Liu et al., 2007).

Scaffold Prototype with 12mm height, and 6mm diameter with three different pore sizes in unit cell were designed by using the 3D design software, SolidWorks®2012 and exported as STL file. Three different classes of porous scaffold prototypes were designed and constructed, as illustrated in Figures 3.1 and 3.2, while their specification is listed in Table 3.1. The classes are denominated as pore size for each unit cell.

Table 3.1: The Specification of CAD design scaffolds.

Pore Size (mm)	Porosity Percentage (%)	Volume of Porous Cylinder (mm³)	Specific Surface area (mm²)
0.4	23.60 %	80.09	948.81
0.6	36.34 %	123.31	909.95
0.8	45.04 %	152.84	812.21







Pore size (mm) Strut Size (mm)	Unit cell	Porous cylinder
0.4 0.6		
0.6 0.6		
0.8 0.6		

Figure 3.1: CAD design of unit cells and porous scaffolds.

In fact, Butscher et al., (2011) mentioned that despite of the massive potential of freeform fabrication methods for making samples with micro-pore size, practically, only scaffolds with pores larger than 500 μm have been successfully fabricated to date.

3.1.2.1 Simulation-based method for scaffold internal architecture design

In this study, besides the cylindrical design, a library of TPMS-based unit cells was subjected to finite element analysis and CFD simulations. Elastic modulus, compressive strength, as well as permeability, were characterized for different volume

fractions of TPMS structures to develop structure-property correlations with emphasis on describing the architectural features of the optimum models. However, due to conflicting biological requirements with mechanical considerations, permeability is discussed versus structural properties. In addition, the concept of stretching and bending dominated deformations was introduced through the analysis of strain energy to take the effect of porosity on deformation mechanism into account. Then, the relationships between deformation behavior and mechanical properties are discussed. In order to evaluate the versatility of the current powder-based 3DP techniques, calcium sulfate scaffolds were designed according to the critical results of computational properties and printed with different cell sizes to address how representative volume elements can be generalized to scaffolds that comprised of the same pore architecture.

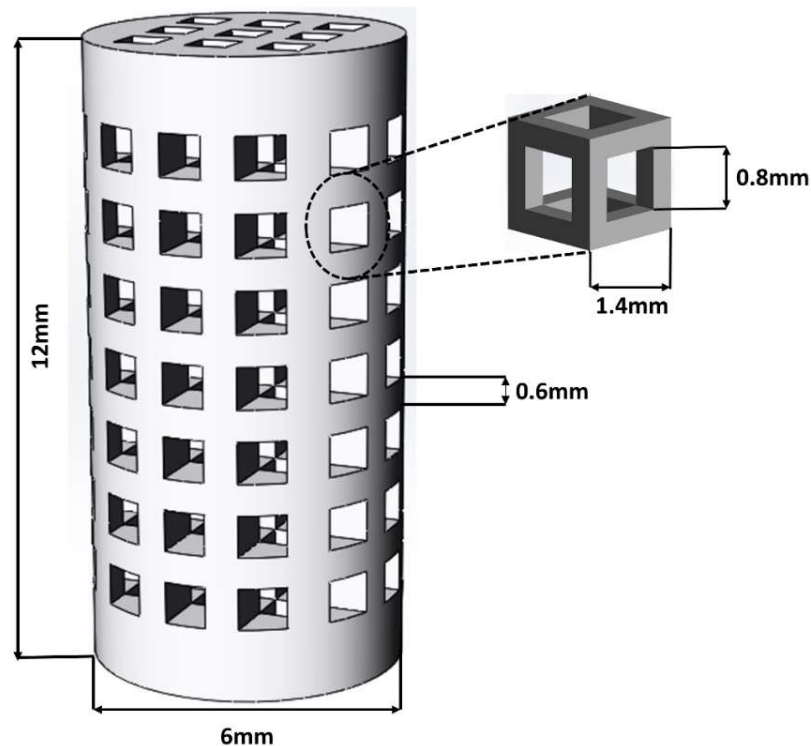


Figure 3.2: Structural details of the porous scaffold via CAD and the unit cell design.

Moreover, in order to assess the biomechanical responses of TPMS-based scaffolds, namely elastic modulus, yield strength, and permeability, 24 most common TPMS geometries; each of which were biphasic and co-continuous, were selected from the explicit equations resulted by nodal approximations of TPMS structures, as presented in Ref. [44]. The general definition of minimal surfaces is represented by Equation 3.1. Relative density for each topology is controllable by manipulating the offset value of C when defining equations of minimal structures were considered to be in the form of $\varphi=C$; in which φ is given (Wang, 2008) in Equation 3.1:

$$\varphi(\mathbf{r}) = \sum_{l=1}^L \sum_{m=1}^M \mu_{lm} \cos(2\pi\kappa_l(\mathbf{P}_m^T \cdot \mathbf{r})) \quad (3.1)$$

Where for each specific TPMS architecture, κ_l is the scale parameter, $\mathbf{P}_m = [a_m, b_m, c_m]^T$ is a basis vector representing a basis plane in the 3-Space, E^3 , $\mathbf{r} = [x, y, z]^T$ is the location vector with homogeneous coordinates, and μ_{lm} is the periodic moment.

Besides, corresponding to each minimal surface-based geometry, 10 volume fractions of their constitutive unit cell (spatial range between 0 and 1 in defining equations) were considered to be studied. Overall, 240 models of Representative Volume Element (RVE) were generated as input for finite element analysis to explore the structure-property relationships for TPMS-based structures. It should be noted that since the emphasis was on scaffold design, thus, for each structure with volume fractions at which the structures remained interconnected had been chosen to be computationally analyzed. Hence, the range of potential volume fractions and consequently, offset values in defining equation, were limited and differed from structure to structure.

Moreover, since the prominent potential of voxel-based models, in particular when dealing with image-based analysis, RVE for each model was discretized with the specific discretization step size according to a convergence study performed in this study. To this, a MATLAB code was developed to design the voxel meshes and to be read by CAE software for FEA. Those elements the center point of which satisfied the condition ($\phi < C$) according to the defining equation, were activated in the mesh domain and positioned layer-by-layer into the design space, as shown in Figure 3.3. In this way, the internal phase of TPMS unit cells were directly meshed to form the whole model for each scaffold geometry and volume fraction.

Before the generated models were subjected to computational analysis, a mesh convergence study was conducted to identify the discretization step size required for the converged solutions. To this, 4 different TPMS models (a combination of architectures with bending and stretching dominated deformation), namely P*, Ixxx-J*, D*, and FFzx-FP2, at 5 volume fractions, were modeled and then subjected to compressive displacement with discretization step sizes ranging from 0.019 to 0.095 (where the unit cell size was set to 1 for all models).

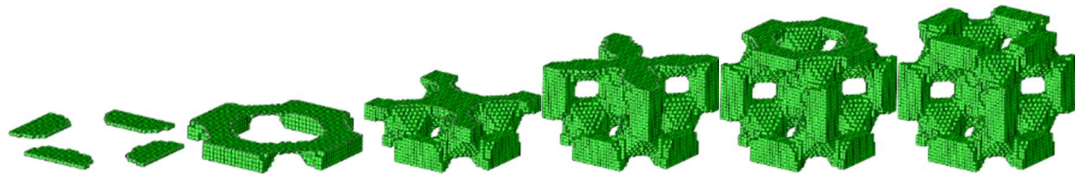


Figure 3.3: Layer-by-layer meshing representation of RVE of scaffolds. Finite element mesh models were developed via additive mesh generation based on the TPMS equations.

After obtaining the required accuracy, 240 voxel meshed models of constitutive unit cells that comprised of 24 aforementioned structures each of which at 10 different relative densities were prepared for both FE analysis of compression and CFD analysis

of unilateral fluid flow. The discretization size was set based on relative density so that for each model, between 22306 and 25268 voxel meshes were generated to ensure deviations less than 2.2%. Then, the ABAQUS implicit code was used to perform the FE analysis on the whole 240 models by considering the perfect plastic constitutive model with the elastic modulus and yield strength of 3.6GPa and 11.2MPa, respectively, with respect to the compressive properties of solid cubic 3D-Printed calcium sulfate samples presented by Feng, et al., (2015). The nodes at the bottom of the models were fixed and those at the top of the model were subjected to 5% compression to simulate the state of compression test. Subsequently, the resulted values of mechanical properties were extracted and normalized based on the constitutive material model.

Moreover, the models for fluid flow analysis (involving inverse phase of TPMS equations as fluid phase) were solved by ABAQUS/CFD solver. The properties for bio-fluid of interest were set at 1080kg/m³ for density and 0.0035Pa.s for viscosity (Viana, et al., 2013) for 20mm cubic scaffolds. Besides, in order to ensure that the fluid flow had remained laminar (to satisfy Darcy's law), a low inlet velocity of 0.001m/s was imposed at the inlet and a zero pressure condition was defined at the outlet. Moreover, no slip condition was defined in the faces of voxels in contact with the scaffold biomaterial. Finally, the average pressure drop was obtained for each model and the permeability coefficient was calculated via Darcy's law (Dias, et al., 2012) given in Equation 3.2:

$$K = \frac{v\mu L}{\Delta P} \quad (3.2)$$

Where v is inlet velocity, μ is fluid viscosity, L is unit cell size, and ΔP is set to the obtained pressure drop under defined boundary conditions. Furthermore, in order to exclude the dimensional effects, the numerical permeability values were normalized by

the permeability for a perfectly porous structure (vacant unit cell) with similar boundary conditions. On top of that, in order to describe the state of deformation in TPMS-based scaffolds, the Euler–Bernoulli beam theory for an internal cell wall (strut) had been employed to a replica of unit cells, thereby the whole scaffold structure. In fact, this study had been sought to distinguish the amount of bending energy from the overall deformation energy to address (1) which type of local strains are cells about to sense, (2) how deformation mode varies by changing apparent density, and (3) how is it correlated to constants of scaling analysis for each architecture. Considering the internal linkages as a cantilever beam, as shown in figure 3.4, the load exerted on the strut's elements can be resolved into tangential and radial components accounting for bending and stretching deformations, respectively.

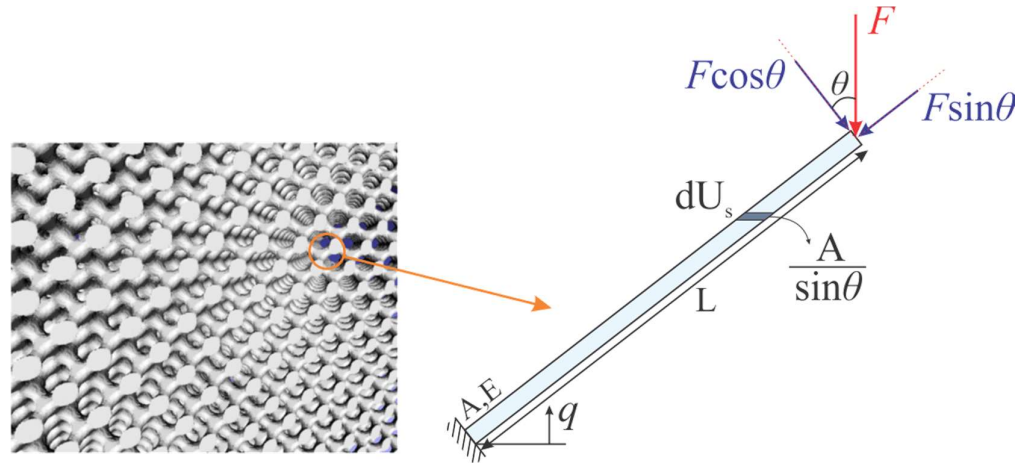


Figure 3.4: Theoretical parameters and boundary condition for cantilever beam that had been considered to model the contribution of deformation modes in energy absorption of the internal struts in porous structure of scaffolds.

Neglecting shearing effects, deformation energy can be written as given in Equation 3.3:

$$U = U_b + U_s \tag{3.3}$$

Where U_b is the portion of energy absorbed by overall bending, and U_s represents that of stretching, as given by Equations 3.4 and 3.5:

$$U_b = \frac{1}{6} (F \cos \theta)^2 \frac{L^3}{6EI} \quad (3.4)$$

$$U_s = \frac{1}{2} (F \sin \theta)^2 \frac{L}{AE} \quad (3.5)$$

The contribution of stretching deformation energy can also be obtained by integrating energy equation along the coordinate q (in direction of loading), as shown in Equation 3.6:

$$dU_s = \frac{F^2 dq}{2EA(q)} \rightarrow U_s = \frac{F^2}{2E} \int_0^{L \sin \theta} \frac{dq}{\frac{A}{\sin \theta}} = \frac{1}{2} (F \sin \theta)^2 \frac{L}{AE} \quad (3.6)$$

In this fashion, the problem is considered as an inclined beam subjected to a compressive load of F in which shearing and bending effects are neglected, thereby the obtained U_s equals to the amount of stretching deformation energy when the Euler–Bernoulli beam relations are applied. In fact, the value of U_s is representative of the maximum possible energy, which can be absorbed by the amount of material. Meanwhile, the same expression is applicable when cross sectional area of A varies, where the above-mentioned integration can be performed on the TPMS unit cell equations. Actually, the value of U_s is indicative of the maximum possible energy that can be absorbed by the whole material and mechanical efficiency can be considered as the ratio of the strain energy computed with finite element simulation to U_s ratio. Since the loading conditions had been similar to the model in finite element analysis, deformation energy obtained from the finite element simulation was assigned to U and consequently, contribution of bending deformation (D_b) is stated in Equation 3.7:

$$D_b = \frac{U_b}{U} = 1 - \frac{U_s}{U} \quad (3.7)$$

The practical potential of manufacturing 3D scaffolds through powder-based 3DP technique was assessed based on the critical designs obtained in FE calculations. To this, high porosity of 70% was held in all scaffold CAD models. Moreover, based on the finite element simulation results, model architectures of Ixxx-J* and Fxyz-Fxxx2 were considered to possess high strength and low stiffness structures, respectively; holding the highest permeability. Then, in CAD modeling, the unit cells were repeated along three global directions to form 20mm cubic scaffolds that comprised of 3×3×3, 4×4×4, and 5×5×5 unit cells for experimentally evaluating cell size effect on mechanical properties, as well as the versatility of powder-based 3DP in producing low scale porous structures at high porosities. Therefore, the unit cell sizes were set to 6.67, 5, and 4mm; corresponding to each of two critical architectures. Besides, in preparing the CAD models, image-based modeling approach was performed by using a MATLAB code, and then, STL files were produced for subsequent production purposes.

Furthermore, mechanical compressive tests were carried out in order to extract the mechanical response of the designed uniform scaffolds. Four samples were produced of each scaffold model, each of which were produced with the same processing parameters. In addition, compression tests were implemented by using an Instron 5848 Micro Tester, a USA instrument equipped with 10KN load cell with the cross-head loading rate of 6mm/min. Load-displacement data were extracted to calculate engineering stress-strain curves by setting 400mm² as the initial surface area and 20mm as the initial specimen length. Then, the graphs were modified according to the onset of elastic region, while the mechanical properties were computed. Elastic modulus and compressive strength were calculated based on the slope of the first linear region in stress strain curves and the highest recorded stress, respectively. Moreover, SEM (Quanta FGG 250, Holland) images were captured to illustrate more details of the printed scaffolds.

3.1.3 Technical parameters

A plan of experiments, based on a full factorial design of experiments, was used to optimize the settings of process parameter values for improving the quality characteristics of the cylindrical-designed scaffold prototypes. Optimal processing parameters were defined as those that yielded parts that most closely resembled an ideal 3DP part. An ideal 3D-printed processed part was defined as one that (a) had sufficient green strength and easily de-powdered, (b) dimensionally accurate, (c) possessed interconnected pores, and (d) proper porosity. The 3DP process parameters examined in this study were layer thickness, the delay time in spreading a new layer, and build orientation. Table 3.2 shows the design of experiment factors and their levels investigated in this study.

3.1.3.1 Layer thickness

In 3DP processes, the layer thickness refers to the height of the powder bed that is spread along the z-axis during the procedure. In fact, some studies conducted by Butscher et al., (2011), Suwanprateeb et al., (2012), and Vaezi, and Chua (2011) displayed that the layer thickness had significant effects on scaffold physical properties.

Table3.2 The design of the experiment factors and their levels

NO.	Parameter	Unit	Level 1	Level 2	Level3	Level 4
1	Layer thickness	μm	88.90≈ 89	101.60≈102	114.30≈114	127.00
2	Delay time	second	0.05	0.10	0.30	0.50
3	Build orientation	-	x	y	z	-

3.1.3.2 Build orientation

Among the various process parameters, part orientation seems to have the greatest impact (Castilho et al., 2013). Therefore, it is rational to consider the interaction of other parameters with respect to orientation. Consequently, orientation was selected as one of the main factors.

The arrangement of a specimen on the build bed and the number of each sample group are shown in Figure 3.5. Besides, due to the location of the binder and its movement, which is from left to right, the samples were placed in three groups for each orientation; eight samples were used for each group to remove the influence of specimen location.

3.1.3.3 Delaying the spreading of the new layer (Delay time)

The Zprinter[®]450 software has a default delay of 100 ms between the ends of spreading one layer to the start of spreading the next. This delay is referred as the *delay time*. Hence, it had been decided to assess if increasing the powder delay time (300 or 500 ms) would allow further binder relaxation and densification, particularly in pores and channels, as each layer would have additional exposure time. However, it was also

hypothesized that the added time could have an impact on the layer-to-layer bonding, which would consequently affect the mechanical behavior of the specimens, as well as their dimensions. Therefore, a shorter time delay, 50 ms, was selected to test this theory.

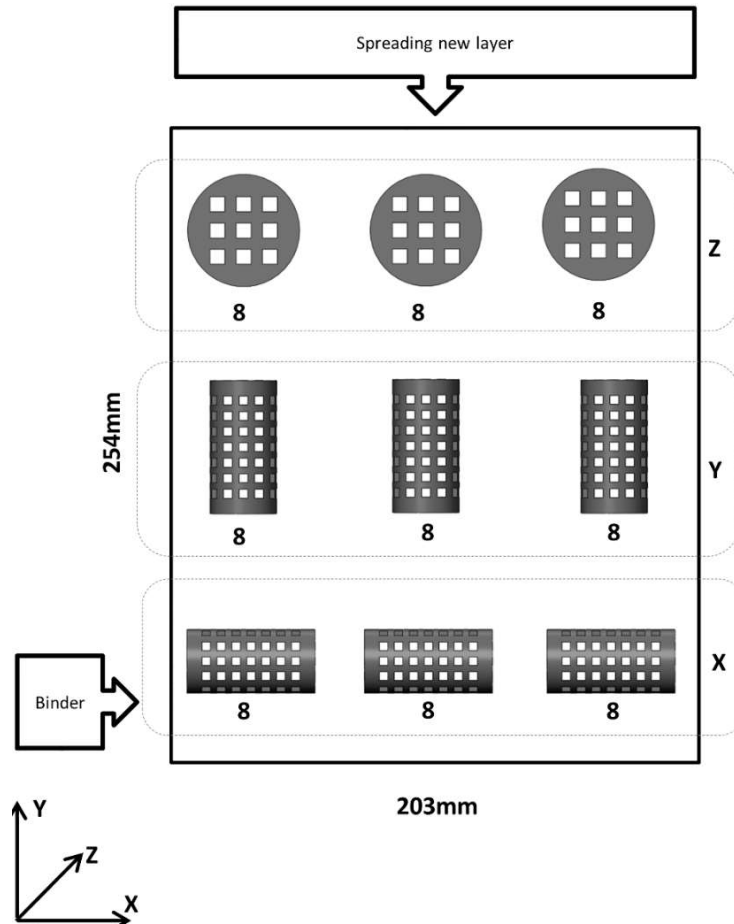


Figure 3.5: Top view of Zp450 Build bed size with the specimens arranged, and the number for each run.

3.2 Evaluation of fabricated scaffolds

The 3D-printed part quality was defined by three characteristic features: 1) mechanical properties, 2) dimensional accuracy, and 3) porosity. These features were employed to evaluate the quality of the printed scaffolds for all design of experiment

(DOE) test samples. The importance of the selected parameters and the methods used for measurements is described in detail in the following sections.

3.2.1 Mechanical properties

Green strength refers to the initial strength after printing and before any post-processing to increase mechanical properties. In this study, no post-processing technique was employed to evaluate the feasibility of 3D machine parameters to build porous scaffolds. Clearly, green strength is a key property of a printed scaffold and describes the mechanical characteristics immediately after extraction from the powder bed and after de-powdering (removing unbound powder) (Butscher et al., 2013). Insufficient green strength may result in shape changes or eventually, mechanical failure of the green body. Even the weight of the unbound powder might be critical for a weak scaffold structure. The green strength of the printed part depends on mainly two factors: the strength of the bonds between adjacent particles, and the bond strength between neighboring layers. Thus, optimal green strength is required to meet the mechanical property demands of scaffolds because green strength can affect the final strength (after any post-processing, e.g., sintering or dipping into a binder solution) (Chumnanklang, et al., 2007).

Nevertheless, uniaxial compressive testing was conducted by using a mechanical testing instrument with 10 kN load-cell (Instron 5848 Micro Tester, USA) and a cross-head loading rate of 0.5 mm min^{-1} . Nine cylinders of each type (6mm in diameter and 12mm in height) were developed for tests. The maximum stress was recorded as the compressive strength, and the slope of linear region was considered before the yield point as the Young's modulus.

3.2.2 Dimensional accuracy

Dimensions (the diameter and the height of two sides of the fabricated specimens) for each of the 24 test parts for 48 runs were measured by using a Mitutoyo digital caliper with the least count of 0.01 mm. The readings were then recorded, averaged, and compared with their target dimension by calculating the deviation as a difference in percentage.

Moreover, a dimensional distortion ratio (DDR) had been defined and those criteria were applied to quantify the distortion or the asymmetry of the printed parts. The DDR can be calculated simply by using Equation 3.8.

$$DDR = \frac{d_{CAD}}{h_{CAD}} - \frac{d}{h} \quad (3.8)$$

Where d and h are the averaged measured values of diameter and height, d_{CAD} and h_{CAD} are the CAD model diameter and height, respectively. When there is no distortion, the DDR is equal to zero. Non-zero numbers mean height or diameter distortion: negative if the height is more than the diameter and positive if the diameter is more than the height.

Isotropy is a measure of the three dimensional asymmetry or the existence or lack of preferential alignment along the specific structural directions. Apart from the percentage volume, the degree of anisotropy (DA) and the general stereology parameters of bone are probably the most important determinants of mechanical strength.

Here, a DA of 0 corresponds to fully isotropic samples and tends to be 1 as samples become increasingly anisotropic (a DA of 1 represents full anisotropy). The DA values were reported by the CT-analyzer software. In this study, the measurements of height and

diameter, DDR, and DA were the three factors considered for evaluation of the dimensional accuracy.

Moreover, scanning electron microscopy (SEM) was employed (Quanta FGG 250, Holland) to capture pictures for calculation of the average pore size and strut size, as well as to study the microstructure of the printed scaffolds. Meanwhile, close up images of the specimens were taken by a digital camera (Canon G12, Japan).

3.2.3 Porosity

Cell seeding efficiency, diffusion properties, and mechanical strength of a scaffold are directly influenced by porosity. However, a successful scaffold must meet several requirements; the one of foremost importance is the existence of interconnecting channels to enable the supply of nutrients and metabolites to allow cell in-growth (Bose et al., 2013a; Will, Detsch, & Boccaccini, 2013). In this context, the analysis of the scaffold porosities is of great relevance. Some of the numerous methods, which can be used to analyze pores, are optical approaches (microscopy), physico-chemical approaches (nitrogen adsorption and desorption), and capillary approaches (mercury porosimetry) (Will et al., 2013). However, only advanced medical imaging techniques, such as micro-computed tomography (micro-CT) and magnetic resonance imaging (MRI), can provide a 3D image of the scaffold.

3D imaging is a non-destructive method that allows close up inspection of a specific location. Hence, one can observe the pore shape, as well as measure the pore size and the strut/wall thickness, the porosity, and the pore interconnectivity by using the 3D

images (Ho & Hutmacher, 2006; Lenthe et al., 2007). One test specimen from each test (Table 4) was scanned by using a micro-CT (SkyScan In-Vivo XRay 1076, Belgium).

The scanner used in the experiments had high resolution with a compact desktop unit. For each specimen, nearly 700 scan slices were taken. When analyzing the porosity of the scaffolds, the threshold to be used was readily obtained for each individual specimen by the threshold histogram offered by the SkyScan software.

3.2.4 Thermal analysis

The thermal behavior of the printed samples was examined with a simultaneous thermal analysis (STA) instrument (Setaram, France) in the 25-1300°C temperature range. The thermogravimetry analysis (TG/DTG) was performed by using a thermal analysis apparatus (Mettler-Toledo, ThermoStar™, Switzerland) in the temperature range of 25-1000°C. A heating rate of 10°C/min in air was used in both experiments.

3.2.5 Statistical analysis

A full factorial design of experiments (DOE) was used to determine the optimal 3DP parameters of scaffold prototype processing. Optimal processing parameters were defined as those that resulted in parts as perfectly processed parts as possible. The multiple performance measures considered herein were the percentage changes in diameter and height of built parts, porosity, and compressive strength.

Other than that, signal to noise (S/N) ratio and analysis of variance (ANOVA) were employed to study the important factors that significantly influenced dimensional accuracy and mechanical properties. ANOVA was performed to determine if the factors were statistically significant through the sum of squares, F-value, and P-value. P-value is the probability value used to identify if an effect in the model is statistically significant (Quinn, & Keough, 2002).

The smaller the value of P, the more significant is the corresponding coefficient. In the present work, a P-value should be less than or equal to 0.05 or 0.01 (95% and 99% confidence levels, respectively) for the effect to be statistically significant. A commercial statistical package, Design-Expert version 7, was utilized for the design of experiments.

3.3 Process parameters optimization methods

3.3.1 Aggregated artificial neural network (AANN)

This section discusses the structure of the proposed model for optimization of the process parameters. As previously mentioned, the AANN model was used as the structure for predicting the model, and the experimental data were used for training it.

The standard topology of AANN is shown in Figure 3.6. It is composed of several single feed-forward neural networks, the outputs of which are added together with some weighting coefficients. An important factor in designing the AANN is to find the fittest weighting coefficients in a manner that AANN has the best performance (minimum prediction error) and the lowest complexity (minimum size) simultaneously. The generalized performance of a neural network is expressed in Equation 3.9:

$$\text{Error} = \text{MSE train} + \text{MSE test} \quad (3.9)$$

where MSE train and MSE test are the mean squared errors in the training and the testing steps. Zero is the ideal performance.

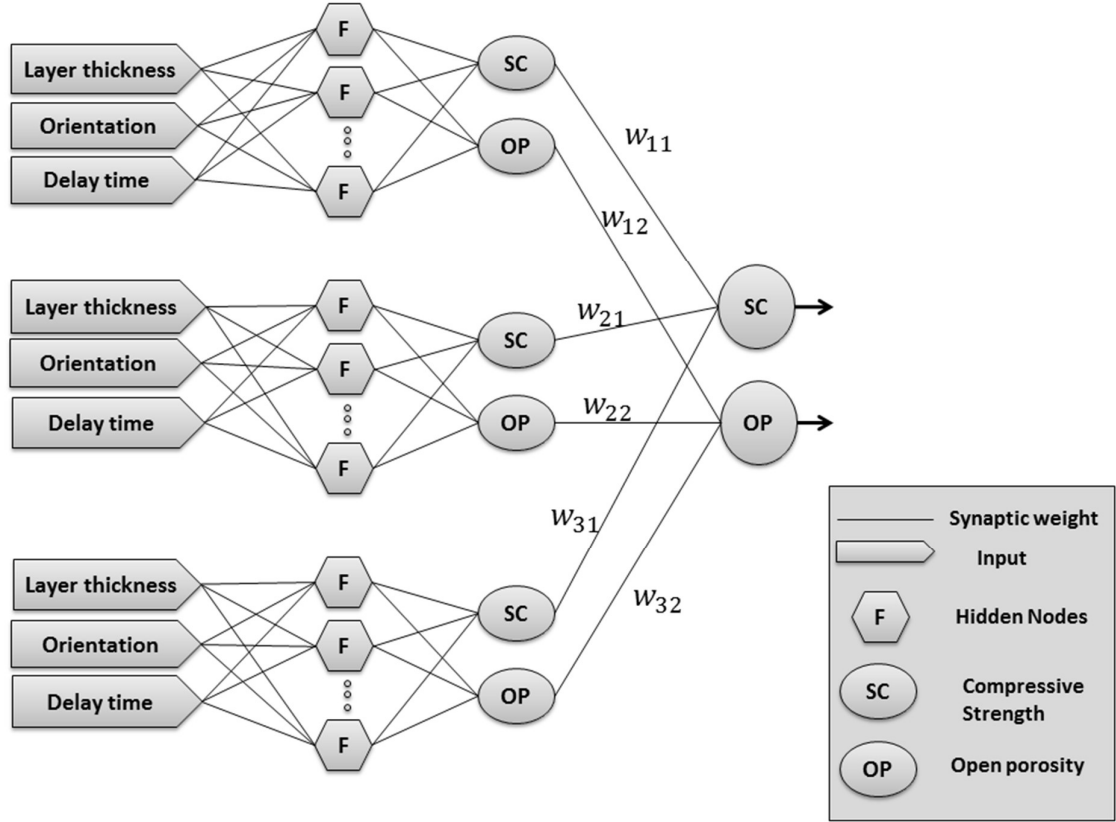


Figure 3.6: The proposed structure of the AANN for 3DP process.

However, in many practical applications, obtaining exactly zero error is impossible, and the authors expect an acceptable generalization from a network with error closer to zero. The mean squared error is defined in Equation 3.10:

$$\text{MSE} = \left(\frac{1}{Nt \cdot No} \right) \cdot \sum_{J=0}^{No} \sum_{i=0}^{Nt} (d_{ij} - y_{ij})^2 \quad (3.10)$$

Where No the number of AANN is outputs, and Nt is the number of training or testing data. Parameters Y and d represent the actual output of AANN and the desired AANN output (target), respectively. Each individual neural network estimates the compressive strength and the open porosity independently, while the actual outputs of AANN are derived from a linear superposition of these independent outputs. These independent outputs are accumulated mathematically to form the actual outputs, as depicted in Equation 3.11.

$$y_j = \sum_{K=0}^{NNno} w_{jk} \cdot y_{jk} \quad (3.11)$$

Where y_j is the j^{th} output of the stacked neural network, $NNno$ is the number of independent networks, while w_{jk} and y_{jk} are the j^{th} weight and output of the k^{th} independent neural network, respectively. Computational complexity is one of the objective values in designing an AANN. Reducing the computational complexity is equivalent to designing a network with the lowest number of neurons in the hidden layers. Therefore, the following criterion is defined as a metric of complexity (Equation 3.12):

$$Complexity = \sum_{k=0}^{NNno} Hn_k \quad (3.12)$$

Where, Hn_k is the number of neurons in the cat independent neural network. To obtain a model with the lowest prediction error and computational complexity, the authors define the following total objective function (Equation 3.13):

$$\min F_1 : f(NNno, w_{jk}, H_n) = \gamma(MSE_{train} + MSE_{test}) + (1 - \gamma) \sum_{k=0}^{NNno} Hn_k \quad (3.13)$$

where γ is the scaling factor between [0, 1] that represents the degree of importance of each objective function. The lowest value of γ means the complexity is more important than the prediction error. In this study, since a limited amount of actual data had been available, the complexity had been as important as efficiency. Moreover, it is noteworthy that as the complexity increases, there are more possibilities for over fitting. Thus, constant value for $\gamma = 0.5$ was considered.

Other than that, the correlation between the actual and the desired output data is another important factor in designing an AANN. The training procedure should be done in such a way that the highest correlation value occurs between the actual and the desired data. For this purpose, a minimum acceptable value of correlation is imposed on the training phase as a constraint. The mathematical expression of the correlation is portrayed in Equations 3.14 and 3.15:

$$r = \left(\frac{1}{No}\right) \cdot \sum_{j=0}^{No} \frac{\sum_{i=0}^{Nt} (y_{ij} - \bar{y}_j)(d_{ij} - \bar{d}_j)}{\sqrt{\sum_{i=0}^{Nt} (y_{ij} - \bar{y}_j)^2 \sum_{i=0}^{Nt} (d_{ij} - \bar{d}_j)^2}} \quad (3.14)$$

$$0.9 < r < 1 \quad (3.15)$$

where r is the correlation, \bar{y}_j is the average of the actual values obtained in the processing element j of the neural network output, and \bar{d}_j is the average of the desired values for the processing element j of the neural network output.

Before entering the training phase, these experimental data were normalized with Equation 3.16:

$$u_i = \frac{2}{up_i - lb_i} \left(u_i - \frac{1}{2} (lb_i + ub_i) \right) , i = 1, 2, 3 \quad (3.16)$$

where up_i , u_i , lb_i , and ub_i are actual input, normalized input, lower bound, and upper bound of the i^{th} input, respectively. It is worth noting that the upper bound and the lower bound values are the maximum and the minimum values of the actual input data. Hence, by applying the above equation, the acceptable range of the inputs is between [-1, 1]. The same pre-processing procedure had been conducted for the outputs.

3.3.2 Particle Swarm Optimization

The PSO algorithm is a population-based soft computing technique that has attracted the attention of many researchers in solving applied engineering optimization problems. This algorithm, which is based on the behavior of a swarm of ants, a flock of birds, or a school of fish, mimics their social behavior in finding food or their actions in encountering danger. This social behavior can be used in developing modern optimization algorithms. Kennedy and Eberhart originally proposed the PSO algorithm in 1995 (Eberhart, & Kennedy, 1995).

In this algorithm, each solution of the optimization algorithm is considered a particle, and a swarm of particles located randomly in the feasible searching domain is initially selected. These particles (i.e., candidate solutions) are updated by using an evolutionary mechanism to obtain a better solution. The proposed evolutionary mechanisms are similar to what happens in nature. In nature, each particle tends to act similar to its best experience in life and moves to the best successful experience of its neighbors. These two behaviors, which are called exploration and exploitation, respectively, can be computationally implemented as follows.

In the PSO algorithm, for an optimization problem $\min f(\mathbf{x})$, each particle is presented by its position vector, as shown in Equation 3.17:

$$\mathbf{x}_{ij}(t) = [\mathbf{x}_{ij}] = [x_{i1}, x_{i2}, \dots, x_{i(n-1)}, x_{in}], i = 1, 2, \dots, N, j = 1, 2, \dots, n \quad (3.17)$$

where, t is the generation time, x_{ij} is the j^{th} variable of i^{th} particles, N is the swarm size, and n is the searching space dimension. Meanwhile, $\mathbf{x}_i(t)$ is the solution of the optimization problem, and the swarm is a set of $\text{swarm} = \{x_1, x_2, \dots, x_N\}$.

To formulate the evolutionary mechanism, a velocity vector is assigned to each particle, as given in Equation 3.18:

$$\mathbf{v}_i(t) = [v_{1i}, v_{2i}, \dots, v_{(n-1)i}, v_{ni}], i = 1, 2, \dots, N, \quad (3.18)$$

where $\mathbf{v}_i(t)$ is the velocity of the i^{th} particle. This velocity specifies the updating direction and updating rates of each particle position. The particles are assumed to move iteratively within the search space.

The best experience of each particle up to time t is stored in a variable called *best position* and is expressed as $\mathbf{p}_i(\mathbf{i}) = [p_{1i}, p_{2i}, \dots, p_{(n-1)i}, p_{ni}]$. The set $\{\mathbf{p}_1, \mathbf{p}_2, \dots, \mathbf{p}_N\}$ is a memory set that shows the best positions of the swarm explored by each particle. Evidently, the best position with the lowest fitness function value of this set becomes the global best solution of the minimization problem. This global minimal position is represented by $\mathbf{p}_g(t)$ and is computed as given in Equation 3.19:

$$\mathbf{p}_g(t) = \arg \min_i (f(\mathbf{p}_i)). \quad (3.19)$$

Nevertheless, in a classic variant of the PSO, the updating rule is mathematically expressed as follows:

$$\mathbf{v}_i(t+1) = w \cdot \mathbf{v}_i(t) + c_1 \cdot R_1 \cdot (\mathbf{p}_i(t) - \mathbf{x}_i(t)) + c_2 \cdot R_2 \cdot (\mathbf{p}_g(t) - \mathbf{x}_i(t)), \quad (3.20)$$

where w is the weighting coefficient, c_1 and c_2 are the cognitive and the social acceleration coefficients, respectively, while R_1 and R_2 are the two random numbers uniformly distributed within $[0, 1]$.

Furthermore, based on Equation 3.20, the weighting coefficient w gives the inertia behavior to the motion of the particle. Higher values of w result in more exploration behavior, whereas a lower value increases the performance of exploitation. This parameter should be controlled during the generation time. After updating the velocity of the particle, each particle adjusts its current position by using the following relation:

$$\mathbf{x}_i(t+1) = \mathbf{x}_i(t) + \mathbf{v}_i(t+1), \quad i = 1, \dots, N. \quad (3.21)$$

In this study, PSO with constant inertia weight had been used and the AANN structural parameters were considered as particle parameters in swarm. In fact, each particle creates AANN network and return network error (Equation 3.13) as PSO min function (Equation 3.22).

$$\begin{aligned} \min F_1 : f(NNno, w_{jk}, Hn) &= \lambda(MSE_{train} + MSE_{test}) + (1 - \gamma) \sum_{n=0}^{NNno} Hn_n \lambda = 0.5 \\ x_i(t) &= [NNno, W_m, Hn_i], i = 1, 2, \dots, N, m = 1, 2, \dots, 2 \times NNno, n = 1, 2, \dots, NNno \end{aligned} \quad (3.22)$$

where NN_{nc} is the number of single neural networks, W_m is the number of weighting coefficients, and H_{n_i} is the number of hidden layers for each single neural network. The topology of AANN, the related coefficients, and the hidden layers are depicted in Figure 3.6.

3.4 Protocols of post-treatments

3.4.1 Heat treatment

Heat treatment of the printed calcium sulfate scaffolds was carried out in an electric box furnace (XY-1600A, Nanyang Xinyu Furnaces LTD, China) equipped with a heating rate controller device. The samples were placed on an alumina foam plate, and heated in air at 300, 500, 900, 1000, 1150, 1200, 1250, and 1300°C with a heating rate of 10°C/min. These temperatures were chosen to correspond to the thermal behavior of the printed samples observed in DTA-TG and TG-DTG thermal analyses. The cylindrical printed specimens were positioned in the furnace as standing on their base. All the samples were soaked in the target temperature for 1h, and followed by furnace-cooling to room temperature. Then, the effect of heating temperature on the 3D-printed calcium sulfate scaffolds was investigated.

3.4.2 Phosphate treatment

Phosphate solution (1mol/L) was prepared with ammonium phosphate monobasic $NH_4H_2PO_4$ (Sigma Aldrich, PubChem Substance ID 24852930), molecular weight

115.03, and distilled water. 115.03 gr of powder in 1L of distilled water was stirred with a stirrer for 1 hour. Ten specimens from the 3D-printed objects, which were heat-treated at 1150, 1200, and 1250 °C, had been immersed in 1 mol/L of solution for 4, 8, 16, and 24 h at 85 °C in oven.

3.5 Characterization of post-treated scaffolds

3.5.1 Mechanical testing

Uniaxial compression tests were performed on a universal testing instrument (Table top 5569, Instron, USA) equipped with a 100 kN load-cell and a cross-head loading rate of 0.05 mm min⁻¹. Each measurement was made on three identical specimens at room temperature. The maximum compressive stress registered in the stress-strain plot and the slope of the linear region before the yield point were considered as compressive strength and compressive elastic modulus, respectively.

3.5.2 Shrinkage and density measurements

The dimensions of test specimens were measured before and after heat treatment by using a digital caliper (Mitutoyo, Model CD-6"CS) with 0–150 mm measurement range and 0.01 mm accuracy. Each feature was measured ten times and the average was reported for ten samples. Besides, the percentages of longitudinal (L%) and radial (R%) shrinkage (shown in Figure 3.7) were calculated by applying Equations 3.23 and 3.24:

$$R\% = [(d_H - d_P) / d_P] \times 100 \quad (3.23)$$

$$L\% = [(l_H - l_P) / l_P] \times 100 \quad (3.24)$$

where (d_H, l_H) and (d_p, l_p) are the diameter and the height of the specimens after and before heat treatment, respectively. The readings were then recorded, averaged, and compared with the CAD-designed dimensions by calculating the deviation as the percentage of difference.

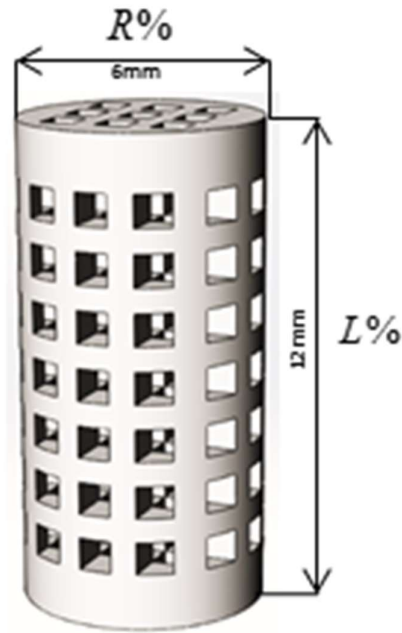


Figure 3.7: Heat treatment of the 3D-printed specimens results in shrinkage for both longitudinal and radial directions.

The weight of the samples was measured with a semi-micro analytical balance (GR-200, A&D, Japan) to four decimal points. The bulk density of the printed samples was calculated by using the mass and bulk volume data obtained from weighing and measuring, respectively.

3.5.3 Composition and microstructure

Powder X-ray diffraction (XRD) characterization was performed in a scan angle (2θ) range of 10 to 80 by using Cu-K α radiation (1.54056Å), 40kV, 30mA, and 0.02°s $^{-1}$ step scan within a DY1032 diffractometer (PANalytical, The Netherlands). Moreover, CrystalDiffract v1.4.7 software was used to acquire the XRD patterns. The major phases of the samples were identified by using the JCPDS files.

The presence of chemical groups that existed in the phosphorized scaffold was determined by using Fourier transform infrared (FTIR) spectrometer (IFS66v/S, Bruker, Germany). The spectra were collected in transmittance mode in the range of 4,000 to 450 cm $^{-1}$.

Other than that, the microstructure of the heat-treated and phosphorized specimens was assessed by using scanning electron microscopy (Phenom Pro X, The Netherlands) equipped with energy dispersive spectroscopy (EDS). A carbon tape was used to fix the specimens on the sample holder to discharge the negative charge present in the microscope. Subsequently, backscattered electron images were taken and the spectra of energy dispersive X-ray microanalysis were obtained.

3.5.4 *In vitro* protocol

MG63 (human osteoblast-like osteosarcoma) cells were obtained from the National Cell Bank of Iran (NCBI), Pasteur Institute (Tehran, Iran). The cell cultures were maintained in DMEM medium (L-glutamine) supplemented with 10% of fetal bovine serum (Gibco) and 1% of penicillin/streptomycin at 37°C in a humidified atmosphere

with 5% of CO₂. Prior to cell seeding, the samples were sterilized by immersing them into 70% ethanol for 1h, and followed by washing several times with sterilized PBS. The cytotoxicity assay was performed according to the ISO 1993–5 protocol. Typically, 0.1g of powder was incubated in 1 ml of sterilized culture medium and at the pre-defined time intervals (1, 3, and 7 days), while the mediums were extracted for use in cellular assays. The culture medium was kept under similar condition as a negative control. The cytotoxicity of the extracts was assessed by using MTT (3-(4, 5-dimethylthiazol-2-yl)-2, 5-phenyltetrazolium bromide) assay. Briefly, the cells were cultured in a 24-well plate at a density of 1×10^4 cells/well. After 24h, the culture medium was replaced by 100 μ L of extracts supplemented with 10 μ L FBS. After 24h of incubation, the medium was discarded and 100 μ L of the MTT solution (0.5mg/mL in PBS) was added to each well. Following the incubation of cells for 4h at 37°C, the dark blue formazan crystals were dissolved by adding 100 μ L of DMSO per well. Finally, 100 μ L of each sample was transferred to a 96-well ELISA plate, and the absorbance was measured at 570nm.

3.5.5 Statistical analysis

The data collected from height, diameter, and weight measurements were evaluated for statistical significance by using a one-way Analysis of Variance (ANOVA). Moreover, the value of $P < 0.001$ was considered to be significantly different. Tests were conducted by employing the SPSS 13.0 software (SPSS, USA).

3.6 Summary

A general methodology section is presented in this chapter. It describes the methods used in designing the scaffolds (both the simple one to fulfil the BTE requirements, and the TPMS model), the materials, and the machines used for fabrication and characterization of the scaffolds, with the process parameters that were considered for studying the effects projected by them on printing the scaffolds. This chapter further details the techniques used for evaluating the printed specimens to obtain the optimal process parameters, as well as the computational methods. Furthermore, the protocols of post-treatments and *in vitro* tests are described.

CHAPTER 4

RESULTS AND DISCUSSION

This chapter contains five subsections and each one focuses on the results and the discussions of the five objectives outlined in the thesis. The first subsection examines the characterization of materials and fabricated specimens, as well as the mechanical, the dimensional, and the morphological features of the scaffolds. Next, the second subsection reports and discusses the results of the design of experiment and predictive models used for obtaining the optimum printer parameters. Meanwhile, the third subsection depicts the TPMS-based model simulation results, the mechanical properties, and the deformation mechanisms, as well as the experimental evaluation of TPMS-based model. Moving on, the fourth subsection reports the results and discusses the composition, the microstructure, and the mechanical, the shrinkage, and the density of heat-treated scaffolds, as well as the *in vitro* evaluation of them. Lastly, the fifth subsection explains the effect of phosphate treatment on composition, microstructure, and mechanical properties of the 3D-printed scaffolds.

4.1 Fabricated scaffolds

4.1.1. Material characterization

Plaster-based powder has the advantage of setting fast with good strength, low in cost, and harmless to humans; making it suitable for model making. Plaster of Paris (Bassanite) or calcium hemihydrate ($\text{CaSO}_4 \cdot 1/2\text{H}_2\text{O}$) was among the first materials used for 3D printers. It can be wetted by commercially formulated binder (98% content water);

subsequently, by activating the self-hydration process, a gypsum paste ($\text{CaSO}_4 \cdot 1/2\text{H}_2\text{O} + 1/2\text{H}_2\text{O} = \text{CaSO}_4 \cdot 2\text{H}_2\text{O}$) forms, as shown by Butscher et al. (2011). This material was supplied by Z-corporation in powder form and was used without further treatment. Figure 4.1 displays the XRD spectra of the zp150 powder and the printed sample. The XRD patterns indicated that the starting powder mainly consisted of the calcium sulfate hemihydrate ($\text{CaSO}_4 \cdot 0.5\text{H}_2\text{O}$) phase. The presence of a trace amount of calcium sulfate dihydrate phase in the starting powder was most likely caused by the ability of the zp150 powder (BET specific surface area, $1.94 \text{ m}^2/\text{g}$) to absorb moisture from the environment, followed by a partial hydration reaction.

The binder used in this work was a commercial solvent containing 2-pyrrolidinone (Safety Data Sheet of zb63 binder, 3D Systems Inc., 2012). The FTIR spectra of the zb63 binder, pure water, and 2-pyrrolidinone are shown in Figure 4.2. A comparison between the FTIR spectra of the zb63 binder and pure water showed that the binder mostly contained water. Some of the unidentified peaks in the $700\text{--}450 \text{ cm}^{-1}$ region of the FTIR spectrum were related to the organic components (2-pyrrolidinone) of the binder solution.

Besides, a hardening process occurred as a consequence of the hydraulic reaction between the calcium sulfate hemihydrate powder and the water-based binder. The powder–binder reaction during the printing process resulted in the formation of a small amount of calcium sulfate dehydrate, along with the hemihydrate phase. Moreover, the XRD spectra showed a mixture of both calcium sulfate dihydrate and hemihydrate phases in the printed scaffolds (Figure 4.1-b). This result was probably caused by the inadequate contact between the binder and the powder in the course of 3DP, and it is a sign of an incomplete chemical reaction.

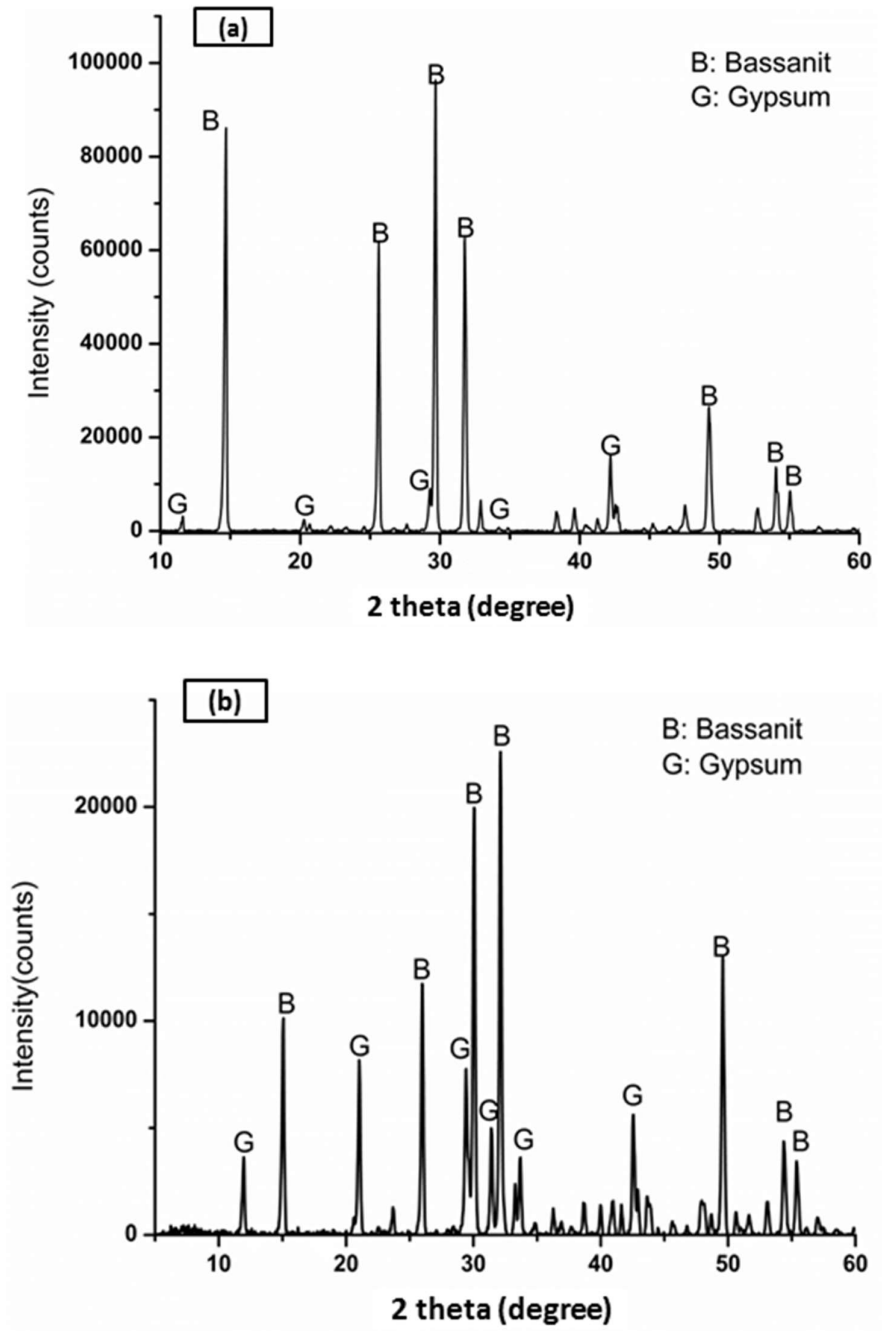


Figure 4.1: XRD patterns of a) the starting powder and b) the printed scaffold.

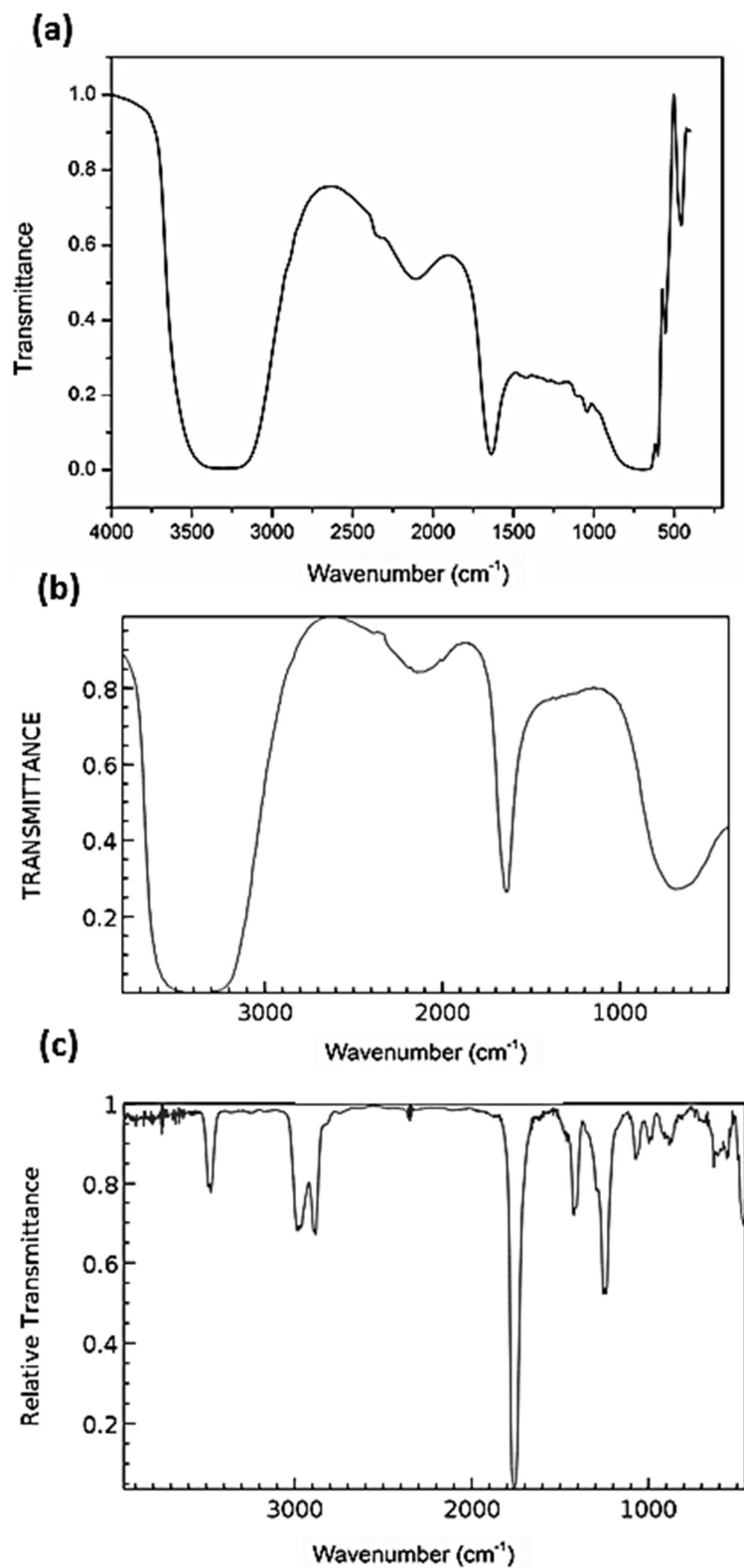


Figure 4.2: FTIR spectra of the a) zb63 binder, b) pure water (National Institute of Standards and Technology, 2011b), and c) 2-pyrrolidinone (National Institute of Standards and Technology, 2011a).

The phase percentages of $\text{CaSO}_4 \cdot 2\text{H}_2\text{O}$ and $\text{CaSO}_4 \cdot 0.5\text{H}_2\text{O}$ in the printed scaffolds were quantified by using the relative intensity ratio of the corresponding and Equation 4.1 (Pattanayak, Dash, Prasad, Rao, & Mohan, 2007):

$$\text{Percent of the phase} = \frac{\text{Intensity of major peak of the phase to be determined}}{\sum \text{Intensity of major peaks of all the phases}} \times 100 \quad (4.1)$$

The XRD analysis of the porous specimens revealed a higher $\text{CaSO}_4 \cdot 0.5\text{H}_2\text{O}$ phase quantity compared to that with lesser amounts for the solid specimens. This finding indicated that the hemihydrate phase remained the major phase during the printing process, whereas the dihydrate phase did not significantly develop due to the powder–binder reaction. The percentages of the calcium sulfate phases in the starting powder, porous, and solid-printed scaffolds are shown in Table 4.1.

Table 4.1: Calcium sulfate phases present in the porous and the solid 3DP scaffolds calculated based on the XRD results.

Samples	$\text{CaSO}_4 \cdot 0.5\text{H}_2\text{O}$ (%)	$\text{CaSO}_4 \cdot 2\text{H}_2\text{O}$ (%)
Powder	94.0	6.0
Porous	89.0	11.0
Solid	63.4	36.6

Other than that, the FTIR spectra of the starting zp150 calcium sulfate powder and the printed scaffold are shown in Figure 4.3. The bands related to the stretching vibration of the O-H groups were detected in the $3700\text{--}3500\text{ cm}^{-1}$ range. The bending vibrations of the O-H bond in the H_2O molecule were associated with the bands at 1724 and 1627 cm^{-1} . The characteristic bands assigned to the vibrations of the S-O bonds in SO_4^{2-} appeared at wave numbers 1146 cm^{-1} (stretching), as well as 659 and 601 cm^{-1} (bending). In the spectrum of the calcium sulfate powder (dotted line), the trace of the C-O band at 1425

and 1370 cm^{-1} , as well as a weak shoulder at 900 cm^{-1} , had been attributed to the presence of CO_3^{2-} groups due to the CO_2 adsorption capacity of the relatively high surface area of the zp150 powder. However, this trace was less noticeable in the spectrum of the printed scaffold (solid line). Besides, the FTIR spectrum of the starting powder was very similar to that of the printed scaffold. Therefore, no significant structural changes occurred in the hydration state of the starting calcium sulfate during the 3DP process, which are in agreement with the results obtained from the XRD analysis discussed earlier.

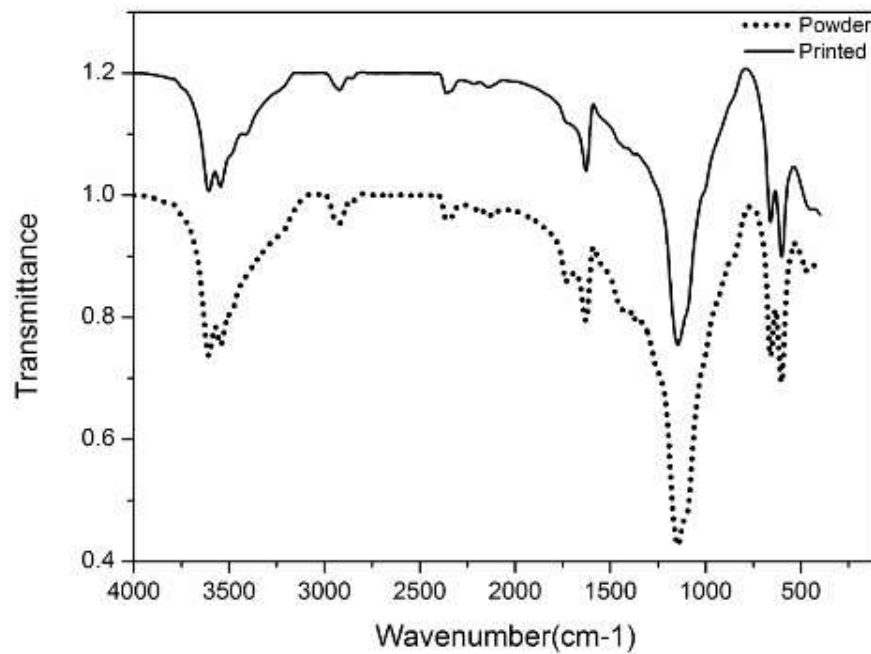


Figure 4.3 :FTIR spectra of the printed scaffold (solid line) and the ZP150 starting calcium sulfate powder (dotted line).

Moreover, the correlation between optimum scaffold pore size and cell activity has always been a conflicting issue in the literature (Murphy, Haugh, & O'Brien, 2010). Large pores ($>0.5\text{ mm}$) favor fast vascularization, but decreases the specific surface area, which in turn, limits cell attachment (Lien et al., 2009). This phenomenon represents a potential limitation of 3DP technology due to the difficulty in removing unbound powder from the small cavities within the scaffold after the printing process.

Therefore, according to Vorndran et al., (2011), the powders must meet the following two conditions for successful application in 3DP: 1) capability to form relatively smooth and even powder layers in the thickness range of 100–200 μm , as well as 2) react with the binder solution during the printing process and harden consequently. The first condition is mainly related to the particle size and the particle size distribution of the starting powder. In fact, a study carried out by Gbureck et al., (2007) explained that appropriate particle sizes should be in the 20–50 μm range. Powders with relatively small particle size can be easily removed from the printed parts. However, the presence of fine particles smaller than 5 μm in the powder encourages the formation of agglomerates up to 1–2 mm in diameter, leading to a heterogeneous powder bed with sizeable grooves that make precise printing almost unachievable (Butscher et al., 2011; Vorndran et al., 2011).

Furthermore, the differential and the cumulative particle size distributions of zp150 powder are shown in Figure 4.4. Employing a starting powder with an appropriate particle size ($d_{10}=0.64 \mu\text{m}$, $d_{50}=27.36 \mu\text{m}$, $d_{90}=68.83 \mu\text{m}$) can significantly reduce the formation of unwanted agglomerates. However, this particle size range may impose a limit on the minimum feature size, particularly when printing scaffolds with complicated geometry and structure. The particle size of the powder also has an influence on the layer thickness that can be attained. Thin powder layers are preferable because a relatively higher level of resolution can be achieved. Besides, the layer thickness must be larger than the largest particle size of the powder. Considering all the necessary factors, 89 μm was chosen as the layer thickness in the present work because the powder particles being used had a $d_{90} = 68.83 \mu\text{m}$. This powder was suitable for the printing process and enabled high printing accuracy, as well as sufficient mechanical strength, to remove the printed samples from the powder bed.

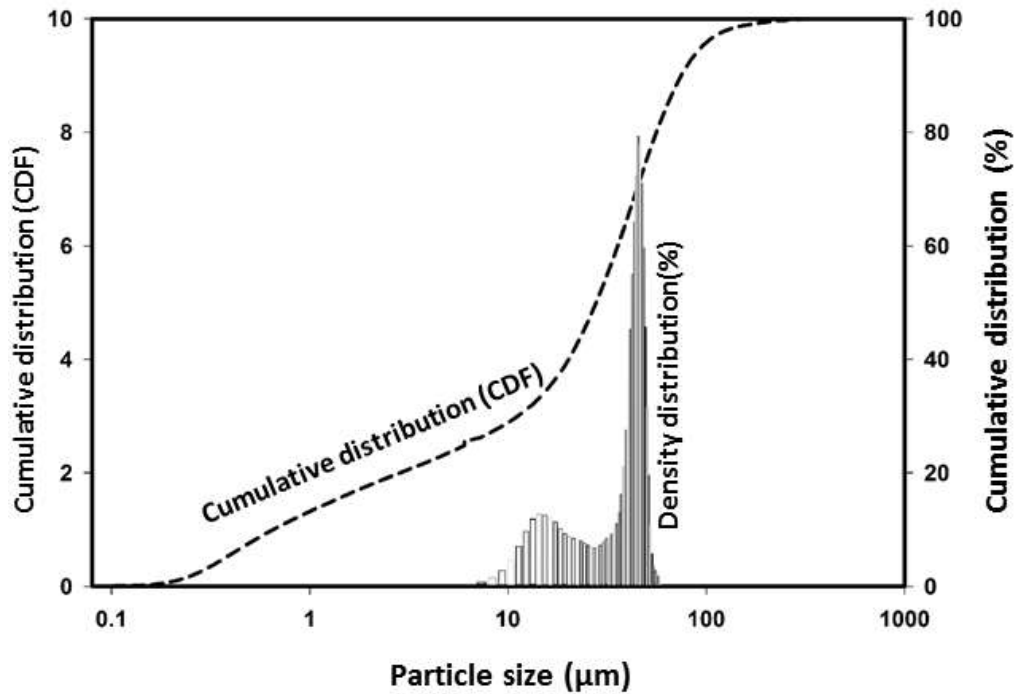


Figure 4.4: Differential and cumulative particle size distributions of the zp150 calcium sulfate starting powder.

Scaffolds were fabricated by using 3DP for each of the design series (pore sizes of 0.4, 0.6, and 0.8 mm). After build-up, all of the scaffolds possessed sufficient green strength to withstand the air gun pressure during removal of the unbound powders (de-powdering process). However, it was difficult to remove all of the unbound powder from the scaffolds with pore sizes 0.4 and 0.6 mm. Therefore, the minimum feature size of 0.8 mm was chosen. The SEM image shown in Figure 4.5 reveals the microstructure of a printed sample.

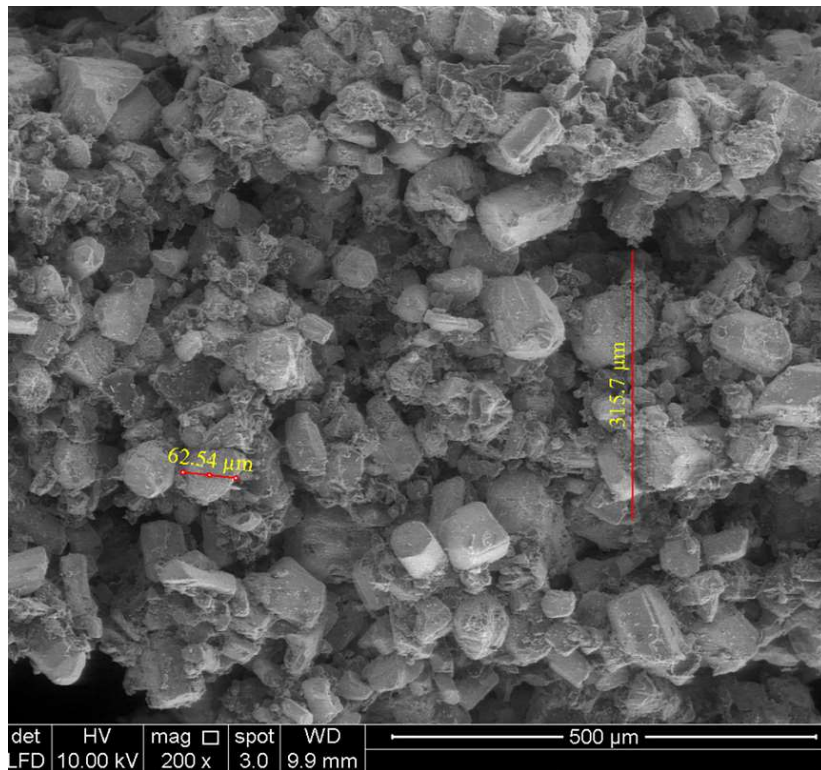


Figure 4.5: SEM Image of powder particles after fabrication.

The results obtained suggested the minimum pore size required for an acceptable definition, for the geometries studied, was 0.8 mm, which is smaller than the results retrieved from Castilho et al., (2011) and Zhou et al., (2014), who found the minimum pore sizes of 1 mm and 1.2 mm, respectively. Figure 4.6 shows the details of a fabricated specimen with pore sizes 0.4, 0.6, and 0.8 mm, which illustrated a lack of parallelism between the faces, and indicated poor geometric control of macro-pores of samples with pore sizes 0.4 and 0.6 mm (Figures 8a and 8b) compared to the pore size of 0.8 mm (Figures 8c and 8d). Moreover, the SEM images and the micro-CT analysis showed that specimens with a pore size of 0.8 mm had an interconnected pore structure indicating that the unbound powder was totally removed in the de-powdering step (Figures 4.7, 4.8, and 4.9).

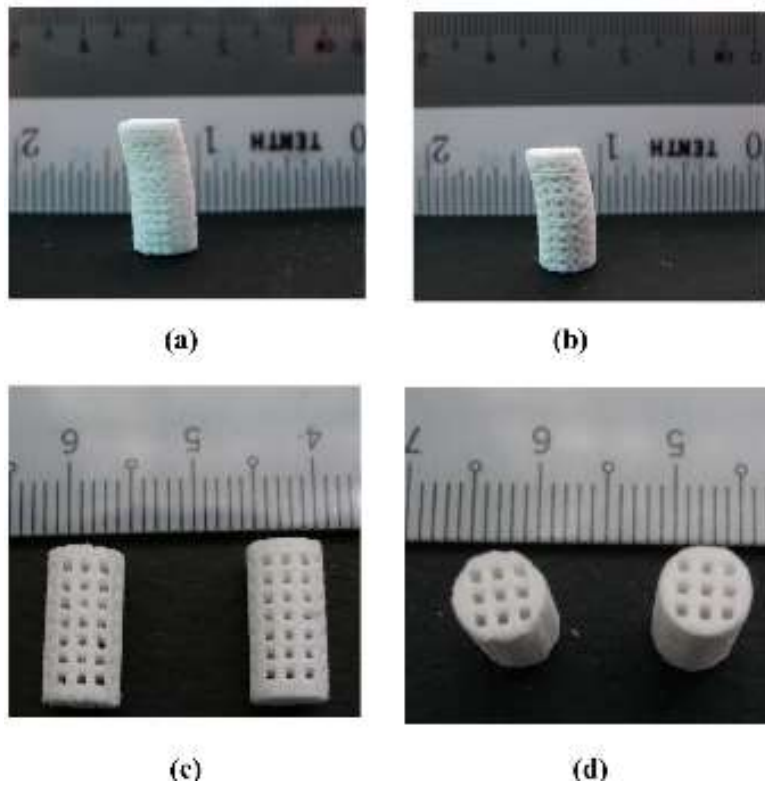


Figure 4.6: Fabricated scaffold using the (a) Unit cell type 1- Pore size: 0.4mm, (b) Unit cell type 2- Pore size: 0.6mm, (c) Side view, (d) Top view of the Unit cell type 3- Pore size: 0.8mm.

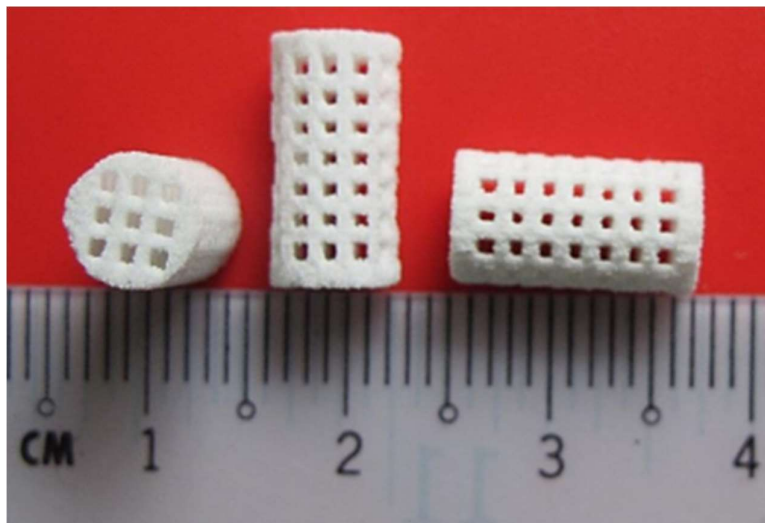


Figure 4.7: Top and side views of the fabricated scaffold using a unit cell with a 0.8 mm pore size.

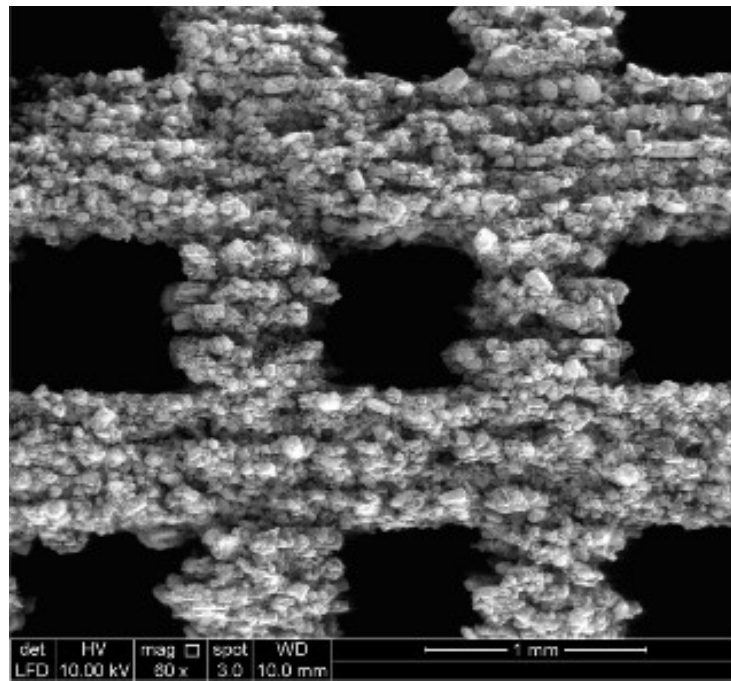


Figure 4.8: SEM images- fabricated scaffold using Unit cell type 3- Pore size: 0.8mm.

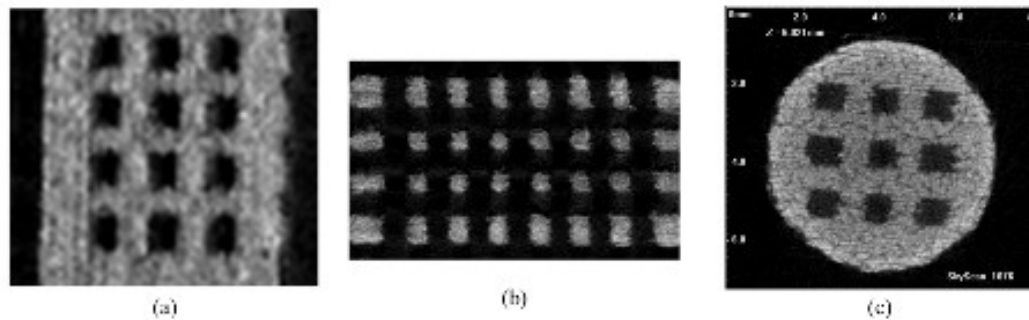


Figure 4.9: Micro-CT images - fabricated scaffold using Unit cell type 3- Pore size: 0.8mm (a) front view, (b) middle cross-section view, (c) Top view.

4.1.2 Dimensional accuracy

In preliminary tests, it was noted that the size of printed parts did not accurately match the CAD design. The deviations were between 1 and 6% for both the diameter and the height. The average measurement of all samples is summarized in Table 4.2.

The results of SEM images (Figure 4.10 as an example) and micro-CT analysis showed the macro-pore size of all specimens was less than the CAD design. This was because; the unbound powder that was not totally removed during the de-powdering process. The

macro-pore size of all specimens was approximately between 680 μm to 750 μm . The specimens fabricated in the x-direction in all test conditions were de-powdered completely and were rapidly compared to other specimens fabricated in other directions. The circular cross section of z-direction fabricated samples and the cylinder wall of the y and x directions fabricated sample required more time to de-powder. This finding could be related to the fact that these sections were the first fabricated layers in the printing procedure for each specimen and due to the amount of binders relative to the powder without any previous printed structure; thus, the powder piled upon itself making the de-powdering step more difficult.

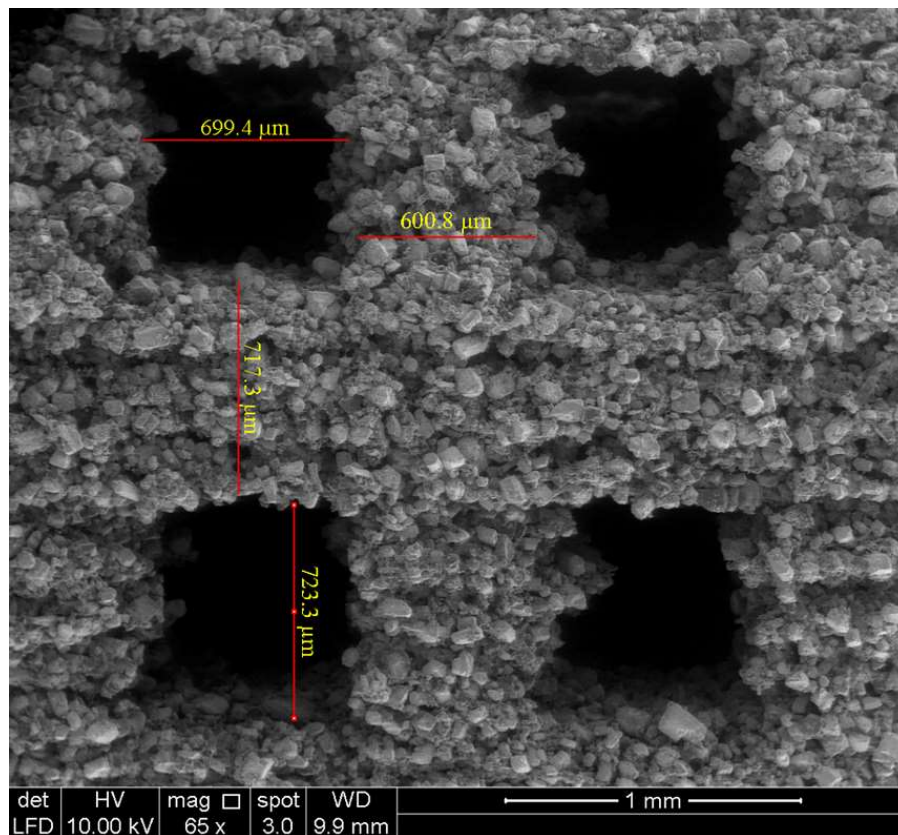


Figure 4.10: SEM image- fabricated scaffold pore and strut dimension.

As a result, the percentage of change in the macro-pore size was between 6% and 15% compared to that with the CAD design. The strut size of all specimens was between

600 and 610 μm , which is in close agreement with the CAD design size. This, in fact, is well-accepted that for BTE purposes, the macro-pore size should be in the range of 200 to 900 μm (Krishnan, et.al, 2012; Lee, & Wu, 2012; Streubel, et.al, 2011). Accordingly, it seems that the macro-pores achieved in this research indicated appropriate scaffolds for BTE applications.

Table4.2: The measurements of diameter and height of the 3D-printed porous scaffolds

Layer thickness (μm)			89				102			
Delay*(ms)			50	100	300	500	50	100	300	500
Diameter (mm)	Orientation	X	5.84	5.99	5.84	5.88	5.79	5.96	5.78	6.04
		Y	5.80	5.93	5.78	5.83	5.77	5.94	5.71	5.85
		Z	5.79	5.82	5.79	5.82	5.78	5.82	5.77	5.76
Height (mm)		X	11.76	11.77	11.73	11.76	11.74	11.76	11.68	11.76
		Y	11.78	11.81	11.78	11.42	11.78	11.82	11.80	11.82
		Z	12.15	12.31	12.08	12.14	12.01	12.14	11.90	12.36
Layer thickness (μm)			114				127			
Delay*(ms)			50	100	300	500	50	100	300	500
Diameter (mm)	Orientation	X	5.78	5.82	5.85	5.85	5.87	5.89	5.85	5.86
		Y	5.82	5.90	5.79	5.82	5.85	5.88	5.82	5.83
		Z	5.79	5.77	5.78	5.76	5.84	5.81	5.80	5.89
Height (mm)		X	11.81	11.76	11.78	11.75	11.78	11.78	11.77	11.83
		Y	11.82	11.86	11.85	11.82	11.83	11.85	11.83	11.90
		Z	11.97	12.17	12.01	12.02	12.09	12.23	11.87	11.89

Table 4.2 portrays that the diameter of all specimens was less than the diameter of the CAD model (6 mm). The height of the scaffolds, except for the specimens fabricated in the z-direction, was also less than that of the design.

Figure 4.11 shows the dimensional deviation ratio of all fabricated specimens. Most of the samples exhibited height deviations during the fabrication. Moreover, samples built in the z-direction in each layer thickness and delay time had more height changes in contrast to other orientations. Besides, samples fabricated in the x-direction for all delay times and layer thicknesses had the least changes in height. Samples printed in the x-direction and with a delay of 300 ms in each of four layer thicknesses had the least distortion.

The ANOVA for the DDR is listed in Table 4.3. The model F-value of 3.66 implied that the model was statistically significant. There was only a 0.28% chance that these values occur due to noise. The P-value of orientation showed that the changes in the orientation value relative to changes in the response variable were significant. For dimensional deviation, the ratio orientation with a 36.62% contribution was the most significant model term. The main effect plot (Figure 4.12) also supported this.

The standard deviation of the model was 0.027. The model signal-to-noise ratio (7.33) indicated an adequate signal because a ratio greater than four was desirable. Other than that, DA plays an important role in dimensional accuracy. In this work, DA=0 represents complete isotropy, while DA=1 represents complete anisotropy.

Since the CAD design was symmetrical, a printed scaffold with a lower DA would possess a greater dimensional accuracy than a sample with a larger DA. The DA values of all 48 samples fabricated scaffolds are listed in Table 9. As evident, the samples printed in the x-direction in all layer thicknesses and all delay times were more isotropic in comparison to those printed in either the z or y direction

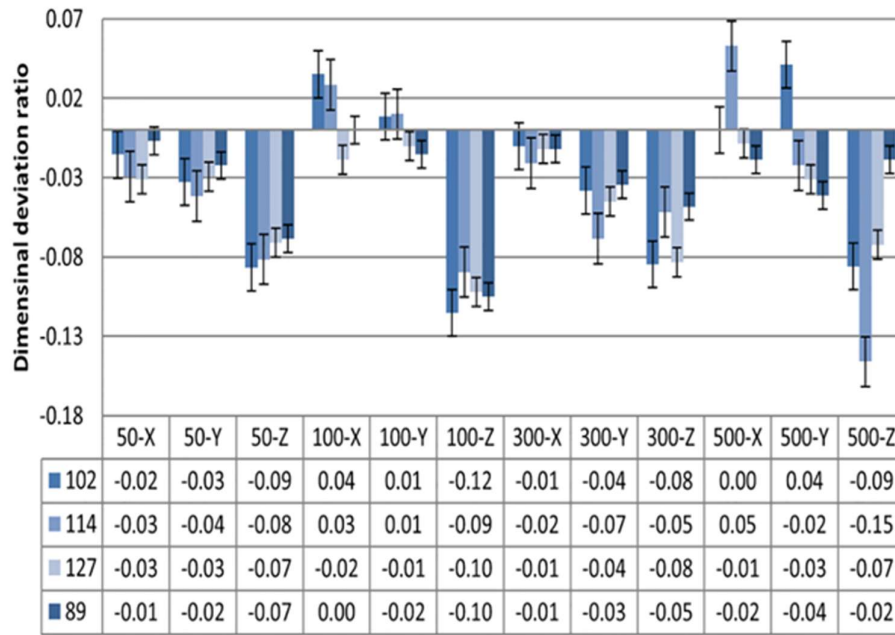


Figure 4.11: The dimensional accuracy ratio of all 48 runs for each layer thickness, delay, and orientation.

Table4.3: Analysis of variance of DDR for full factorial design model-classic sum of square (type II).

Source	Sum of square	df	Mean Square	F Value	P-value	Prob>F	PCR*
Model	0.071	29	2.463E-003	3.66	0.0028	-	-
A-Layer thickness	9.448E-004	3	3.149E-004	0.47	0.7085	0.44	0.44
B-Delay	1.902E-003	3	6.340E-004	0.94	0.4413	0.89	0.89
C-Orientation	0.052	2	0.026	38.91	< 0.0001	36.62	36.62
AB	2.622E-003	9	2.913E-004	0.43	0.8999	0.41	0.41
AC	5.167E-003	6	8.612E-004	1.28	0.3157	1.21	1.21
BC	8.364E-003	6	1.394E-003	2.07	0.1083	1.96	1.96
Residual	0.012	18	6.735E-004	-	-	-	-
Cor Total	0.084	47	-	-	-	-	-

*. Percentage of contribution ratio.

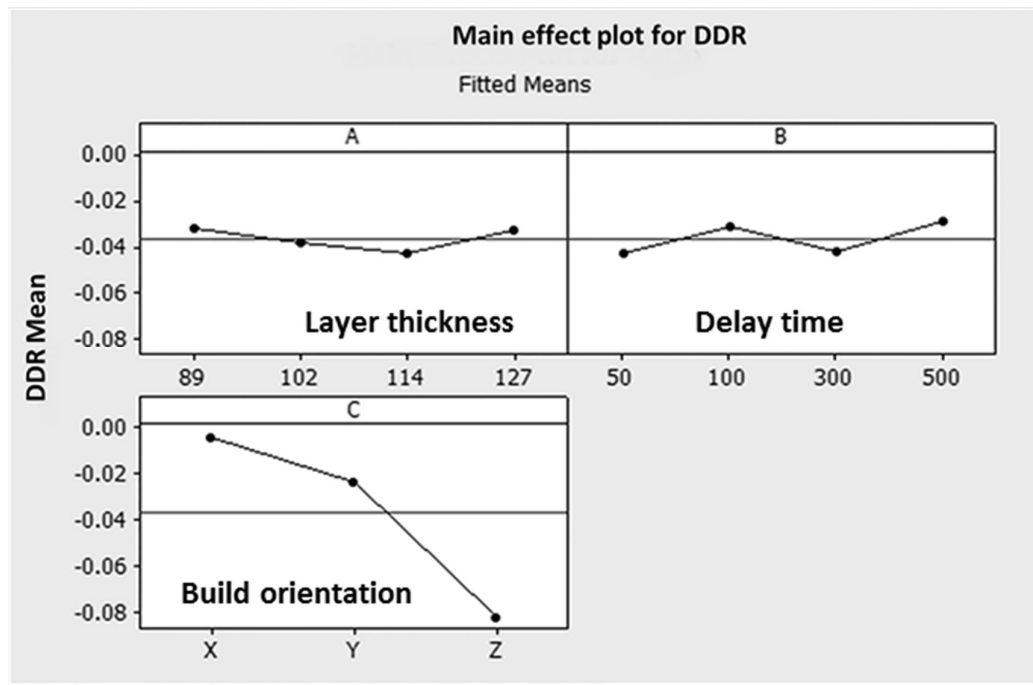


Figure 4.12: Main effect plot for dimensional deviation ratio.

Table 4.4: Degree of anisotropy of all 48 runs for each layer thickness, delay time, and orientation.

Layer thickness (μm)			89				102			
Delay*(ms)			50	100	300	500	50	100	300	500
Degree of anisotropy	Orientation	X	0.64	0.59	0.43	0.49	0.51	0.63	0.45	0.49
		Y	0.71	0.66	0.62	0.62	0.64	0.60	0.59	0.60
		Z	0.77	0.74	0.68	0.78	0.70	0.70	0.70	0.80
Layer thickness (μm)			114				127			
Delay*(ms)			50	100	300	500	50	100	300	500
Degree of anisotropy	Orientation	X	0.55	0.55	0.54	0.59	0.51	0.62	0.47	0.47
		Y	0.66	0.68	0.67	0.69	0.72	0.71	0.56	0.67
		Z	0.77	0.77	0.77	0.77	0.77	0.77	0.69	0.73

Due to the greater degree of isotropy, samples fabricated in the x-direction were also selected for further investigation. Figure 4.13 shows the DA of specimens, which were printed in the x-direction for each layer thickness and delay time. The specimens that were fabricated with 300 ms delay time had lower DA values than the other samples. Moreover, specimens fabricated with thinner layer thicknesses, and with a delay of 300ms, were the most isotropic. The prototypes printed with a layer thickness of 89 μm and a delay time of 300 ms were the most isotropic samples.

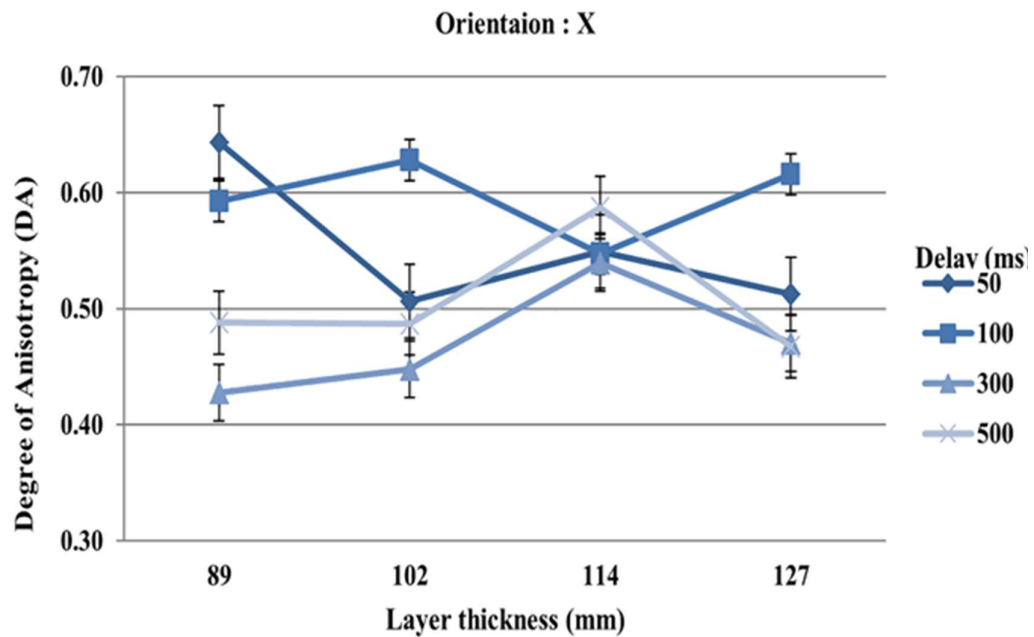


Figure 4.13: Degree of anisotropy of fabricated specimens in X direction for all layer thicknesses and delay time.

The ANOVA results for the DA are shown in Table 4.5. The F-value (11.60) indicated that the model was significant. "Prob > F" value of orientation (c) suggested that orientation was the most significant term in the model with a 37 % contribution, while layer thickness delay was also significant, but to a lesser degree. Figure 4.14 supports this result. Meanwhile, the model signal-to-noise ratio was 12.980.

There were two main factors that directly had an effect on dimensional accuracy: 1) solidity of each layer, and 2) compaction of sequential layers (Butscher et al., 2011;

Khalyfa et al., 2007). Previous studies indicated that powder and binder reactivity play a considerable role in the 3DP procedures. Additionally, adequate timing significantly affects the reactivity of the powder, the binder, as well as their bonding (Bose et al., 2013a; Chumnanklang et al., 2007)

Table 4.5: Analysis of variation of DA for full factorial design model-classic sum of square (type II).

Source	Sum of square	df	Mean Square	F Value	P-value Prob>F	PCR*
Model	0.46	29	0.016	11.60	< 0.0001	-
A-Layer thickness	0.021	3	6.897E-003	3.70	0.0310	1.50
B-Delay	0.026	3	8.714E-003	9.12	0.0007	1.89
C-Orientation	0.34	2	0.17	132.12	< 0.0001	36.96
AB	0.034	9	3.766E-003	2.04	0.0953	0.82
AC	5.046E-003	6	8.410E-004	0.48	0.8132	0.18
BC	0.017	6	2.883E-003	2.06	0.1096	0.63
Residual	0.030	18	1.657E-003	-	-	-
Cor Total	0.47	47	-	-	-	-

. Both the DDR and the DA results suggested that an increase in the delay time resulted in better bonding between powder and binder, as well as in producing 3D objects with an improved dimensional accuracy and isotropy. However, there is a trade-off between choosing time for better bonding of powder intra-layer and inter-layer. A greater delay time might cause complete binder dryness, which is desirable for reactivity of binder and powder within a layer, but reduces the bonding capability of the powder to the next layer; resulting in discrete layering rather than a homogenous part. This condition significantly influences the dimensional accuracy and the mechanical features of the 3D-printed parts.

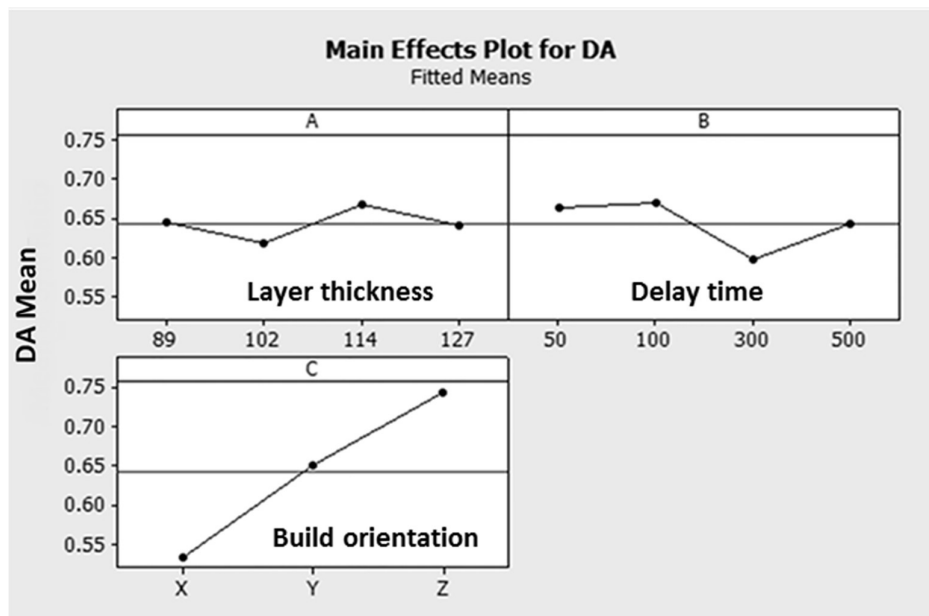


Figure 4.14: Main effect plot for degree of anisotropy.

In supporting these hypotheses, the results also showed that additional time exposure of a printed layer allowed further binder relaxation and had a positive effect on the structural features of a printed sample. In contrast, a delay time greater than 300 ms had a negative effect on the prototypes due to poor bonding between neighboring printed layers.

In this study, by evaluating sample dimensions (diameter and height), as well as DDR and DA factors, it was found that the specimens fabricated in the x-direction using the minimum layer thickness and a 300 ms delay time yielded the greatest dimensional accuracy.

4.1.3 Mechanical properties

The results of mechanical compression tests (Table 4.6) showed that differences in each process parameter resulted in various compressive strength values and Young's modulus. Specimens fabricated in the x-direction in each layer thickness and delay time

had greater compressive strength than specimens built in either the z or y direction. Besides, insufficient compressive strengths of z-direction fabricated led to fracture in some samples during de-powering. For all layer thicknesses and build orientations, specimens fabricated with 300 ms delay time had greater compressive strengths than the others did.

The results also projected that the orientation of the powder-spreading and binder jetting affected the mechanical behavior of the printed parts. In the x-direction fabricated samples, the compressive load was applied parallel to the direction of printed layers and perpendicular to the direction of the binder jetting. In contrast, in the y-direction printed samples, the compressive loads were applied parallel to the direction of printed layers and perpendicular to the direction of binder jetting. Moreover, a decrease in layer thickness caused an increase in the number of layers. This may result in higher integrity that in turn will increase the strength of the specimens.

These results also indicated the interaction between the layer thickness and the delay time parameters had a considerable effect on the mechanical strength of printed samples. By focusing on x-direction fabricated specimens (Figure 4.16), which have the greatest compressive strengths, it had been concluded that the specimens fabricated by thinner layer thicknesses and lower delay times possessed lower mechanical integrity due to poor bonding between powder particles in each layer and also the densification of neighboring layers.

The Micro-CT image of samples after mechanical testing is illustrated in Figure 4.15. Supporting the previous results, one can observe in these images that the specimens printed in the Z direction displayed varied fracture behavior from specimens printed in

other directions. The cracks appeared more in the struts, and breaking was in the upper layers near the region on which the load was carried out. The specimens printed in the X and Y directions were sliced from the cylindrical wall, which had been parallel to their print orientation. The specimens printed in the Y direction exhibited more cracks in their struts than the specimens printed in the X direction.

Table4.6: Mechanical property assessment of porous 3D-printed specimens.

Layer thickness (μm)			89				102			
Delay*(ms)			50	100	300	500	50	100	300	500
Compressive strength (MPa)	Orientation	X	0.44	0.37	0.75	0.62	0.56	0.34	0.58	0.48
		Y	0.25	0.27	0.42	0.26	0.34	0.20	0.31	0.27
		Z	0.18	0.23	0.37	0.21	0.25	0.22	0.30	0.22
Young's Modulus	Orientation	X	27.70	19.65	47.15	26.26	36.27	17.96	34.47	23.16
		Y	11.80	10.36	18.27	11.89	16.60	7.41	12.29	9.13
		Z	4.21	4.28	7.72	3.84	4.98	3.95	4.61	2.09
Layer thickness (μm)			114				127			
Delay*(ms)			50	100	300	500	50	100	300	500
Compressive strength (MPa)	Orientation	X	0.40	0.47	0.76	0.65	0.46	0.50	0.56	0.50
		Y	0.17	0.37	0.39	0.30	0.24	0.43	0.44	0.28
		Z	0.19	0.32	0.33	0.25	0.19	0.25	0.30	0.25
Young's Modulus	Orientation	X	23.71	29.22	46.08	25.12	27.10	21.56	26.67	24.77
		Y	12.01	17.05	19.56	16.03	10.42	17.13	17.52	9.24
		Z	2.27	7.06	5.64	3.05	2.79	4.01	5.08	2.83

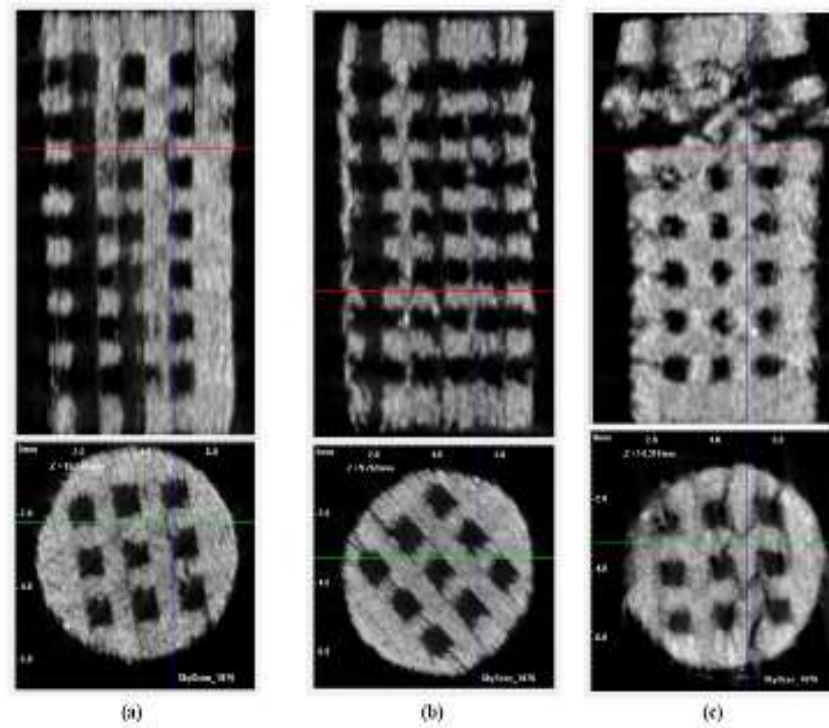


Figure 4.15: The Micro-CT images of the front and top views of the specimens printed in the (a) X, (b) Y, and (c) Z directions after the compressive mechanical test.

Generally, samples printed in the Z direction were farther from the precision. They typically had some fractures and deformations. Samples printed in the X and Y directions were more intact. This may be related to the fact that the samples printed in the Z direction had the most number of layers. Consequently, more layer transposition can take place in the Z-direction printed samples, resulting in more alteration and cracks in the struts. Furthermore, the direction of binder-jetting and powder-spreading seemed to have a significant effect on the mechanical behavior of the samples (Figure 4.17).

In the Z-direction printed specimens, the successive layers and the direction of binder-jetting in each layer were perpendicular to the applied load. Meanwhile, in the X-direction printed specimens, the applied load was parallel to the layers and perpendicular to the binder-jetting direction, while vice versa in Y-printed specimens. Notably, in the

X-direction printed specimens, the binder jet traveled a longer path than in the two other directions.

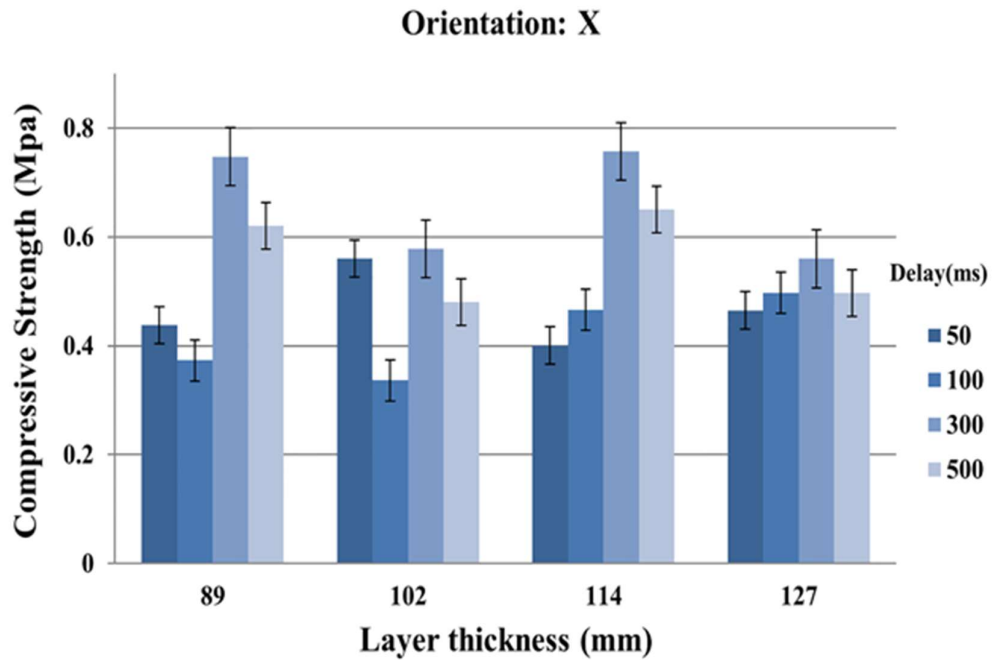


Figure 4.16: Compressive strength of specimens fabricated in X orientation in each layer thickness and delay time.

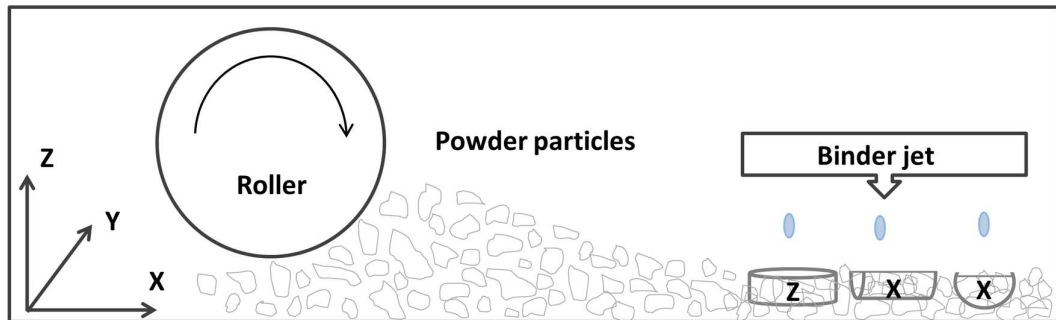


Figure 4.17: Binder-jetting and powder-spreading directions.

Table 4.7 summarizes the mechanical features derived from the ANOVA results. The model F-value of 17.58 implied that the statistical model was significant at the selected confidence level. In this case, some of the significant model terms applied were delay, orientation, interaction between layer thickness and delay time. Among these, orientation with a nearly 34% contribution, had been the most significant term. These

results were supported by the data presented in Figure 4.18. Furthermore, the model signal-to-noise ratio (16.612) showed an acceptable signal.

Table 4.7: Analysis of variance of compressive strength for full factorial design model-classic sum of square (type II).

Source	Sum of square	df	Mean Square	F Value	P-value Prob>F	PCR*
Model	1.01	29	0.035	17.58	< 0.0001	-
A-Layer thickness	0.012	3	3.983E-003	2.01	0.1486	0.39
B-Delay	0.16	3	0.054	27.41	< 0.0001	5.35
C-Orientation	0.67	2	0.34	169.32	< 0.0001	33.66
AB	0.095	9	0.011	5.33	0.0013	1.09
AC	0.016	6	2.608E-003	1.32	0.3001	0.26
BC	0.054	6	8.956E-003	4.52	0.0058	0.89
Residual	0.036	18	1.981E-003	-	-	-
Cor Total	1.05	47	-	-	-	-

* Percentage of contribution ratio.

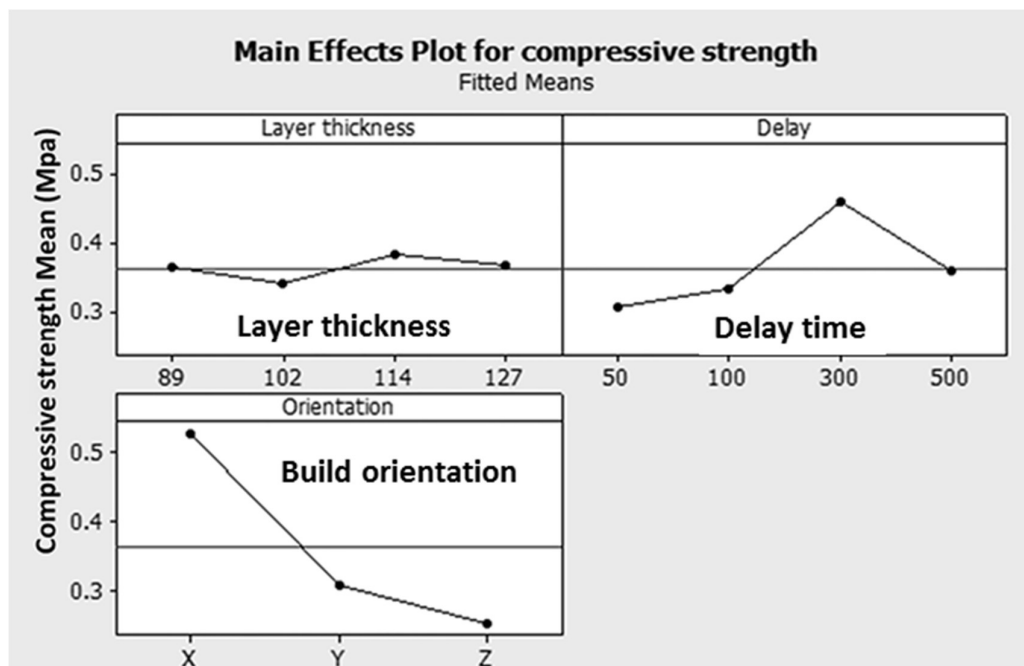


Figure 4.18: Main plot for Compressive strength.

Table 4.8: Porosity of 3D-printed specimens.

Layer thickness (μm)			89				102			
Delay*(ms)			50	100	300	500	50	100	300	500
Closed porosity	Orientation	X	0.83	0.25	0.29	0.20	0.17	0.05	0.90	0.14
		Y	0.81	0.01	0.08	0.18	0.19	0.05	0.88	0.08
		Z	0.79	0.01	0.06	0.90	0.27	0.02	0.08	0.77
Open porosity		X	65.17	45.18	67.62	61.56	61.37	40.91	63.01	57.29
		Y	66.00	43.06	62.61	61.62	64.50	43.34	60.86	55.45
		Z	64.78	42.54	61.93	63.40	71.49	42.78	60.88	61.72
Total Porosity		X	65.46	45.32	67.71	61.64	61.43	40.93	63.34	57.35
		Y	66.28	43.07	62.64	61.70	64.57	43.36	61.20	55.48
		Z	65.06	42.55	61.95	63.73	71.56	43.93	60.91	62.01
Layer thickness (μm)			114				127			
Delay*(ms)			50	100	300	500	50	100	300	500
Closed porosity	Orientation	X	0.02	0.46	0.73	0.61	0.22	0.91	0.10	0.24
		Y	0.02	0.76	0.50	0.60	0.83	0.87	0.11	0.10
		Z	0.46	0.73	0.59	0.89	0.98	1.28	0.08	0.09
Open porosity		X	38.25	72.07	63.33	63.70	62.82	63.31	60.85	59.33
		Y	35.28	67.94	65.16	65.79	65.62	63.31	63.32	61.27
		Z	61.21	66.75	66.65	65.87	65.17	62.37	60.79	55.93
Total Porosity		X	38.26	72.20	63.60	63.92	62.90	63.65	60.89	59.43
		Y	35.29	68.18	65.34	65.99	65.90	63.63	63.36	61.31
		Z	61.39	66.99	66.85	66.17	65.51	62.86	60.82	55.97

4.1.4 Porosity

The results for porosity (Table 4.8) showed that specimens built in the x-direction were more porous than the samples printed in the z or y direction. Specimens with a 114 μm layer thickness and 100 ms delay time printed in the x-direction had the maximum porosity, which supported a previous report (Farzadi, Solati-Hashjin, Asadi-Eydivand, & Osman, 2014).

According to Will et al., (2013), there is a general agreement that 3D bone scaffolds should have a highly open porous structure (>40-60%). Moreover, in BTE, the key factor in bone regeneration is the ability of scaffolds to conduct fluid flow. This parameter, called permeability, directly depends on porosity and interconnectivity of the printed samples (Dias et al., 2012; Mitsak, Kemppainen, Harris, & Hollister, 2011).

Table 4.9: Analysis of variance of porosity for full factorial design model-classic sum of square (type II).

Source	SUM OF SQUARE	df	Mean Square	F Value	P-value Prob>F	PCR*
Model	3509.69	29	121.02	8.79	< 0.0001	-
A-Layer thickness	183.02	3	61.01	4.43	0.0168	1.73
B-Delay	476.69	3	158.90	11.55	0.0002	4.52
C-Orientation	39.02	2	19.51	1.42	0.2680	0.50
AB	2528.70	9	280.97	20.42	< 0.0001	8.00
AC	121.13	6	20.19	1.47	0.2448	0.58
BC	161.13	6	26.86	1.95	0.1269	0.7
Residual	247.69	18	13.76	-	-	-
Cor Total	3757.38	47	-	-	-	-

* Percentage of contribution ratio.

The model F-value was 8.79. Layer thickness, delay time, as well as two-way interaction between delay time and layer thickness, played important roles in porosity and had been some of the significant model terms, among which, the interaction between delay time and layer thickness with an 8% contribution was the most significant factor in porosity (Table 4.9). Similarly, the main effect plot (Figure 4.19) showed that layer thickness and delay time significantly affected the porosity of the printed scaffolds. Besides, the model signal to ratio (10.901) indicated an adequate signal.

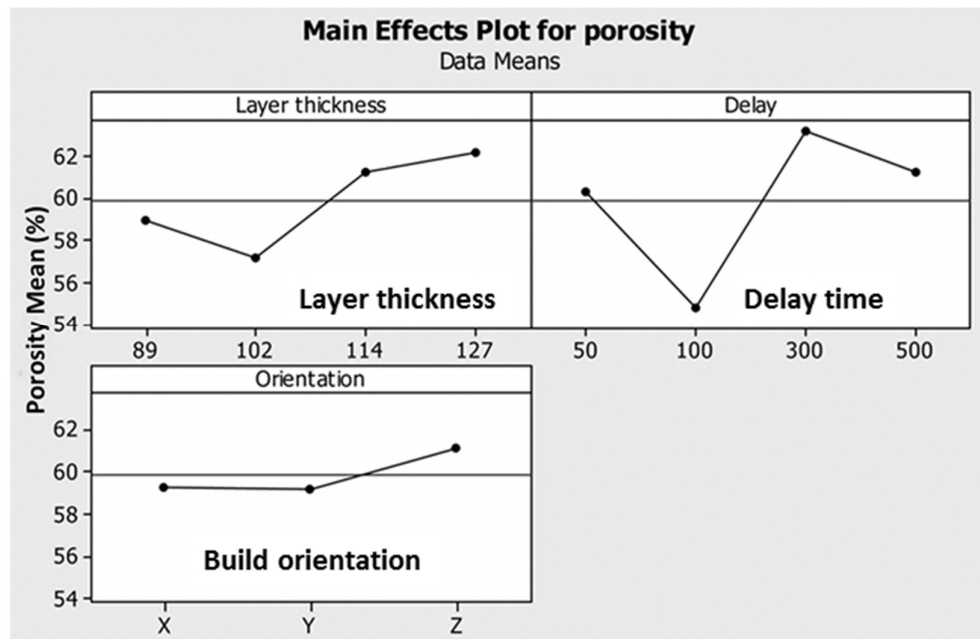


Figure 4.19: Main effect plot for porosity.

Table 4.10 summarizes the results of two specimens printed in the X direction and that with the highest compressive strength. Despite of the fact that these two samples approximately had the same compressive strength, the samples printed with an 89 μm layer thickness and 300 ms delay time were more isotropic and porous with better pore spacing and openness. These samples also had greater Young's moduli. Thus, the optimal 3DP processing conditions were x-direction orientation with a minimum layer thickness and 300 ms delay time for scaffold prototypes in relation to BTE applications. These results, compared with those obtained by Farzadi et al., (2014), showed that by choosing the minimum layer thickness, an additional 200 ms had been needed for consistent setting of powder and binder. This additional time allowed better densification of adjacent powder particles and between sequential layers, which improved the mechanical strength of the printed specimens.

Among the many different rapid prototyping techniques, 3D powder printing is particularly attractive for its rapid and inexpensive ability to form accurate structures. In

a study conducted by Asadi-Eydivand, Solati-Hashjin, Farzad, and Osman (2016), further post-treatment was avoided to focus only on the design of experiment factors that affected the dimensional accuracy and the mechanical behavior of the printed parts. Nonetheless, in the present work, the 3DP scaffolds were subjected to a heating process to evaluate the influence of heat treatment on the structure, the mechanical performance, and the *in vitro* response of the 3DP scaffolds.

Table4.10: The optimum fabricated scaffolds in terms of compressive strength.

Layer thickness (μm)	Delay time (ms)	Degree of anisotropy	Compressive strength (Mpa)	Young's modulus	Close porosity	Open porosity	Total porosity (%)
89	300	0.43	0.75	47.15	0.29	67.62	67.71
114	300	0.64	0.76	46.08	0.73	63.33	63.60

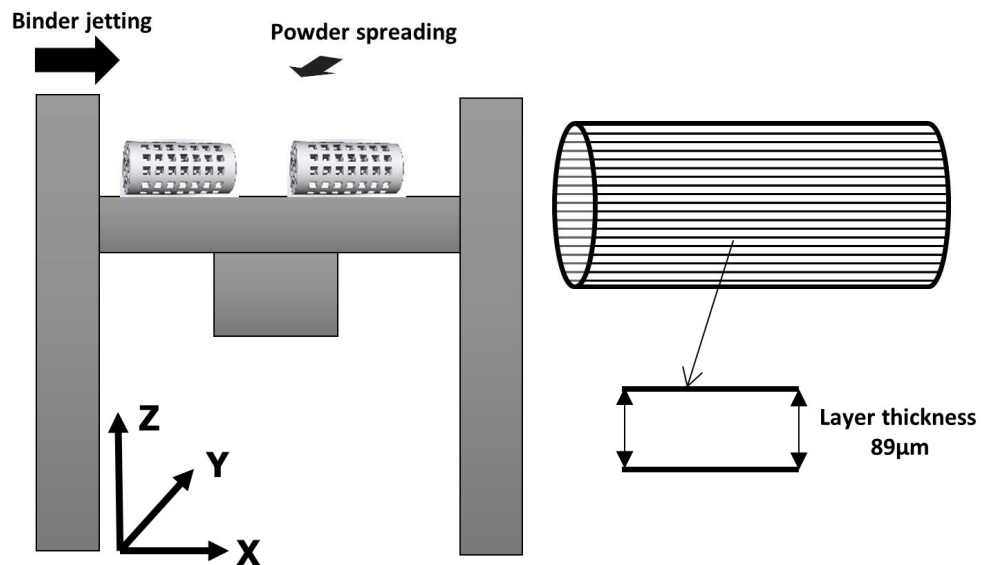


Figure 4.20: Schematic of the build bed-printing layout and printing parameters.

4.2 Optimum process parameters

In this part, a predictive model for 3DP process had been extracted. The model predicted the mechanical strength, and the open porosity of a part fabricated using this process. Mechanical strength and open porosity are the two fundamental properties in tissue engineering applications. The influencing parameters are build orientation, delay time, and layer thickness. Moreover, sufficient green strength is necessary for the de-powdering step, and more compressive strength decreases the need for further post-processing. Therefore, the input parameters of the AANN model include orientation, thickness, and delay time, while its output parameters are mechanical strength and open porosity. The required identification data were prepared by conducting experimental tests at different values and permutations of input parameters. The orientation input could be any axis along the X, Y, and Z directions. For the layer thickness, four levels of 89, 102, 114, and 127 μm were used, and the chosen delay times were 50, 100, 300, and 500 ms between the spreading of each layer. Besides, the total number of experimental tests was 48. All the samples, after printing and drying (1.5 h), were de-powdered and then characterized for compressive strength and porosity.

4.2.1 Effect of process parameters on compressive strength

Figure 4.21 shows the effect of each parameter on the compressive strength. The compressive strength of the printed porous specimens, which was printed in the X direction, was significantly higher than that of the specimens printed in other directions. Insufficient compressive strengths of the Z-direction fabrication led to the fracture of some samples during de-powdering. Furthermore, samples printed with 300 ms delay

time between spreading each layer had more compressive strength compared to other samples. As shown in Figure 4.21 (a), the effect of each input on the process outputs is complicated and non-linear, and besides, no meaningful trend existed between them. The X-printed samples with 89 μm and 114 μm , as well as a delay time of 300 ms between spreading of each layer, had more strength than the other printed samples. The direction of the print and the direction of the applied compression load significantly affected the strength of the specimens. The loads applied parallel to the layers of the printed structure were fabricated along the X and Y axes, whereas those applied perpendicular to the layers were fabricated in the Z-printed samples. In addition, the cross section in which the Z samples were mathematically sliced and then printed layer-over-layer was circular, but that for the X and Y specimens was cylindrical. The samples printed in the Z direction were fabricated by more layers to be completed, but the samples printed in the X and Y directions needed the overlay of the fewest layers because of their cross section. Thus, more layer displacement occurred in the Z-printed samples that resulted in more distortion and fractures in struts.

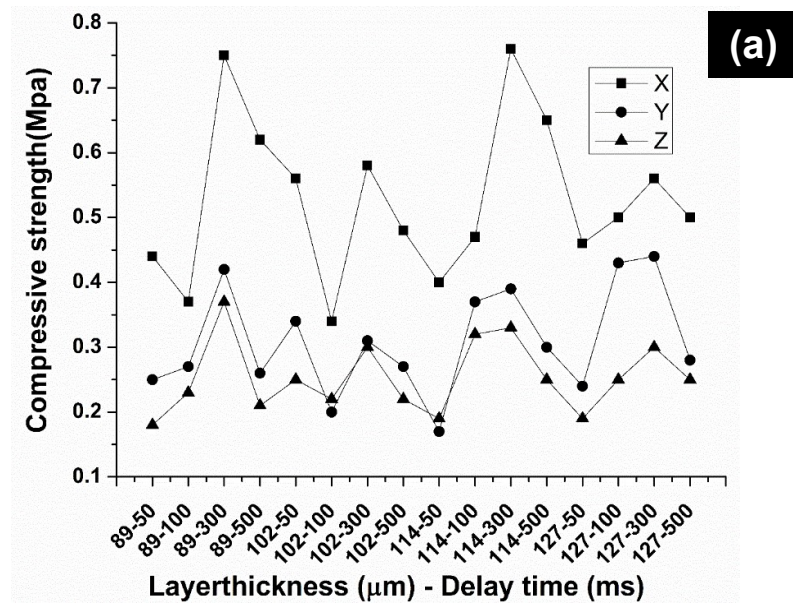


Figure 4.21: Effects of 3DP setting parameters on the compressive strength: (a) compressive strength vs. layer thickness, and delay time for X, Y, and Z build orientations. Distribution of compressive strength in each (b) delay time, (c) orientation, and (d) layer thickness.

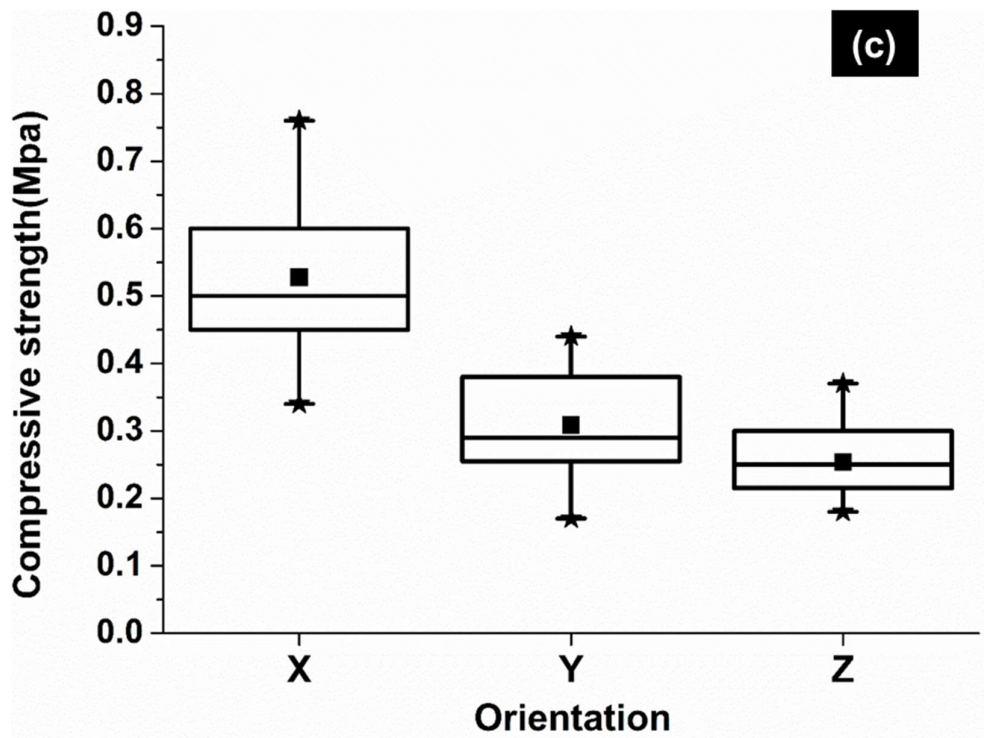
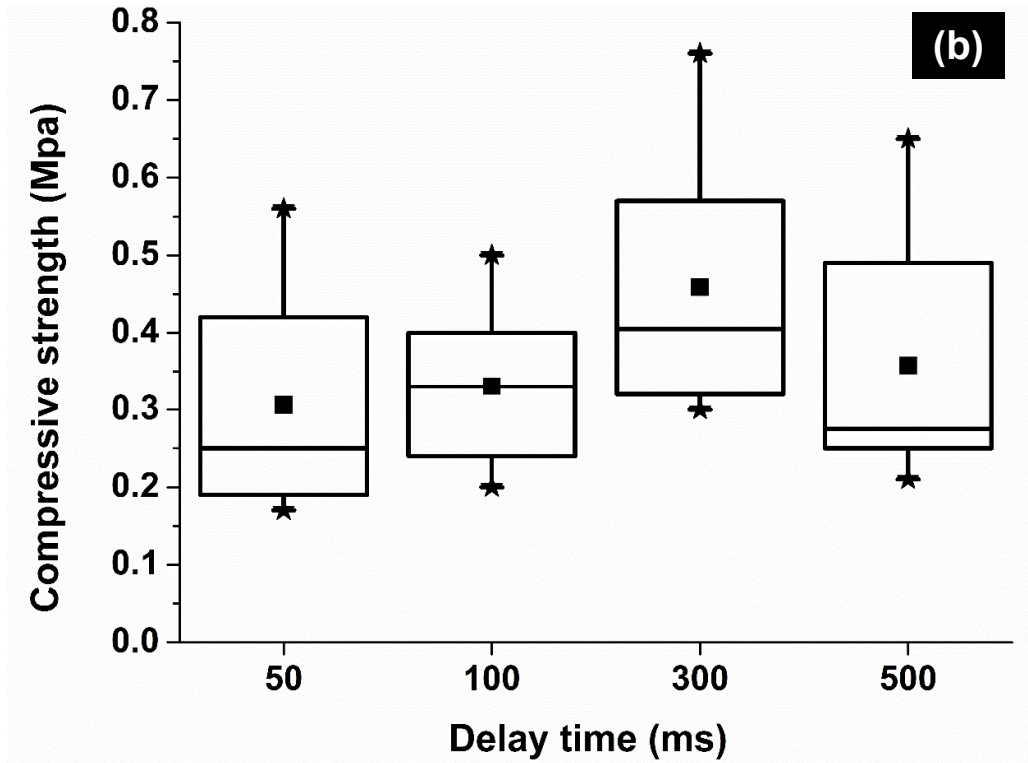


Figure 4.21, Continued.

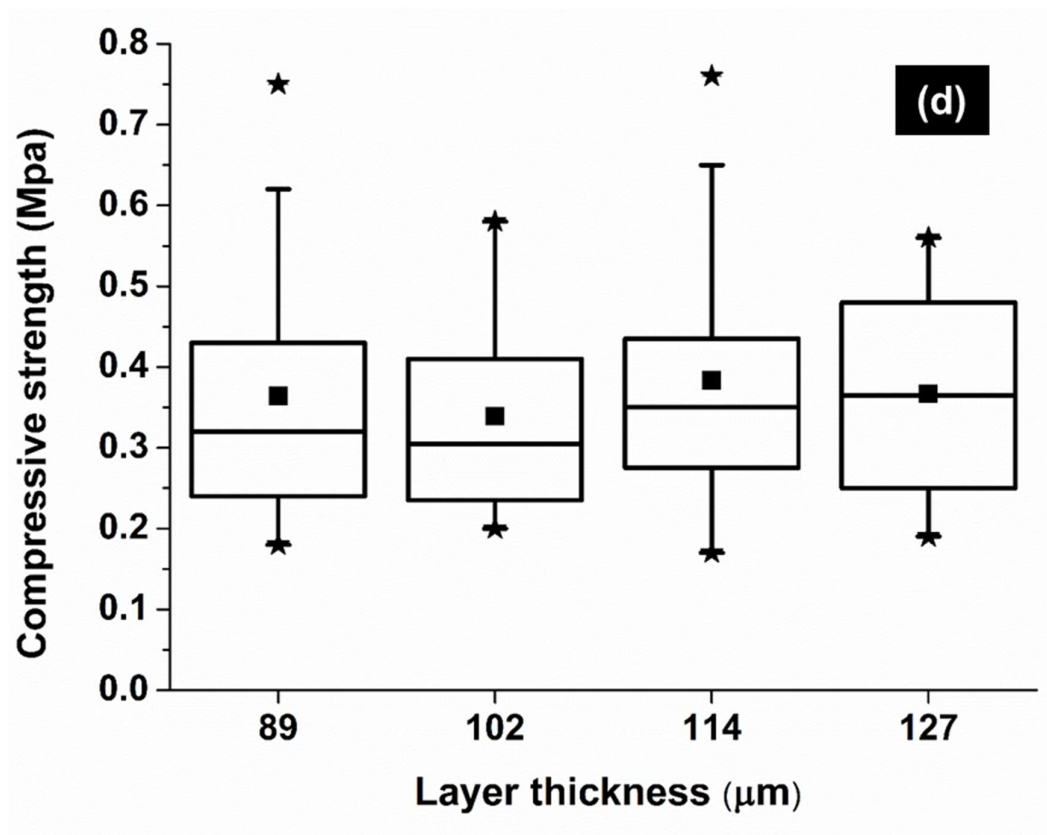


Figure 4.21, Continued.

4.2.2 Effect of process parameters on porosity

Figure 4.22 shows the effect of each setting parameter on the porosity of printed specimens. The specimens printed in the X direction with 114 μm layer thickness and 100 ms delay between spreading each layer, as well as the specimens printed in the Z direction with 102 μm layer thickness and 500 ms delay, had the most open porosity. In total, the specimens printed in the Y and Z directions were more porous than the other prototypes. However, although porous scaffolds were desired, the compressive strength should not be compromised.

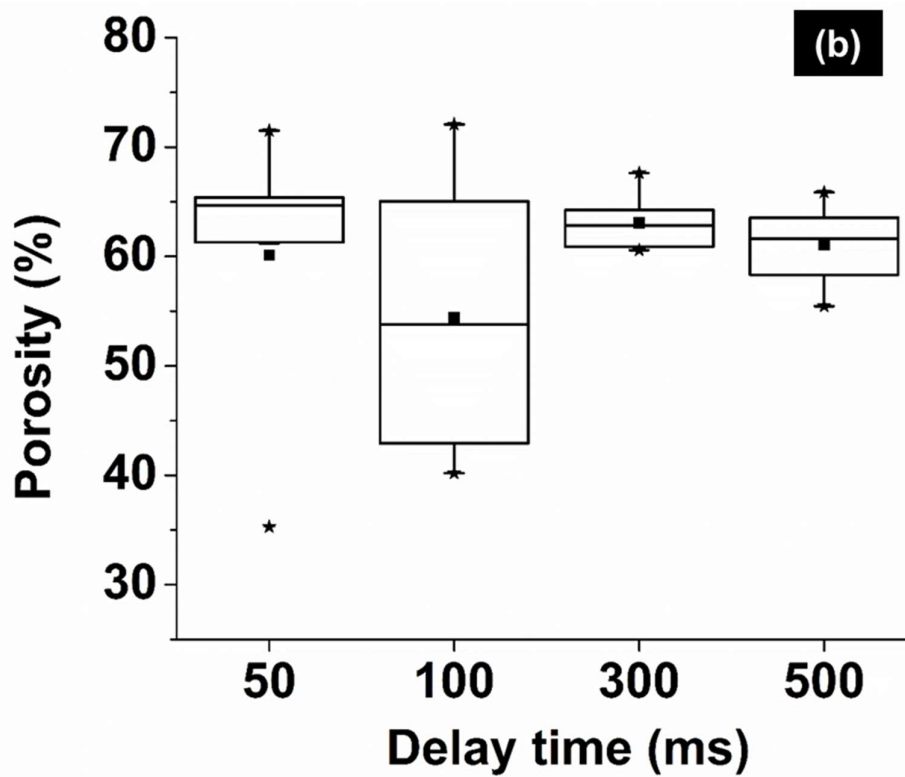
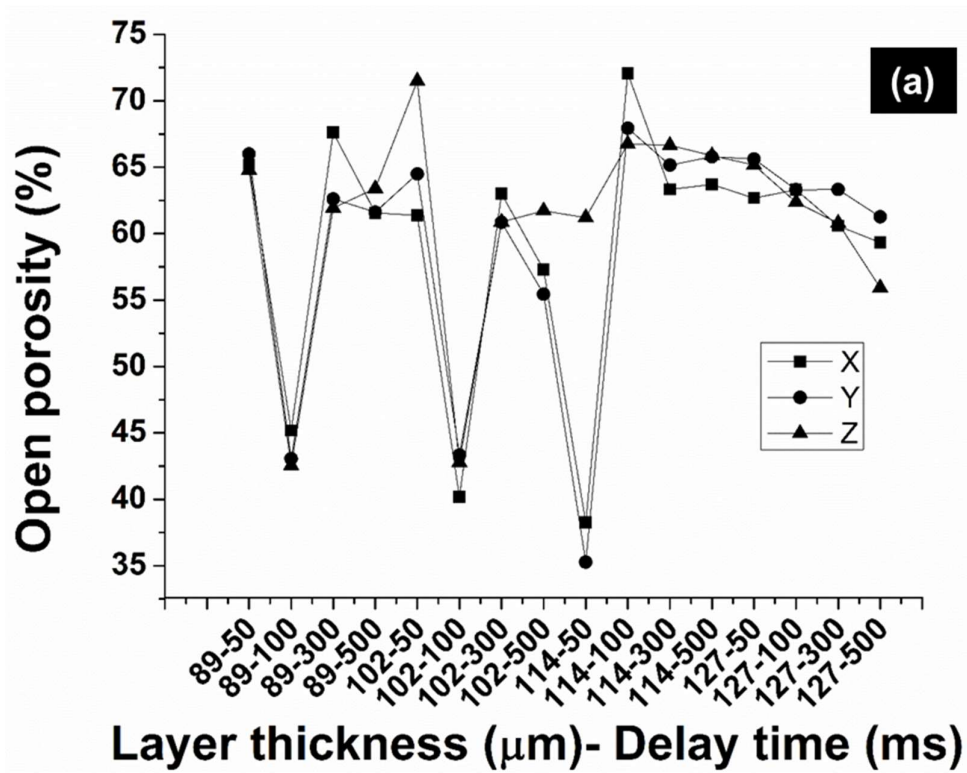


Figure 4.22: Effects of the 3DP setting parameters on open porosity: (a) open porosity vs. layer thickness, and delay time for the X, Y, and Z build orientations. Distribution of open porosity in each (b) delay time, (c) layer thickness, and (d) orientation.

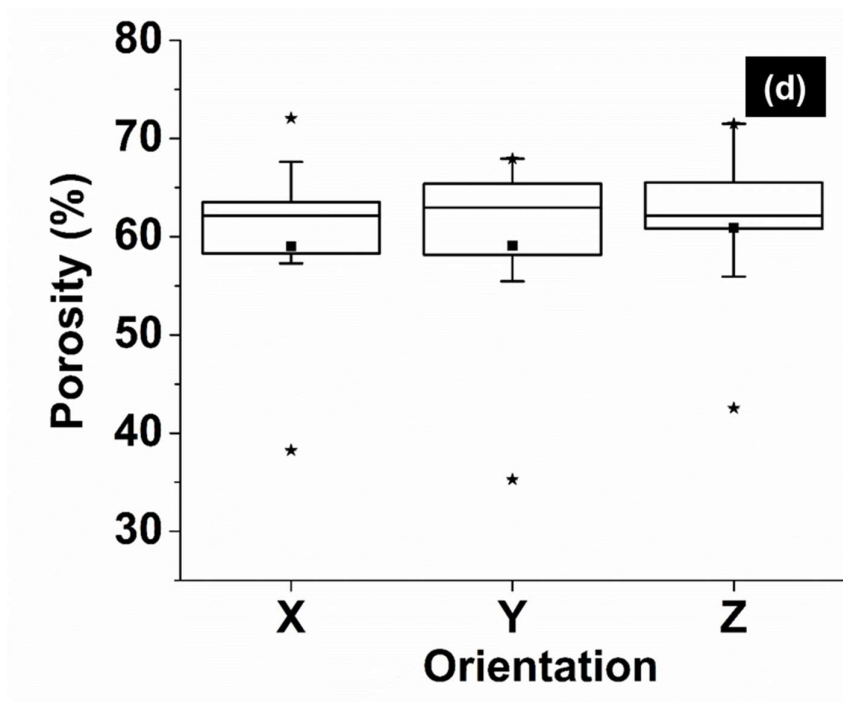
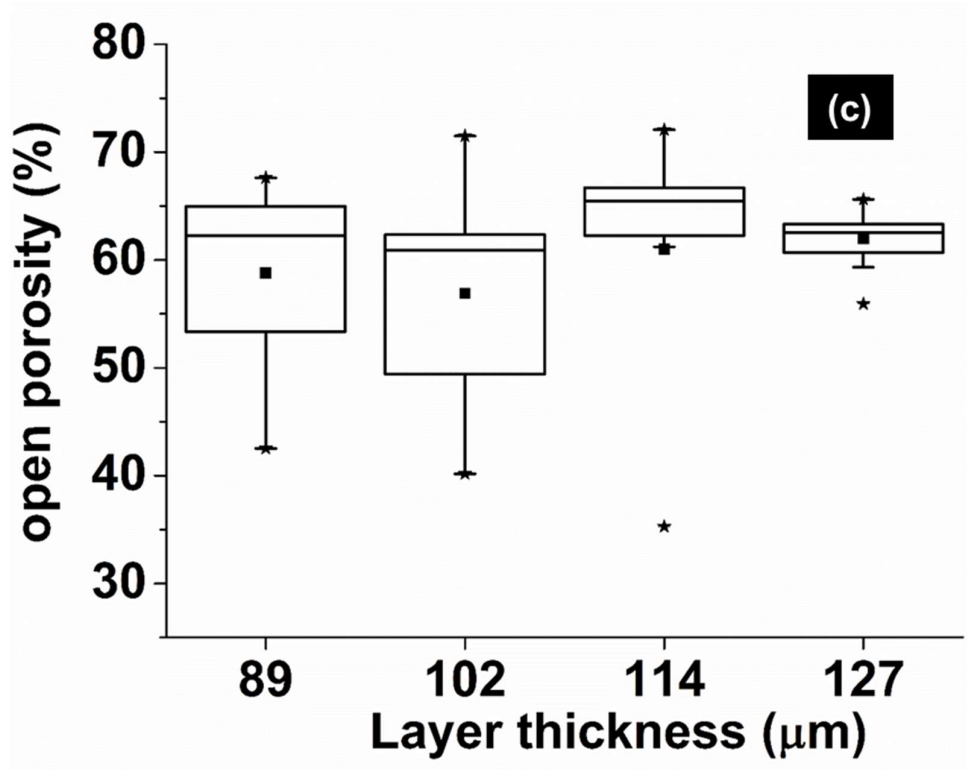


Figure 4.22, Continued.

Figure 4.22(a) shows the effect of each input on the process outputs. The effect was complicated and non-linear, and besides, no meaningful trend existed between them. Open porosity refers to both macro and micro pores. As the CAD model porosity was 45.04%, the increase in open porosity had been related to the micro pores of the powder particles.

4.2.3 Proposed topology for AANN and optimization

The proposed topology of the AANN model included $2NNno + 1$ independent variables. In this relation, $NNno$ is the number of single neural networks, while $2NNno$ is the number of weighting coefficients. Aside from these unknown parameters, each single neural network was also unknown. Moreover, the number of neurons in each hidden layer of a single neural network, as well as its weighting and biasing coefficients were undetermined. These variables should be obtained in such a manner that the prediction error should be as small as possible. The training process was conducted at two levels. At the lower level, each single neural network was trained according to the well-known back propagation algorithm called quasi Newton learning technique. In this study, 300 epochs were considered as the stopping criterion for the quasi Newton training method. At a higher level, which is called the supervising level, the PSO algorithm was employed as a supervising optimization algorithm to determine the optimal topology.

At the supervising level, the number of single networks had been limited to 2, 3, and 4, while the Input vector had 6, 9, and 12 independent variables respectively. The variable indicated the weighting coefficients the number of hidden layer of each single network. Thus, in order to identify the best number of single neural networks in the structure of AANN, this process had been implemented for a number of AANNs with a

different number of single neural networks. With this method, the quasi Newton learning technique was employed to train each of the single network and 300 epochs were considered as a criterion to stop the procedure. The experience displayed that the combination of PSO and quasi-Newton method was a useful tool in determining the optimal topology of AANN. The independent variables of solution vector are listed in Table 4.11. Meanwhile, the optimum solution of the AANN is shown in Table 4.12, which indicated a topology with three single neural networks. Consequently, six weighting coefficients (W) became the best AANN model for the 3DP process. Moreover, the number of neurons in the hidden layers had been 5, 4, and 8 (Hn). After the optimum AANN structure was discovered, PSO was applied once again under this structure to determine the optimum weighting coefficients, as this process actually led to a more accurate solution. This solution is shown in Table 4.13. Moreover, in order to ensure that the selected parameters are stable, the simulation with the selected parameters were carried out for 30 independent runs and it was observed that the variation of the final solutions over independent runs was very trivial, which augurs the robustness of the searching mechanism.

Table 4.11: Variables of solution vector.

weighting coefficients							number of neurons in the hidden layers				
w_{11}	w_{12}	w_{21}	w_{22}	w_{31}	w_{32}	w_{41}	w_{42}	Hn_1	Hn_2	Hn_3	Hn_4

Figure 4.23 shows the training and the testing accuracy of the obtained AANN in predicting mechanical compression strength. In these figures, aside from the compression strength (in normalized value); regression analysis, mean square predicting error, and normal distribution of predicting error are also presented for both training and testing. Clearly, the prediction error was within the acceptable range, and the resulting AANN network was found to be reliable in predicting compression strength.

Table 4.12: Parameters of the optimum AANN structure.

NO	NN_{no}	w_{11}	w_{12}	w_{21}	w_{22}	w_{31}	w_{32}	w_{41}	w_{42}	Hn_1	Hn_2	Hn_3	Hn_4	MSE
1	2	1	0.792	0.087	-0.035	0	0	0	0	5	4	0	0	0.046
2	2	0.392	-0.374	0.609	1	0	0	0	0	4	4	0	0	0.05
3	3	0.99	0.33	-0.37	1	0.27	-0.28	0	0	4	4	6	0	0.05
4	3	0.331	1	-0.308	0.044	1	0.155	0	0	5	4	8	0	0.045
5	3	0.15	0.944	1	-0.039	-0.101	0.197	0	0	6	3	8	0	0.047
6	4	0.616	1	0.535	1	-0.975	-1	1	-0.108	5	8	4	5	0.075

Table 4.13: Parameters of optimum weighting coefficients with fixed optimum AANN structure.

NN_{no}	w_{11}	w_{12}	w_{21}	w_{22}	w_{31}	w_{32}	Hn_1	Hn_2	Hn_3	MSE
3	0.522	1	0.0115	0.0741	0.553	0.0023	5	4	8	0.035

Similar to compression strength, the same results are shown in Figures 4.24 for the open porosity parameter. Unlike compressive strength, open porosity in some regions of the testing does not match with the training data, and higher prediction errors can be seen. These errors indicate that open porosity is a more sensitive parameter than mechanical strength, and that many uncertainties may influence it. For example, if some internal channels are blocked or filled by unbound powder during the imperfect de-powdering step, porosity will decrease. These uncontrolled effects will produce some distributed data. Therefore, obtaining highly correlated data is not possible.

Figure 4.25 shows the variations of open porosity with respect to the variations of delay time and layer thickness for different depositing directions. The behavior of open

porosity was complicated and non-linear. Other than that, the related surfaces showed that the orientations were ineffective in open porosity, whereas delay time and thickness were significant.

Regarding the mechanical compression strength, similar results were obtained for the variation of mechanical strength as a result of the process parameter variations. Figure 4.26 shows the mechanical strength behavior when time delay and thickness varied, while the orientation was kept constant. By contrast, the open porosity and the non-linearity of mechanical strength were low, whereas the deposition orientation was effective for the obtained mechanical strength.

In this step, the AANN model was used for the optimal designing of the 3DP process parameters to fabricate the desired scaffold. As both mechanical strength and open porosity are fitness functions, a multi-objective optimization algorithm had been used. In the multi-objective optimization context, the Pareto front is a comprehensive solution. By determining the Pareto front, a designer can select the desirable solution based on the imposed constraints. In this research, the Pareto front for the 3DP process regarding scaffold fabrication is shown in Figure 4.27. Based on the Pareto front, open porosity contradicted the mechanical strength in such a way that increasing the open porosity resulted in a decrease in mechanical strength, and vice versa. This figure is summarized in Table 4.14, which shows that the orientation and the layer thickness had been ineffective, whereas delay time was the most effective parameter.

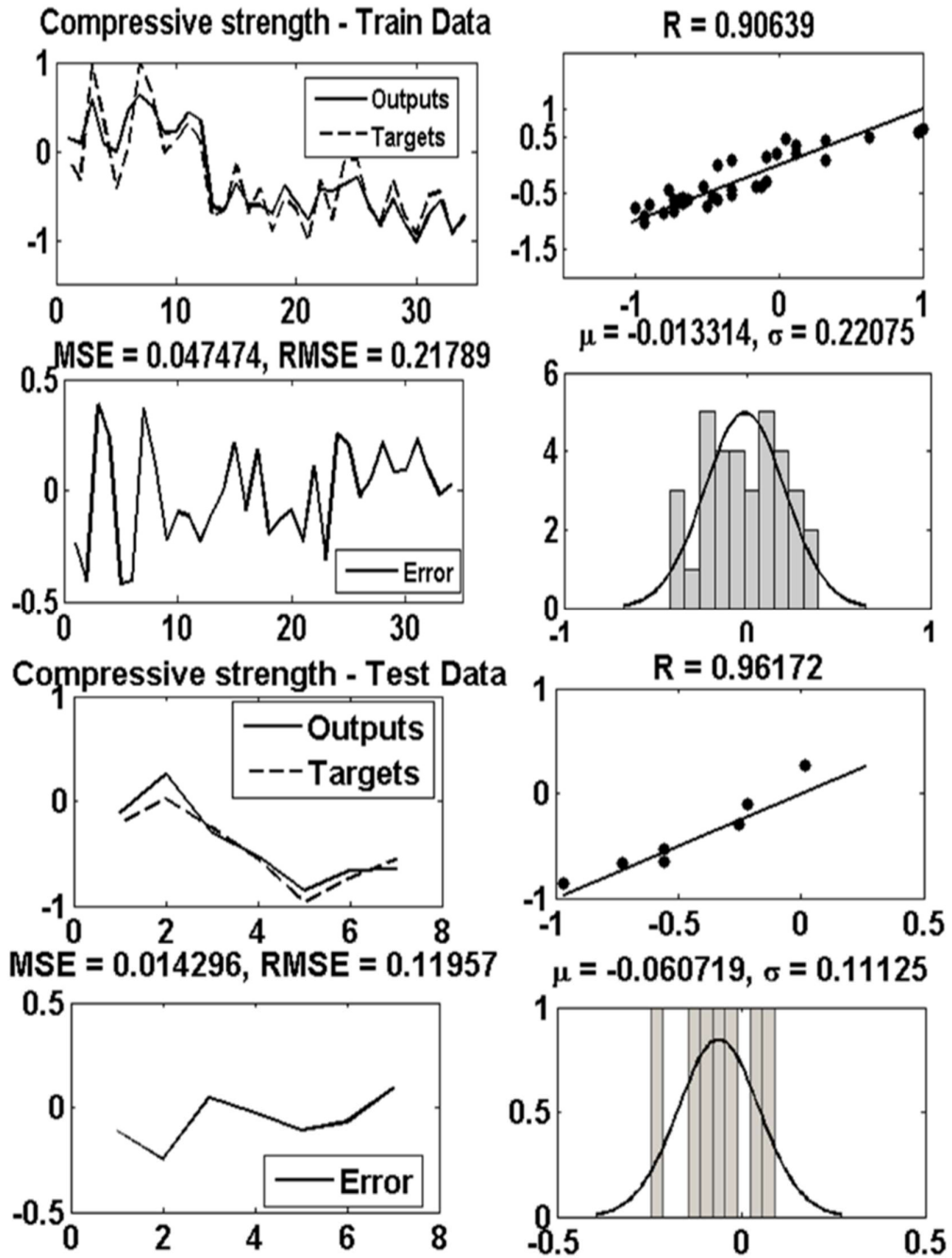


Figure 4.23: Training and testing accuracy of the obtained AANN in predicting the mechanical compression strength.

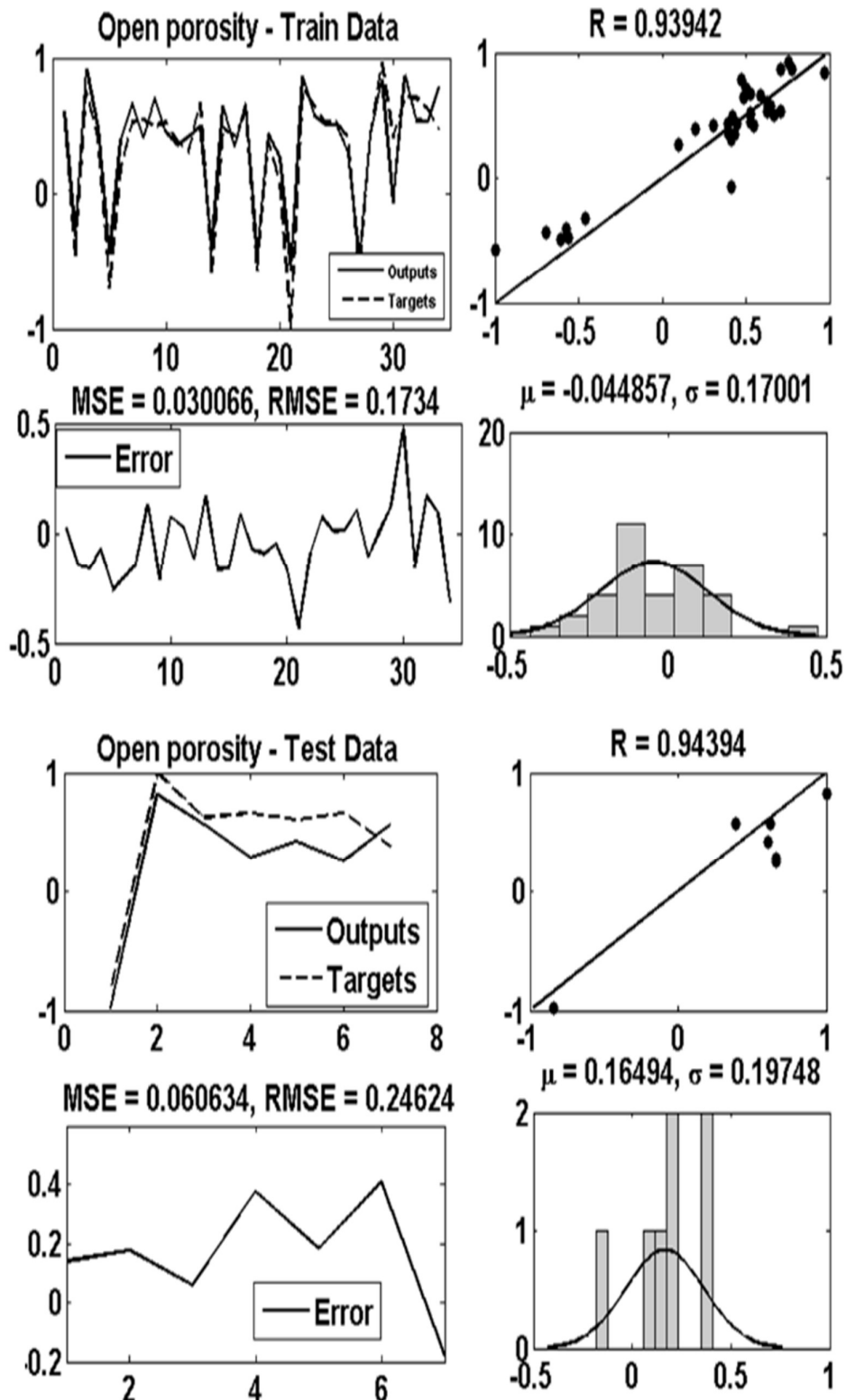


Figure 4.24: Open porosity parameter modeling performance for both of (a) training and (b) testing phases.

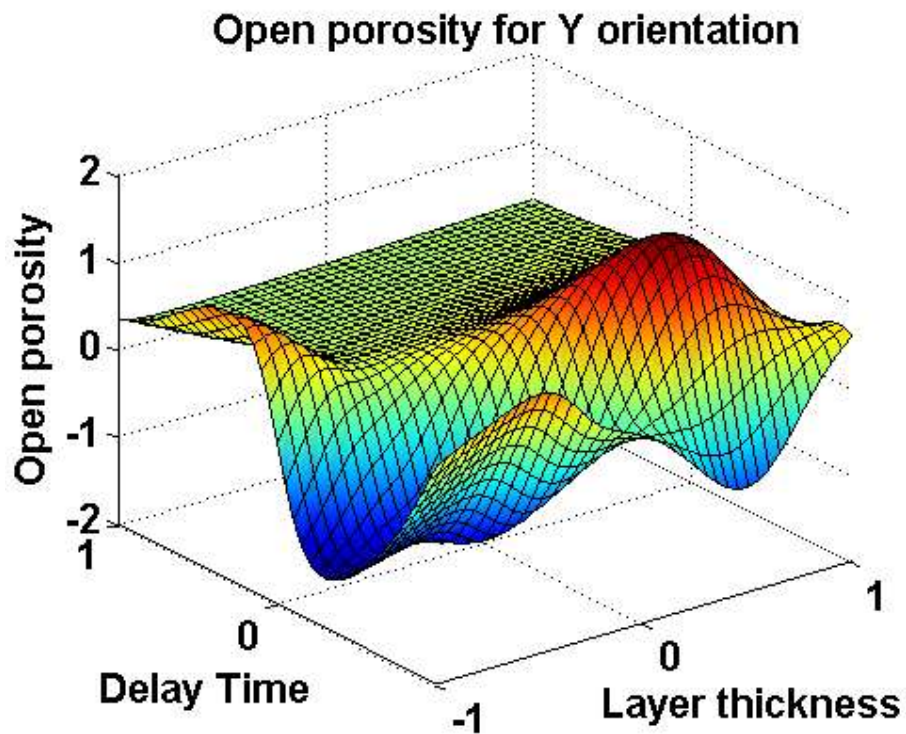
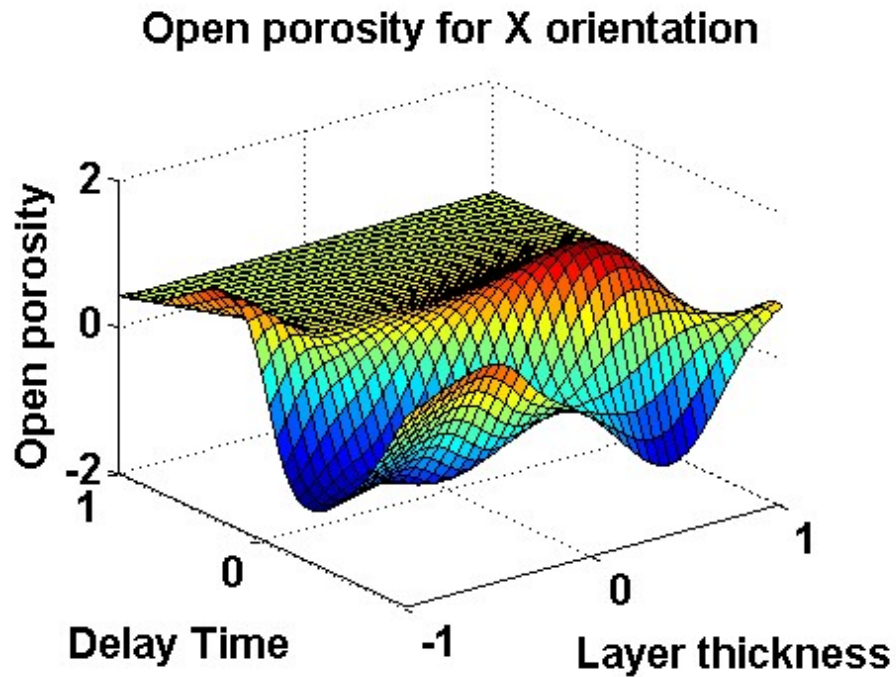


Figure 4.25: Variations of open porosity with respect to the variations of delay time and layer thickness for different depositing directions.

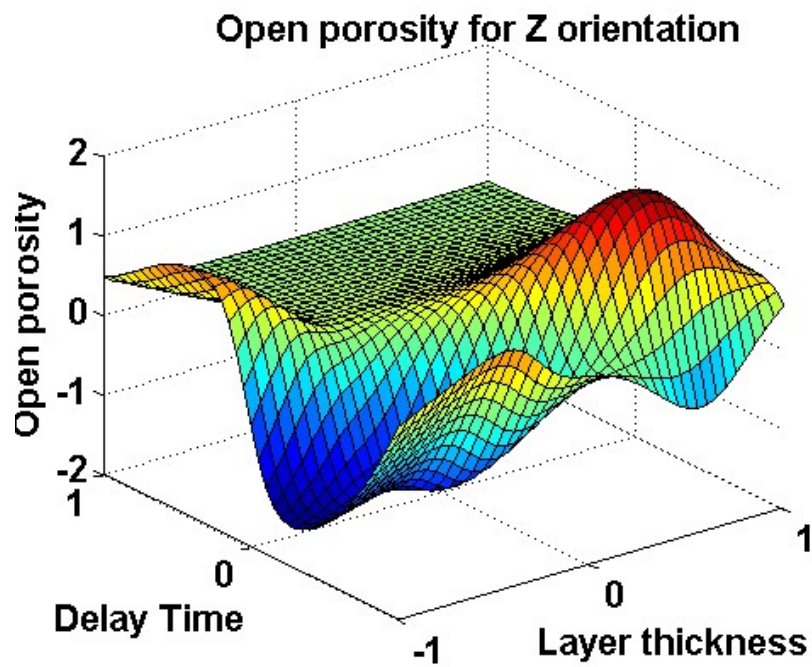


Figure 4.25, Continued.

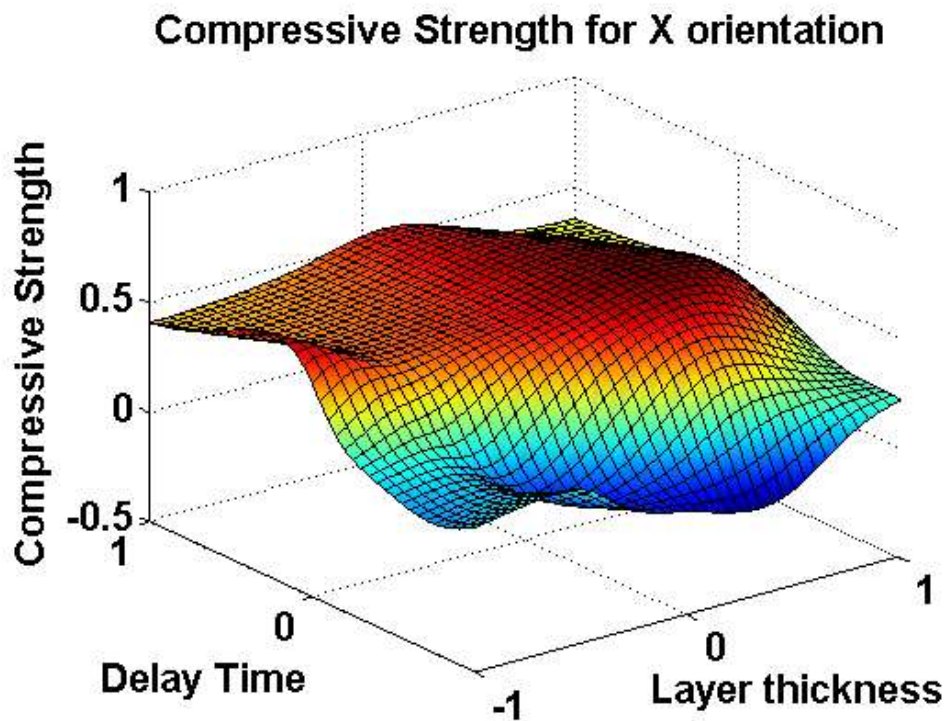


Figure 4.26: Variations of mechanical strength with respect to the variations of delay time and layer thickness for different depositing directions.

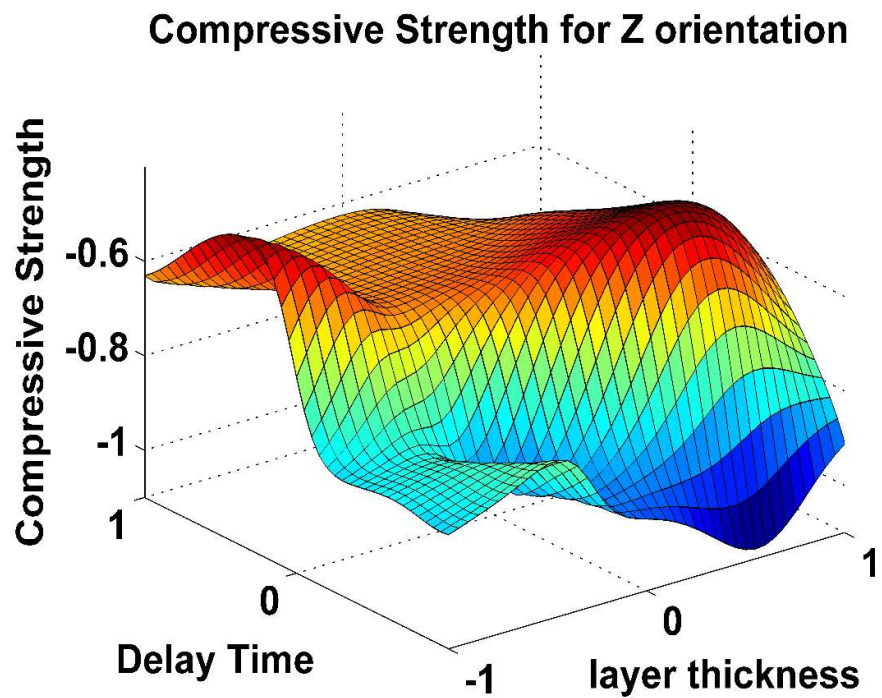
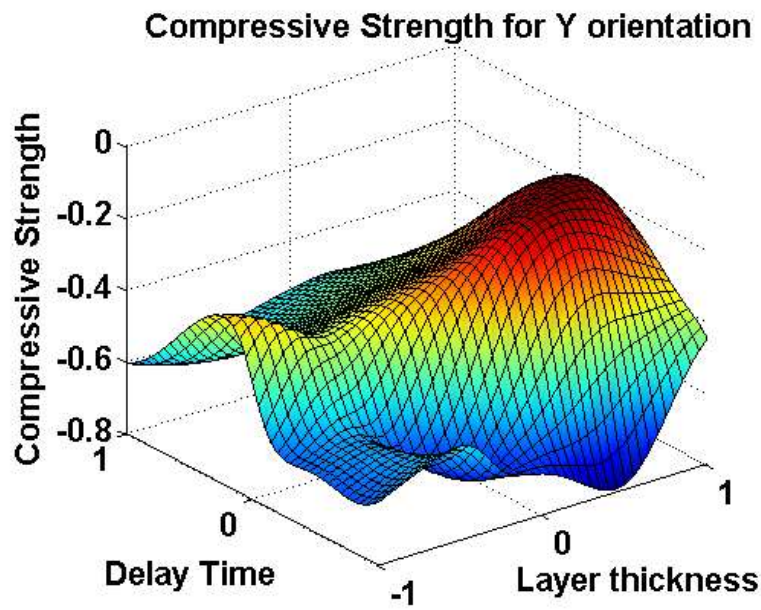


Figure 4.26, Continued.

In order to obtain a scaffold with the highest mechanical strength, the delay time should be selected at around 200 ms, but it should be at around 135 ms to achieve the highest porosity.

The ANN-based model is a powerful tool to predict the compressive strength and the porosity of 3D-printed scaffolds over a wide range of layer thicknesses, delay time of spreading each layer, and print orientations, using a limited set of experiments designed using the full factorial design of experiments.

The results predicted the best mechanical strength and porosity based on the setting parameters. The third contribution of the current study is that the trained model had been used to precisely analyze the properties of the scaffolding procedure.

The presented results and the discussion offer informative information to practitioners who want to design a porous structure, and to those in need to know the impact of influential design parameters, e.g. layer thickness, delay time between spreading of each powder layer, and printing orientation, on the porosity and the compression strength of the porous structures.

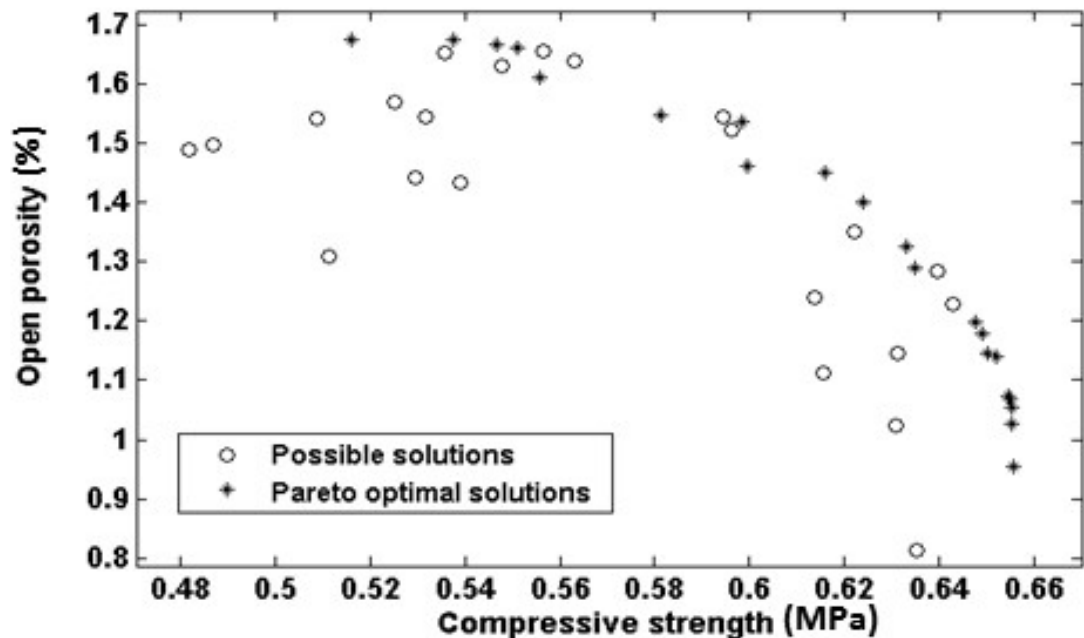


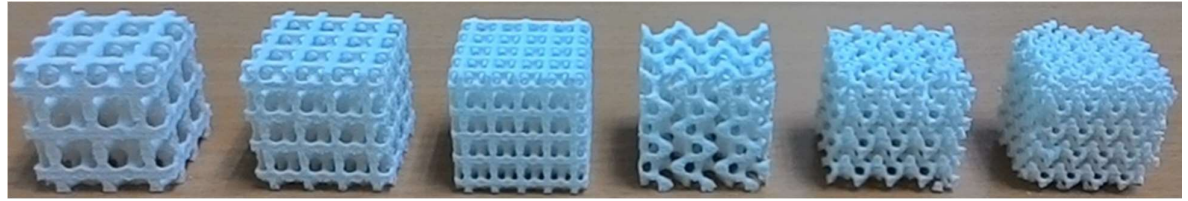
Figure 4.27: Pareto front of the 3DP process.

Table 4.14: Results of the 3DP process Pareto front.

Orientation	Thickness(μm)	Delay Time (s)	Compressive strength (MPa)	Open porosity (%)
Z	116.9181	222.5858	0.657847	73.96035
X	116.3945	221.2233	0.65751	74.33443
Z	117.0416	218.1657	0.657399	74.45063
X	117.2369	216.7491	0.657211	74.51172
Z	116.7496	212.3214	0.656504	75.34638
X	116.7496	212.3214	0.656504	75.34638
Y	115.938	207.314	0.655142	76.42069
X	116.8491	192.7778	0.651335	77.69252
X	114.5619	194.6488	0.650057	78.8029
Y	114.0856	199.1619	0.65032	78.14137
Y	114.9023	191.1381	0.649532	79.24855
X	114.9023	191.1381	0.649532	79.24855
X	114.406	173.8025	0.641215	82.02113
X	114.0551	168.0211	0.637215	82.92268
Z	113.3972	169.0771	0.635966	82.93031
X	113.3972	169.0771	0.635966	82.93031
Y	114.8493	162.0596	0.634992	83.10563
X	114.2021	156.9322	0.630174	83.97093
Z	113.7616	155.8011	0.628088	84.21507
X	116.4608	153.2911	0.425926	85.33019
X	115.5881	151.6539	0.424372	85.74368
X	115.5881	151.6539	0.424372	85.74368
X	115.2897	150.8305	0.423479	85.79899
X	115.2093	150.2231	0.423022	85.83232
X	115.2093	150.2231	0.423022	85.83232
X	117.524	154.3595	0.337439	88.23763
Y	116.7904	140.9573	0.334002	89.41571
X	117.7489	137.2071	0.332093	89.87606
X	117.7489	137.2071	0.332093	89.87606

4.3. TPMS-based model and simulation results

Figure 4.28 represents the printed calcium sulfate scaffolds with three different cell sizes of two critical TPMS-based pore architectures, which had been printed on the optimal printing condition (X direction, 300ms delay time between spreading each layer, and 89 μm layer thickness).



(a) (b) (c) (d) (e) (f)

Figure 4.28: Representation of 70% porosity scaffolds designed for evaluating mechanical properties according to the critical models obtained in finite element simulations. (a-c) Ixxx-J* and (d-f) Fxyz-Fxxx2 architectures were 3D-printed with three different cell sizes of 6.67, 5.00, and 4.00mm.

4.3.1 Voxel Mesh Convergence Study for TPMS-based Unit Cells

Figure 4.29 presents the results of convergence study conducted on 5 volume fractions of 4 different TPMS unit cell topologies. The absolute percentages of deviation from the smallest mesh size (0.019 mm where unit cell size is considered to be 1 mm) were conglomerated for different geometries in the graph according to the mesh numbers resulting from 11 discretization step sizes to identify the upper bound of deviation from converged solution. Nevertheless, there was a substantial increase in discrepancies relative to the smallest seed size when the mesh number decreased, for instance, when the mesh number was less than 500, the critical errors exceeded by 35%. Considering the upper band of error at different mesh numbers, a relationship was suggested to estimate the deviation relative to the converged solution as $Dev = 57.757n^{-0.774}$, where n is the number of voxel meshes per unit cell. Besides, it is worth noting that when simulating regular porous structures, neither geometry nor relative density of unit cell, plays a role in determining the upper limit of deviation. An approximation of (n) is estimated by using the discretization step size, as given in Equation 4.2:

$$n = RD \times int \left(\frac{CS}{ST} \right)^3 \quad (4.2)$$

Where, ST is discretization step size, CS is unit cell size, and RD represents relative density of constitutive unit cell. Therefore, to ensure convergence, considering the number of meshes alone gives a reliable estimation of discretization step size in modelling and meshing procedure by combining Equation 4.2 with the curve fitted to data ($Dev = 57.757n-0.774$), as given in Equation 4.3:

$$ST < \frac{0.471 CS \sqrt[3]{RD}}{Dev^{-0.431}} \quad (4.3)$$

In terms of gradient topologies, it should be kept in mind that Equation (4.3) should be satisfied for those regions of the scaffold with minimum local relative density to assure convergence in finite element simulation.

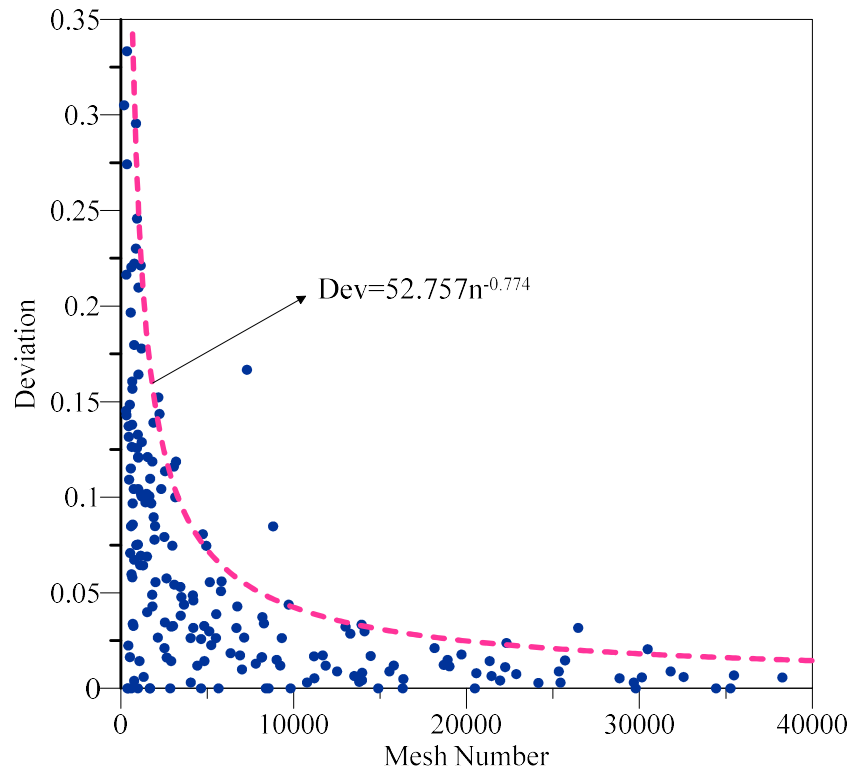


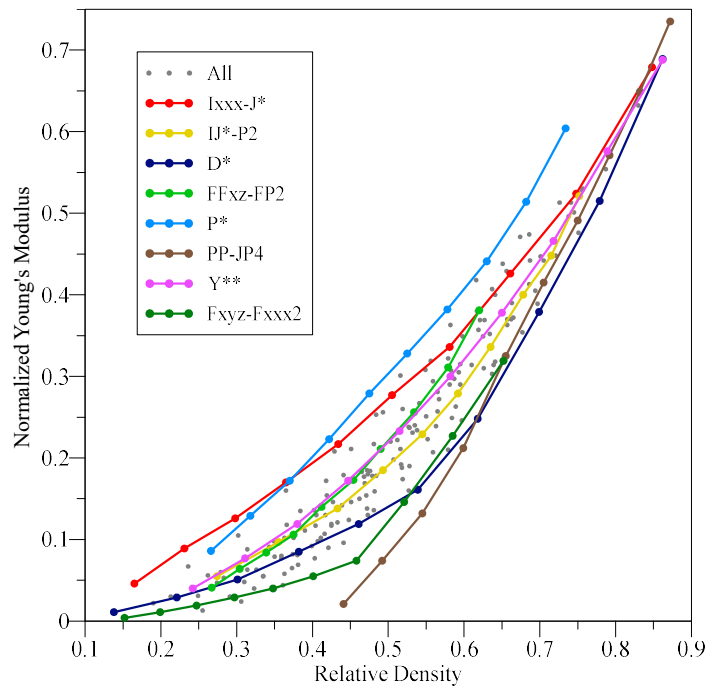
Figure. 4.29: Convergence representation of finite element simulations for voxel-based models with 11 different seed sizes of pre-selected unit cell models. Convergence was found to be dependent on mesh number alone, thereby all results were conglomerated to propose a relationship between mesh number and convergence.

4.3.2. Development of Structure-Elastic Properties Correlations

In order to illustrate structure-property correlations in a more distinct manner, detailed data on elastic modulus and yield strength for 8 selected TPMS architectures frequently addressed in literature, as well as those with critical behavior, are depicted in Figure 4.30 by solid lines. The results for all models also are shown in dotted format to highlight the domain of mechanical properties provided by the TPMS structures. It is intuitively obvious that samples with higher relative densities enjoyed higher mechanical properties. There were considerable differences between the upper and lower limit of mechanical properties provided by TPMS unit cells when comparing scaffolds at the same

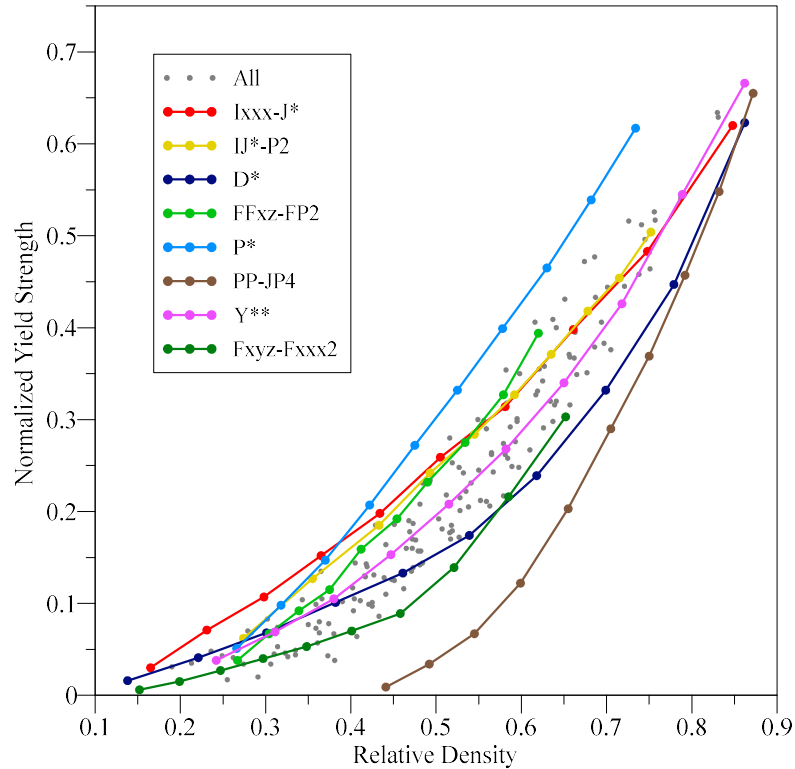
volume fractions. It implies the substantial sensitivity of elastic properties to pore configuration so that the less relative density, the more relative discrepancy was found through manipulating unit cell structure.

In addition, limited mechanical properties also were predicted for Fxyz-Fxxx2 structure at 0.152 volume fraction with 0.4% and 0.6% normalized stiffness and strength, respectively. Moreover, the least volume fraction in which biomaterial remained continuous in two phases was seen to be provided by D* with 13.8% of relative density. The highest possible values among all structures for normalized elastic modulus and yield strength were 0.878 and 0.871 (in Yxxx*-S** structure at 0.95 volume fraction), respectively and corresponding values for the less properties were 0.004 and 0.006 (in Fxyz-Fxxx2 structure at 0.15 volume fraction).



(a)

Figure 4.30: The domain of numerical (a) elastic modulus and (b) compressive strength versus volume fraction. The results for 8 well-known TPMS architectures are shown by solid lines to address the trend of variations for different topologies. Architectures with more homogeneous material distribution in which the less bending takes place under compression showed greater specific mechanical properties.



(b)

Figure 4.30 : Continued.

Among well-known TPMS structures, the highest elastic properties were exhibited by P* and Ixxx-J* structures throughout all volume fractions. In relative densities less than almost 0.37, Ixxx-J* had the greater properties, while the figures for P* overtook Ixxx-J* architecture at 0.37 relative density in both Young's modulus and yield strength. This is explained by the intrinsic heterogeneous material distribution in lower volume fractions of P* structure, thereby increasing stress concentration in the struts between unit cells. Furthermore, figures for yield strength were by far the lowest for PP-JP4 so that the structure with 0.441 relative density was predicted to yield at 0.9% of the material's yield strength. This critical behavior was directly correlated to highly weakened 45° inclined linkages, which connected aggregated amounts of material in unit cell. Therefore, through inhomogeneous material distribution, it is feasible to decrease stiffness values, along with increasing specific surface area for enhanced cell

differentiation. Second, in volume fractions of less than nearly 0.55, Fxyz-Fxxx2 and in the remnant range, D* indicated the least mechanical properties.

Comparing the configuration of joints and struts according to the mechanical properties indicated that the architectures, especially ligaments and linkages, were mostly oriented parallel to loading direction (in particular, semi-tubular architectures) that favored the highest specific elastic properties, such as P* and Ixxx-J*. Conversely, those in which material was inclined relative to load, possessed less stiffness and strength. Moreover, smooth variation of cross sections in joints (such as P* in higher volume fractions) hindered stress concentration, which is common in lattice-based cellular materials. As aforementioned, structures with low stiffness are of interest to unify biomaterial properties with the native tissue, especially in regions in contact with biological elements. However, loss of strength is a challenging issue and needs to be addressed in design.

Figure 4.31 represents the relationships between yield strength and elastic modulus for the TPMS architectures in detail. For the required normalized yield strength less than 0.1, Fxyz-Fxxx2 (in volume fractions less than 0.4) was a promising architecture, while for those between 0.1 and 0.4, IJ*-P2 (in volume fractions between 0.3 and 0.65) exhibited less stiffness for similar strength values.

For higher yield strengths, P* structure (in volume fractions higher than almost 0.6) was found to adequately meet the structural requirements in scaffold design. It implies consideration of changing pore architecture, along with variation of porosity, in designing functionally graded scaffolds and the Young's modulus is set to be a constant parameter, in order to retain structural requirements all over the scaffold.

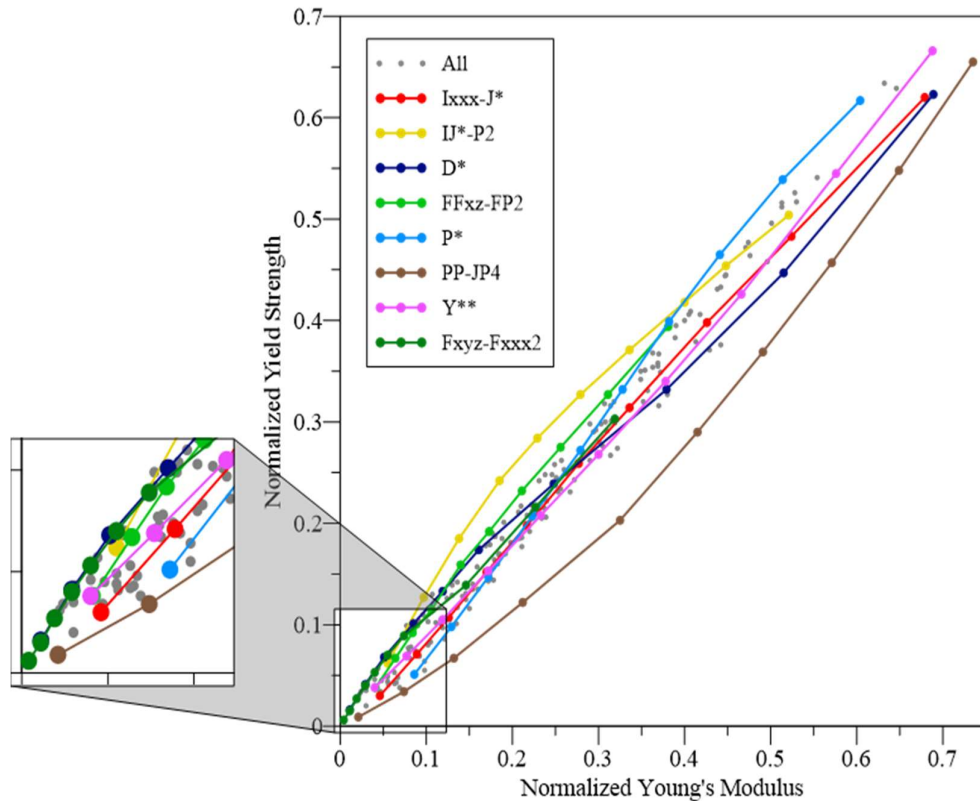


Figure 4.31: Relationships between compressive yield strength and Young's modulus for different TPMS unit cell geometries. Depending on the normalized stiffness of interest, different architectures (namely Fxyz-Fxxx2, IJ*-P2, and P*) provide superior compressive strength values. It implies the necessity of changing pore architecture, along with volume fraction in gradient scaffold design when stiffness is the constant parameter.

When the scaffold is designed to be implanted in dynamic environments, a high yield strain can assure the mechanical stability of scaffold (Wisner et al., 2014). Besides, for the applications in which shape memory effects are essential, topological parameters can affect superelasticity of the structure by improving yield strain (Petrini & Migliavacca, 2011). Normalized yield strain with respect to the constitutive material for porous architectures is shown for different volume fractions in Figure 4.32. Based on the results, introducing porosity into the bulk material had been expected to change the initial yield strain by almost 0.4~1.5 times, depending on the architecture and the volume

fraction of porous structure. For some architectures, increasing relative density was found to increase yield strain, while for the others, the converse behavior was observed.

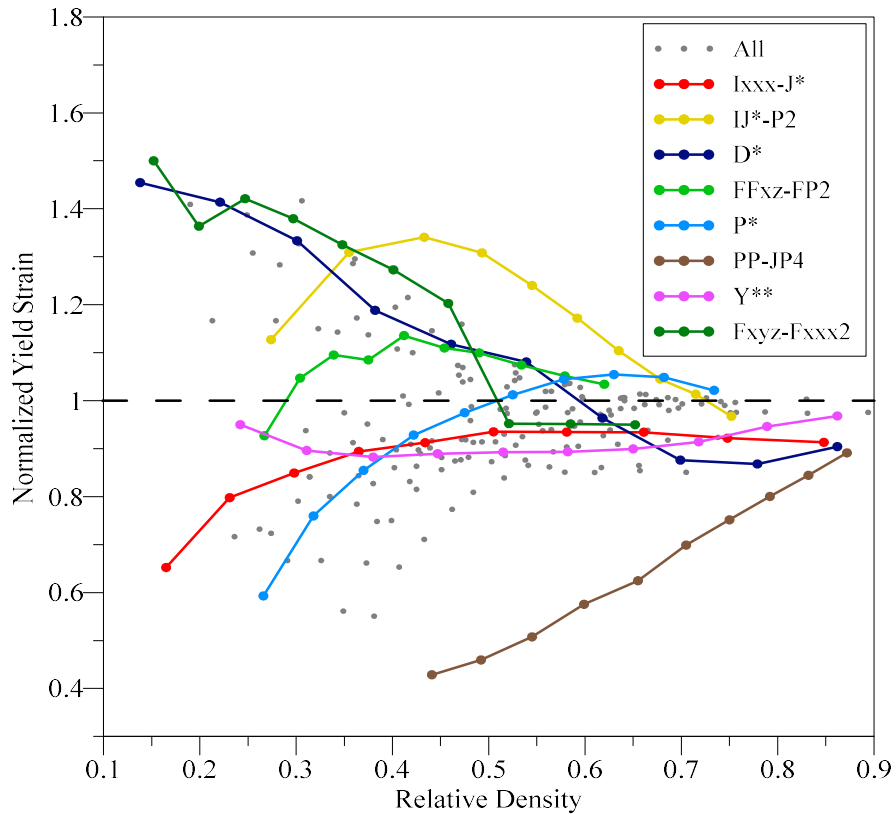


Figure 4.32: The effect of relative density and pore architecture on the normalized yield strain. Introducing porosity can increase elastic strain range by almost 50% through Fxyz-Fxxx2 and D* structures. Pore architecture plays a key role in whether porosity increases or decreases yield strain.

This effect is seen to be more striking in lower volume fractions as Fxyz-Fxxx2 and D* structures up to 35% of relative density, and thereafter, IJ*-P2 showed the highest elastic strain range. Generally, it can be inferred that preventing stress concentration or equivalently more homogeneous stress distribution led to higher elastic strain range. These findings have been further confirmed by the experimental results obtained by Kadkhodapour, Montazerian, and Raeisi (2014), as the increasing volume fraction of P* from 30 to 60% caused yield strain to increase from 0.019 to 0.039, while the corresponding figures for D* architecture displayed a decrease from 0.043 to 0.033.

4.3.3. Mechanical Properties versus Deformation Mechanisms

Physiological loads have been reported to bring about micro-motions inside the porous structure of scaffolds, thereby mechanical stimuli is directly transferred to cells (Jamshidinia et al., 2014). Deformation density varies from region to region according to the dominant deformation mode, which is controlled by pore architecture. On the other hand, a comprehensive relationship between deformation mechanisms and mechanical properties has been introduced by Ashby (2006) via scaling law analysis with respect to relative density in lattice-based cellular materials, as given in Equation 4.4:

$$\frac{X}{X_S} = C \left(\frac{V}{V_S} \right)^n \quad (4.4)$$

Where X/X_S represents normalized specific mechanical properties and V/V_S is volume fraction of structure. The exponential value of n has been theoretically shown to be dependent on configuration of struts relative to loading direction. This can be related to early deformation mechanisms so that in terms of elastic modulus (E/E_S), the exponential values (n) near 1 are assigned to stretching dominated deformation and as it increases, the deformation mode tends to be bending dominated. Therefore, by generalizing Equation 4.3 for each TPMS structure, the constants of power fit to 10 volume fractions for each TPMS architecture had been calculated and the structures were sorted according to the exponential values (n) of power fit to elastic modulus, as depicted in Table 4.15.

Table 4.15: Results of curve fitting to express variations of biomechanical properties with relative density, and the contours showing the critical regions at onset of plastic deformation, as well as the state of bio-fluid velocity flow into the porous structure of scaffolds. The structures are sorted according to the exponential value (n) for normalized Young's Modulus to address deformation mechanism-property relationships.

Structure Label	Deformation Mechanism (Plastic Strain)	Bio-fluid Velocity Contour	Normalized Young's Modulus $E_n = a(RD)^n$			Normalized Compressive Strength $S_n = a(RD)^n$			Normalized Permeability $K_n = ae^{-n(RD)}$		
			a	n	R ²	a	n	R ²	a	n	R ²
			Ixxx-J*			0.869	1.668	0.997	0.807	1.695	0.999
P2-Iwz			0.859	1.719	0.999	0.902	1.921	0.999	0.806	6.935	0.978
P*			1.044	1.816	0.998	1.185	2.043	0.994	0.932	7.397	0.958
Fxxx*			0.921	2.098	0.998	0.869	2.167	0.998	0.495	6.129	0.964
Y**			0.948	2.132	1.000	0.929	2.282	0.999	0.783	6.700	0.985
(PPxxx)*			1.159	2.164	0.984	1.368	2.549	0.975	0.309	7.650	0.988
S*			0.927	2.201	0.999	0.866	2.015	0.999	0.447	6.288	0.983
Yxxx**-S*			0.998	2.346	1.000	0.971	2.271	0.999	0.823	8.150	0.973

Table 4.15, continued

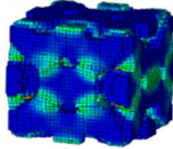
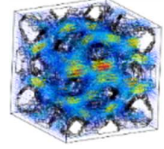
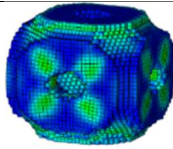
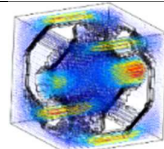
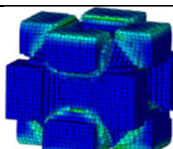
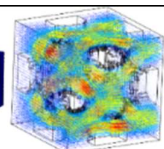
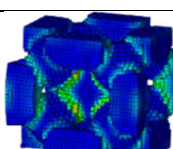
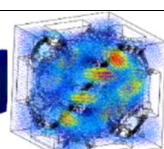
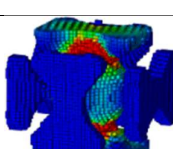
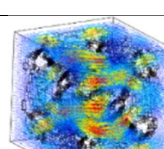
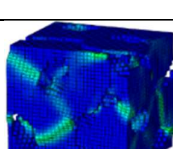
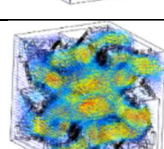
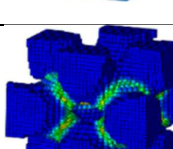
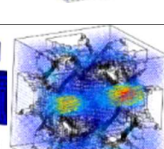
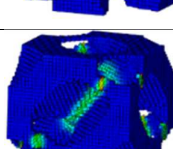
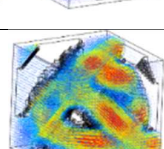
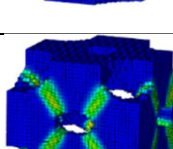
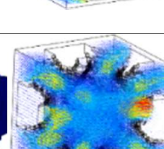
Structure Label	Deformation Mechanism (Plastic Strain)	Bio-fluid Velocity Contour	Normalized Young's Modulus $E_n = a(RD)^n$			Normalized Compressive Strength $S_n = a(RD)^n$			Normalized Permeability $K_n = ae^{-n(RD)}$		
			a	n	R ²	a	n	R ²	a	n	R ²
			J*IxxxIzx-IP2Iz			1.040	2.361	0.999	1.090	2.496	0.997
IJ*-P2			1.013	2.401	0.998	0.850	1.831	0.998	0.334	7.046	0.978
(PJ)*			1.215	2.406	0.996	1.367	2.661	0.992	1.317	8.610	0.963
FFzx-FP2			1.246	2.504	0.999	1.235	2.391	0.996	0.677	8.231	0.975
(PJx)*			1.185	2.509	0.997	1.208	2.531	0.995	1.380	9.291	0.989
(FxxxFxyz)*			0.982	2.548	0.999	0.854	2.196	0.998	0.306	5.780	0.988
PPJPxxx-J			1.326	2.621	0.997	1.091	2.527	0.998	1.123	8.997	0.981
F*(D)			1.106	2.694	0.999	0.989	2.579	0.997	0.333	5.498	0.972
PPJ-Jx			1.157	2.715	0.998	0.983	2.702	0.996	0.804	6.603	0.988

Table 4.15, continued

Structure Label	Deformation Mechanism (Plastic Strain)	Bio-fluid Velocity Contour	Normalized Young's Modulus $E_n = a(RD)^n$			Normalized Compressive Strength $S_n = a(RD)^n$			Normalized Permeability $K_n = ae^{-n(RD)}$		
			a	n	R ²	a	n	R ²	a	n	R ²
D*			1.052	2.876	0.997	0.873	2.542	0.989	0.407	6.110	0.976
(P2Y*SV2P2Yyz*)*			1.106	2.893	0.998	0.981	2.640	0.999	0.249	5.948	0.988
FFxxx-FFxxx			1.483	2.953	0.994	1.761	3.373	0.991	1.023	8.629	0.989
Fxxx*			1.512	3.018	0.995	1.956	3.692	0.992	1.810	9.327	0.964
(P2Y*SVP2Yyz*)*			1.294	3.207	0.998	1.195	2.986	0.998	0.307	6.660	0.990
PP-JP4			1.215	3.349	0.982	1.212	4.300	0.993	0.434	6.886	0.989
Fxyz-Fxxx2			1.469	3.554	0.994	1.088	3.031	0.991	0.421	5.969	0.992

In comparing the exponential values of Young's modulus with deformation contours of FE, which had been demonstrated as n increased, critical struts and linkages each of which are the most susceptible for plastic collapse and bear the highest load, were more inclined relative to loading direction. The more inclination of critical struts to 45°, the greater n in scaling relations of elastic modulus appeared and consequently,

deformation mode was observed to be bending dominated due to global shearing of linkages when compressive loads were applied. Conversely, when the struts were positioned parallel to loading direction, stretching was dominated on deformation mechanism; leading to higher specific elastic properties (such as that obtained for Ixxx-J*, P2-Iwz, and Fxyz-Fxxx2 structures).

Nonetheless, previous experiments in the laboratory indicated that the deformation mode did not only depend on pore architecture, but also volume fraction [51]. Figure 4.33 presents the computational results of percentage contribution for bending deformation versus relative density obtained from 7 selected TPMS geometries. Generally, lower bending energy was seen for P*, P2-Iwx, and Ixxx-J* structures.

Furthermore, it is comparable with their corresponding exponential values of scaling analysis in elastic modulus (the lowest observed values in the range of 1.67 to 1.82). In contrast, the structures in which the linkages are positioned inclined relative to loading direction (those with less specific mechanical properties) showed the highest bending contribution in their total deformation. Moreover, the effect of pore architecture was notable at lower volume fractions and when the structure approached to a perfectly solid unit cell, internal architecture had no impact on bending contribution since the overall trend to stretching dominated deformation as expected. From the mechanical efficiency viewpoint, structures with less bending in deformation had been expected to engage the higher capacity of material in load bearing according to the definition presented in this methodology. Therefore, it can be inferred that stretching dominated structures possessed the highest specific mechanical properties; thanks to the greater mechanical efficiency.

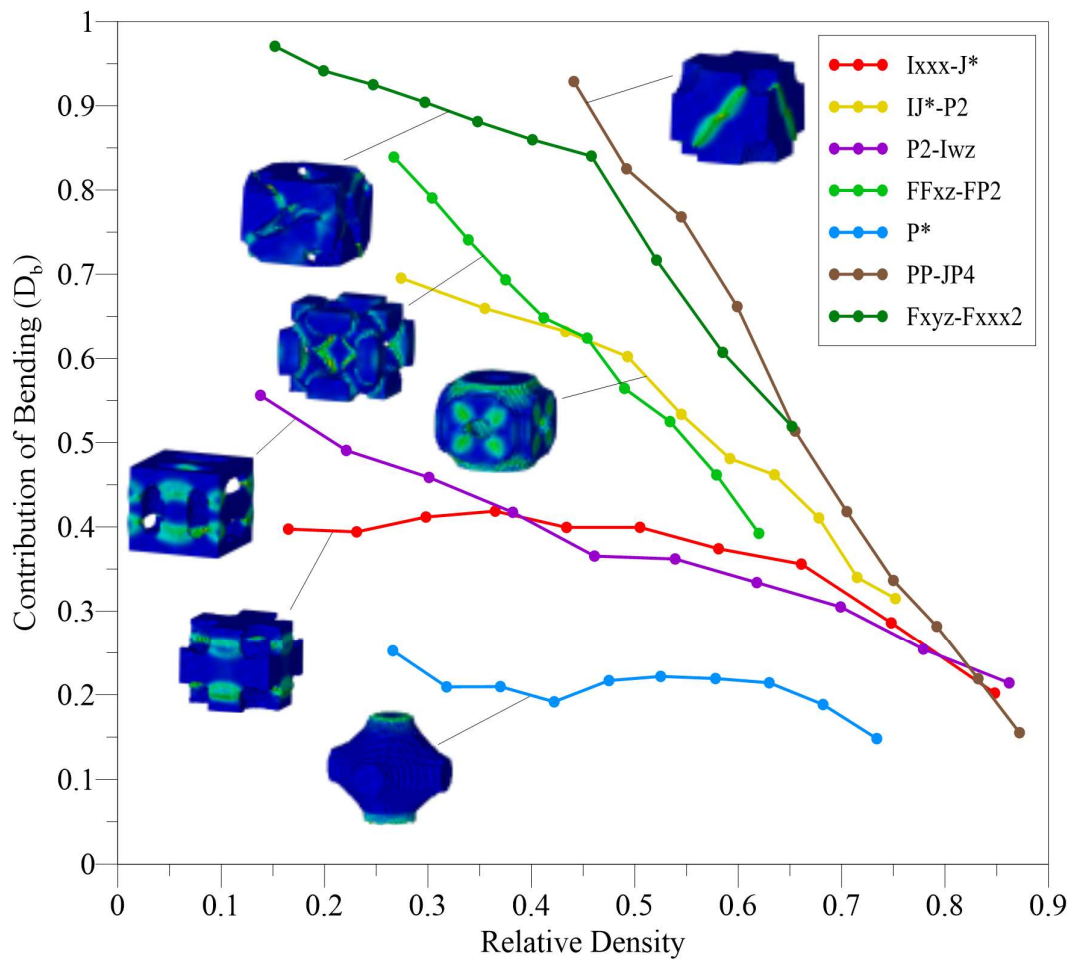


Figure 4.33: The results of calculated percentage contribution of bending in compressive deformation versus volume fraction for different TPMS topologies. For each graph, the corresponding contour of plastic strain is represented. Effects of bending deformation become more significant at lower volume fractions. The comparison between the obtained results and the power fit to elastic properties showed correlations between the exponential values (n) and the overall contribution of bending.

4.3.4. Bio-Fluid Permeability Characterization of TPMS Architectures

In order to describe the ability of internal architecture for stimulating cell in-growth, the results for fluid permeability of chosen geometries at different relative densities are compared in Figure 4.34. Additionally, the relationships between normalized permeability and volume fraction obtained by curve fittings are presented in Table 1, along with the bio-fluid velocity contours resulted by CFD calculations. The most striking

figures were found for Ixxx-J* structure in all of volume fractions. Other than that, in the second stage, Y** and P* were the most permeable structures, respectively. The results for Ixxx-J* and P* were comparable with elastic properties versus volume fraction.

Hence, it can be concluded that at constant volume fractions, the trend to tubular strut configuration did not only lead to the highest structural properties, but also improved permeability of the scaffold. Conversely, there was a tremendous drop in permeability when pore architecture approached (PPxxx)*. It implied preventing abrupt variation in fluid cross section according to the topological features of (PPxxx)*. Generally, despite of the absolute differences in lower relative densities that were notable, relative differences were found to be higher in high volume fractions as a result of manipulating pore architecture. Therefore, the less porosity, the more sensitivity of permeability to pore architecture. Besides, Ixxx-J* at 0.165 volume fraction showed the highest normalized permeability (0.2273) among the studied TPMS structures, while the less was found for Yxxx**-S* at 0.95 relative density (0.00019).

Concurrent considerations of scaffold stiffness and permeability are vital in determining local topology and porosity in scaffolds based on the required function. Hence, normalized Young's modulus versus permeability is plotted in Figure 4.35. As observed, pore morphology plays a decisive role, particularly for designing low stiffness structures. It was also noted that especially in lower stiffness values (which corresponds to lower volume fractions), Ixxx-J* was by far the most permeable structure among known TPMS structures. This preponderance was shared with P* when normalized Young's modulus exceeded by almost 0.27. Moreover, it should be noted that the range of TPMS geometries at which the structure remained interconnected had been limited. Hence, for the normalized elastic modulus less than 4.6%, D* and Fxyz-Fxxx2 portrayed

as promising architectures. As noted, PP-JP4 showed inappropriate behavior not only from structural standpoints, but also in permeability. Furthermore, it is worth noting that albeit the superior strength to stiffness ratio provided by IJ*-P2 in volume fractions between 0.1 and 0.4, it was inefficient for cell migration compared to other topologies. Meanwhile, Ixxx-J* and to some extent, P*, had been capable of improving cell migration, as well as bearing mechanical loads.

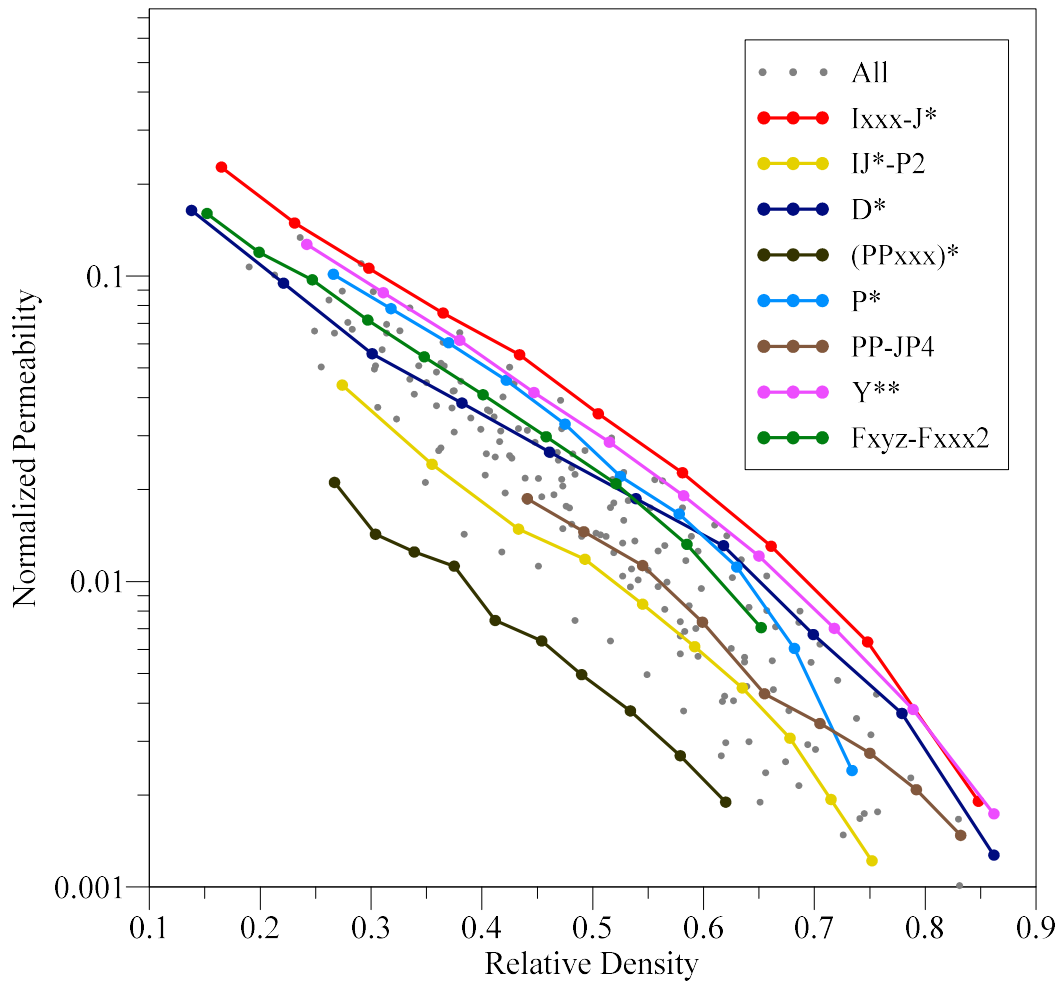


Figure 4.34: Variation of computational normalized permeability with relative density for different TPMS architectures. Ixxx-J* and subsequently, Y**, were found to be the most capable structures in conducting bio-fluid flow.

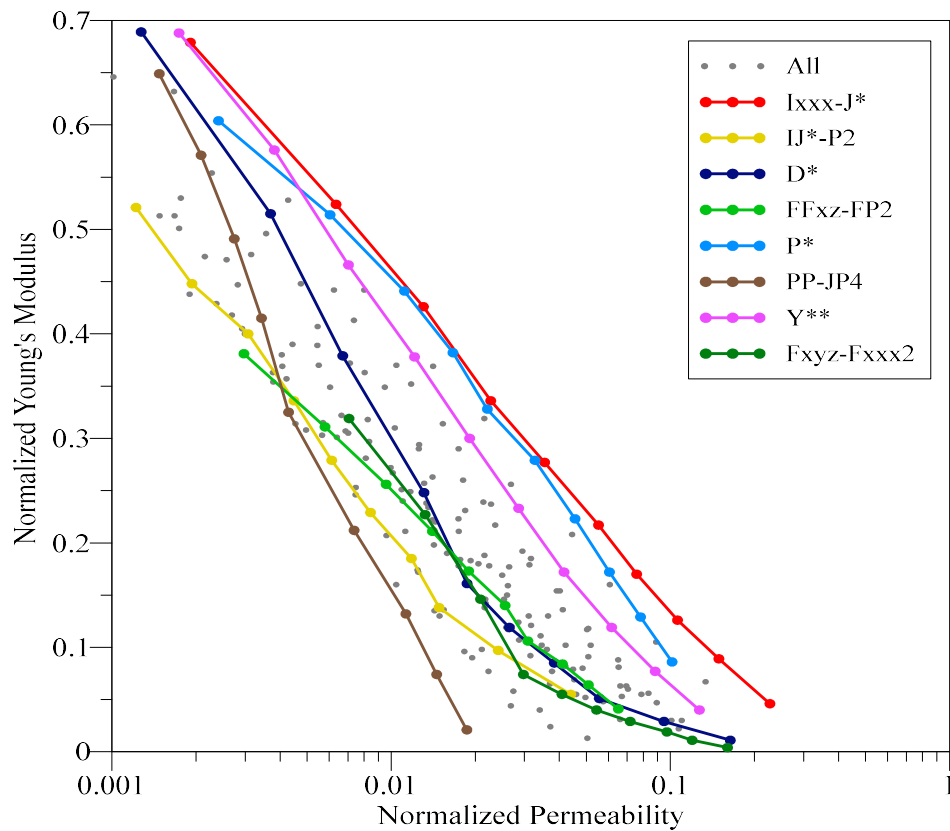


Figure 4.35: Normalized Young's modulus versus normalized permeability. For the regions of scaffolds in which high permeability, along with very low stiffness values are required, Fxyz-Fxxx2 and D* architectures met the requirements at higher volume fractions which improved manufacturability of scaffold.

4.3.5 Experimental Evaluation of TPMS-based Ceramic Scaffolds

Aside from the prominent consistency between the chemical configurations of ceramic based scaffolds (Cox et al., 2015), especially those of calcium phosphate and calcium sulfate families, lack of mechanical strength and rapid resorption (Z. Zhou et al., 2014) still have remained a challenge in additively manufactured ceramic scaffolds. The stiffness provided by ceramic scaffolds has been shown to be well in a range of natural bones, however, fragile nature of material, in particular when it comes to porous architectures, has limited its use to low-load bearing applications.

Hence, very high porosity scaffolds, which are more mechanically challenging, were considered to tailor TPMS structures for the desired function. Based on the numerically resulted properties of the TPMS library presented in this study, at fixed porosity of 70%, it had been reported to be desirable for biological activities, while the representative volume element (RVE) of Ixxx-J* structure exhibited the highest strength among all high porosity structures and at the same time, held the highest permeability. Moreover, Fxyz-Fxxx2 structure was found to be the strongest structure, in which the stiffness was the lowest and concurrently, possessed high permeability compared to other low stiffness architectures. In this way, cylindrical topological transition in pore architecture from Fxyz-Fxxx2 to Ixxx-J* or vice versa, which depended on the implantation site, can be suggested as a multifunctional design, where mechanical consistency with host tissue, cell penetrability, as well as mechanical stability, are promoted.

Furthermore, in order to characterize the mechanical properties of scaffolds that comprised of the abovementioned critical RVE architectures, compressive stress-strain curves for 20mm cubic samples with 6.67, 5.00, and 4.00mm unit cell sizes are presented in Figure 4.36. The discrepancies for each scaffold had been associated with high sensitivity of mechanical properties to processing parameters, such as CAD model slicing procedure, and loading direction with respect to the printing direction. De-powdering process is also a major challenge in accounting for the majority of error resources, especially when porosity increases (Cox et al., 2015). Besides, for all the experimental results, a post-yield softening was observed due to the first global failure of the struts. Moreover, this was observed by comparing the results of solid cubic samples printed by Feng et al., (2015), which suggested porosity leads to failure for mechanism to

systematically change to a progressive layer-by-layer failure and thus, a plastic region was observed in stress strain curves despite of the high brittleness of constitutive material.

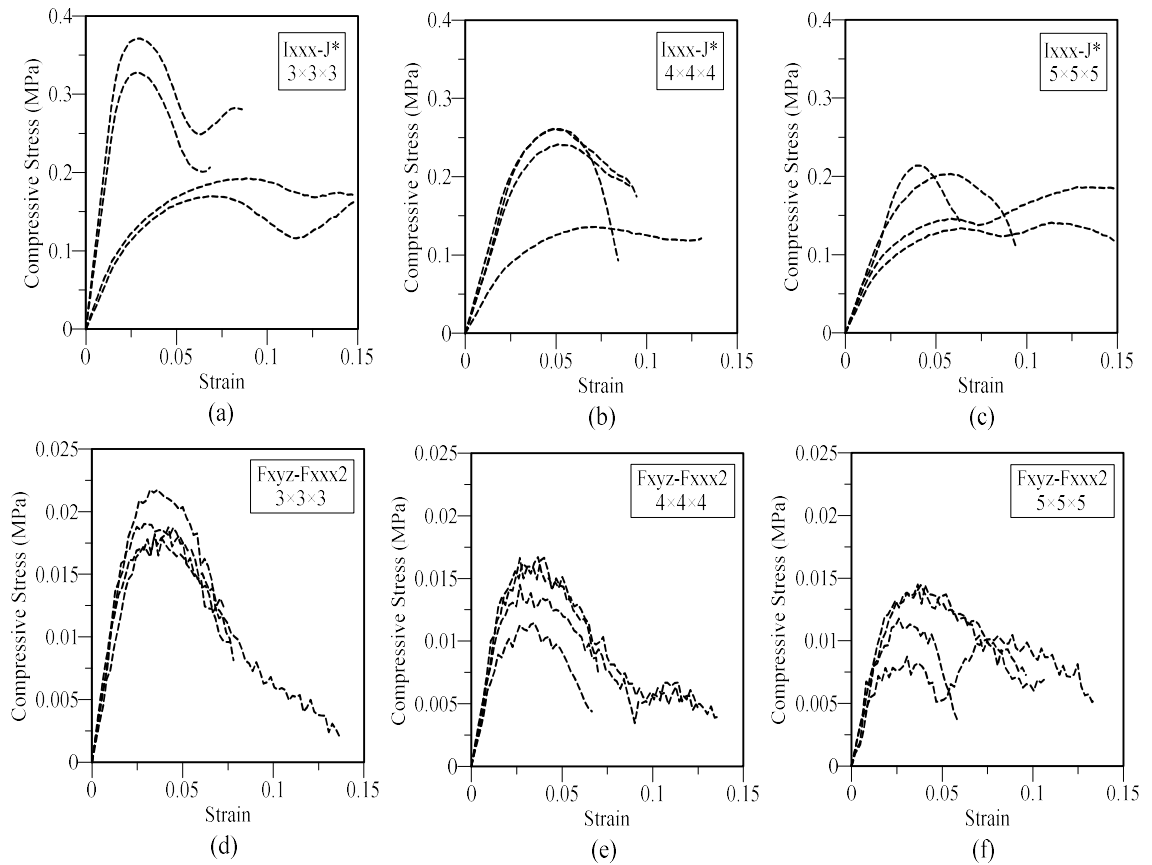


Figure 4.36: Experimental compressive stress-strain curves for Ixxx-J* and Fxyz-Fxxx2 structures with (a,d) 6.67, (b,e) 5.00 (c,f), and 4.00mm unit cell sizes, respectively. Four samples were tested for each design and a post-yield softening was observed for all scaffolds because of the first stage of global failure under compressive load.

The elastic properties elicited from the experimental stress strain curves were compared for different unit cell sizes of Ixxx-J* and Fxyz-Fxxx2 structures in Figure 4.37. Although cell size effect had a significant impact on mechanical responses, Ixxx-J* structure was found to possess, by far, the highest specific mechanical properties as it was expected from the analysis of representative unit cells in the previous sections. Increasing the number of unit cells or correspondingly reducing cell and consequently pore size, decreased the elastic modulus, as well as compressive strength in calcium sulfate scaffolds. Many studies, in fact, have shown that the mechanical properties

improved when pore size decreased (Bose, Vahabzadeh, & Bandyopadhyay, 2013b). However, it should be kept in mind that smaller pore sizes in TPMS structures are accompanied by weakening of the internal struts, thereby, the overall mechanical properties are diminished. Moreover, in the case of powder-based 3D-printed scaffolds, the imperfections due to the narrow strut sizes further decreased the properties. Furthermore, comparing the experimental results of Ixxx-J* versus Fxyz-Fxxx2 indicated the substantial impact of internal architecture on specific mechanical response so that at the same volume porosity of 70%, Young's modulus for Ixxx-J* was found to be between 7.9 and 12.5 times greater than that of Fxyz-Fxxx2 for different cell sizes. The corresponding figures were between 12.8 and 14.2 times improvement in compressive strength for Ixxx-J*. This implied that as internal struts and linkages were oriented parallel to loading direction, high mechanical properties were successfully achieved due to the overall trend of structure to stretching deformation and conversely, when pore topology induced shearing deformations, mechanical properties and efficiency decreased due to high sensitivity of internal struts to shearing mode of deformation.

SEM images of 3D-Printed scaffolds are illustrated in Figure 4.38. For the porosity of 70%, when cell size decreased to 4mm, some defects were found in the internal structure of both Ixxx-J* and Fxyz-Fxxx2 architectures. Moreover, printability became limited when the diameter of the internal struts fell below the 0.6mm in powder-based 3DP techniques. Hence, as shown in Figure 4.38(c), decreasing cell size, especially when porosity increases, causes internal defects, which are more probable to occur during the de-powdering process.

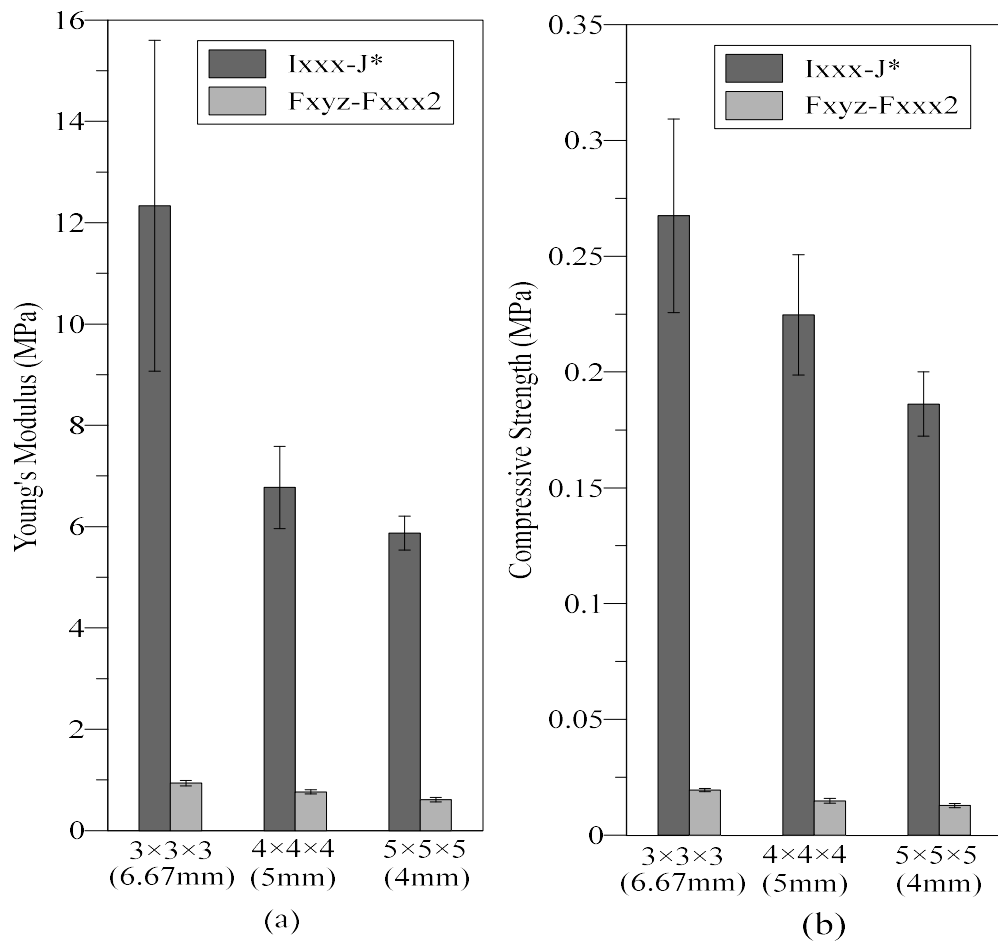


Figure 4.37: Comparing the average elastic modulus and the compressive strength for three different cell sizes of Ixxx-J* and Fxyz-Fxxx2 structures.

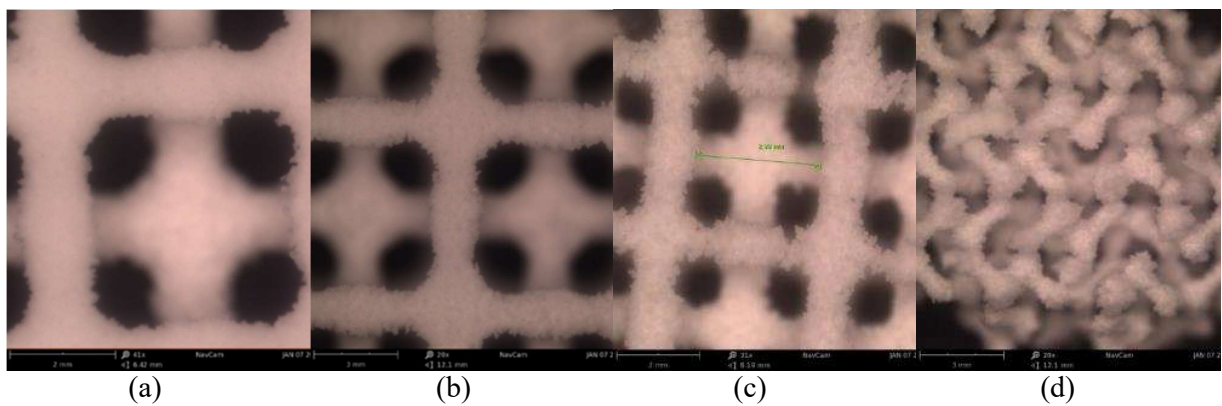


Figure 4.38: SEM Images of 3D-printed scaffolds, Ixxx-J* with cell sizes of (a) 6.67mm, (b) 5.00mm, (c) 4.00mm and Fxyz-Fxxx2 with cell size

4.4 Heat treatment

4.4.1 Composition and microstructure

During the heat treatment of the 3DP calcium sulfate samples, several processes occurred, including water exit, decomposition and combustion of the organic binder, as well as formation of new phases. Figure 4.39 shows the thermal behavior of the printed sample in the temperature range of 50 °C–1000 °C.

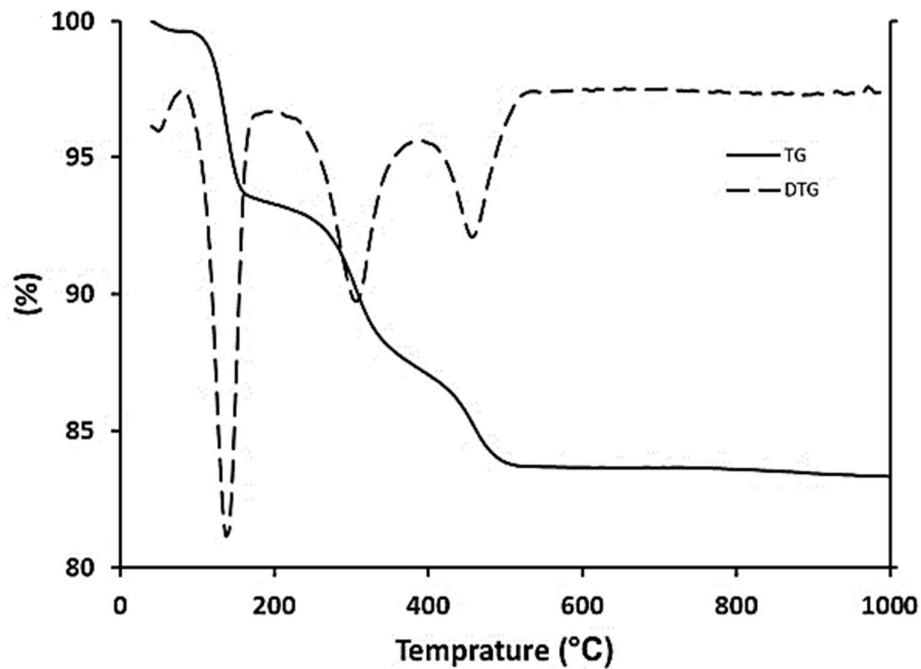


Figure 4.39: TG curve of the printed scaffold and its derivative (DTG).

The TG-DTG curves revealed a total mass loss of 14% from room temperature to 1000 °C in four distinguished weight loss steps:

- 1) The 6.3% of weight loss from room temperature to 200 °C could be attributed to the loss of residual water from the sample, as well as the partial dehydration of the calcium sulfate hemihydrate phase.
- 2) The 6.1% of weight loss between 200 °C and 390 °C may be mainly assigned to the burning and exit of organic species of the starting powder and binder, as well as the

completion of hemihydrate ($\text{CaSO}_4 \cdot 0.5\text{H}_2\text{O}$) dehydration. In addition, the 300 °C samples underwent an emphasized color change. Although the printed samples were white, the samples heated at 300 °C changed color from white to brown (Figure 4.40), which was an apparent indication of the existence of some organic matters in the commercial starting powder (ZP150) and binder solution (zb63) used in this work.

3) The 1.3% of weight loss from 390 °C to 520 °C could be related to the completion of the removal of the remaining water molecules from the basanite structure and the formation of anhydrite (CaSO_4).

4) No significant weight change was observed from 520 °C to 1000 °C because there was no more molecular water to exit or organic binder to burn out, and the anhydrite structure was stable in this temperature range.

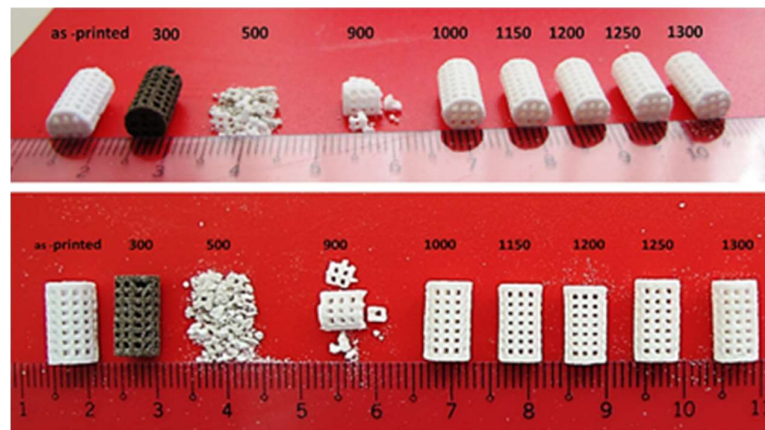


Figure 4.40: Samples heat-treated at various temperatures.

The thermal events above 1000 °C were investigated by using a DTA-TG apparatus. Figure 4.41 shows the DTA-TG curve of the printed sample in the temperature range of 1000 °C–1300 °C. An endothermic peak appeared at 1200 °C, which may be attributed to the formation of calcium oxide as a result of the partial thermal decomposition of anhydrous calcium sulfate based on the following reaction (Swift, et.al, 1976):



The 1200 °C peak was also related to the low- to high-temperature phase transformation of CaSO₄ at 1200 °C, which is reversible during the cooling cycle (Aghajani, Hasratiningsih, & Mori, 2004). The weight loss was more significant after 1200 °C, suggesting that the partial decomposition of anhydrite and the formation of CaO were accelerated based on Equation (4.1). This result was supported by the XRD and SEM-EDS analyses that clearly showed the formation of the CaO phase at 1200 °C and above.

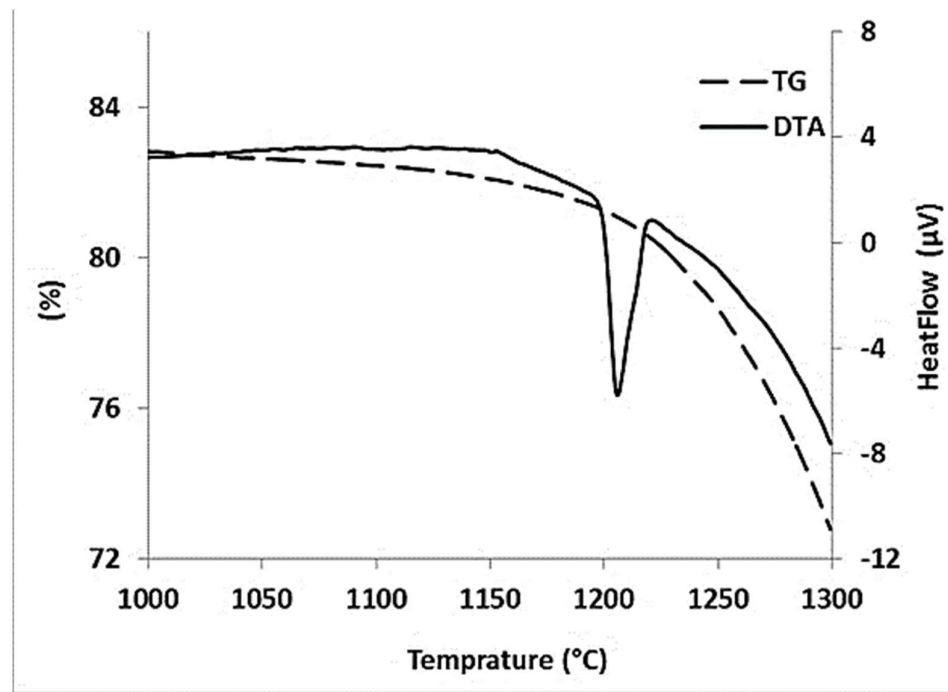


Figure 4.41: TG-DTA curve of the printed scaffold.

The XRD patterns of the printed scaffolds after heat treatment at various temperatures from 300 °C to 1300 °C are shown in Figure 4.42, with the major peaks labeled. The XRD analysis of the printed scaffolds prior to heat treatment showed characteristic peaks of dihydrate and hemihydrate CaSO₄ (designated as G and B in the XRD pattern, respectively). This result disclosed that the zp150 calcium sulfate

hemihydrate ($\text{CaSO}_4 \cdot 0.5\text{H}_2\text{O}$) powder reacted with the water-based binder throughout the 3DP process and formed calcium sulfate dihydrate ($\text{CaSO}_4 \cdot 2\text{H}_2\text{O}$).

The $\text{CaSO}_4 \cdot 2\text{H}_2\text{O}$ peaks almost disappeared after heat treatment at 300 °C. However, the dehydration process was not completed at 300 °C, as suggested by traces of some faded peaks of the $\text{CaSO}_4 \cdot 0.5\text{H}_2\text{O}$ phase. All representative peaks of $\text{CaSO}_4 \cdot 2\text{H}_2\text{O}$ and $\text{CaSO}_4 \cdot 0.5\text{H}_2\text{O}$ disappeared when the samples were heated above 300 °C, which implied the full removal of water molecules from the chemical structure of the printed calcium sulfate scaffolds.

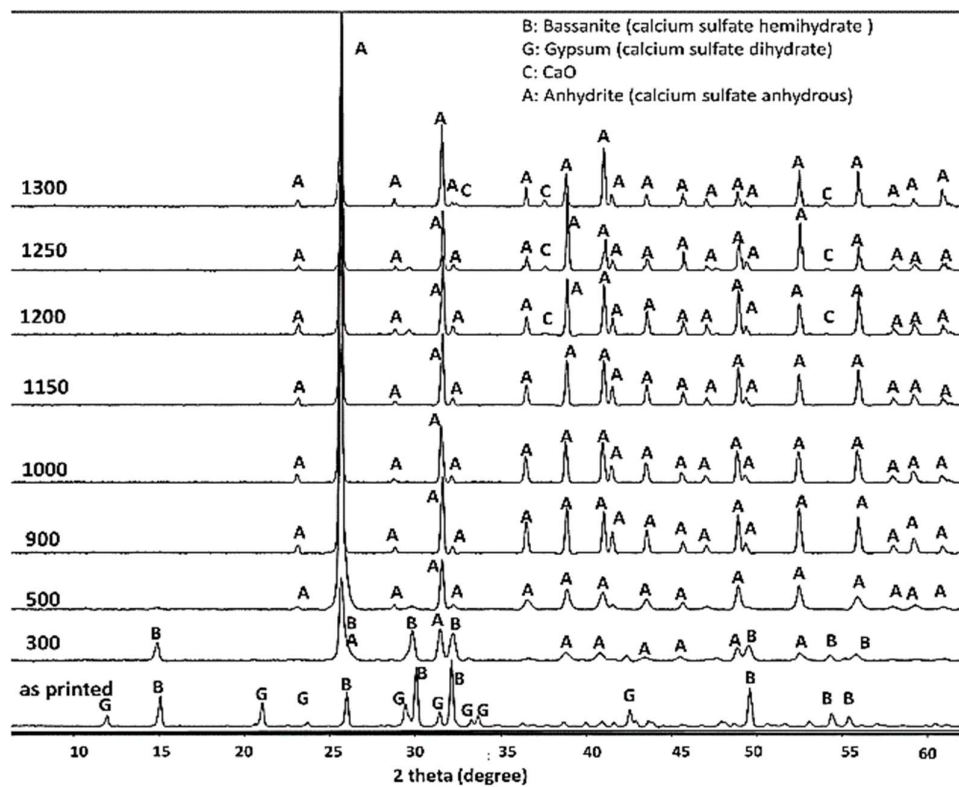


Figure 4.42: XRD patterns of the printed scaffolds after heat treatment at various temperatures from 300 °C to 1300 °C.

On top of that, no clear difference was observed in the XRD patterns of the scaffolds heat-treated at 500 °C, 900 °C, 1000 °C, and 1150 °C. The anhydrous form of calcium sulfate (CaSO_4 or anhydrite) was the only crystalline phase that existed in the samples in

this temperature range.

Besides, traces of calcium oxide were observed in the XRD patterns of all scaffolds heat treated at temperatures higher than 1200 °C (Figure 4.42). Correspondingly, SEM micrographs and EDS revealed small but scattered CaO regions in the microstructure of the specimens that were heat treated at 1200 °C (Figure 4.43), 1250 °C, and 1300 °C.

Other than that, the microstructural features and the surface topography of the 3DP prototypes, as well as the samples that were heat-treated at various temperatures, were studied by SEM micrographs obtained in the backscattered mode.

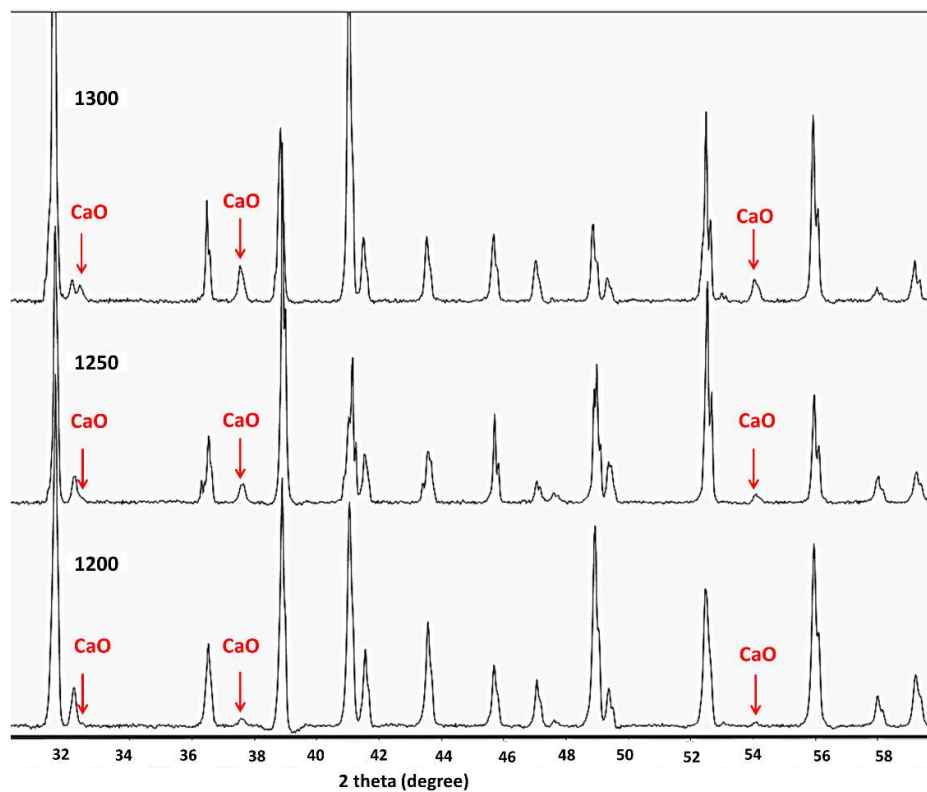


Figure 4.43: XRD patterns of the printed scaffold after heating at 1200 °C, 1250 °C, and 1300 °C. The appearance of CaO peaks (red arrows) confirms the formation of calcium oxide after the partial thermal decomposition of CaSO₄.

The microstructures of the as-printed scaffold and samples that were heat-treated at 300 °C, 500 °C, 900 °C, and 1000 °C are shown in Figure 4.44. Anhydrite crystal prisms with relatively regular shape were observed in the microstructure of the sample heated at 300 °C. Randomly distributed, smaller, and irregularly formed or broken

particles were also observed, which may be attributed to the calcium sulfate hemihydrate phase present in the sample (confirmed by the XRD pattern of the 300 °C sample in Figure 13). The hemihydrate phase was almost completely converted to the anhydrous phase when heated to 500 °C. Consequently, the microstructure changed noticeably, and crystals with remarkably different morphologies appeared along with larger particles, similar to those of the 300 °C sample. Nevertheless, these particles were not new compositions. The XRD and the SEM-EDS results confirmed that the specimen only consisted of anhydrite crystals.

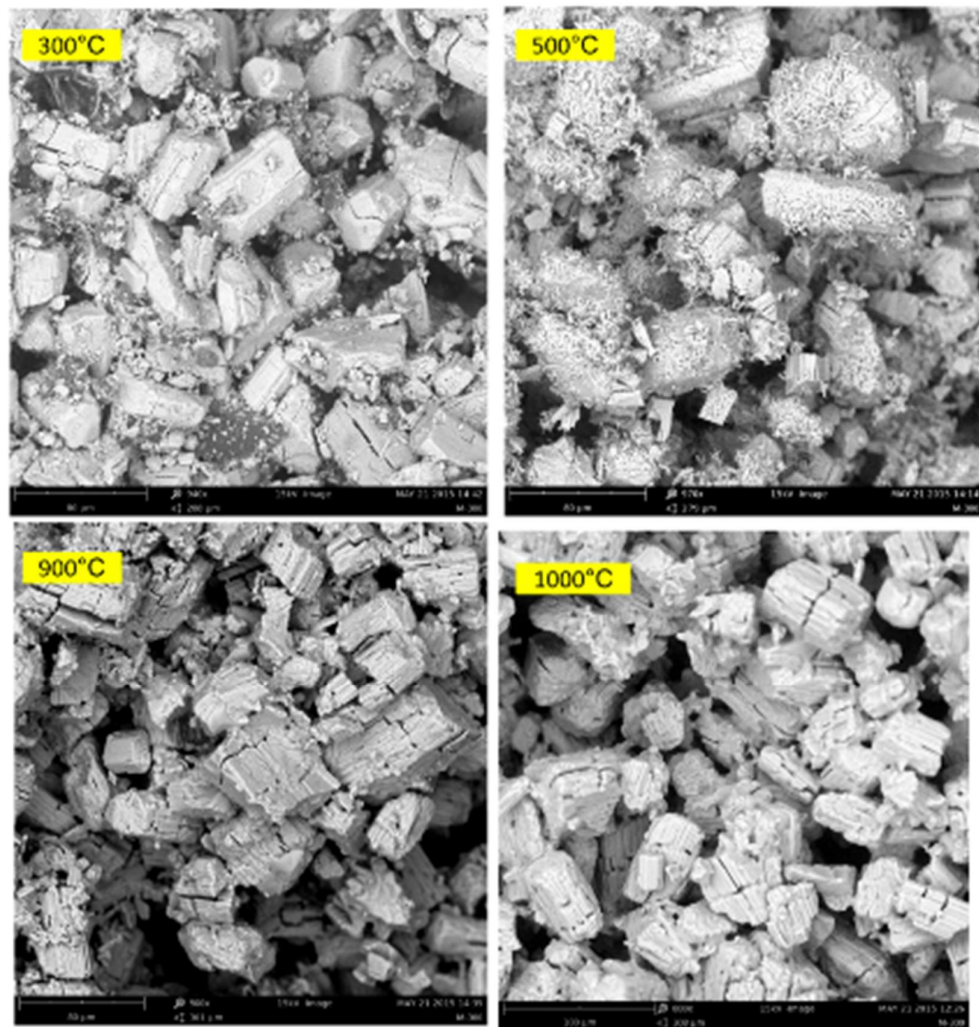


Figure 4.44: SEM backscattered mode image of the microstructures of the printed scaffolds and samples heat-treated at 300 °C, 500 °C, 900 °C, and 1000 °C.

The microstructure of the samples that were heat-treated at 900 °C and 1000 °C looked almost the same. The SEM images showed individual particles that were weakly-bonded together. As expected, there was no sign of densification caused by sintering in the 300 °C–1000 °C temperature range. Besides, the lack of strength was the main feature of the specimens that were heat-treated in this range. Clear evidence of some intragranular cracks in the microstructure of all heat-treated samples were also observed, which may be attributed to the internal stresses induced due to the different calcium sulfate phase transformations that occurred during heat treatment. Figure 4.45 shows the SEM micrographs of the microstructure of the scaffolds heat-treated at 1150 °C, 1200 °C, 1250 °C, and 1300 °C. Based on the SEM images, although the particles were considerably densified, the contact between the particles was insufficient. Therefore, considering the individual particles, the sintering process progressed noticeably. However, the bulk density of the porous samples sintered at 1150 °C and above was still far from the density of the solid sample due to their low green bulk density, which was attributed to the presence of induced micro- and pre-designed macro-porosity.

Nonetheless, the most considerable feature after heating at temperatures higher than 1200 °C was the appearance of discrete regions of calcium oxide in the anhydrite microstructure. This finding is in agreement with the information obtained from the XRD patterns of the 1200 °C, 1250 °C, and 1300 °C samples (Figure 4.43), which is further supported by the EDS analysis results (Figure 4.50). SEM-EDS elemental map analysis of the printed scaffold is shown in Figure 4.46. Besides the Ca, S, and O elements that apparently came from the calcium sulfate body, a significant amount of C (25.6%) was also present, which represented the organic constituents of the zp150 powder and the zb63 binder used in this work for 3DP.

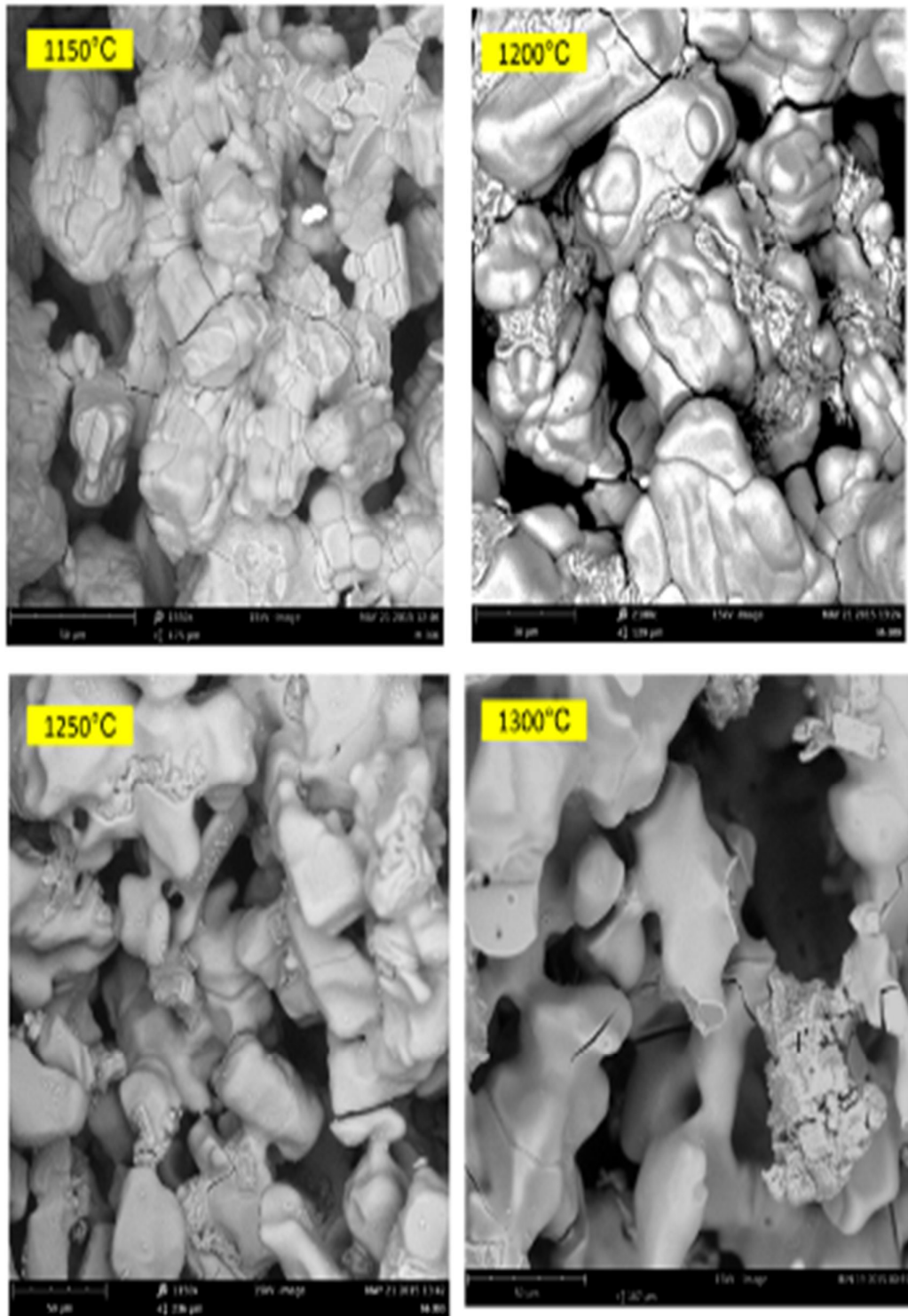


Figure 4.45: SEM backscattered mode images of the microstructures of the samples heat-treated at 1150 °C, 1200 °C, 1250 °C, and 1300 °C.

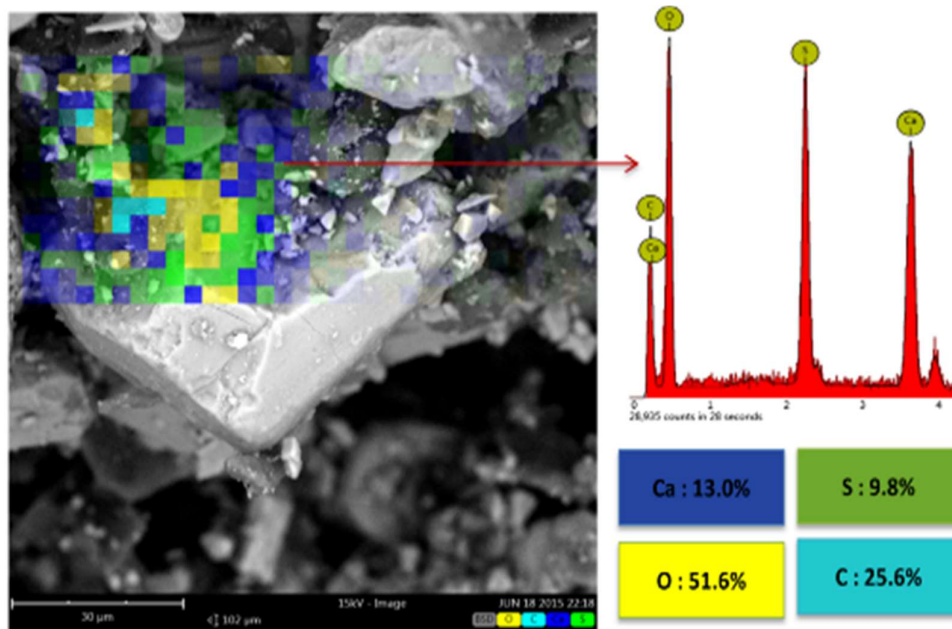


Figure 4.46: SEM-EDS elemental map analysis of the printed scaffold.

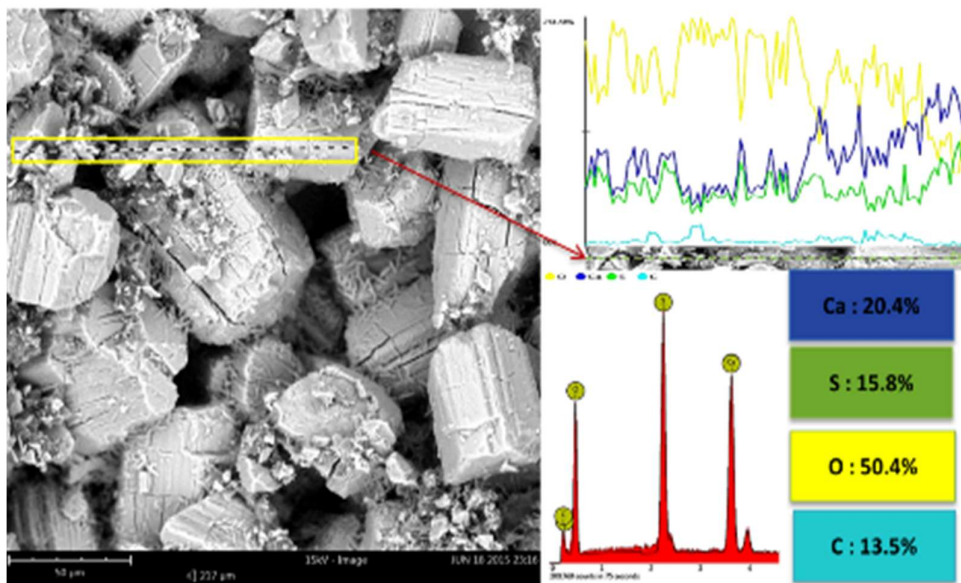


Figure 4.47: SEM-EDS (line scan) analysis of the specimen heated at 300 °C.

SEM-EDS line scan analysis of the sample heated at 300 °C is shown in Figure 4.47. A considerable amount of carbon (13.5%) was detected, which indicated that 300 °C was not sufficient to remove all the organic substances present in the printed scaffolds.

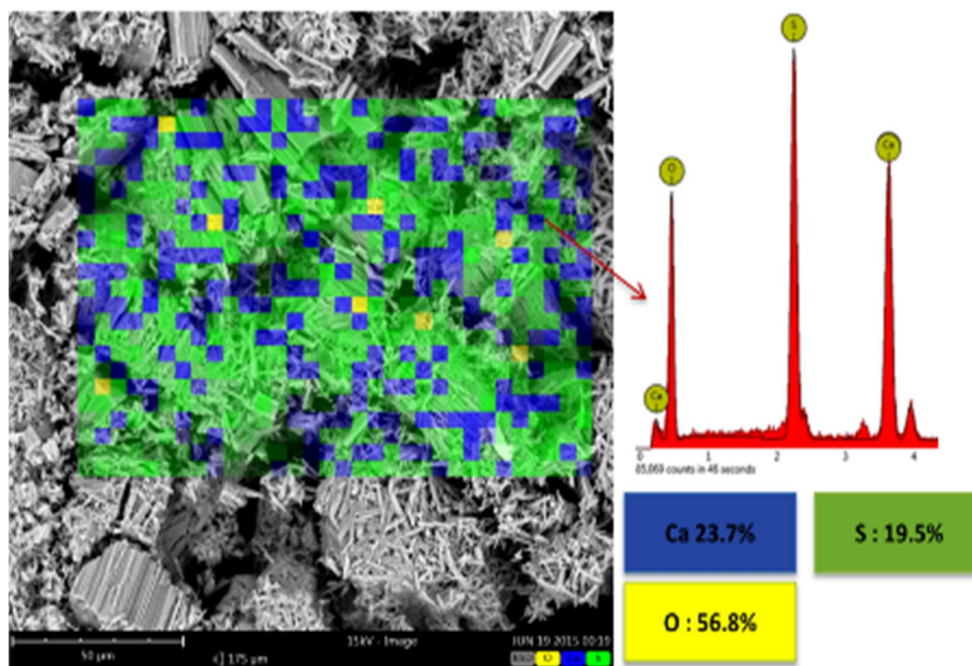


Figure 4.48: SEM-EDS elemental map analysis of the specimen heated at 500 °C.

Figure 4.48 shows the result of SEM-EDS elemental map analysis of the sample heat-treated at 500 °C. Meanwhile, element distribution analysis only showed Ca, S, and O. The total absence of C peaks in the EDS spectra suggested the complete burn out and elimination of organic materials introduced by the starting powder and binder at 500 °C. No sign of carbon was observed. The microstructure and the SEM-EDS analyses of the samples that were heat-treated at 900 °C, 1000 °C, and 1150 °C were more or less similar to those of the 500 °C specimen. The chemical composition of all these samples was almost identical and consisted of anhydrous calcium sulfate (anhydrite) as the only crystalline phase in the structure (see the SEM-EDS elemental map analysis in Figure 4.49 and XRD patterns in Figure 4.42).

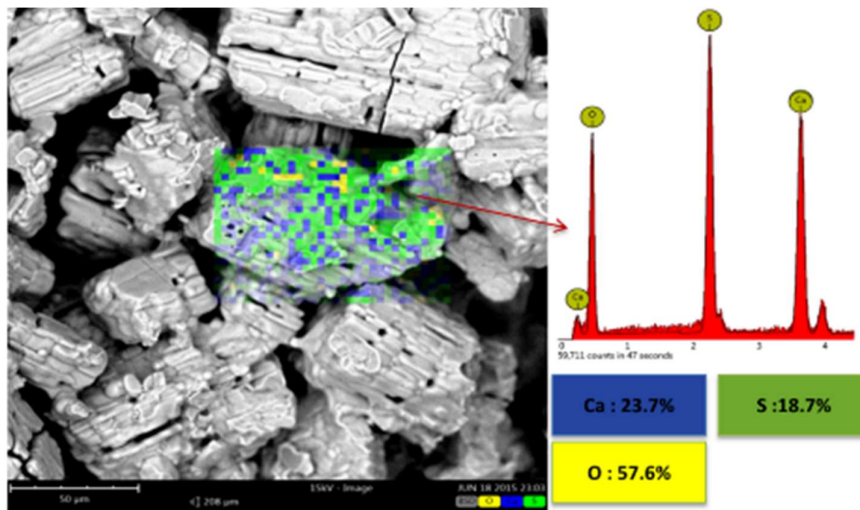


Figure 4.49: SEM-EDS elemental map.

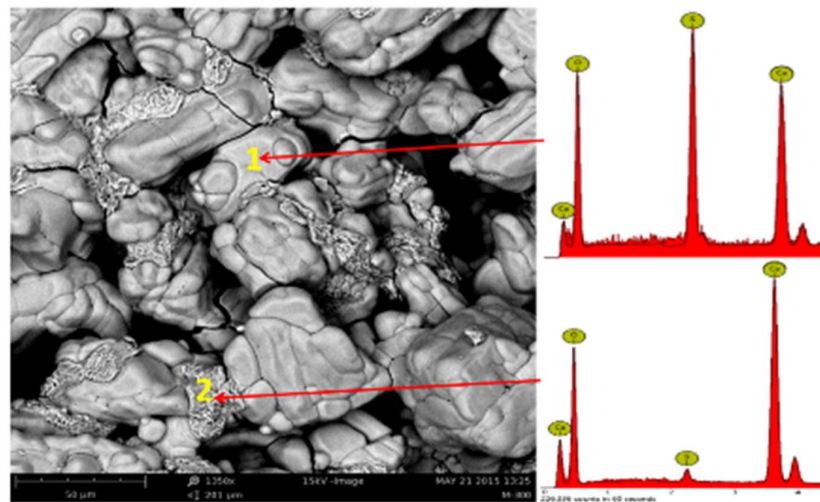


Figure 4.50: SEM micrograph of the sample heated at 1200 °C. Formation of calcium oxide (spot 2) is shown following partial thermal decomposition of CaSO₄ (spot 1).

The printed scaffolds underwent partial decomposition when heated above 1200 °C. Calcium oxide appeared in the microstructure of the samples after heat treatment at 1200 °C, 1250 °C, and 1300 °C.

The SEM micrograph of the sample heated at 1200 °C is shown in Figure 4.50. Spot EDS chemical analysis confirmed the formation of calcium oxide based on Equation

(4.1). The results of the chemical analysis of two typical CaSO₄ and CaO spots are shown in Table 4.16. As anticipated, no significant quantity of sulphur was detected in the spot chemical analysis of the discrete regions attributed to the calcium oxide in the microstructure of the 1200 °C sample.

Table 4.16: Chemical analysis of spots 1 and 2 (in Figure 4.32) attributed to calcium sulfate and calcium oxide in the microstructure of the sample heated at 1200 °C.

Element	SPOT 1 (%)	SPOT 2 (%)
Ca	22.5	34.5
O	60.1	64.2
S	17.4	1.3

4.4.2 Mechanical features, shrinkage, and density

The mechanical behaviors of the printed and the heat-treated scaffolds were investigated by using a universal testing instrument with compression test fixtures. The compressive tests were carried out until the sample was broken. Figure 4.51 shows a typical 3DP test specimen before and after critical failure.

The strain–stress curves of the porous scaffolds heat-treated at 300 °C, 1000 °C, 1150 °C, 1200 °C, 1250 °C, and 1300 °C are shown in Figure 4.52. Ultimate compressive strength and compressive elastic modulus were calculated by using the maximum compressive stress recorded in the stress–strain curve, as well as the slope of the linear region before the yield point. The scaffolds that were heat-treated at temperatures higher than 1200 °C showed an increase in compressive strength and Young’s modulus.



Figure 4.51: Specimens under compression test.

An extension of the plastic region was also observed, which suggested higher toughness. The results of the compressive strength test, the Young's modulus, and the bulk density of the porous and solid samples after heat treatment at various temperatures are summarized in Table 4.17, while the trends are shown in Figure 4.53. The trend of compressive strength and Young's modulus change with temperature had been roughly identical for both solid and porous specimens, although the strength values and the rates of change were lower in the porous samples compared to those in the solid ones. Meanwhile, shrinkage of the printed porous and the solid samples was determined by measuring the diameter and the thickness of the cylinder-shaped samples before and after heat treatment.

The results are summarized in Table 4.18. Other than that, Figure 4.54 shows the bulk density, the volume, and the weight of both the porous and solid specimens versus the heat treatment temperature. The thickness and the diameter shrinkage percentages of the samples as a function of heat treatment temperature are also shown in Figure 4.55.

Table 4.17: Results of compressive strength test, Young’s modulus, and bulk density of the porous and the solid samples after heat treatment at various temperatures.

Samples temperature (°C)	Compressive strength(MPa)		Young’s modulus(MPa)		Density (g/cm ³)	
	Solid	Porous	Solid	Porous	Solid	Porous
As-printed	2.47	0.70	52.11	45.13	1.35	0.76
300	0.49	0.48	48.56	41.89	1.17	0.646
500	0.25	-	42.13	-	1.26	-
900	0.29	-	30.25	-	1.31	-
1000	0.32	0.08	48.78	42.1	1.33	0.76
1150	1.06	0.17	54.36	48.26	1.47	0.786
1200	2.75	0.40	56.34	50.1	1.51	0.75
1250	2.95	0.55	65.32	58.12	1.22	0.595
1300	2.90	0.52	64.98	57.98	1.22	0.59

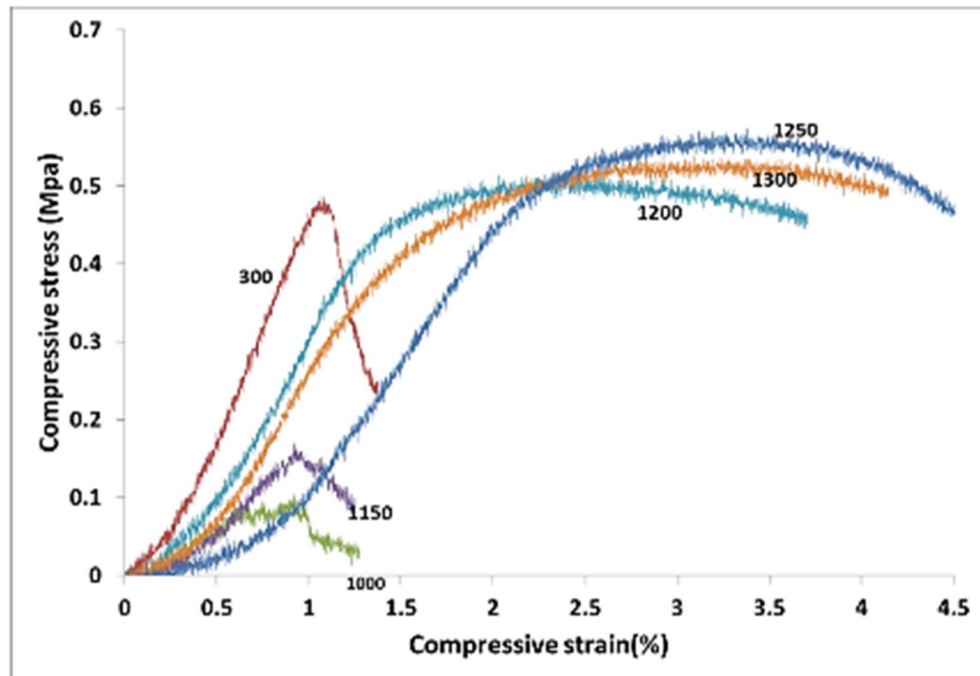


Figure 4.52: Strain–stress curves for porous scaffolds heat-treated at 300 °C, 1000 °C, 1150 °C, 1200 °C, 1250 °C, and 1300 °C.

Heating the printed scaffolds at 300 °C significantly decreased the compressive strength from 2.47 MPa to 0.48 MPa and 0.7 MPa to 0.48 MPa for the solid and porous samples, respectively. The same trend was observed for Young’s modulus. The elastic modulus decreased from 52.11 MPa to 48.56 MPa for the solid samples, and fell from 45.13 MPa to 41.89 MPa for the porous scaffolds. Meanwhile, the bulk density of the

scaffolds heat-treated at 300 °C decreased by 18% (from 0.76 g/cm³ to 0.64 g/cm³) and 12% (from 1.35 g/cm³ to 1.17 g/cm³) for the solid and porous samples, respectively, compared to those of the printed samples. The significant weight loss caused by decomposition and exit of organic species, as well as dehydration of the starting hemihydrate calcium sulfate, had been the main reasons for the decrease in density.

Heating the scaffolds at temperatures higher than 300 °C resulted in an undesirable mechanical failure. The compressive test could not be performed on the 500 °C and 900 °C porous samples because they were extremely fragile, weak, and could break down easily (see Figure 4.40). Therefore, no compressive strength and elastic modulus had been documented in this work for the porous samples that were heat-treated at temperatures higher than 300 °C and lower than 1000 °C. The inadequate mechanical strength of the samples heat-treated at this temperature range could be explained due to the lack of necessary bonding between the printed layers and the adjacent particles.

Table 4.18: Shrinkage of the cylinder-shaped porous and solid samples after heat treatment at various temperatures.

Samples-temperature(°C)	R%		L%	
	Solid	Porous	Solid	Porous
As-printed	0.017	-2.67	-1.47	-2.25
300	-1.62	-4.3	-2.90	-3.67
500	-7.05	-9.67	-5.27	-6
900	-7.56	-10.17	-7.05	-7.83
1000	-7.75	-10.33	-7.72	-8.5
1150	-10.62	-13.33	-10.93	-9.42
1200	-11.44	-14.17	-11.71	-12.42
1250	-6.10	-8.83	-6.02	-6.75
1300	-7.37	-10	-8.77	-9.5

This finding was mainly attributed to the partial combustion of the organic binder at 300 °C and its complete removal at 500 °C. Below 1000 °C, the calcium sulfate system showed no evidence of sintering, and the densification (and increase in strength) of the 3DP prototypes had yet to begin. Thus, practically neither the organic binder nor the

sintering process contributed to particle and layer bonding when the printed scaffolds were heat-treated at the 300 °C–1000 °C temperature range.

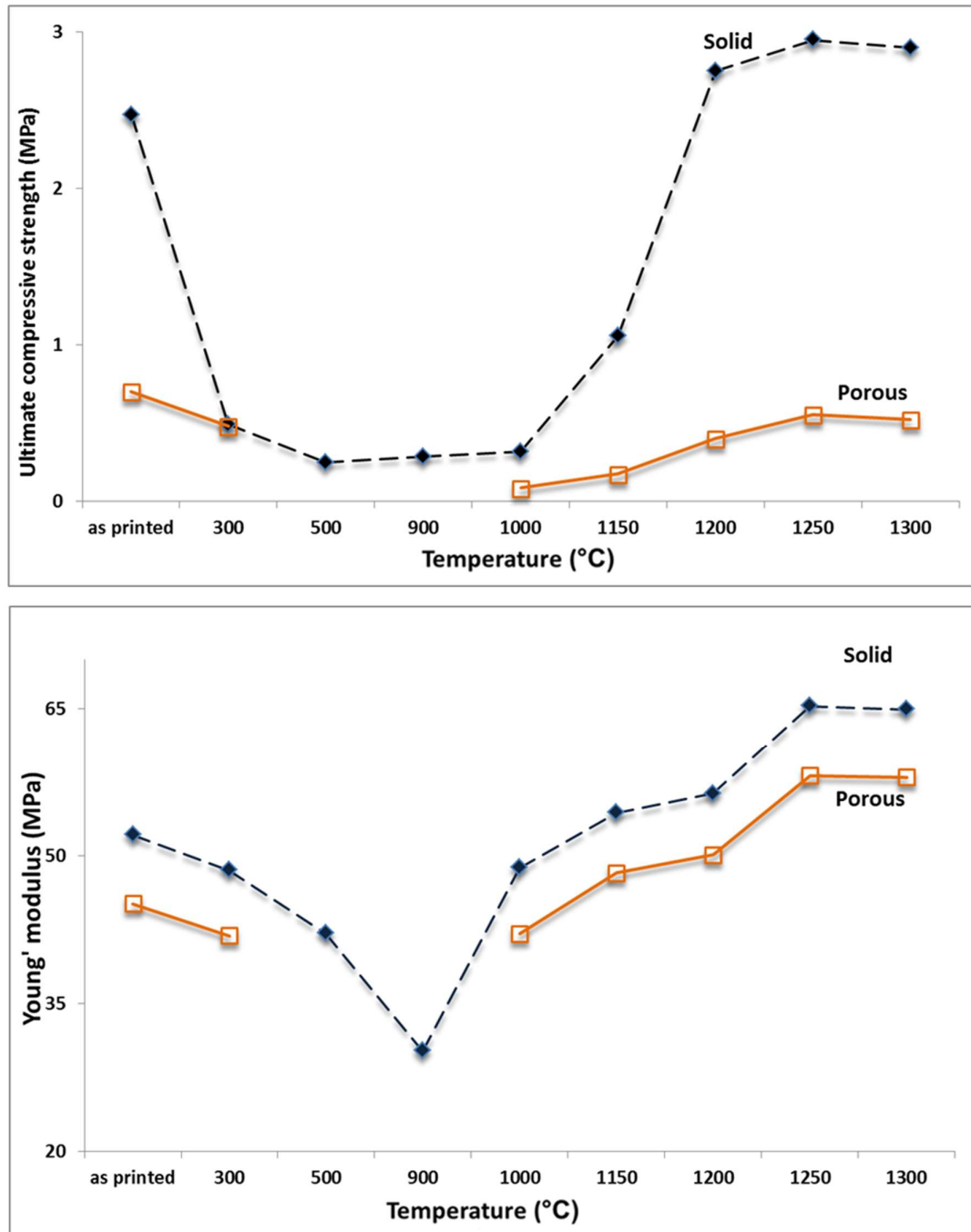


Figure 4.53: Changes in compressive strength and Young's modulus of the porous and solid specimens with heat treatment temperature.

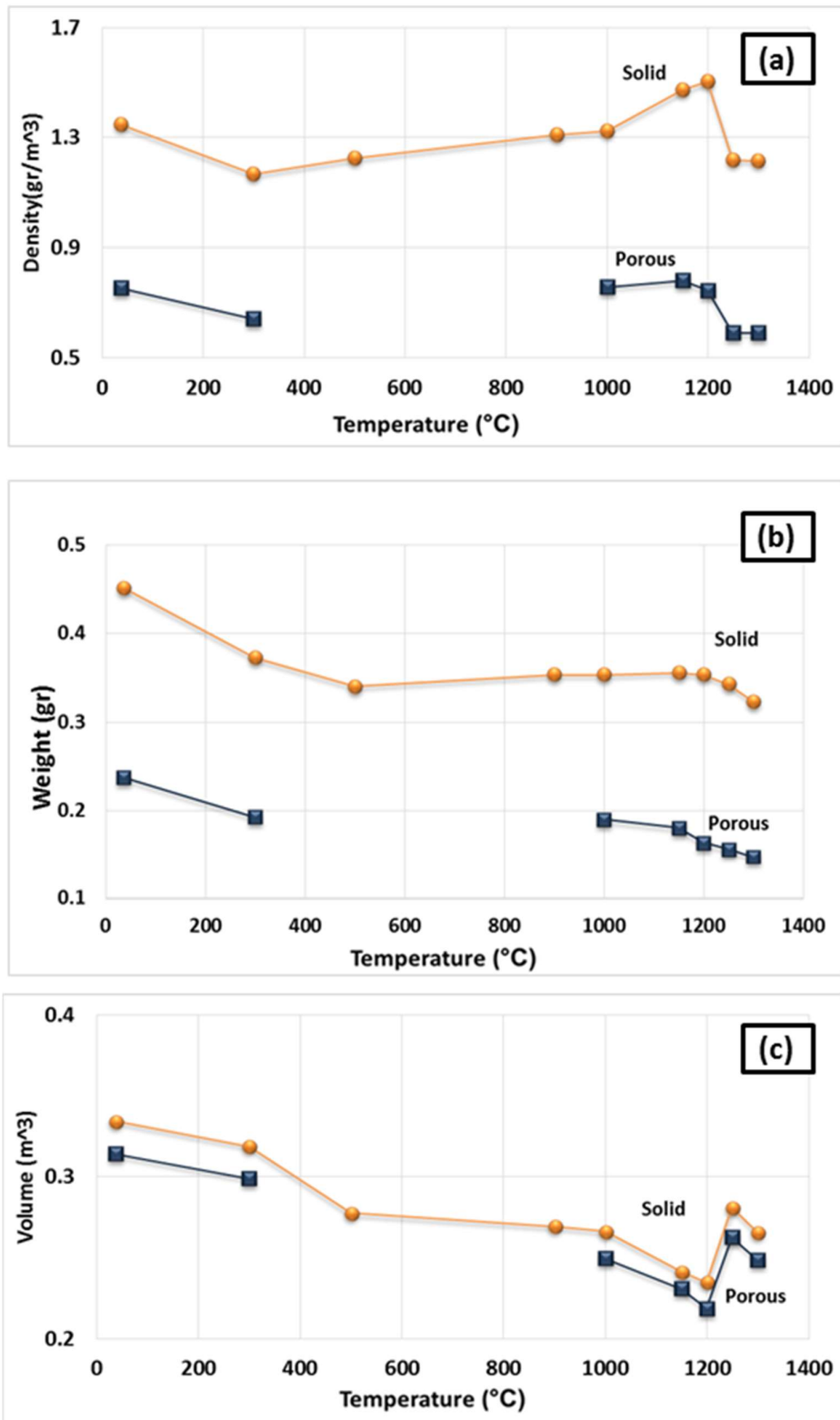


Figure 4.54: Bulk density (a), volume (b), and weight (c) of the porous and solid specimens versus heat treatment temperature.

A very minor increase in the trend of density versus temperature curve was observed from 500 °C to 1000 °C. However, no considerable weight loss was observed in this temperature range, and an insignificant density increase was mostly caused by a slight decrease in volume. The XRD and SEM-EDS results showed no phase change, whereas microstructural coarsening began at 900 °C. Furthermore, heating the scaffolds at 1000 °C and higher temperatures substantially increased the density and improved the compressive strength, as well as elastic modulus in both porous and solid samples. For the solid samples, the maximum compressive strength (2.95 MPa) and Young's modulus (65.32 MPa) had been achieved at 1250 °C, which exceeded the compressive strength (2.47 MPa) and Young's modulus (52.11 MPa) of the solid printed samples. Similarly, the compressive strength of the porous samples increased from 0.08 MPa at 1000 °C to 0.55 MPa at 1250 °C, which was in a range comparable with that of the initial printed scaffold (0.7 MPa). The elastic modulus also increased from 42.1 MPa at 1000 °C to 58.12 MPa at 1250 °C, which was higher than that of the printed scaffold (45.13 MPa). This result was mainly attributed to the progress of the sintering process at temperatures higher than 1000 °C, which densified the calcium sulfate scaffolds and improved the mechanical properties of the struts. At 1200 °C, a portion of the CaSO₄ phase decomposed and converted to CaO in expense of the exit of a considerable amount of SO₃ resulting in considerable weight loss and reduction in density. The decomposition reaction was theoretically associated with 58.81% of weight loss. From 1250 °C to 1300 °C, its density remained almost unchanged because of a compromise between the acceleration of the sintering process and the weight loss caused by the decomposition of calcium sulfate.

The shrinkage of scaffolds that were heat-treated at 300 °C was 4.3% in diameter and 3.67% in height for the porous samples, whereas 1.62% in diameter and 2.9% in

height for the solid samples. The dimensions of the scaffolds remained relatively constant between 300 °C and 900 °C. From 900 °C to 1200 °C, the diameter and the height of the porous samples experienced 14.17% and 12.42% shrinkage, respectively. From 1200 °C to 1250 °C, although the progress of sintering at high temperatures was expected to increase shrinkage, the samples practically shrunk less. In fact, a trade-off was observed between the acceleration of the sintering process and the weight loss, while the decrease in the volume was caused by the decomposition of calcium sulfate that resulted in decreased shrinkage. Further heating from 1250 °C to 1300 °C facilitated the sintering process and increase in shrinkage.

Therefore, in determining the significance level, ANOVA was performed for dimension and weight tests. The results are summarized in Table 4.19.

The SS, the df, and the F corresponded to the sum of squares, degree of freedom, and F value, respectively. The ANOVA results demonstrated that the tests were highly significant, with $P < 0.001$.

Table 4.19: Results of ANOVA for diameter, height, and weight.

Source of variation	Diameter				Height				Weight			
	SS	df	Variance	F	SS	df	Variance	F	SS	df	Variance	F
Between group	4.01	8	0.50	140.57	13.19	8	1.64	525.65	0.11	8	0.01	414
Within group	0.29	81	0.00	-	0.25	81	0.00	-	0.00	81	0.00	-
Total	4.29	89	-	-	13.44	89	-	-	0.11	89	-	-

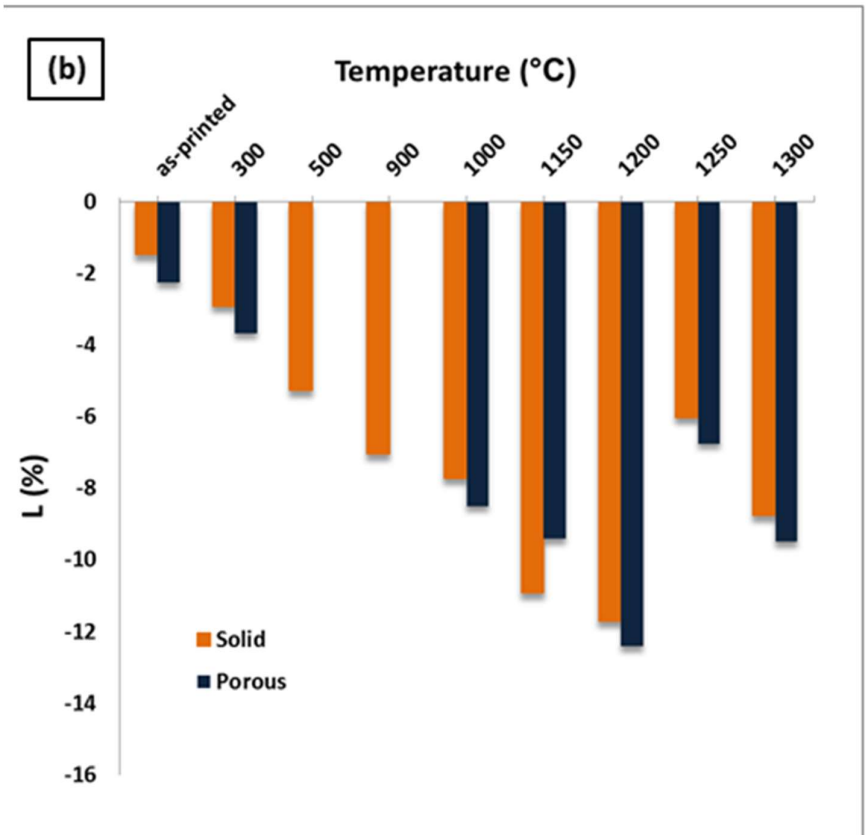
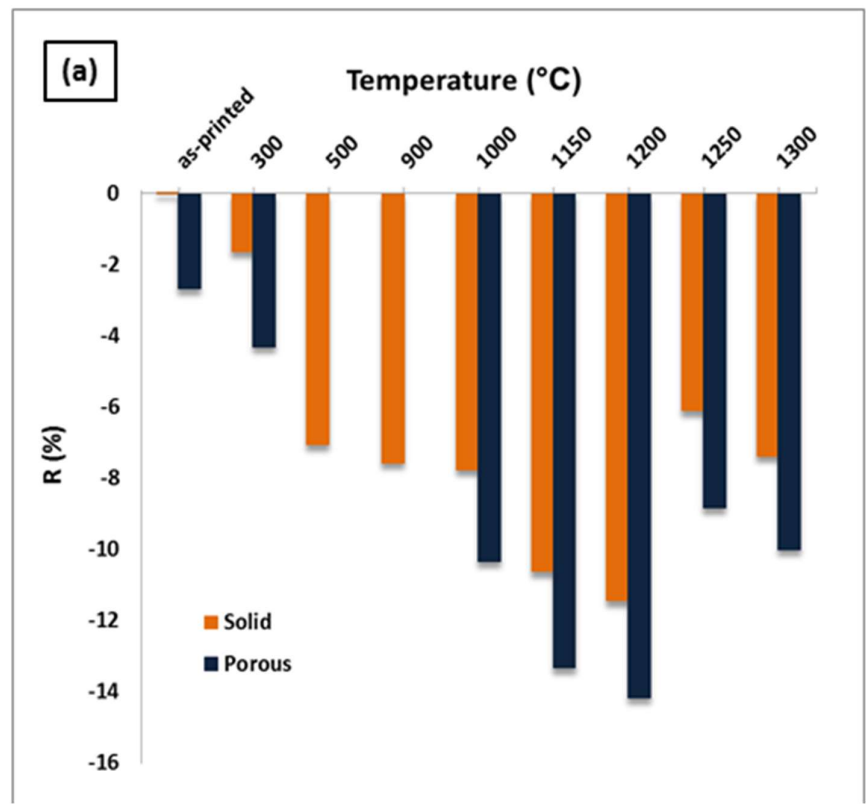


Figure 4.55: Thickness and diameter shrinkage percentages of the samples as a function of heat treatment temperature.

4.4.3 *In vitro* evaluation of the printed and heat-treated scaffolds

The MTT measurement results are shown in Figure 4.56. According to the standard protocols, the extracts of the powders were collected on days 1, 3, and 7. Subsequently, MG63 cells were exposed to different extractions of samples for 24 h. The results showed a significant reduction in viability for the powder and printed samples below 60%. This reduction was attributed mainly to the composition of the printed scaffolds due to the presence of organic constituents in the zp150 powder and the zb63 binder used in this work for 3DP.

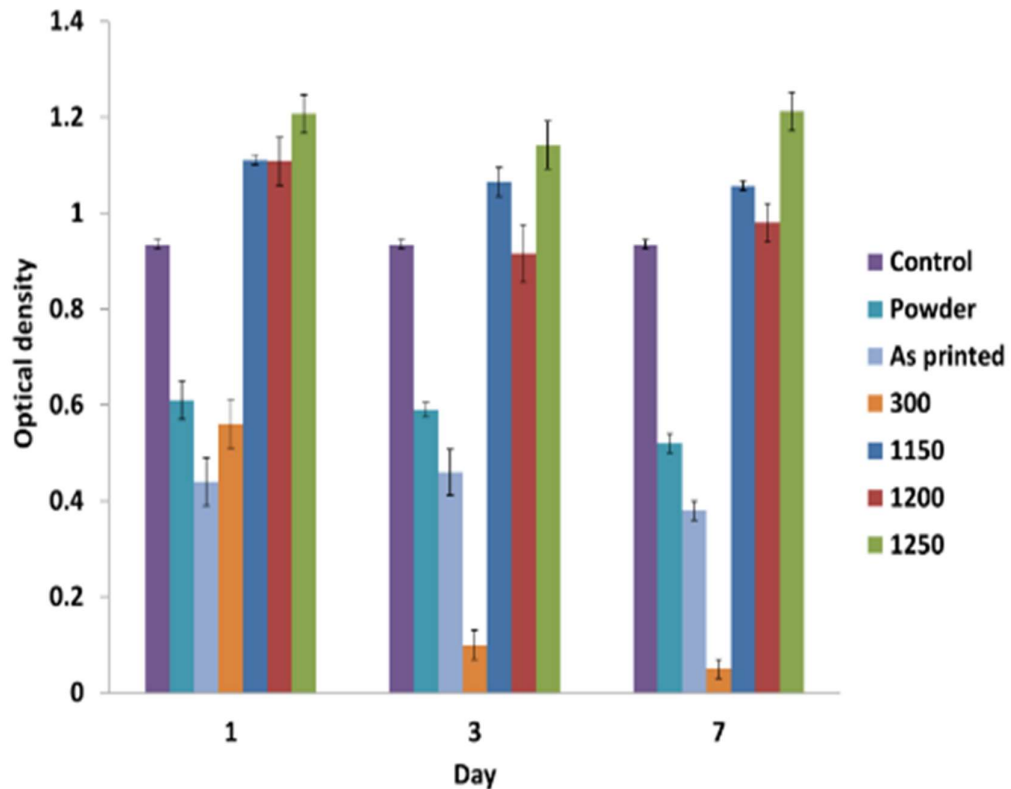


Figure 4.56: Results of MTT assay on the ZP150 powder, printed scaffold, as well as samples heated at 300 °C, 1150 °C, 1200 °C, and 1300 °C.

The sample that was heat-treated at 300 °C had significant toxic effects on cells, which was mainly caused by the products resulting from the partial decomposition and

combustion of the organic materials present at the commercial binder (zb63) and powder (zp150). Hence, this temperature may not be sufficient for the complete combustion of organic additives.

Therefore, to completely eliminate the organic additives and to improve the mechanical properties of the samples, the printed samples were heat-treated at a higher temperature. The samples that were heat-treated at 1150 °C, 1200 °C, and 1250 °C showed significantly greater viability compared to the control, as shown in Figure 4.56. This result may be due to the complete removal of the toxic organic species during the high-temperature heating process.

4.5 Phosphate treatment

4.5.1 Composition and microstructure

Samples heat-treated at 1150, 1200, and 1250°C for 1h in air had enough strength to withstand phosphatization process. The phosphate treatment of the sample was performed by soaking the printed and heated samples at 85°C ammonium phosphate solution for 4, 8, 16, and 24h. The transformation by treatment was examined via XRD. The microstructural features of the phosphate-treated 3DP specimens were studied by using SEM-EDX micrographs obtained in the backscattered mode. The XRD patterns of the scaffolds that were heat-treated at 1150°C and phosphate-treated for 4, 8, 16, and 24h are shown in Figure 4.57 with the major peaks labeled.

The XRD analysis showed characteristic peaks of calcium sulfate phases (mostly anhydrous, with a trace of dihydrate and hemihydrate CaSO_4) designated as CS in the

XRD pattern. The calcium phosphate phase formed essentially dicalcium phosphate, which is labeled as CP. The diffractograms disclosed that calcium sulfate scaffolds were partially converted to calcium phased as a result of chemical reaction between calcium sulfates and ammonium phosphate solution. The presence of CP phases is more emphasized in 16 and 24h samples. However, even after 24h soaking in the ammonium phosphate solution, the CS phases were the major phases present.

The microstructure of the samples heat-treated at 1150°C and phosphate-treated at 85°C for 24h is shown in Figure 4.58. The presence of regions of calcium phosphate was the most significant feature of the microstructure of phosphate-treated calcium sulfates. Spot EDS chemical analysis confirmed the formation of calcium phosphate phases.

The result of the chemical analysis of a typical calcium phosphate spot is also shown in Figure 4.58. As anticipated, no sulfur was detected in the spot chemical analysis of the discrete regions attributed to the calcium phosphate in the microstructure of the sample. This finding is in agreement with the data obtained from the XRD patterns of the sample heat-treated at 1150°C and phosphate-treated at 85°C for 24 h (Figure 4.57-d).

Figure 4.59 shows the XRD patterns of 3D-printed scaffolds after heat treatment at 1200°C and soaking in phosphate solution for 4, 8, 16, and 24h. As observed, the calcium sulfate samples were mostly converted into brushite $\text{CaHPO}_4 \cdot 2\text{H}_2\text{O}$ (JCPDS card No. 09- 077). Although some calcium phosphate phases were formed, no noticeable amount of HA (JCPDS card no. 09-432) was seen in the patterns projected by the samples.

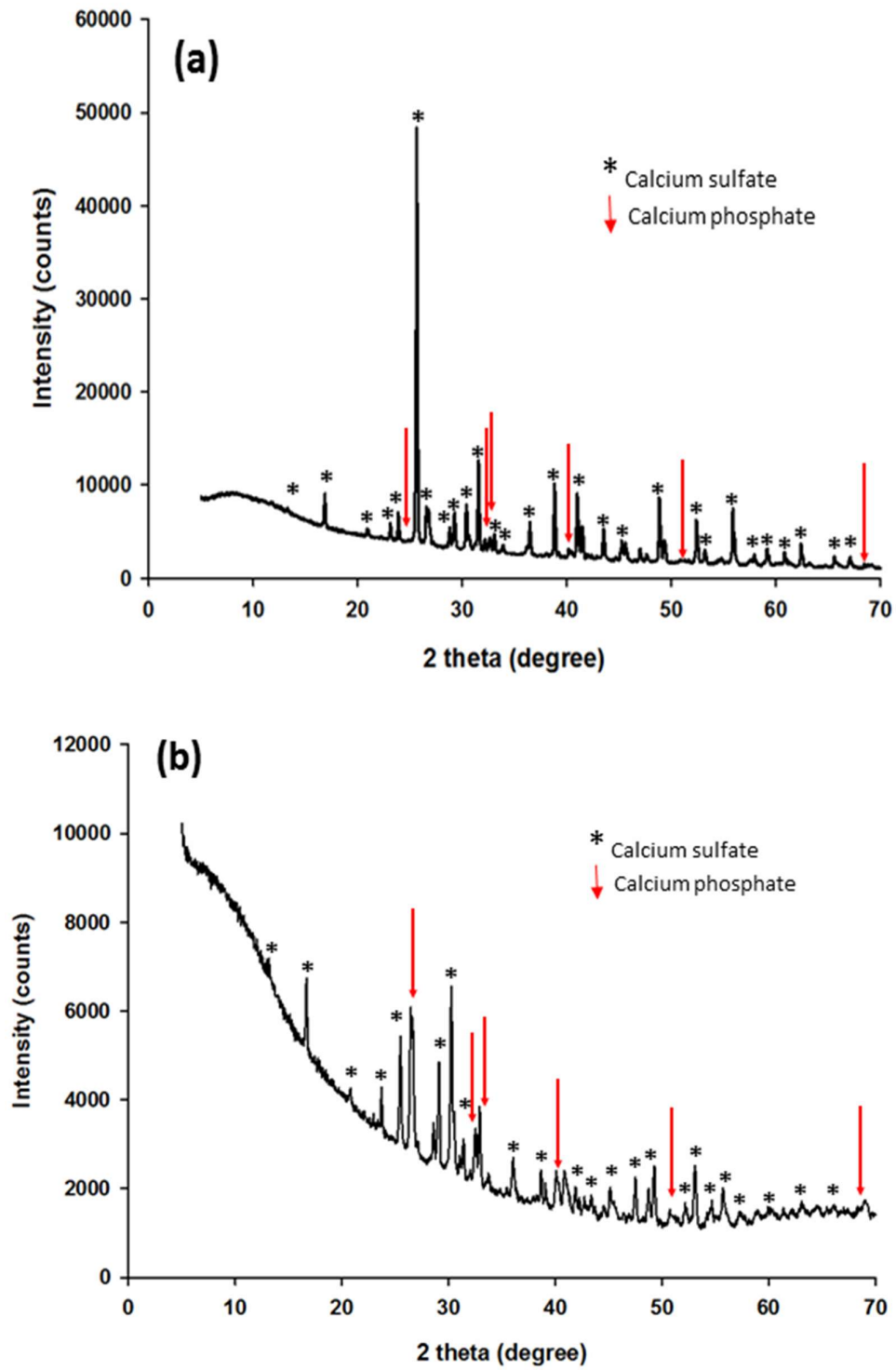


Figure 4.57: XRD patterns of the 3D-printed scaffolds after heat treatment at 1150°C and phosphate treatment for (a) 4, (b) 8, (c) 16, and (d) 24h.

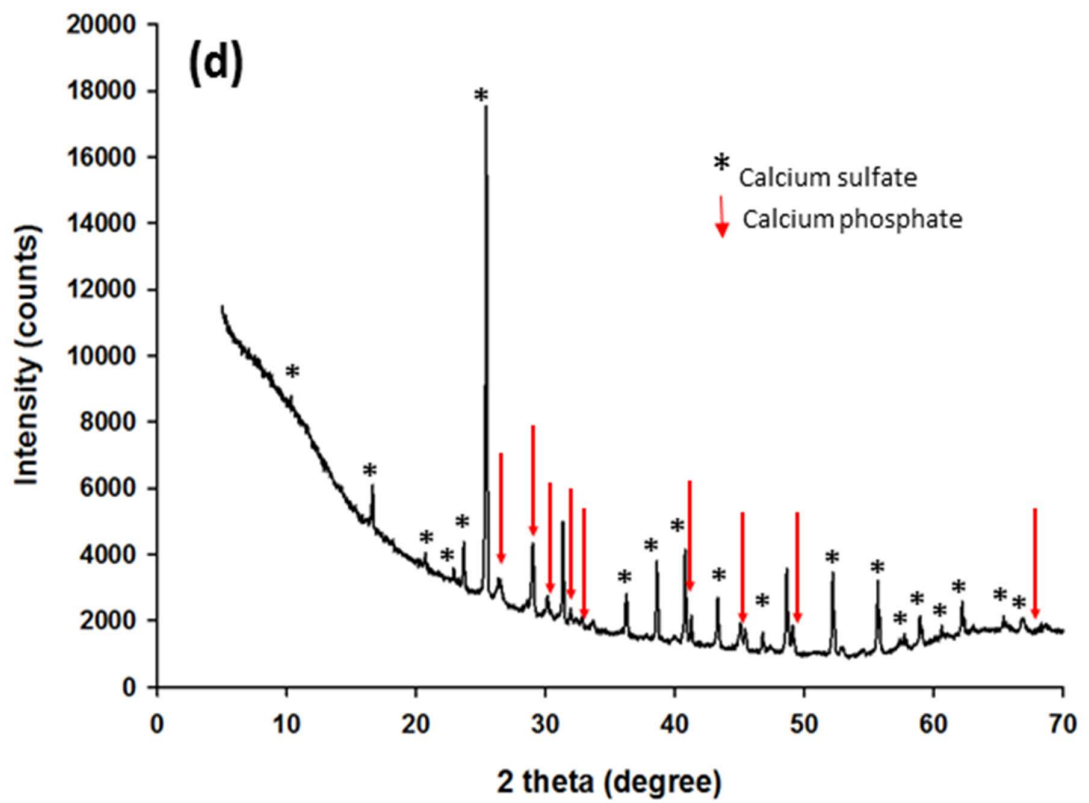
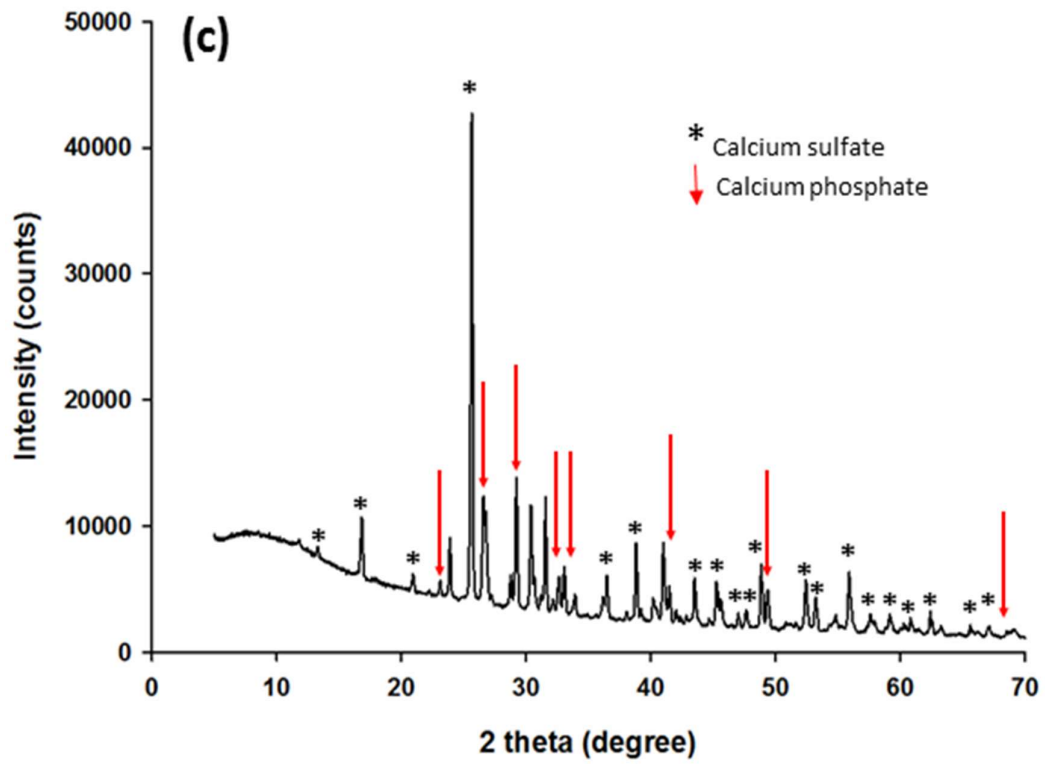


Figure 4.57, Continued.

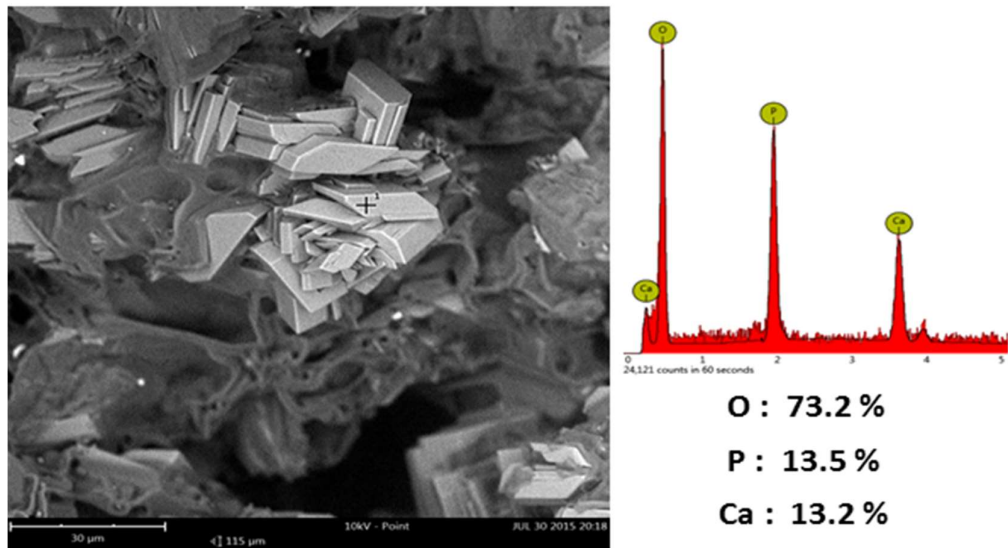


Figure 4.58. SEM-EDX micrograph of the samples heat-treated at 1150°C and phosphate-treated at 85°C for 24h.

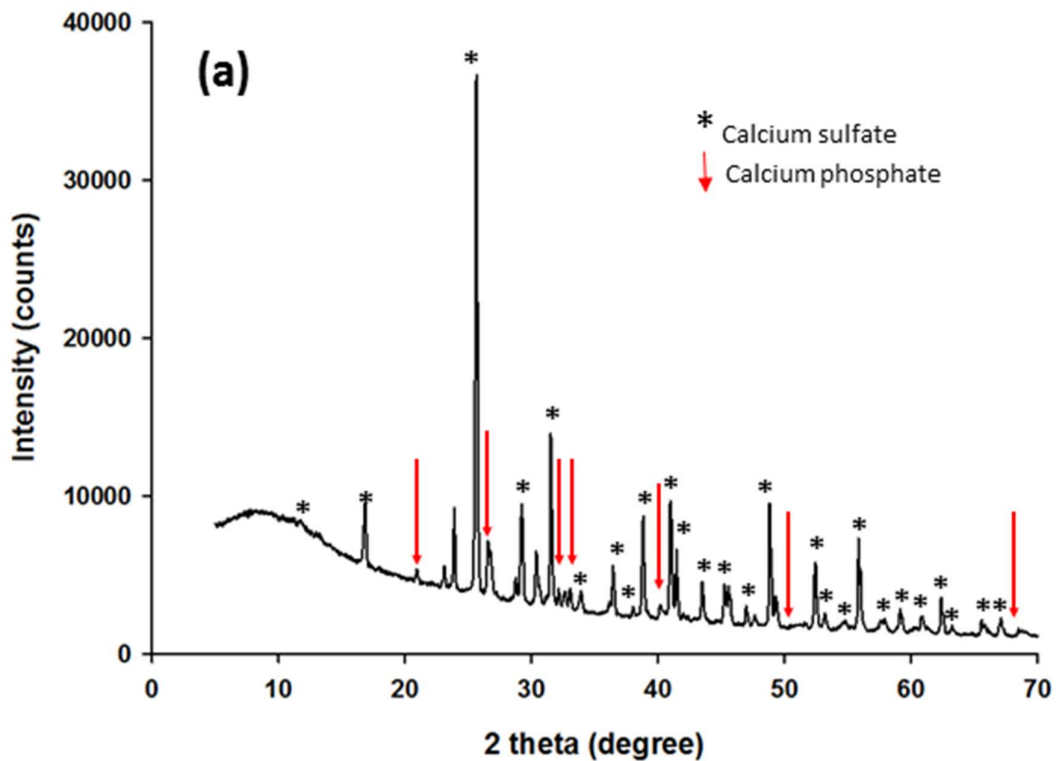


Figure 4.59: XRD patterns of the 3D-printed scaffolds after heat treatment at 1200°C and phosphate treatment for 4, 8, 16, and 24h.

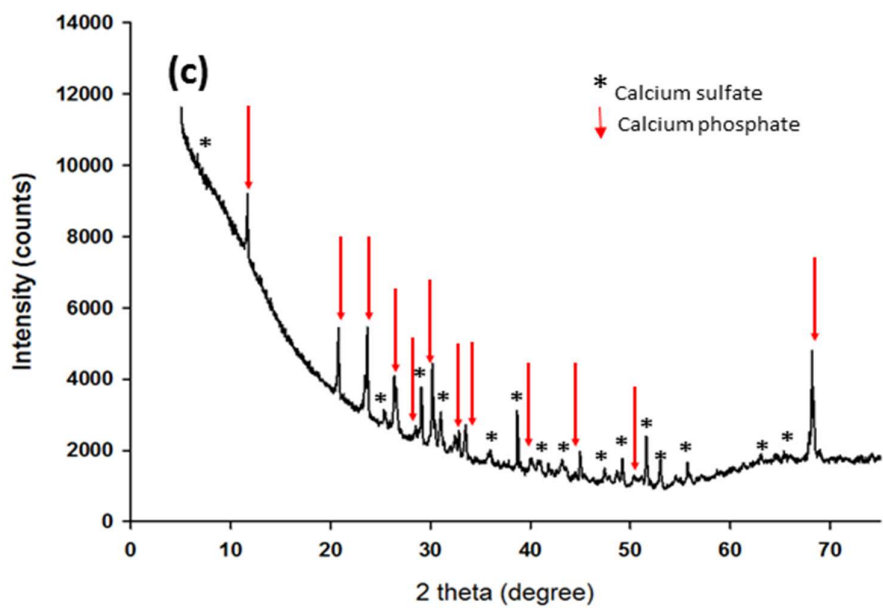
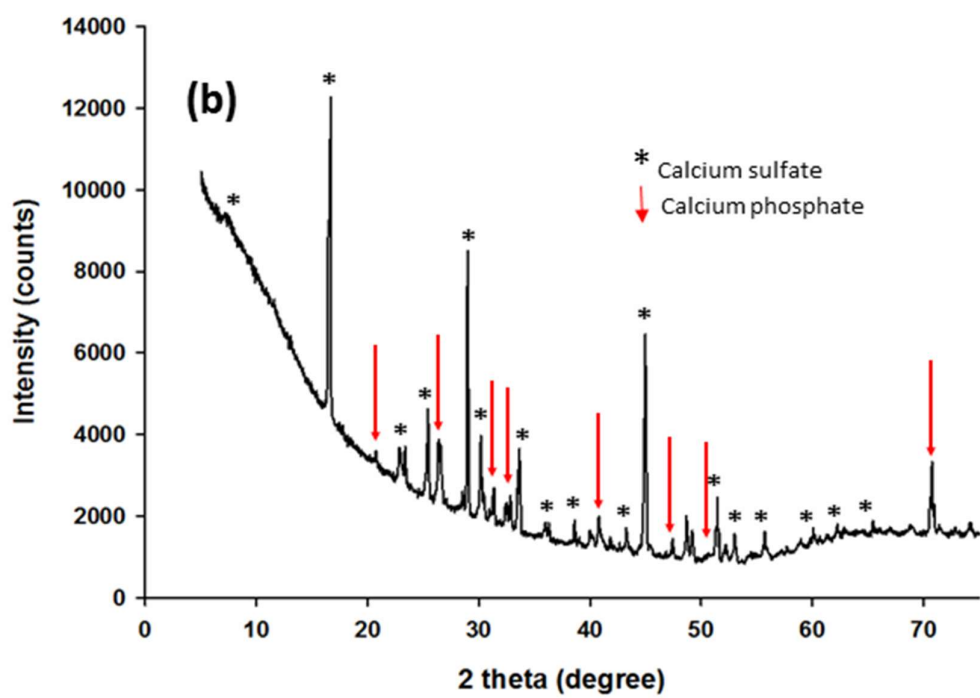


Figure 4.59, Continued.

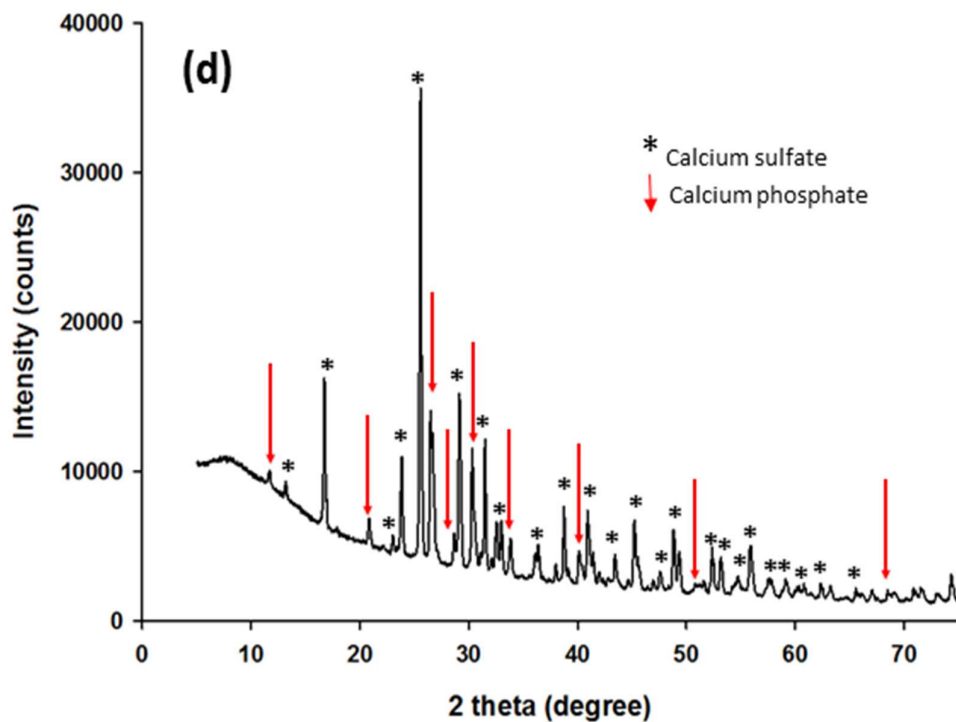


Figure 4.59, Continued.

SEM-EDS (line scan) analyses of the specimens heat-treated at 1200°C and phosphate-treated at 85°C for 24h are shown in Figure 4.60. Besides, regular-shaped crystals, attributed to both calcium sulfate and calcium phosphate phases, were presented in the microstructure of the post-treated scaffolds, which was confirmed via spot and line EDX chemical analyses, as well as the XRD pattern of 24h sample (Figure 4.59-d). This was a clear sign that CS phases were partially converted to CP phases in the when heated at 1200°C and chemically-treated at ammonium phosphate solution for 24h.

The XRD diffractograms in Figure 4.61 show the phases that existed in the specimens heated at 1250°C and reacted with a phosphate solution for 4, 8, 16, and 24h. These patterns are somehow comparable with the XRD patterns of phosphate-treated

samples after being heated at 1150 and 1200°C. Here again, calcium phosphate phases (mostly as di-calcium phosphate) were present as a product of the phosphorization reaction. No significant amount of HA phase, however, was developed at various soaking times. Correspondingly, SEM micrographs, as well as EDS spot and line chemical analyses (Figure 4.62), revealed scattered CP regions in the microstructure of 1250°C specimens.

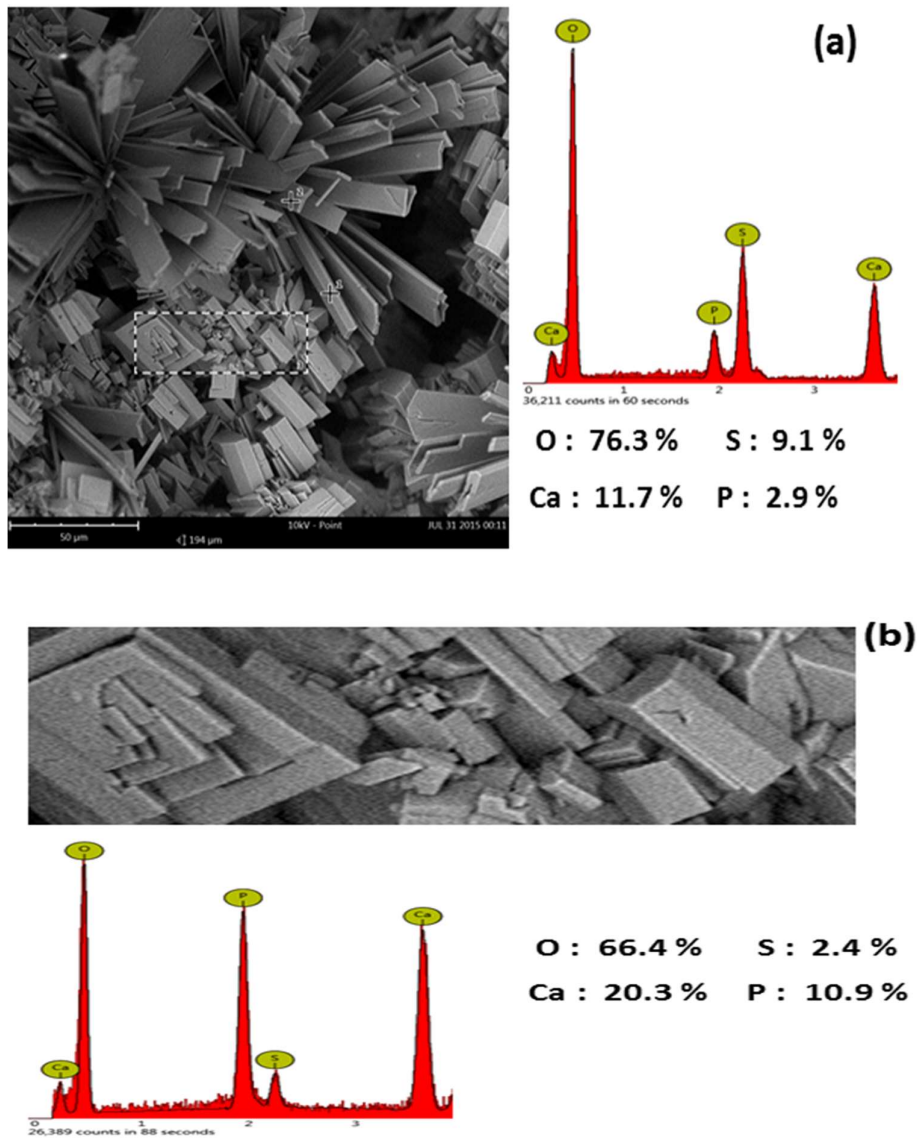


Figure 4.60: SEM-EDS (line scan) analysis of the specimen heat-treated at 1200°C and phosphate-treated at 85°C for 24h.

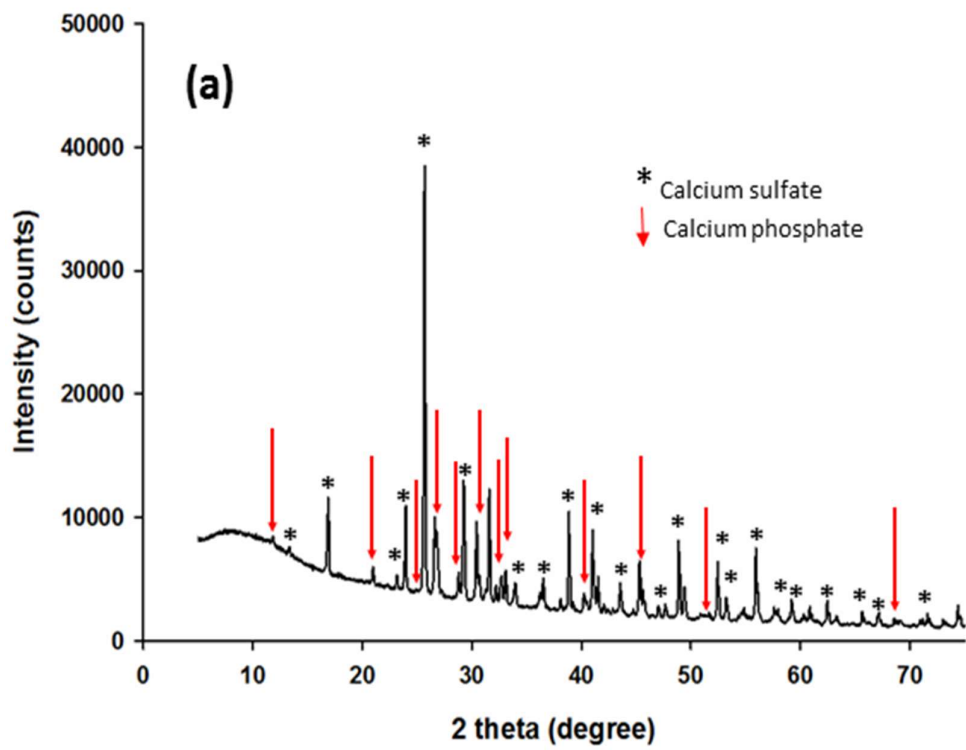
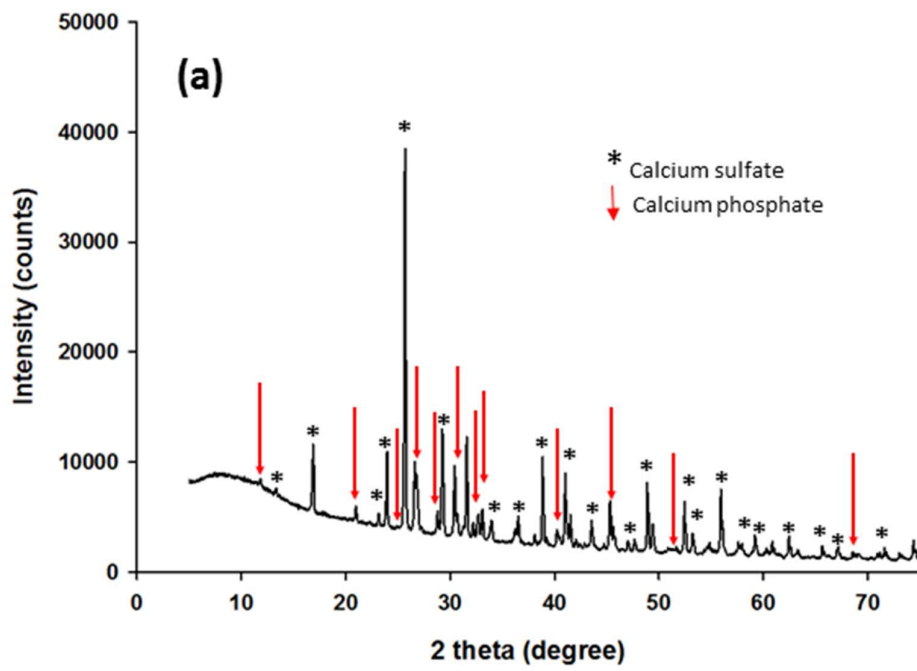


Figure 4.61: XRD patterns of the 3D-printed scaffolds after heat treatment at 1250°C and phosphate treatment for 4, 8, 16, and 24h.

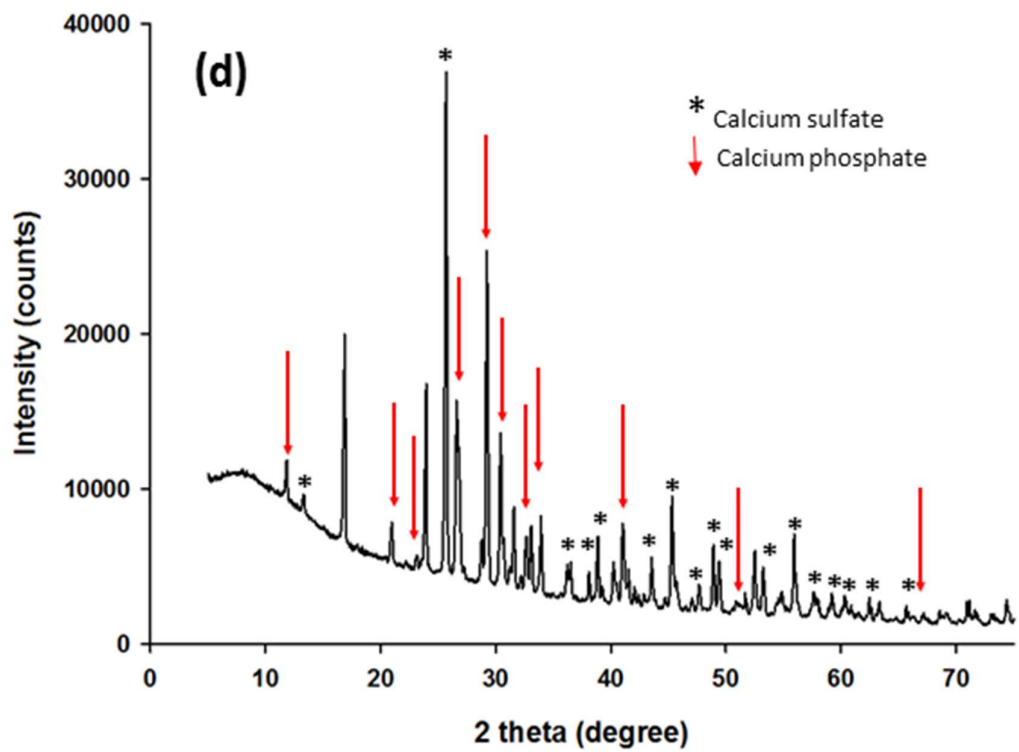
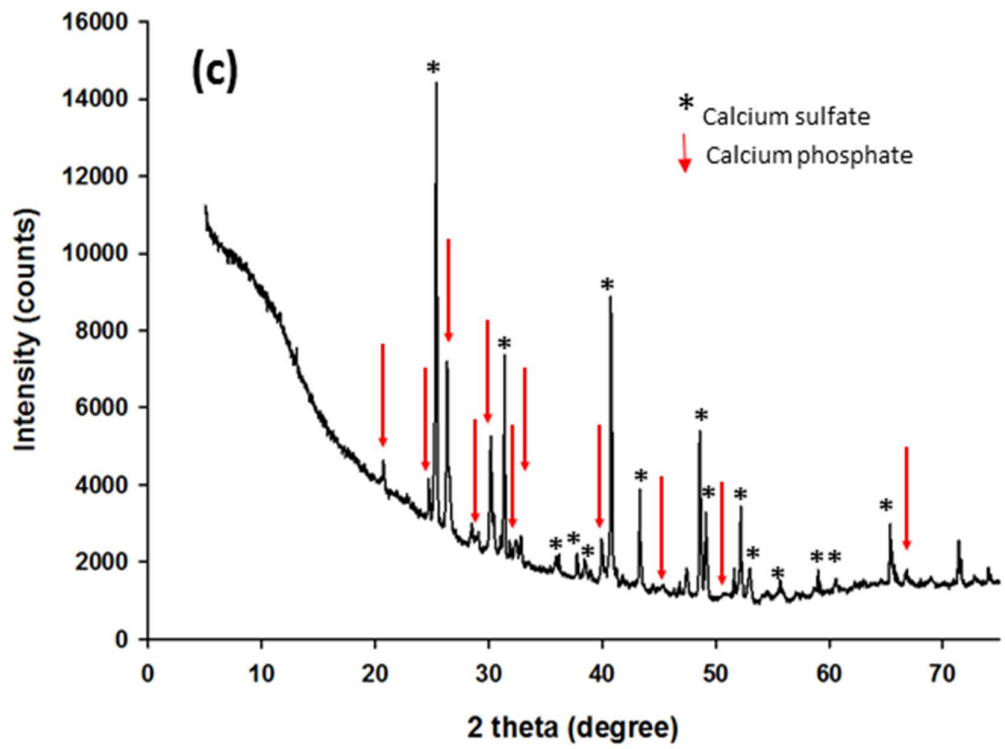


Figure 4.61, Continued.

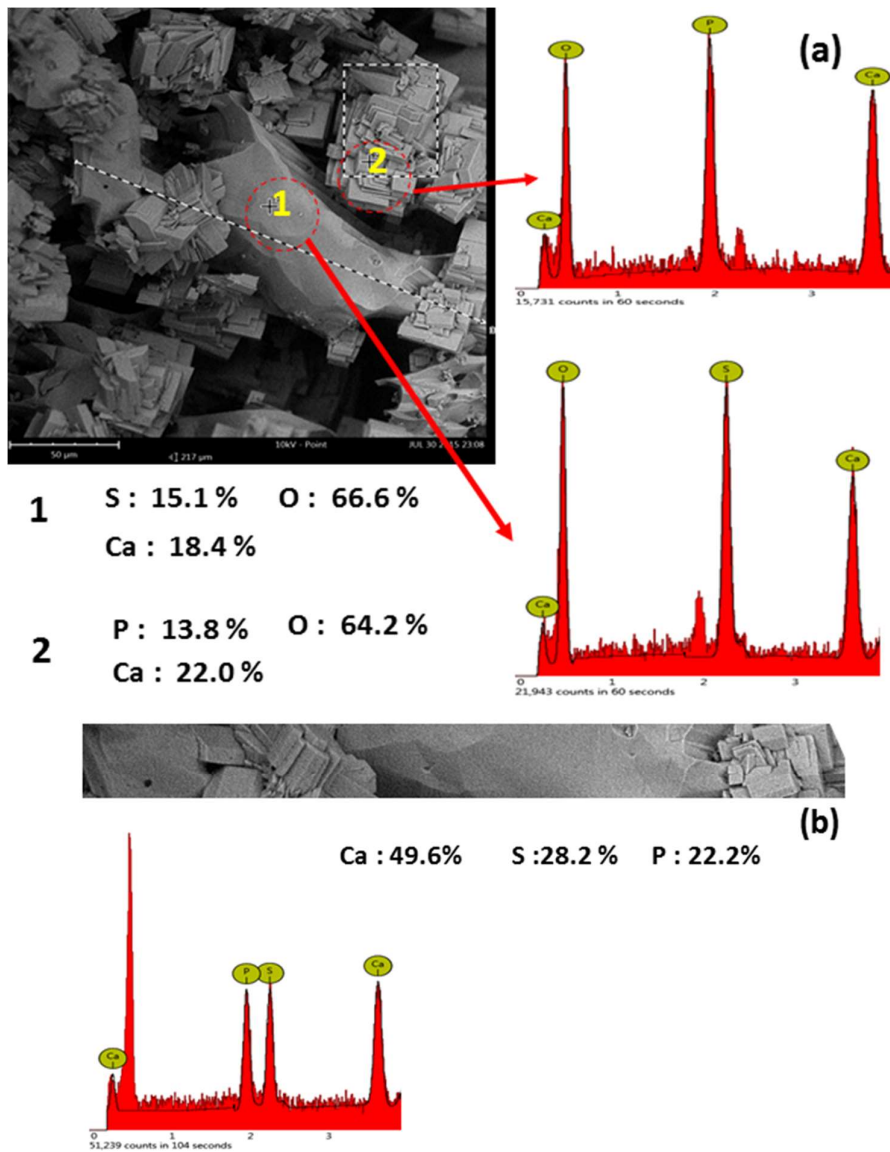


Figure 4.62: SEM-EDS (spot and line scan) analysis of the specimen heat-treated at 1250°C and phosphate-treated at 85°C for 24h.

As the reaction period was extended from 2 h to 6 h, the crystalline CP peaks became more distinct. The calcium sulfate phases, originating from the commercial ZP150 powder used in the 3D printer, were also detected; however, the detailed investigation of CS to CP conversion had been considered trivial within the general scope of the present work.

4.5.2 Mechanical features

The mechanical behaviors of the phosphate treatment scaffolds were investigated by using a universal testing instrument with compression test fixtures. The compressive tests were carried out until the sample was broken. The results of the compressive strength test and Young's modulus of samples after heat treatment at various temperatures are summarized in Table 4.12, while the trends are shown in Figure 4.63.

As the reaction period was extended for 24h, the crystalline CP peaks became more distinct and the formation of CP was more significant, so just the strain–stress curves of heat-treated scaffolds at 1150 °C, 1200 °C, 1250 °C, which underwent phosphate treatment for 24h, are shown in Figure 4.64. Ultimate compressive strength and compressive elastic modulus were calculated by using the maximum compressive stress recorded in the stress–strain curve, as well as the slope of the linear region before the yield point. The trend of compressive strength and Young's modulus change of phosphate-treated scaffolds had been roughly identical for different temperatures and time.

The compressive strengths of phosphate-treated specimens for 24h significantly increased from 0.4 MPa to 1.2 MPa and 0.1 MPa to 0.4 MPa for the samples heat-treated at 1150 °C and 1200 °C respectively and fell from 0.29 MPa to 0.19 MPa for the samples heat-treated at 1250°C. The same trend was observed for Young's modulus. The elastic modulus increased from 18.03 MPa to 65.03 MPa and 17.43 MPa to 42.03 MPa for the samples heat-treated at 1150 °C and 1200 °C respectively, but decreased from 38.45 MPa to 21.98 MPa for the samples heat-treated at 1250 °C.

Phosphate-treated scaffolds, which were heat-treated at temperatures higher than 1150 °C showed a decrease in compressive strength and Young's modulus. An extension of the plastic region was also observed, which suggested lower toughness.

Table 4.20: Results of compressive strength test, Young's modulus, and bulk density of the phosphate-treated specimens.

Samples temperature (°C)- Time(h)	Compressive strength(MPa)	Young's modulus(MPa)
1150-4	0.40	18.03
1150-8	0.63	21.76
1150-16	0.63	20.87
1150-24	1.20	65.03
1200-4	0.10	17.43
1200-8	0.20	19.74
1200-16	0.25	20.01
1200-24	0.48	42.03
1250-4	0.29	38.45
1250-8	0.18	24.03
1250-16	0.18	23.34
1250-24	0.19	21.98

However, the trend of compressive strength and Young's modulus change at the time of phosphate treatment had been roughly identical for each heat-treated specimen, although the strength values and the rates of change were noticeably greater in the samples heat-treated at 1150 °C.

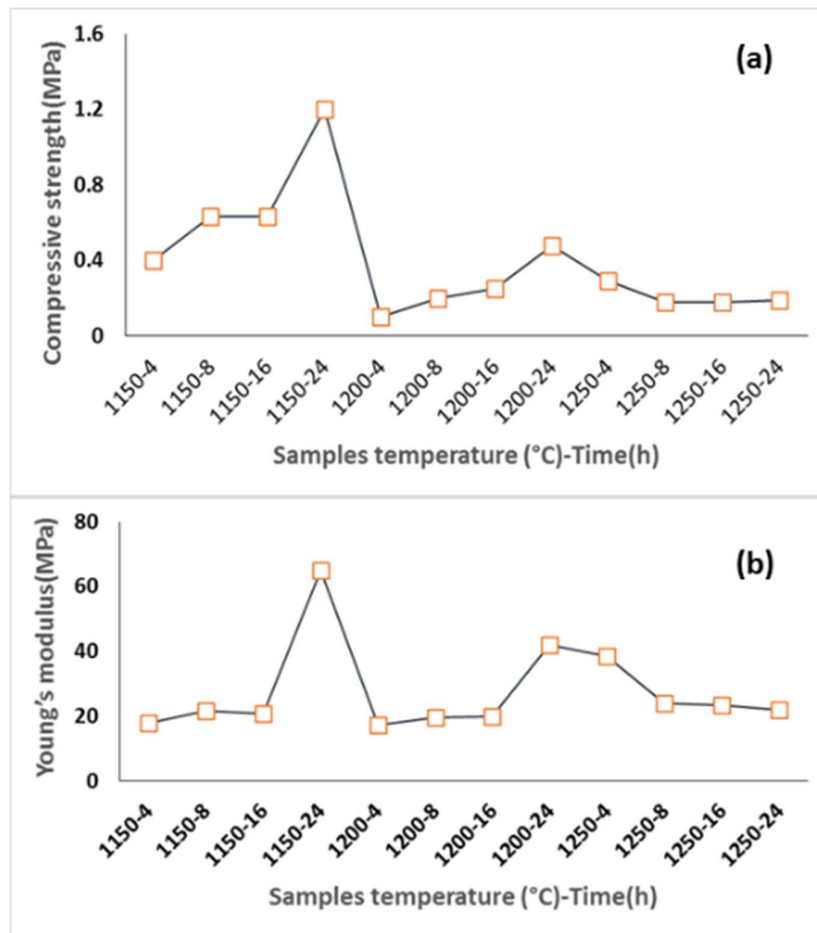


Figure 4.63: Trend of compressive strength and young's modulus of phosphate- treated samples at different temperatures and time

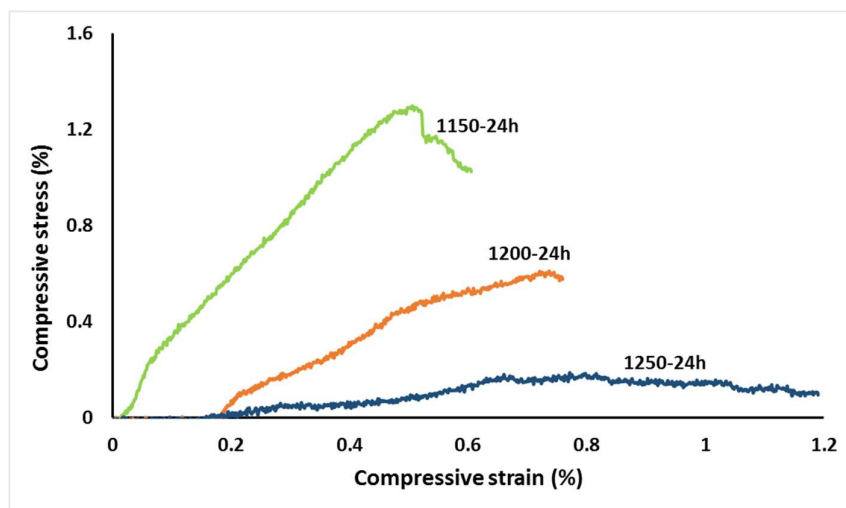


Figure 4.64: Strain-stress curve of phosphate-treated specimens at different temperatures for 24 h.

Conclusively, phosphate treatment could convert the CS heat-treated scaffolds to the CP ones and improve their compressive strength, especially in the samples heat-treated at 1150°C. However, the results of mechanical properties may not be satisfying and not in the acceptable range of BTE, but the results hinted the promising potential of phosphate treatment to improve the properties of CS 3D-printed scaffolds.

4.6 Summary

In this chapter, the results of five studies that focused on the five objectives of the thesis are discussed. First, cylindrical scaffolds were designed and fabricated with pore size: 0.8mm, and strut size 0.6mm. Besides, a full factorial DOE was used to investigate the process parameters. Optimal processing parameters are defined as those that resulted in parts best resembling the CAD model. The various measures for analyzing the part quality were percentage changes in diameters and heights, porosity, and compressive strength. Other than that, the S/N ratio and ANOVA were employed to study the optimal 3DP parameters for processing prototypes. The study outcomes showed that the specimens fabricated in the x-direction with the minimum layer thickness (89 mm) and that 300 ms delay time provided the highest quality scaffold prototypes.

Besides the cylindrical design for studying the machine parameters and optimal processing parameters, other designs were also studied in this research. To this, design maps for TPMS structures were introduced based on the computational results for biomechanical properties of 10 volume fractions of 24 different TPMS architectures. Higher specific mechanical properties were found for those architectures with lower exponential value of n , which reflected the stretching dominated architectures. In

addition, versatility of the current powder-based 3DP techniques were explored through experimental procedures.

Furthermore, the outcomes of computational models for optimum process parameters are reported in this section. The results predicted the best mechanical strength and porosity based on the setting parameters. The third contribution of the current study is that the trained model was used to precisely analyze the properties of the scaffolding procedure. The presented results and discussion can give informative information to practitioners who would want to design a porous structure, and to those in need to know the impact of influential design parameters.

Finally, the results of post-treatments, which comprised of heat treatment and phosphate treatment, are reported in this section. Heat-treatment specimens displayed significant improvement in their cytotoxicity, while phosphate-treatment procedure successfully converted the CS scaffolds to the CP ones and further improved the mechanical properties of the scaffolds.

CHAPTER 5

CONCLUSION AND FUTURE DIRECTION

Additive manufacturing (AM), especially powder-based 3DP, plays a key role in the fabrication of BTE scaffolds. Although a number of successful production experiments were conducted, the quality assessment of the fabricated parts remains to be one of the main challenges. However, not many studies have looked into mechanical properties and porosity together for the fabrication of tiny pores on scaffolds in the application of BTE. Therefore, from both the technological and the economic points of view, selecting the process parameters for the optimization of manufactured parts is highly essential. Besides, as mentioned in section 2.3, the major weakness of 3D-printed porous bio-ceramics is the relatively low mechanical performance; owing to the brittle nature of ceramic materials. Hence, usually, a post-processing treatment is employed to improve the strength of the printed objects. Therefore, the five specific goals in the current thesis were:

- i. To design a porous structure to meet BTE scaffold requirements.
- ii. To evaluate the effects of technical parameters on dimensional accuracy, mechanical properties, and porosity of the printed scaffolds.
- iii. To determine the optimum printing conditions for the designed scaffolds.
- iv. To investigate the effect of heat treatment on structural, mechanical properties, and *in vitro* behavior of 3D-printed scaffolds.

- v. To explore the influence of phosphate treatment (conversion of calcium sulfate scaffolds into calcium phosphates) on mechanical properties and morphology of 3D-printed scaffolds.

5.1 Conclusion

Accordingly, some conclusions were drawn for each specific aim:

- 1. Cylindrical calcium sulfate-based porous scaffold prototypes were successfully designed with three different pore sizes. Besides the cylindrical design, design maps for TPMS structures were introduced based on the computational results for biomechanical properties of 10 volume fractions of 24 different TPMS architectures.**

In this study, cylindrical calcium sulfate-based porous scaffold prototypes were successfully designed with three different pore sizes and fabricated with different setting parameters by using a commercial 3D printer. Besides the cylindrical design to study the machine parameters and optimal processing parameters, other designs were also studied in this research. Architectural impacts on biomechanical properties, namely Young's modulus, compressive strength, and permeability, were addressed for a library of scaffolds formed of minimal architectures to develop structure-property correlations in scaffold design procedure. Designing multifunctional scaffolds is feasible by locally controlling the biomechanical responses by changing pore architecture and/or relative density in different regions of scaffold by manipulating the equations of TPMS structures. To this, design maps for TPMS structures were introduced based on the computational results for biomechanical properties of 10 volume fractions of 24 different TPMS architectures. Other than that, convergence of voxel-based finite element solutions were studied and the required seed size for converged solution was found to be dependent on

minimum volume fraction in the structure. An approximation of deviation from converged solution was suggested with respect to the number of meshes as $Dev=57.757n-0.774$. Based on the results, when porosity is required to be fixed in scaffold, variation of mechanical properties (elastic modulus and compressive strength) versus relative density for different TPMS structures indicated those in which critical struts (regions of onset of plastic deformation) were oriented parallel to loading direction, namely P^* and $I_{xxx}-J^*$, held the greater specific properties. Although P^* was mechanically superior architecture at relative densities greater than 0.37, stress concentration at lower volume fractions diminished its preponderance and instead, $I_{xxx}-J^*$ was found to be prominent at low relative densities. When the design was implemented based on normalized stiffness, $F_{xyz}-F_{xxx2}$ structure was found to be the strongest and the most permeable at the same time for the normalized Young's modulus values of less than 0.4. Meanwhile, for the figures between 0.4 and 0.6, and greater than 0.6, IJ^*-P2 and P^* architectures were found to provide greater strength. Moreover, the highest yield strain was seen to be provided by $F_{xyz}-F_{xxx2}$ and D^* architectures for relative densities less than $\sim 35\%$, whereas IJ^*-JP2 for greater values. Taking permeability into account, $I_{xxx}-J^*$ was not only prominent in specific mechanical properties, but also showed the highest permeability of bio-fluid flow. Moreover, with the significance of deformation behavior from both biological and mechanical standpoints, the deformation mode, which can be related to relative density, had been addressed, in addition to the structure itself. Hence, mechanical efficiency was related to the contribution of bending deformation and the concept of bending versus stretching deformation was developed through scaling law analysis of elastic properties. Higher specific mechanical properties were found for those architectures with lower exponential value of n , which were referred as to stretching dominated architectures. In addition, the versatility of the current powder-based 3DP techniques was explored through experimental procedures. Cell size effect was studied for the critical geometries,

namely Ixxx-J* and Fxyz-Fxxx2. 70% of porosity in calcium sulfate scaffolds were 3D-printed and the compressive tests showed an almost 10-fold improvement in specific mechanical properties for stretching-dominated structure (Ixxx-J*) compared to the bending-dominated one (Fxyz-Fxxx2). Furthermore, scaling down the cell size caused the mechanical properties to be diminished, as they were exacerbated with the restrictions of printing delicate parts at small scales.

2. Three significant factors that affect the printing process of porous specimens, namely, layer thickness, the delay time of applying the new layer, and build orientation, which were systematically investigated in this study based on the design of experimental approach.

Three significant factors that affect the printing process of porous specimens, namely, layer thickness, delay time of applying the new layer, and build orientation, were systematically investigated in this study based on a design of experimental approach. This study revealed that fabricated scaffold prototypes with pore sizes of 0.4 and 0.6 mm deviated significantly from the CAD design on the bases of parallelism, distortion, as well as unconnected and closed pores; only prototypes with a pore size of 0.8 mm were considered for the design of experimental investigation. Besides, a full factorial DOE was used to investigate the process parameters. Optimal processing parameters are defined as those that resulted in parts best resembling the CAD model. The various measures for analyzing the part quality were percentage changes in diameters and heights, porosity, and compressive strength. Furthermore, the S/N ratio and ANOVA were used to determine the optimal 3DP parameters for processing prototypes. The study outcomes showed that the specimens fabricated in the x-direction with the minimum layer thickness (89 μ m) and that 300 ms delay time offered the highest quality scaffold prototypes.

Samples made with these parameters are deemed proper for BTE applications due to high compressive strength, sufficient porosity, and dimensional accuracy, which are the most important factors for consideration when designing a bone scaffold. Moreover, this study demonstrated that the most significant parameters that directly influenced dimensional accuracy, compressive strength, and porosity had been orientation and delay time. Furthermore, the setting time needed for both binder and powder reactions depended on the size of the layer thickness and it was indeed another factor that affected the physical properties of the part. The objective of this work was to re-tune the control factors of an existing rapid prototyping process for the given machine. These goals were achieved without any major changes in the already developed hardware and software architectures. The optimal printing parameters were developed for the material used in this study. If one were to use another material formulation, these optimal printing parameters might be inappropriate. Nevertheless, the findings obtained from this work can serve as a guideline to adjust the printing parameters for fabrication of other materials for different applications, as well as to improve the ultimate characteristics of printed scaffolds.

3. The AANN was used to investigate the simultaneous effects of layer thickness, delay time between spreading each layer, and print orientation on compressive strength and porosity of cylindrical-designed porous structure prototypes.

In this research, the AANN was used to investigate the simultaneous effects of layer thickness, delay time between spreading each layer, and print orientation on compressive strength and porosity of cylindrical-designed porous structure prototypes. Two optimization methods were applied to obtain the optimal 3D parameter settings for printing tiny porous structures as a real BTE problem. First, the PSO algorithm was

implemented to obtain the optimum topology of the AANN. Then, the Pareto front optimization was employed to determine the optimal setting parameters for the fabrication of the porous structure with high compressive strength and porosity. Other than that, the relationship between layer thickness, delay time between spreading each layer, and print orientation of powder-based 3D-printed scaffolds, as well as their compressive strength, as an index of mechanical performance and porosity are also discussed. The ANN-based model is a powerful tool to predict the compressive strength and the porosity of the 3D-printed scaffolds over a wide range of layer thicknesses, delay time of spreading each layer, and print orientations, by using a limited set of experiments designed using the full factorial design of experiments. The results predicted the best mechanical strength and porosity based on the setting parameters. The third contribution of the current study is that the trained model was used to precisely analyze the properties of the scaffolding procedure. The presented results and discussion offer informative information to practitioners who want to design a porous structure, and for those in need to know the impact of influential design parameters, e.g. layer thickness, delay time between spreading of each powder layer, and printing orientation, on the porosity and the compression strength of the porous structures.

4. The effects of heat treatment on structural, mechanical, and physical properties, as well as *in vitro* behavior of calcium sulfate prototypes fabricated by using 3DP, were investigated.

3D-printed calcium sulfate scaffolds are a promising biomaterial in BTE. However, they still require much improvement in properties in terms of BTE application requirements. A post-processing approach is usually employed to improve the physical, the chemical, and the biological properties of the 3DP scaffolds. Hence, this study

investigated the effects of heat treatment, as well as phosphate treatment, on structural, mechanical, and physical properties of calcium sulfate prototypes fabricated via 3DP. The results of different microscopy, spectroscopy, and biological characterization techniques showed that the printed scaffolds and the specimens that were heat-treated at 300°C exhibited severe cytotoxicity *in vitro*, but possessed almost adequate compressive strength. Heat treatment of the specimens at the 500°C, 900°C, and 1000°C temperature range resulted in less cytotoxic scaffolds with insufficient mechanical strength. This result was attributed to the lack of binding strength between the particles and the layers due to the exit of the organic binder before 500°C and insufficient densification below 1000°C. With progress of the sintering process at temperatures higher than 1000°C, higher compressive strength and greater viability were achieved. Moreover, the printed sample was mainly composed of the hemihydrate calcium sulfate phase. Anhydrous calcium sulfate was the only crystalline phase that existed in the samples heated at 500°C, 900°C, 1000°C, and 1150°C. Nonetheless, at temperatures higher than 1200°C, some of the calcium sulfate decomposed to calcium oxide and sulfur oxide, resulting in considerable weight loss. Furthermore, a substantial improvement in viability of the heat-treated scaffolds was observed in this study, even though the compression strength was not improved significantly compared to that of natural bone.

5. Calcium sulfate prototypes were successfully converted to calcium phosphate ones via phosphate treatment. Besides, the effects of phosphate treatment on mechanical and compositional properties of the prototypes were investigated.

Unfortunately, limitations in mechanical properties were still observed in the heat-treated scaffold, even though calcium phosphates 1) are more similar to the inorganic part of natural bone; 2) show better mechanical behavior in comparison to calcium sulfates; and 3) can be printed with commercial printers without changing the hardware of the machine

that needs a lot of customization in both powder and binder physical properties. Thus, this project had attempted to transform calcium sulfate into calcium phosphate by employing a thermo-chemical process, a second post-treatment, in order to investigate the feasibility of improving the scaffold properties to get one step closer to fulfil the BTE requirements through the use of available commercial printers and materials. Samples that were heat-treated at 1150, 1200, and 1250°C for 1h in air had enough strength to withstand the phosphatization process. The phosphate treatment of the sample was performed by soaking the printed samples and heating them at 85°C in ammonium phosphate solution for a varied time range. The transformation by treatment was examined by XRD. The microstructural features of the phosphate-treated 3DP specimens were studied by using the SEM-EDX micrographs obtained in the backscattered mode. The presence of regions of calcium phosphate was the most significant feature of the microstructure of phosphate-treated calcium sulfates. In fact, spot EDS chemical analysis confirmed the formation of calcium phosphate phases. Compressive strength and also young's modulus were improved after phosphate treatment for specimens heated at 1150 °C and phosphorized for 24 hours, even though the compression strength was not improved significantly compared to that of natural bone. Thus, limitations in mechanical properties were still present in the phosphate-treated scaffolds, which call for future studies. Nevertheless, the findings retrieved from this study offer a better insight into the complex nature of the process of fabrication pertaining to synthetic bone grafts and scaffolds via post-treatment of 3DP calcium sulfate prototypes.

5.2 Future direction

Although, this study has exhibited the great potential of powder-based 3DP in the application of BTE, still, several improvements could be made in future studies. In the optimum process optimization aspect, some of the predictive factors could be adjusted by using the 3D printer machine with some changes in both the hardware and the software of the machine, and on top of that, print objects with arbitrary properties. Besides, the TPMS models used in this thesis could be employed for MRI image of the patient's fractured bones and print the patient's specific scaffold. Nonetheless, future studies could tackle the issue concerning toxicity of the binder, as well as mixing powder with other bio-compatible powders, to improve the mechanical properties of the printed objects. Additionally, some *in vivo* tests also could be carried out on the post-treated objects, for instance, solubility, resorbability, and degradation time of the printed parts, could be further examined in the future.

REFERENCES

- Aghajani, F., Hasratiningsih, Z., & Mori, T. (2004). Gypsum-bonded investment and dental precision casting (IV) transformation of III-CaSO₄ to II-CaSO₄. *Dental materials journal*, 23(3), 373-378.
- Almeida, H. A., & Bártolo, P. J. (2014). Design of tissue engineering scaffolds based on hyperbolic surfaces: Structural numerical evaluation. *Medical engineering & physics*, 36(8), 1033-1040.
- Andreykiv, A., Prendergast, P., Van Keulen, F., Swieszkowski, W., & Rozing, P. (2005). Bone ingrowth simulation for a concept glenoid component design. *Journal of biomechanics*, 38(5), 1023-1033.
- Asadi-Eydivand, M., Solati-Hashjin, M., Farzad, A., & Abu Osman, N. A. (2016). Effect of technical parameters on porous structure and strength of 3D printed calcium sulfate prototypes. *Robotics and Computer-Integrated Manufacturing*, 37, 57-67.
- Ashby, M. (2006). The properties of foams and lattices. *Philosophical Transactions of the Royal Society of London A: Mathematical, Physical and Engineering Sciences*, 364(1838), 15-30.
- Bateman, J., Intini, G., Margarone III, J., Goodloe III, S., Bush, P., Lynch, S. E., & Dziak, R. (2005). Platelet-derived growth factor enhancement of two alloplastic bone matrices. *Journal of periodontology*, 76(11), 1833-1841.
- Bergmann, C., Lindner, M., Zhang, W., Koczur, K., Kirsten, A., Telle, R., & Fischer, H. (2010). 3D printing of bone substitute implants using calcium phosphate and bioactive glasses. *Journal of the European Ceramic Society*, 30(12), 2563-2567.
- Bernstein, A., Niemeyer, P., Salzmann, G., Südkamp, N., Hube, R., Klehm, J., . . . Görz, L. (2013). Microporous calcium phosphate ceramics as tissue engineering scaffolds for the repair of osteochondral defects: histological results. *Acta biomaterialia*, 9(7), 7490-7505.
- Bingol, O. R., & Durucan, C. (2012). Hydrothermal synthesis of hydroxyapatite from calcium sulfate hemihydrate. *Am. J. Biomed. Sci*, 4(1), 50-59.
- Blom, A. (2007). (V) Which scaffold for which application? *Current Orthopaedics*, 21(4), 280-287.
- Bohner, M., Loosli, Y., Baroud, G., & Lacroix, D. (2011). Commentary: deciphering the link between architecture and biological response of a bone graft substitute. *Acta biomaterialia*, 7(2), 478-484.
- Bose, S., Roy, M., & Bandyopadhyay, A. (2012). Recent advances in bone tissue engineering scaffolds. *Trends in Biotechnology*, 30(10), 546-554.

- Bose, S., Vahabzadeh, S., & Bandyopadhyay, A. (2013a). Bone tissue engineering using 3D printing. *Materials Today*, *16*(12), 496–504.
- Bose, S., Vahabzadeh, S., & Bandyopadhyay, A. (2013b). Bone tissue engineering using 3D printing. *Materials Today*, *16*(12), 496-504.
- Brand, R. A. (2012). 50 Years Ago in CORR: The Use of Plaster of Paris to Fill Defects in Bone Leonard F. Peltier, MD CORR 1961;21:1–31. *Clinical Orthopaedics and Related Research*, *470*(12), 3628-3629. doi:10.1007/s11999-012-2571-5
- Bulstrode, C., Buckwalter, J., Carr, A., Marsh, L., Fairbank, J. C. T., Wilson-MacDonald, J., & Bowden, G. (2002). *Oxford textbook of orthopedics and trauma*: Oxford University Press Oxford New York.
- Burg, K. J., Porter, S., & Kellam, J. F. (2000). Biomaterial developments for bone tissue engineering. *Biomaterials*, *21*(23), 2347-2359.
- Butscher, A., Bohner, M., Doebelin, N., Galea, L., Loeffel, O., & Müller, R. (2012). Moisture based three-dimensional printing of calcium phosphate structures for scaffold engineering. *Acta biomaterialia*, *9*(2): 5369-5378.
- Butscher, A., Bohner, M., Doebelin, N., Hofmann, S., & Müller, R. (2013). New depowdering-friendly designs for three-dimensional printing of calcium phosphate bone substitutes. *Acta biomaterialia*, *9*(11), 9149-9158.
- Butscher, A., Bohner, M., Hofmann, S., Gauckler, L., & Müller, R. (2011). Structural and material approaches to bone tissue engineering in powder-based three-dimensional printing. *Acta biomaterialia*, *7*(3), 907-920.
- Butscher, A., Bohner, M., Roth, C., Ernstberger, A., Heuberger, R., Doebelin, N., . . . Müller, R. (2012). Printability of calcium phosphate powders for three-dimensional printing of tissue engineering scaffolds. *Acta biomaterialia*, *8*(1), 373-385.
- Cao, M., & Qiao, P. (2008). Neural network committee-based sensitivity analysis strategy for geotechnical engineering problems. *Neural Computing and Applications*, *17*(5-6), 509-519.
- Cao, M., Qiao, P., & Ren, Q. (2009). Improved hybrid wavelet neural network methodology for time-varying behavior prediction of engineering structures. *Neural Computing and Applications*, *18*(7), 821-832.
- Castilho, M., Dias, M., Gbureck, U., Groll, J., Fernandes, P., Pires, I., . . . Vorndran, E. (2013). Fabrication of computationally designed scaffolds by low temperature 3D printing. *Biofabrication*, *5*(3), 035012.
- Castilho, M., Moseke, C., Ewald, A., Gbureck, U., Groll, J., Pires, I., . . . Vorndran, E. (2014). Direct 3D powder printing of biphasic calcium phosphate scaffolds for substitution of complex bone defects. *Biofabrication*, *6*(1), 015006.

- Castilho, M., Pires, I., Gouveia, B., & Rodrigues, J. (2011). Structural evaluation of scaffolds prototypes produced by three-dimensional printing. *The International Journal of Advanced Manufacturing Technology*, 56(5-8), 561-569.
- Chan, B., & Leong, K. (2008). Scaffolding in tissue engineering: general approaches and tissue-specific considerations. *European spine journal*, 17(4), 467-479.
- Chaturvedi, D. K. (2008). *Soft Computing: Techniques and its Applications in Electrical Engineering*: Springer-Verlag Berlin Heidelberg v(103), p 612.
- Chen, A. A., Tsang, V. L., Albrecht, D. R., & Bhatia, S. N. (2007). 3-D fabrication technology for tissue engineering *BioMEMS and Biomedical Nanotechnology* (pp. 23-38): Springer.
- Chia, H. N., & Wu, B. M. (2015). Recent advances in 3D printing of biomaterials. *Journal of biological engineering*, 9(1), 4.
- Chumnanklang, R., Panyathanmaporn, T., Sitthiseripratip, K., & Suwanprateeb, J. (2007). 3D printing of hydroxyapatite: Effect of binder concentration in pre-coated particle on part strength. *Materials Science and Engineering: C*, 27(4), 914-921.
- Costa-Pinto, A. R., Reis, R. L., & Neves, N. M. (2011). Scaffolds based bone tissue engineering: the role of chitosan. *Tissue Engineering Part B: Reviews*, 17(5), 331-347.
- Cox, S. C., Thornby, J. A., Gibbons, G. J., Williams, M. A., & Mallick, K. K. (2015). 3D printing of porous hydroxyapatite scaffolds intended for use in bone tissue engineering applications. *Materials Science and Engineering: C*, 47, 237-247.
- Danilevicius, P., Georgiadi, L., Pateman, C. J., Claeysens, F., Chatzinikolaidou, M., & Farsari, M. (2015). The effect of porosity on cell ingrowth into accurately defined, laser-made, polylactide-based 3D scaffolds. *Applied Surface Science*, 336, 2-10.
- Datta, H., Ng, W., Walker, J., Tuck, S., & Varanasi, S. (2008). The cell biology of bone metabolism. *Journal of clinical pathology*, 61(5), 577-587.
- Dias, M., Fernandes, P., Guedes, J., & Hollister, S. (2012). Permeability analysis of scaffolds for bone tissue engineering. *Journal of biomechanics*, 45(6), 938-944.
- Dias, M. R., Fernandes, P. R., Guedes, J. M., & Hollister, S. J. (2012). Permeability analysis of scaffolds for bone tissue engineering. *J Biomech*, 45(6), 938-944.
- Dias, M. R., Guedes, J. M., Flanagan, C. L., Hollister, S. J., & Fernandes, P. R. (2014). Optimization of scaffold design for bone tissue engineering: a computational and experimental study. *Medical engineering & physics*, 36(4), 448-457.
- Doty, H. A., Leedy, M. R., Courtney, H. S., Haggard, W. O., & Bumgardner, J. D. (2014). Composite chitosan and calcium sulfate scaffold for dual delivery of vancomycin and recombinant human bone morphogenetic protein-2. *Journal of Materials Science: Materials in Medicine*, 25(6), 1449-1459.

- Eberhart, R. C., & Kennedy, J. (1995). *A new optimizer using particle swarm theory*. Paper presented at the Proceedings of the sixth international symposium on micro machine and human science (Vol. 1, pp. 39-43).
- Farzadi, A., Solati-Hashjin, M., Asadi-Eydivand, M., & Osman, N. A. A. (2014). Effect of Layer Thickness and Printing Orientation on Mechanical Properties and Dimensional Accuracy of 3D Printed Porous Samples for Bone Tissue Engineering. *PloS one*, *9*(9), e108252.
- Fathi, A., & Mozaffari, A. (2013). Identification of a dynamic model for shape memory alloy actuator using Hammerstein-Wiener Gray Box and Mutable Smart Bee Algorithm. *International Journal of Intelligent computing and Cybernetics*, *6*(4), 328-357.
- Feng, P., Meng, X., Chen, J.-F., & Ye, L. (2015). Mechanical properties of structures 3D printed with cementitious powders. *Construction and Building Materials*, *93*, 486-497.
- Fereshteh, Z., Nooeaid, P., Fathi, M., Bagri, A., & Boccaccini, A. R. (2015). The effect of coating type on mechanical properties and controlled drug release of PCL/zein coated 45S5 bioactive glass scaffolds for bone tissue engineering. *Materials Science and Engineering: C*, *54*, 50-60.
- Frascati, J. (2007). *Effects of position, orientation, and infiltrating material on three dimensional printing models*. University of Central Florida Orlando, Florida (Thesis) P 17-19 .
- Furth, M. E., Atala, A., & Van Dyke, M. E. (2007). Smart biomaterials design for tissue engineering and regenerative medicine. *Biomaterials*, *28*(34), 5068-5073.
- Furtuna, R., Curteanu, S., & Cazacu, M. (2011). Optimization methodology applied to feed-forward artificial neural network parameters. *International Journal of Quantum Chemistry*, *111*(3), 539-553.
- Furtuna, R., Curteanu, S., & Leon, F. (2012). Multi-objective optimization of a stacked neural network using an evolutionary hyper-heuristic. *Applied Soft Computing*, *12*(1), 133-144.
- Gbureck, U., Hölzel, T., Klammert, U., Würzler, K., Müller, F. A., & Barralet, J. E. (2007). Resorbable dicalcium phosphate bone substitutes prepared by 3D powder printing. *Advanced Functional Materials*, *17*(18), 3940-3945.
- Gentile, P., Chiono, V., Carmagnola, I., & Hatton, P. V. (2014). An overview of poly (lactic-co-glycolic) acid (PLGA)-based biomaterials for bone tissue engineering. *International journal of molecular sciences*, *15*(3), 3640-3659.
- Gomes, M. E., Holtorf, H. L., Reis, R. L., & Mikos, A. G. (2006). Influence of the porosity of starch-based fiber mesh scaffolds on the proliferation and osteogenic differentiation of bone marrow stromal cells cultured in a flow perfusion bioreactor. *Tissue engineering*, *12*(4), 801-809.
- Granitto, P. M., Verdes, P. F., Navone, H. D., & Ceccatto, H. A. (2002, 2002). *Aggregation algorithms for neural network ensemble construction*. Paper presented at the Neural Networks, 2002. SBRN 2002. Proceedings. VII Brazilian Symposium on.

- Guo, B., Lei, B., Li, P., & Ma, P. X. (2015). Functionalized scaffolds to enhance tissue regeneration. *Regenerative biomaterials*, 2(1), 47-57.
- Han, L.-H., Lai, J. H., Yu, S., & Yang, F. (2013). Dynamic tissue engineering scaffolds with stimuli-responsive macroporosity formation. *Biomaterials*, 34(17), 4251-4258.
- Henkel, J., Woodruff, M. A., Epari, D. R., Steck, R., Glatt, V., Dickinson, I. C., . . . Hutmacher, D. W. (2013). Bone regeneration based on tissue engineering conceptions—a 21st century perspective. *Bone research*, 1(3), 216.
- Ho, S. T., & Hutmacher, D. W. (2006). A comparison of micro CT with other techniques used in the characterization of scaffolds. *Biomaterials*, 27(8), 1362-1376.
- Hollinger (2011). An Introduction to Biomaterials CRC Press, ISBN 0-8493-2282-0.. 64(3), 399–399.
- Hollister, S., Maddox, R., & Taboas, J. (2002). Optimal design and fabrication of scaffolds to mimic tissue properties and satisfy biological constraints. *Biomaterials*, 23(20), 4095-4103.
- Hollister, S. J., Lin, C., Saito, E., Schek, R., Taboas, J., Williams, J., . . . Wilke, E. (2005). Engineering craniofacial scaffolds. *Orthodontics & craniofacial research*, 8(3), 162-173.
- Hoyt, A. J., Yakacki, C. M., Fertig, R. S., Carpenter, R. D., & Frick, C. P. (2015). Monotonic and cyclic loading behavior of porous scaffolds made from poly (para-phenylene) for orthopedic applications. *Journal of the mechanical behavior of biomedical materials*, 41, 136-148.
- Hsu, T. J., & Lai, W. H. (2010). Manufacturing parts optimization in the three-dimensional printing process by the Taguchi method. *Journal of the Chinese Institute of Engineers*, 33(1), 121-130.
- Huang, S. H., & Hong-Chao, Z. (1993, 4-6 Oct 1993). *Neural networks in manufacturing: A survey*. Paper presented at the Electronic Manufacturing Technology Symposium, 1993, Fifteenth IEEE/CHMT International.
- Hutmacher, D. W. (2000). Scaffolds in tissue engineering bone and cartilage. *Biomaterials*, 21(24), 2529-2543.
- Impens, D. (2015). An Experimental Approach to Assess the Impact of Post Processing Variables on the Mechanical Characteristics of 3D Printed (Powder Binding Process) Parts.
- Insights, P. (2013) Bone Regeneration With Calcium sulfate Platelet Rich Plasma & Immediate Implant Placement in Lower Jaw 4(3), 78–81 .
- Jamshidinia, M., Wang, L., Tong, W., & Kovacevic, R. (2014). The bio-compatible dental implant designed by using non-stochastic porosity produced by Electron Beam Melting®(EBM). *Journal of Materials Processing Technology*, 214(8), 1728-1739.

- Ji, C., Khademhosseini, A., & Dehghani, F. (2011). Enhancing cell penetration and proliferation in chitosan hydrogels for tissue engineering applications. *Biomaterials*, 32(36), 9719-9729.
- Johnell, O., & Kanis, J. (2006). An estimate of the worldwide prevalence and disability associated with osteoporotic fractures. *Osteoporosis International*, 17(12), 1726-1733.
- Kadkhodapour, J., Montazerian, H., & Raeisi, S. (2014). Investigating internal architecture effect in plastic deformation and failure for TPMS-based scaffolds using simulation methods and experimental procedure. *Materials Science and Engineering: C*, 43, 587-597.
- Kameda, T., Mano, H., Yamada, Y., Takai, H., Amizuka, N., Kobori, M., . . . Ikeda, K. (1998). Calcium-sensing receptor in mature osteoclasts, which are bone resorbing cells. *Biochemical and biophysical research communications*, 245(2), 419-422.
- Kapfer, S. C., Hyde, S. T., Mecke, K., Arns, C. H., & Schröder-Turk, G. E. (2011). Minimal surface scaffold designs for tissue engineering. *Biomaterials*, 32(29), 6875-6882.
- Kar, S., Das, S., & Ghosh, P. K. (2014). Applications of neuro fuzzy systems: A brief review and future outline. *Applied Soft Computing*, 15, 243-259.
- Karageorgiou, V., & Kaplan, D. (2005). Porosity of 3D biomaterial scaffolds and osteogenesis. *Biomaterials*, 26(27), 5474-5491.
- Karande, T. S., Ong, J. L., & Agrawal, C. M. (2004). Diffusion in musculoskeletal tissue engineering scaffolds: design issues related to porosity, permeability, architecture, and nutrient mixing. *Annals of biomedical engineering*, 32(12), 1728-1743.
- Kassim, B., Ivanovski, S., & Mattheos, N. (2014). Current perspectives on the role of ridge (socket) preservation procedures in dental implant treatment in the aesthetic zone. *Australian dental journal*, 59(1), 48-56.
- Khalyfa, A., Vogt, S., Weisser, J., Grimm, G., Rechtenbach, A., Meyer, W., & Schnabelrauch, M. (2007). Development of a new calcium phosphate powder-binder system for the 3D printing of patient specific implants. *Journal of Materials Science: Materials in Medicine*, 18(5), 909-916.
- Kim, Y.-H. (2005). Long-term results of the cementless porous-coated anatomic total hip prosthesis. *Journal of Bone & Joint Surgery, British Volume*, 87(5), 623-627.
- Klammert, U., Gbureck, U., Vorndran, E., Rödiger, J., Meyer-Marcotty, P., & Kübler, A. C. (2010). 3D powder printed calcium phosphate implants for reconstruction of cranial and maxillofacial defects. *Journal of Cranio-Maxillofacial Surgery*, 38(8), 565-570.
- Krishnan, S., Dawood, A., Richards, R., Henckel, J., & Hart, A. (2012). A review of rapid prototyped surgical guides for patient-specific total knee replacement. *Journal of Bone & Joint Surgery, British Volume*, 94(11), 1457-1461.

- Lam, C. X. F., Mo, X., Teoh, S.-H., & Hutmacher, D. (2002). Scaffold development using 3D printing with a starch-based polymer. *Materials Science and Engineering: C*, 20(1), 49-56.
- Lee, J. J., Lee, J. W., Yi, J. H., Yun, C. B., & Jung, H. Y. (2005). Neural networks-based damage detection for bridges considering errors in baseline finite element models. *Journal of Sound and Vibration*, 280(3), 555-578.
- Lee, M., & Wu, B. M. (2012). Recent advances in 3D printing of tissue engineering scaffolds *Computer-Aided Tissue Engineering* (pp. 257-267): Springer.
- Leong, K., Cheah, C., & Chua, C. (2003). Solid freeform fabrication of three-dimensional scaffolds for engineering replacement tissues and organs. *Biomaterials*, 24(13), 2363-2378.
- Leong, K., Chua, C., Sudarmadji, N., & Yeong, W. (2008). Engineering functionally graded tissue engineering scaffolds. *Journal of the mechanical behavior of biomedical materials*, 1(2), 140-152.
- Lichte, P., Pape, H., Pufe, T., Kobbe, P., & Fischer, H. (2011). Scaffolds for bone healing: concepts, materials and evidence. *Injury*, 42(6), 569-573.
- Lien, S.-M., Ko, L.-Y., & Huang, T.-J. (2009). Effect of pore size on ECM secretion and cell growth in gelatin scaffold for articular cartilage tissue engineering. *Acta biomaterialia*, 5(2), 670-679.
- Lin, C. Y., Kikuchi, N., & Hollister, S. J. (2004). A novel method for biomaterial scaffold internal architecture design to match bone elastic properties with desired porosity. *Journal of biomechanics*, 37(5), 623-636.
- Liu, C., Xia, Z., & Czernuszka, J. (2007). Design and development of three-dimensional scaffolds for tissue engineering. *Chemical Engineering Research and Design*, 85(7), 1051-1064.
- Lowmunkong, R., Sohmura, T., Suzuki, Y., Matsuya, S., & Ishikawa, K. (2009). Fabrication of freeform bone-filling calcium phosphate ceramics by gypsum 3D printing method. *Journal of Biomedical Materials Research Part B: Applied Biomaterials*, 90(2), 531-539.
- Mann, K. A., & Damron, L. A. (2002). Predicting the failure response of cement-bone constructs using a non-linear fracture mechanics approach. *Journal of biomechanical engineering*, 124(4), 462-470.
- Mazzoli, A., Ferretti, C., Gigante, A., Salvolini, E., & Mattioli-Belmonte, M. (2015). Selective laser sintering manufacturing of polycaprolactone bone scaffolds for applications in bone tissue engineering. *Rapid Prototyping Journal*, 21(4), 386-392.
- Melchels, F. P., Barradas, A. M., Van Blitterswijk, C. A., De Boer, J., Feijen, J., & Grijpma, D. W. (2010). Effects of the architecture of tissue engineering scaffolds on cell seeding and culturing. *Acta biomaterialia*, 6(11), 4208-4217.

- Mirhassani, S. M., Zourmand, A., & Ting, H.-N. (2014). Age Estimation Based on Children's Voice: A Fuzzy-Based Decision Fusion Strategy. *The Scientific World Journal*, 2014 1–9.
- Mitsak, A. G., Kemppainen, J. M., Harris, M. T., & Hollister, S. J. (2011). Effect of polycaprolactone scaffold permeability on bone regeneration in vivo. *Tissue Engineering Part A*, 17(13-14), 1831-1839.
- Moore, W. R., Graves, S. E., & Bain, G. I. (2001). Synthetic bone graft substitutes. *ANZ journal of surgery*, 71(6), 354-361.
- Mozaffari, A., Fathi, A., Khajepour, A., & Toyserkani, E. (2013). Optimal design of laser solid freeform fabrication system and real-time prediction of melt pool geometry using intelligent evolutionary algorithms. *Applied Soft Computing*, 13(3), 1505-1519.
- Munch, E., Franco, J., Deville, S., Hunger, P., Saiz, E., & Tomsia, A. (2008). Porous ceramic scaffolds with complex architectures. *JOM*, 60(6), 54-58.
- Murphy, C. M., Haugh, M. G., & O'Brien, F. J. (2010). The effect of mean pore size on cell attachment, proliferation and migration in collagen–glycosaminoglycan scaffolds for bone tissue engineering. *Biomaterials*, 31(3), 461-466.
- Nair, M. B., Varma, H., Mohanan, P., & John, A. (2011). Tissue-engineered triphasic ceramic coated hydroxyapatite induced bone formation and vascularization at an extraskeletal site in a rat model. *Bulletin of Materials Science*, 34(7), 1721-1731.
- Nelles, O. (2013). *Nonlinear system identification: from classical approaches to neural networks and fuzzy models*: Springer Science & Business Media 104–143.
- Ni, Y., Zhou, X., & Ko, J. (2006). Experimental investigation of seismic damage identification using PCA-compressed frequency response functions and neural networks. *Journal of Sound and Vibration*, 290(1), 242-263.
- Nyan, M., Sato, D., Oda, M., Machida, T., Kobayashi, H., Nakamura, T., & Kasugai, S. (2007). Bone formation with the combination of simvastatin and calcium sulfate in critical-sized rat calvarial defect. *Journal of pharmacological sciences*, 104(4), 384-386.
- Olivares, A. L., Marsal, È., Planell, J. A., & Lacroix, D. (2009). Finite element study of scaffold architecture design and culture conditions for tissue engineering. *Biomaterials*, 30(30), 6142-6149.
- Palaniappan, R., & Paramesran, R. (2002). Using genetic algorithm to identify the discriminatory subset of multi-channel spectral bands for visual response. *Applied Soft Computing*, 2(1), 48-60.
- Park, Y. B., Mohan, K., Al-Sanousi, A., Almaghrabi, B., Genco, R. J., Swihart, M. T., & Dziak, R. (2011). Synthesis and characterization of nanocrystalline calcium sulfate for use in osseous regeneration. *Biomedical Materials*, 6(5), 055007.

- Patirupanusara, P., Suwanpreuk, W., Rubkumintara, T., & Suwanprateeb, J. (2008). Effect of binder content on the material properties of polymethyl methacrylate fabricated by three dimensional printing technique. *Journal of Materials Processing Technology*, 207(1), 40-45.
- Pattanayak, D. K., Dash, R., Prasad, R., Rao, B., & Mohan, T. R. (2007). Synthesis and sintered properties evaluation of calcium phosphate ceramics. *Materials Science and Engineering: C*, 27(4), 684-690.
- Peel, N. (2012). Disorders of bone metabolism. *Surgery (Oxford)*, 30(2), 61-66.
- Peltier, L. F., Bickel, E. Y., Lillo, R., & Thein, M. S. (1957). The use of plaster of Paris to fill defects in bone. *Annals of surgery*, 146(1), 61.
- Pérez, M., García, J., & Doblaré, M. (2005). Analysis of the debonding of the stem–cement interface in intramedullary fixation using a non-linear fracture mechanics approach. *Engineering fracture mechanics*, 72(8), 1125-1147.
- Pina, S., Oliveira, J. M., & Reis, R. L. (2015). Natural-Based Nanocomposites for Bone Tissue Engineering and Regenerative Medicine: A Review. *Advanced Materials*, 27(7), 1143-1169.
- Polo-Corrales, L., Latorre-Esteves, M., & Ramirez-Vick, J. E. (2014). Scaffold design for bone regeneration. *Journal of nanoscience and nanotechnology*, 14(1), 15.
- Quinn, G. P., & Keough, M. J. (2002). *Experimental design and data analysis for biologists*: Cambridge University Press ISBN 0 521 81128 7 P 35-87.
- Rahmani-Monfared, K., Mozaffari, A., Rabiee, M., & Fathi, A. (2012). Application of self-learning evolutionary algorithm for optimal design of a porous PMMA scaffold fabricated by Laser drilling process. *Proceedings of the Institution of Mechanical Engineers, Part E: Journal of Process Mechanical Engineering*, 227(3), 211–224
- Rajagopalan, S., & Robb, R. A. (2006). Schwarz meets Schwann: design and fabrication of biomorphic and durataxic tissue engineering scaffolds. *Medical Image Analysis*, 10(5), 693-712.
- Rajzer, I., Menaszek, E., Kwiatkowski, R., Planell, J. A., & Castano, O. (2014). Electrospun gelatin/poly (ϵ -caprolactone) fibrous scaffold modified with calcium phosphate for bone tissue engineering. *Materials Science and Engineering: C*, 44, 183-190.
- Rauschmann, M., Vogl, T., Verheyden, A., Pflugmacher, R., Werba, T., Schmidt, S., & Hierholzer, J. (2010). Bioceramic vertebral augmentation with a calcium sulphate/hydroxyapatite composite (Cerament™ SpineSupport) in vertebral compression fractures due to osteoporosis. *European Spine Journal*, 19(6), 887-892.
- Rauschmann, M. A., Wichelhaus, T. A., Stirnal, V., Dingeldein, E., Zichner, L., Schnettler, R., & Alt, V. (2005). Nanocrystalline hydroxyapatite and calcium sulphate as biodegradable

composite carrier material for local delivery of antibiotics in bone infections. *Biomaterials*, 26(15), 2677-2684.

Rose, F. R., Cyster, L. A., Grant, D. M., Scotchford, C. A., Howdle, S. M., & Shakesheff, K. M. (2004). In vitro assessment of cell penetration into porous hydroxyapatite scaffolds with a central aligned channel. *Biomaterials*, 25(24), 5507-5514.

Sachs, E., Cima, M., Williams, P., Brancazio, D., & Cornie, J. (1992). Three dimensional printing: rapid tooling and prototypes directly from a CAD model. *Journal of Manufacturing Science and Engineering*, 114(4), 481-488.

Sadeghpour, S., Amirjani, A., Hafezi, M., & Zamanian, A. (2014). Fabrication of a novel nanostructured calcium zirconium silicate scaffolds prepared by a freeze-casting method for bone tissue engineering. *Ceramics International*, 40(10), 16107-16114.

Sadiasa, A., Nguyen, T. H., & Lee, B.-T. (2013). In vitro and in vivo evaluation of porous PCL-PLLA 3D polymer scaffolds fabricated via salt leaching method for bone tissue engineering applications. *Journal of Biomaterials Science, Polymer Edition*, 25(2), 150-167.

Salgado, A. J., Coutinho, O. P., & Reis, R. L. (2004). Bone tissue engineering: state of the art and future trends. *Macromolecular bioscience*, 4(8), 743-765.

Sandino, C., Krolczek, P., McErlain, D. D., & Boyd, S. K. (2014). Predicting the permeability of trabecular bone by micro-computed tomography and finite element modeling. *Journal of biomechanics*, 47(12), 3129-3134.

Shen, Y., Yang, S., Liu, J., Xu, H., Shi, Z., Lin, Z., Yan, S. (2014). Engineering Scaffolds Integrated with Calcium Sulfate and Oyster Shell for Enhanced Bone Tissue Regeneration. *ACS applied materials & interfaces*, 6(15), 12177-12188.

Sottosanti, J. (1992). Calcium sulfate: a biodegradable and biocompatible barrier for guided tissue regeneration. *Compendium (Newtown, Pa.)*, 13(3), 226-228, 230, 232-224.

Spears, I. R., Pfliegerer, M., Schneider, E., Hille, E., Bergmann, G., & Morlock, M. M. (2000). Interfacial conditions between a press-fit acetabular cup and bone during daily activities: implications for achieving bone in-growth. *Journal of biomechanics*, 33(11), 1471-1477.

Stolk, J., Verdonchot, N., & Huiskes, R. (2001). Hip-joint and abductor-muscle forces adequately represent in vivo loading of a cemented total hip reconstruction. *Journal of biomechanics*, 34(7), 917-926.

Streubel, P. N., Ricci, W. M., Wong, A., & Gardner, M. J. (2011). Mortality after distal femur fractures in elderly patients. *Clinical Orthopaedics and Related Research®*, 469(4), 1188-1196.

Suwanprateeb, J., Sangam, R., & Panyathanmaporn, T. (2010). Influence of raw powder preparation routes on properties of hydroxyapatite fabricated by 3D printing technique. *Materials Science and Engineering: C*, 30(4), 610-617.

- Suwanprateeb, J., Suvannapruk, W., & Wasoontarat, K. (2010). Low temperature preparation of calcium phosphate structure via phosphorization of 3D-printed calcium sulfate hemihydrate based material. *Journal of Materials Science: Materials in Medicine*, 21(2), 419-429.
- Suwanprateeb, J., Thammarakcharoen, F., Wasoontarat, K., & Suvannapruk, W. (2012). Influence of printing parameters on the transformation efficiency of 3D-printed plaster of paris to hydroxyapatite and its properties. *Rapid Prototyping Journal*, 18(6), 490-499.
- Swift, W., Panek, A., Smith, G., Vogel, G., & Jonke, A. (1976). *Decomposition of calcium sulfate: a review of the literature.*[62 refs] P 61-75.
- Syahrom, A., Kadir, M. R. A., Abdullah, J., & Öchsner, A. (2013). Permeability studies of artificial and natural cancellous bone structures. *Medical engineering & physics*, 35(6), 792-799.
- Tay, B. K., Patel, V. V., & Bradford, D. S. (1999). CALCIUM SULFATE–AND CALCIUM PHOSPHATE–BASED BONE SUBSTITUTES: Mimicry of the Mineral Phase of Bone. *Orthopedic Clinics of North America*, 30(4), 615-623.
- National Institute of Standards and Technology, N. I. o. S. a. (2011a). 2-pyrrolidinone Infrared Spectrum. <http://webbook.nist.gov/cgi/cbook.cgi?ID=C616455&Mask=80>
- National Institute of Standards and Technology, N. I. o. S. a. (2011b). Water Infrared Spectrum. <http://webbook.nist.gov/cgi/cbook.cgi?ID=C7732185&Type=IR-SPEC&Index=1#IR-SPEC>
- Thomas, M. V., & Puleo, D. A. (2009). Calcium sulfate: Properties and clinical applications. *Journal of Biomedical Materials Research Part B: Applied Biomaterials*, 88B(2), 597-610.
- Thomas, M. V., Puleo, D. A., & Al-Sabbagh, M. (2005). Calcium sulfate: a review. *Journal of long-term effects of medical implants*, 15(6).
- Ting, H.-N., Yong, B.-F., & Mirhassani, S. M. (2013). Self-adjustable neural network for speech recognition. *Engineering Applications of Artificial Intelligence*, 26(9), 2022-2027.
- Trdnost, Modelov, T. T. (2013). Influence of processing factors on the tensile strength of 3d-printed models. *Materiali in tehnologije*, 47(6), 781-788.
- Truscello, S., Kerckhofs, G., Van Bael, S., Pyka, G., Schrooten, J., & Van Oosterwyck, H. (2012). Prediction of permeability of regular scaffolds for skeletal tissue engineering: a combined computational and experimental study. *Acta biomaterialia*, 8(4), 1648-1658.
- Utela, B., Storti, D., Anderson, R., & Ganter, M. (2008). A review of process development steps for new material systems in three dimensional printing (3DP). *Journal of Manufacturing Processes*, 10(2), 96-104.

- Vaezi, M., & Chua, C. K. (2011). Effects of layer thickness and binder saturation level parameters on 3D printing process. *The International Journal of Advanced Manufacturing Technology*, 53(1-4), 275-284.
- Vallet-Regi, M., & González-Calbet, J. M. (2004). Calcium phosphates as substitution of bone tissues. *Progress in Solid State Chemistry*, 32(1), 1-31.
- van Lenthe, G. H., Hagenmüller, H., Bohner, M., Hollister, S. J., Meinel, L., & Müller, R. (2007). Nondestructive micro-computed tomography for biological imaging and quantification of scaffold–bone interaction in vivo. *Biomaterials*, 28(15), 2479-2490.
- Viana, T., Biscaia, S., Almeida, H. A., & Bártolo, P. J. (2013). Permeability Evaluation of Lay-down Patterns and Pore Size of Pcl Scaffolds. *Procedia Engineering*, 59, 255-262. doi:10.1016/j.proeng.2013.05.119
- Vivanco, J., Aiyangar, A., Araneda, A., & Ploeg, H.-L. (2012). Mechanical characterization of injection-molded macro porous bioceramic bone scaffolds. *Journal of the mechanical behavior of biomedical materials*, 9, 137-152.
- Vorndran, E., Moseke, C., & Gbureck, U. (2015). 3D printing of ceramic implants. *MRS Bulletin*, 40(02), 127-136.
- Vorndran, E., Wunder, K., Moseke, C., Biermann, I., Müller, F. A., Zorn, K., & Gbureck, U. (2011). Hydraulic setting Mg₃(PO₄)₂ powders for 3D printing technology. *Advances in Applied Ceramics*, 110(8), 476-481.
- Voronov, R., VanGordon, S., Sikavitsas, V. I., & Papavassiliou, D. V. (2010). Computational modeling of flow-induced shear stresses within 3D salt-leached porous scaffolds imaged via micro-CT. *Journal of biomechanics*, 43(7), 1279-1286.
- Wang, Y. (2008). Degree elevation and reduction of periodic surfaces. *Computer-Aided Design and Applications*, 5(6), 841-854.
- Widmer, R. P., & Ferguson, S. J. (2013). On the interrelationship of permeability and structural parameters of vertebral trabecular bone: a parametric computational study. *Computer methods in biomechanics and biomedical engineering*, 16(8), 908-922.
- Will, J., Detsch, R., & Boccaccini, A. (2013). Structural and Biological Characterization of Scaffolds. In A. Bandyopadhyay & S. Bose (Eds.), *Characterization of Biomaterials* (pp. 299-310). Oxford: Academic Press: Oxford: Academic Press.
- Wismer, N., Grad, S., Fortunato, G., Ferguson, S. J., Alini, M., & Eglin, D. (2014). Biodegradable electrospun scaffolds for annulus fibrosus tissue engineering: effect of scaffold structure and composition on annulus fibrosus cells in vitro. *Tissue Engineering Part A*, 20(3-4), 672-682.
- Withell, A., Diegel, O., Grupp, I., Reay, S., de Beer, D., & Potgieter, J. (2011). *Porous ceramic filters through 3D printing*. Paper presented at the Innovative Developments in Virtual and Physical Prototyping: Proceedings of the 5th International Conference on Advanced

Research in Virtual and Rapid Prototyping, Leiria, Portugal, 28 September-1 October, 2011

- Wu, S., Liu, X., Yeung, K. W., Liu, C., & Yang, X. (2014). Biomimetic porous scaffolds for bone tissue engineering. *Materials Science and Engineering: R: Reports*, 80, 1-36.
- Yan, C., Hao, L., Hussein, A., & Young, P. (2015). Ti-6Al-4V triply periodic minimal surface structures for bone implants fabricated via selective laser melting. *Journal of the mechanical behavior of biomedical materials*, 51, 61-73.
- Yang, S., Leong, K.-F., Du, Z., & Chua, C.-K. (2001). The design of scaffolds for use in tissue engineering. Part I. Traditional factors. *Tissue engineering*, 7(6), 679-689.
- Yang, S., Leong, K.-F., Du, Z., & Chua, C.-K. (2002). The design of scaffolds for use in tissue engineering. Part II. Rapid prototyping techniques. *Tissue engineering*, 8(1), 1-11.
- Yang, X.-S. (2008). *Nature-Inspired Metaheuristic Algorithms*: Luniver Press.
- Yeung, W., & Smith, J. (2005). Damage detection in bridges using neural networks for pattern recognition of vibration signatures. *Engineering Structures*, 27(5), 685-698.
- Yoo, D. J. (2011). Porous scaffold design using the distance field and triply periodic minimal surface models. *Biomaterials*, 32(31), 7741-7754.
- Yu, F., Mao, Z., Jia, M., & Yuan, P. (2014). Recursive parameter identification of Hammerstein-Wiener systems with measurement noise. *Signal Processing*, 105(0), 137-147.
- Yuan, X., Ryd, L., & Huiskes, R. (2000). Wear particle diffusion and tissue differentiation in TKA implant fibrous interfaces. *Journal of biomechanics*, 33(10), 1279-1286.
- Zeltinger, J., Sherwood, J. K., Graham, D. A., Müller, R., & Griffith, L. G. (2001). Effect of pore size and void fraction on cellular adhesion, proliferation, and matrix deposition. *Tissue engineering*, 7(5), 557-572.
- Zhang, G. P. (2000). Neural networks for classification: a survey. *Systems, Man, and Cybernetics, Part C: Applications and Reviews, IEEE Transactions on*, 30(4), 451-462. doi:10.1109/5326.897072
- Zhang, Q., Lu, H., Kawazoe, N., & Chen, G. (2014). Pore size effect of collagen scaffolds on cartilage regeneration. *Acta biomaterialia*, 10(5), 2005-2013.
- Zhou, Z.-H., Wu, J., & Tang, W. (2002). Ensembling neural networks: many could be better than all. *Artificial intelligence*, 137(1), 239-263.
- Zhou, Z., Buchanan, F., Mitchell, C., & Dunne, N. (2014). Printability of calcium phosphate: Calcium sulfate powders for the application of tissue engineered bone scaffolds using the 3D printing technique. *Materials Science and Engineering: C*, 38, 1-10.
- Zhou, Z., Buchanan, F., Mitchell, C., & Dunne, N. (2014). Printability of calcium phosphate: calcium sulfate powders for the application of tissue engineered bone scaffolds using the 3D printing technique. *Mater Sci Eng C Mater Biol Appl*, 38(0), 1-10.

- Zhou, Z., Mitchell, C. A., Buchanan, F. J., & Dunne, N. J. (2013). Effects of Heat Treatment on the Mechanical and Degradation Properties of 3D-Printed Calcium-Sulphate-Based Scaffolds. *ISRN Biomaterials*, 2013 1-10.
- Zhu, M., Wang, K., Mei, J., Li, C., Zhang, J., Zheng, W., Kong, D. (2014). Fabrication of highly interconnected porous silk fibroin scaffolds for potential use as vascular grafts. *Acta biomaterialia*, 10(5), 2014–2023.

APPENDIX A

PUBLICATIONS

1. **Asadi-Eydivand, Mitra**, Mehran Solati-Hashjin, Arghavan Farzad, and Noor Azuan Abu Osman. "Effect of technical parameters on porous structure and strength of 3D printed calcium sulfate prototypes." *Robotics and Computer-Integrated Manufacturing* 37 (2016): 57-67.
2. **Asadi-Eydivand, Mitra**, Mehran Solati-Hashjin, Alireza Fathi, Mobin Padashi, and Noor Azuan Abu Osman. "Optimal design of a 3D-printed scaffold using intelligent evolutionary algorithms." *Applied Soft Computing* 39 (2016): 36-47.
3. **Asadi-Eydivand, Mitra**, Solati-Hashjin M, Shafiei SS, Mohammadi S, Hafezi M, Abu Osman NA (2016) Structure, Properties, and In Vitro Behavior of Heat-Treated Calcium Sulfate Scaffolds Fabricated by 3D Printing. *PLoS ONE* 11(3): e0151216. doi: 10.1371/journal.pone.0151216
4. **Asadi-Eydivand, Mitra**, Mehran Solati-Hashjin, Min yu Lim, and Noor Azuan Abu Osman. "Printability of the minimum pore size of the 3D-printed porous structure for bone tissue engineering applications." *International journal of precision Engineering and manufacturing.* (under review)

5. **Asadi-Eydivand, Mitra**, Mehran Solati-Hashjin, and Noor Azuan Abu Osman. " Mechanical behavior of calcium sulfate scaffold prototypes made by solid freeform fabrication method." Rapid prototyping journal. (under review)



Effect of technical parameters on porous structure and strength of 3D printed calcium sulfate prototypes



Mitra Asadi-Eydivand^{a,*}, Mehran Solati-Hashjin^{a,b}, Arghavan Farzad^a,
Noor Azuan Abu Osman^a

^a Department of Biomedical Engineering, Faculty of Engineering, University of Malaya, 50603 Kuala Lumpur, Malaysia

^b Biomaterials Center of Excellence, Amirkabir University of Technology, 15914 Tehran, Iran[†]

ARTICLE INFO

Article history:

Received 16 January 2015

Received in revised form

18 June 2015

Accepted 25 June 2015

Keywords:

Process optimization

3D printing

Mechanical properties

Bone tissue Engineering

Dimensional accuracy

Rapid prototyping

ABSTRACT

Additive manufacturing methods such as three-dimensional printing (3DP) show a great potential for production of porous structure with complex internal and external structures for bone tissue engineering applications. To optimize the 3DP manufacturing process and to produce 3D printed parts with the requisite architecture and strength, there was a need to fine-tune the printing parameters. The purpose of this study was to develop optimal processing parameters based on a design of the experiments approach to evaluate the ability of 3DP for making calcium sulfate-based scaffold prototypes. The major printing parameters examined in this study were layer thickness, delay time of spreading the next layer, and build orientation of the specimens. Scaffold dimensional accuracy, porosity, and mechanical stiffness were systematically investigated using a design of experiment approach. Resulting macro-porous structures were also studied to evaluate the potential of 3DP technology for meeting the small-scale geometric requirements of bone scaffolds. Signal-to-noise ratio and analysis of variance (ANOVA) were employed to identify the important factors that influence optimal 3D printed part characteristics. The results showed that samples built using the minimum layer thickness (89 μm) and x-direction of build bed with 300 ms delay time between spreading each layer yielded the highest quality scaffold prototypes; thus, these parameters are suggested for fabrication of an engineered bone tissue scaffold. Furthermore, this study identified orientation and new layer spreading delay time as the most important factors influencing the dimensional accuracy, compressive strength, and porosity of the samples.

© 2015 The Authors. Published by Elsevier Ltd. This is an open access article under the CC BY license

(<http://creativecommons.org/licenses/by/4.0/>).

1. Introduction

Scaffolds play an important role in tissue engineering solutions to bone healing. Bone itself is known for its self-healing ability. However, a typical bone remodeling processes may not repair large-scale bone defects, and addressing significant bone losses remains a major challenge. Bone tissue engineering (BTE) is a potential solution to this problem as it integrates the use of cells and engineered materials to restore bone tissue. BTE scaffolds must possess myriad properties to meet application requirements [1]. Essentially, BTE scaffolds must provide a host-tissue-like mechanical support to promote neo-tissue growth and function. In fact, an ideal scaffold should resemble the natural extracellular matrix (ECM) of the cells. Scaffolds can be made from either natural or synthetic materials capable of forming a helpful micro-

environment that allows proper generation of neo-tissue to repair and replace damaged or weakened organs and tissues [2]. Such scaffolds should provide sufficient porosity and permeability for nutrient transfer and removal of metabolic wastes [3]. In addition, for the reconstruction of complex bone defects such as osteoporotic fractures, we need patient-specific BTE implants with proper internal structure and mechanical properties. Appropriate materials and processing techniques should be employed to make implants and scaffolds with the requisite properties.

Rapid prototyping (RP) techniques which are promising potential fabrication methods for BTE scaffolds. RP techniques, can fabricate a complex internal and external structure based on computer tomography (CT) data or prefabricated structure design such that it is possible to fabricate scaffolds with predetermined properties [4,5].

The high reproducibility of RP is an added benefit for clinical applications [6]. RP techniques typically begin with a CT scan of the defect site that gives the necessary data for making an accurate and precise three-dimensional (3D) shape of the defect. This pattern then is used as a guide to fabricate the 3D object [7]. One

Text for Footnote 1

* Corresponding author.

E-mail address: mitra@um.edu.my (M. Asadi-Eydivand).

<http://dx.doi.org/10.1016/j.rcim.2015.06.005>

0736-5845/© 2015 The Authors. Published by Elsevier Ltd. This is an open access article under the CC BY license (<http://creativecommons.org/licenses/by/4.0/>).



Optimal design of a 3D-printed scaffold using intelligent evolutionary algorithms



Mitra Asadi-Eydivand^{a,*}, Mehran Solati-Hashjin^b, Alireza Fathi^c, Mobin Padashi^c,
Noor Azuan Abu Osman^{a,**}

^a Department of Biomedical Engineering, Faculty of Engineering, University of Malaya, 50603 Kuala Lumpur, Malaysia

^b Department of Biomedical Engineering, Amirkabir University of Technology, 15914 Tehran, Iran

^c Department of Mechanical Engineering, Babol University of Technology, Iran

ARTICLE INFO

Article history:

Received 13 April 2015

Received in revised form 3 November 2015

Accepted 3 November 2015

Available online 14 November 2015

Keywords:

Scaffolds

3D printer

Aggregated artificial neural network

(AANN)

Particle swarm optimization (PSO)

Porous structure

Mechanical strength

ABSTRACT

Fabrication of three-dimensional structures has gained increasing importance in the bone tissue engineering (BTE) field. Mechanical properties and permeability are two important requirements for BTE scaffolds. The mechanical properties of the scaffolds are highly dependent on the processing parameters. Layer thickness, delay time between spreading each powder layer, and printing orientation are the major factors that determine the porosity and compression strength of the 3D printed scaffold.

In this study, the aggregated artificial neural network (AANN) was used to investigate the simultaneous effects of layer thickness, delay time between spreading each layer, and print orientation of porous structures on the compressive strength and porosity of scaffolds. Two optimization methods were applied to obtain the optimal 3D parameter settings for printing tiny porous structures as a real BTE problem. First, particle swarm optimization algorithm was implemented to obtain the optimum topology of the AANN. Then, Pareto front optimization was used to determine the optimal setting parameters for the fabrication of the scaffolds with required compressive strength and porosity. The results indicate the acceptable potential of the evolutionary strategies for the controlling and optimization of the 3DP process as a complicated engineering problem.

© 2015 The Authors. Published by Elsevier B.V. This is an open access article under the CC BY-NC-ND license (<http://creativecommons.org/licenses/by-nc-nd/4.0/>).

1. Introduction

Additive manufacturing (AM) is a layer-over-layer manufacturing technique. In most cases, enables complex components to be manufactured that are difficult to fabricate or cannot be made using conventional methods. Among AM practices, powder-based three-dimensional printing (3DP) is the most capable technique for bone tissue engineering (BTE) applications [1–6].

Seeding and cultivating scaffolds with bone cells is the standard method in BTE. Scaffolds are highly porous 3D structures that aim to imitate the natural extracellular matrix (ECM) of bone on a temporary basis. From a technical point of view, scaffold engineering sets high demands on design and materials. In addition to chemistry, interconnected porosity, permeability, and mechanical strength are critical parameters that define the performance of a scaffold. These

factors cannot be controlled precisely through conventional fabrication processes [7–9].

The immense potential for fabrication of scaffolds due to its maximum control over porosity and its ability to reproduce the customized anatomical design with great fidelity to the 3D medical pictures are the main advantages of the powder-based 3DP [10–12].

Fig. 1 shows a schematic illustration of the 3DP process. First, the chosen physical object is modeled on a computer-aided design (CAD) system. Then, the CAD model is converted to the stereolithography (STL) file format. A software program analyzes the STL file and mathematically slices the model into cross sections based on the selected layer thickness. The cross sections are recreated using the reaction of the powder and the binder. This process is repeated layer by layer until a 3D object similar to the design is formed. During the fabrication process, the printer head jets a liquid into thin layers of powder according to the object profile created by the software. Subsequently, a build chamber (build-bed) containing the powder bed is lowered to enable the spreading of the next powder layer. Following the consecutive application of layers, the unbound powder is removed, and the 3D part is produced

* Corresponding author. Tel.: +60 1123288084; fax: +60 3 7956 1378.

** Corresponding author.

E-mail addresses: mitra@um.edu.my (M. Asadi-Eydivand), azuan@um.edu.my (N.A. Abu Osman).

<http://dx.doi.org/10.1016/j.asoc.2015.11.011>

1568-4946/© 2015 The Authors. Published by Elsevier B.V. This is an open access article under the CC BY-NC-ND license (<http://creativecommons.org/licenses/by-nc-nd/4.0/>).

RESEARCH ARTICLE

Structure, Properties, and *In Vitro* Behavior of Heat-Treated Calcium Sulfate Scaffolds Fabricated by 3D Printing

Mitra Asadi-Eydivand¹, Mehran Solati-Hashjin^{2,3*}, Seyedeh Sara Shafiei⁴, Sepideh Mohammadi², Masoud Hafezi¹, Noor Azuan Abu Osman^{1*}

1 Department of Biomedical Engineering, Faculty of Engineering, University of Malaya, 50603, Kuala Lumpur, Malaysia, **2** Biomedical Engineering Faculty, Amirkabir University of Technology, 15914, Tehran, Iran, **3** Biomaterials Center of Excellence, Amirkabir University of Technology, 15914, Tehran, Iran, **4** Stem Cell and Regenerative Medicine Group, National Institute of Genetic Engineering and Biotechnology, Tehran, 14965/161, Iran

* solati@aut.ac.ir (MS-H); azuan@um.edu.my (NAAO)



CrossMark
click for updates

OPEN ACCESS

Citation: Asadi-Eydivand M, Solati-Hashjin M, Shafiei SS, Mohammadi S, Hafezi M, Abu Osman NA (2016) Structure, Properties, and *In Vitro* Behavior of Heat-Treated Calcium Sulfate Scaffolds Fabricated by 3D Printing. PLOS ONE 11(3): e0151216. doi:10.1371/journal.pone.0151216

Editor: Jorge Sans Bums, University Hospital of Modena and Reggio Emilia, ITALY

Received: October 18, 2015

Accepted: February 23, 2016

Published: March 21, 2016

Copyright: © 2016 Asadi-Eydivand et al. This is an open access article distributed under the terms of the Creative Commons Attribution License, which permits unrestricted use, distribution, and reproduction in any medium, provided the original author and source are credited.

Data Availability Statement: All relevant data are within the paper.

Funding: This study was supported by High Impact Research Grant UM.CHIR/MOHE/ENG/14 D000014-16001 from the University of Malaya.

Competing Interests: The authors have declared that no competing interests exist.

Abstract

The ability of inkjet-based 3D printing (3DP) to fabricate biocompatible ceramics has made it one of the most favorable techniques to generate bone tissue engineering (BTE) scaffolds. Calcium sulfates exhibit various beneficial characteristics, and they can be used as a promising biomaterial in BTE. However, low mechanical performance caused by the brittle character of ceramic materials is the main weakness of 3DP calcium sulfate scaffolds. Moreover, the presence of certain organic matters in the starting powder and binder solution causes products to have high toxicity levels. A post-processing treatment is usually employed to improve the physical, chemical, and biological behaviors of the printed scaffolds. In this study, the effects of heat treatment on the structural, mechanical, and physical characteristics of 3DP calcium sulfate prototypes were investigated. Different microscopy and spectroscopy methods were employed to characterize the printed prototypes. The *in vitro* cytotoxicity of the specimens was also evaluated before and after heat treatment. Results showed that the as-printed scaffolds and specimens heat treated at 300°C exhibited severe toxicity *in vitro* but had almost adequate strength. By contrast, the specimens heat treated in the 500°C–1000°C temperature range, although non-toxic, had insufficient mechanical strength, which was mainly attributed to the exit of the organic binder before 500°C and the absence of sufficient densification below 1000°C. The sintering process was accelerated at temperatures higher than 1000°C, resulting in higher compressive strength and less cytotoxicity. An anhydrous form of calcium sulfate was the only crystalline phase existing in the samples heated at 500°C–1150°C. The formation of calcium oxide caused by partial decomposition of calcium sulfate was observed in the specimens heat treated at temperatures higher than 1200°C. Although considerable improvements in cell viability of heat-treated scaffolds were observed in this study, the mechanical properties were not significantly improved, requiring further investigations. However, the findings of this study give a better insight into the complex nature of the problem in the fabrication of synthetic bone grafts and scaffolds via post-fabrication treatment of 3DP calcium sulfate prototypes.